

THE SPECTROPHOTOMETRIC PROPERTIES OF ICY WORLDS

A Dissertation
Presented to the Faculty of the Graduate School
of Cornell University
in Partial Fulfillment of the Requirements for the Degree of
Doctor of Philosophy

by
Nicholas Walter Scott Kutsop
August 2022

© 2022 Nicholas Walter Scott Kutsop
ALL RIGHTS RESERVED

THE SPECTROPHOTOMETRIC PROPERTIES OF ICY WORLDS

Nicholas Walter Scott Kutsop, Ph.D.
Cornell University 2022

Icy worlds are the moons and small planets of the solar system which are primarily composed of volatile material, such as water, ammonia, and methane. They are geologically active bodies that may harbor the key to understanding the emergence of life, as well as natural laboratories where we can test our understanding of physical processes in environments very different from that of Earth. We study these worlds using remote sensing observations carried out by spacecraft which either orbit or flyby the target body. These spacecraft carry a range of instrumentation which observe these worlds at infrared, ultraviolet, visible, and radio wavelengths. In this thesis, I will present my investigations into the atmospheres of Pluto and Titan, as well as research on Titan's surface processes. I use observations of Pluto taken from the Multispectral Visual Imaging Camera onboard the New Horizons spacecraft to study the particle size distribution of haze in Pluto's atmosphere. From these results I am able to identify the rate of production of different sized particles and place constraints on the microphysical properties including charge and fractal dimension. I use observations of Titan taken from the Visual and Infrared Mapping Spectrometer formerly onboard the Cassini spacecraft to study stratospheric haze features and the spectral diversity of Titan's equator. From the survey I performed of the band of haze I identified in Titan's stratosphere I have found evidence supporting and expanding upon seasonal circulation models. I also determined that the stratosphere is offset from the rotation axis of Titan's solid body and is fixed in an inertial reference frame. I developed several techniques to expand the usable Cassini data and optimize observations of Titan's surface. From this investigation I discovered a series of compositional pathways at Titan's equator which provide evidence to explain erosion and sediment transport processes.

Biographical Sketch

I was born and raised in Mountainside, New Jersey. I attended Deerfield Elementary and Middle School, Governor Livingston High School, Northern Arizona University, and Cornell University. My earliest memory of astronomy was in kindergarten when my teacher, Ms. Gerding, showed us a picture of a new spacecraft. Considering this was 1997, this may have been the Cassini-Huygens spacecraft, which is ironic as 25 years later I wrote this thesis in large part based on the work done with the Cassini-Huygens. I didn't realize this until a few years ago but I was introduced to science and engineering by my Grandpa, Walter Kutsop. I went over to his house every day and he taught me how to work with tools, build things, and take things apart. As I write this, it is 9:00PM and I am hunched over my laptop with a single light directly overhead. I can't help but be reminded of working late into the night at my Grandpa's workbench, taking apart a radio or lawn mower as the single bulb with a pull string hangs above me. I fell in love with planetary science after reading a book in the library about Mars in the second grade. Ever since the Mars Exploration Rovers started sending back images of Mars' surface, I've wanted nothing more than to work on missions and spacecraft. My first research experience was with Nadine Barlow, studying the sinuosity of lobate Martian crater ejecta with the THEMIS instrument. While I've come to work on many projects since then, I will always have a special place in my heart for impact craters. I was born Catholic but only truly discovered my faith in high school thanks to Gregory "Coach Dunk" Dunkerton. Since then I have come to embrace my faith and am a proud Catholic scientist.

For Dr. Barlow, thank you for teaching me how to be a professional astronomer.

For Grandpa, thank you for giving me my first workshop and fostering my curiosity and problem solving.

And for Corrie, thank you for helping me become a better person and for being my best friend. I never would have made it through without your support and love. I love you with all my heart and soul.

Acknowledgements

Becoming a planetary scientist has been a dream of mine since I was 8 years old. Now, over two decades later, I have finally reached the summit of the first mountain on that journey with the receipt of my doctorate. For years I have been both dreaming about and dreading writing these acknowledgments. Dreaming, because there are some people who have truly left their mark on my life, who have forever changed me for the better, and I'll finally be able to put to paper my deepest gratitude. Dreading, because there is no way I could thank everybody, and I know some people will be left out. To those who look through and see I've only written a short note, or worse, left their name out altogether, please know that you haven't been forgotten. If you feel like you were my friend and that you helped me along the way, you are absolutely correct! You did! Even if we only chatted once a month while in the elevator, you were still a part of my life and my experience would have been lesser without you.

First, and foremost I would like to thank my committee, **Alex Hayes, Jonathan Lunine, Christophe Sotin, Steve Squyres, and Terry Herter**. Thank you all for your guidance and support these last eight years.

Alex Hayes. I don't really remember the first time I saw your name. I'm pretty sure I was doing some research at Cornell after I heard Steve give a keynote address in Flagstaff. But I do remember what Nadine said when I asked her about you and if you would be a good advisor. She said that you were young but a "super star, rising rapidly." She was right; since joining your group I've seen you grow by leaps and bounds as a scientist, father, and advisor. One of the first things I appreciated about you was your desire to build a good group. You let us know, in word and actions, that we were working together, not working for you. You also encouraged us to come to you with brutally honest criticism and what's more, you took those criticisms to heart and always tried to do better. But what I've come to admire most about you is that you deeply care about the students you work with and that you'll stand rock solid in their corner. I never once had to truly worry about my funding because you made it clear from day one that for however long I was here you would support me. That security allowed me to venture off and explore my science in ways I never could have with many advisors. No matter what I needed you always did your best to provide it for me, be that a laptop, time off, or by ingratiating me into a vast network of collaborators. When potential students ask me what it's like working with you, the first and last thing I always say is "No matter what, Alex will always have your back." So from the bottom of my heart, thank you Alex. Thank you for your unyielding support and unflinching determination to get me across the finish line.

Jonathan Lunine. *"For where two or three have gathered together in My name, I am there in their midst. Mathew 18:20."* Some are lucky to have one advisor who cares deeply for their

success, few can say they had two advisors who worked tirelessly for their students. It has been a blessing to have you as an advisor Jonathan. You have always supported me, even when my ideas are just tiny sparks which may look silly to others. Talking to you always made me feel confident and helped stabilize me as I battled self-doubt and impostor syndrome. Through your example I grew my confidence not only as a scientist, but also as a Catholic scientist. I have watched as you've given invited lectures to hundreds of our colleagues, and I've watched you read scripture before our community, both delivered with the same zeal, conviction, and faith. So thank you Jonathan. Thank you for being my mentor to the stars and my brother in Christ.

Christophe Sotin. Dare Mighty Things. Christophe, you obviously recognize this as the motto of JPL. The ironic thing is before I ever knew this motto, Alex asked me in the first month of grad school to dare and head out to JPL every winter and summer to work with you. And this leap of faith has borne such great fruits, as you introduced me to VIMS, fostered my curiosity and creativity, established collaborations with stalwart colleagues, and welcomed me into your home both in Pasadena and Nantes. I have greatly appreciated how supportive you have been of my science and how you are always interested in looking at new cool image. I also appreciate your sense of humor, because I'm sure I would have been kicked to the curb long ago for all my old jokes by anybody else. Thank you Christophe for completing my trifecta of advisors and helping me accomplish my dreams. And thank you for introducing me to Titan.

Avani "Nani" Gowardhan. You were my first friend at Cornell and I shudder to think how close I came to losing your friendship. I guess I have the boy to thank for that (even if I did suggest you dump him ...). You blend together cutting honesty with gentle compassion, all wrapped in a snarky 1-meter bundle. Thank you for being one of my best friends and helping me make it through. I love you!

Eiden Leung. You are such a special person to me. At times you utterly perplex me, but it is that unique quality of your personality that I've come to cherish. Your kindness and friendship do not come from any courtesy or societal pressure, you love me for who I am because that is what you want, nothing more, nothing less. I am honored that you turn to me in times of distress and I in turn, am blessed to have such a reliable friend I can always turn to. Thank you for being one of my best friends, so much so that I think of you as family. I love you!

Jack Madden. Hey buddy. I finally did the thing. You, more than anyone else, know how hard this was, and I'm really lucky to have you by my side. I seem to be drawn to people with ... interesting ... personalities (like attracts like I suppose!) and I wouldn't have it any other way. You are one of the most stalwart people I know. Your sense of responsibility and duty let me truly feel at ease around you. You are one of very few people who I can trust utterly

and let them help me with some of my responsibilities. Thank you for being one of my best friends and helping me through the tough times. I love you!

Father Joe Marcoux. Thank you, padre, for all the love and support you've given me over the years. You have seen me at my very lowest and each time you've lifted me back up. I really would not have made it through without you. Thank you for keeping me on the path and bringing me back to God every time I strayed. I thank God from the bottom of my heart that I was able to meet you because you are such an incredible person. So thank you, padre, and God bless you.

Chloe Seigel. There's so, so much I want to thank you for but just can't here and that breaks my heart. So instead I'll thank you for introducing me to so many wonderful people, helping me learn more about myself. I am a better person for having known you. You are perfect and I love you!

Marika Leitner. You have been my friend for years and I've always appreciated your company. But one of the silver linings to the pandemic is that I was able to build such a stronger relationship with you. You've now become one of my very dear friends and you've taught me so much about being an empathetic and kind person. I love you!

Jordan Johnson. I've only known you for less than a year but you've already left a mark on my life. I hope we can continue to grow our friendship because I think you're pretty cool and one of my dear friends. Thank you for helping me get across the finish line. I love you!

Paul Corlies. Thank you for just being such a great and funny person. My nights in the office would have sucked way more without you around. You really are one of the kindest people I know and I'm lucky to have you as a friend.

Mary Mulvanerton. You are beyond kind and took care of me as if I were family. The light of Christ shines out of you with incredible radiance. Thank you for being my friend and making sure I stayed out of trouble!

Cece Thieberger. I checked and I can't put emojis in my thesis, but if I could I would give you the rolling eyes and flat expression. But, I guess I am one of the luckiest mentors in the world for having a mentee like you. I'm so proud of you and really fortunate to call you a friend. You are going to do incredible things and I can't wait to see them!

Ken Lawrence. Thank you for not kicking me out of your office, no matter how obnoxious I got. You really are a great friend and helped me become the scientist I am today.

Phil Nicholson. I don't know if anyone knows this but for a long time I've thought of you as my secret fourth advisor. I truly appreciate you always letting me bug you and making sure I didn't stay too late. Thank you for all the help, guidance, and patience you've given me.

To my family, who have loved me, raised me, supported me, and helped me grow into the man I am today, thank you!

Dad, Mom, Sharon, Julie, Jaxxon, Ashleigh, Brittany, McKenna, Ma, Shiloh, Ethan, Paige, Mr. Seigenthaler, Uncle Dale, Tante Carol, Oma, Grandma Spinelli, Aunt Joyce, Uncle Joe, Aunt Lori, Uncle Frank, Aunt Pam, Mooma, Mary Ann, Betty, Uncle Phil, Julius, Ellie, Mr. Korn, Mrs. Korn, Jenny, Baba, Christian, Nicole, Charlie.

To all my friends who have made sure the building was clean, my paycheck came on time, supported me spiritually, and in general fixed all the problems and disasters I created, thank you!
Ed Anderson, Fr. Joe Astarita, Monica Carpenter, Doug, Jamie Householder, Jason Jennings, Jessica Jones, Fr. Matt Lowry, Dave Pawelczyk, Tom Shannon, Lynda Sovocool, Bez Thomas

To all the incredible colleagues who have generously shared their brilliance and friendship with me, thank you!

Jason Barnes, Megan Barrington, Sam Birch, Lea Bonnefoy, Ellen Czaplinski, Siteng Fan, Kendra Farnsworth, Randy Gladstone, Paul Helfenstein, Jason Hofgartner, Yu-Cian Hong, Abhinav Jindal, Klára Kalousová, Rick Kline, Carrie Lawrence, Weigang Liang, Rosaly Lopes, Tom Lored, Shannon MacKenzie, Mike Malaska, Marco Mastrogiuseppe, Julia Miller, Samantha Moruzzi, Stéphane Le Mouélic, Maryame El Moutamid, Connor Nixon, Valerio Poggiali, Zoe Learner Ponterio, Marica Raguso, Pascal Rannou, Julie Rathbun, Sébastien Rodriguez, Ashley Schoenfeld, Benoît Seignovert, Jason Soderblom, Bridgette Sotin, Henrik Spoon, Steve Squyres, Harry Tang, Christian Tate, Peter Thomas, Zibi Turtle, Georgios Valogiannis, Amit Vishwas, Lukas Wenzl, Leslie Young, Xinting Yu

To my professors and mentors who always let me pester you, thank you for your patience, insight and guidance!

Lori Allen, Gary Bowman, Bonnie Buratti, William "Buzz" Delinger, David Cole, Gregory Dunkerton, Kathy Eastwood, Peter Gierasch, Mark James, Lisa Kaltenegger, Bart De Pontieu, David Trilling

To my furry friends who gave me the best snuggles and unconditional love, thank you!
Link, Puck, Layla, Fred, Anak (not Willow)

To the communities, businesses, and institutions that have taught me, provided me with friendship and fed me, thank you!

St. Catherine's of Siena, Ithaca Bakery, Space Science Building, Jet Propulsion Laboratory, NASA, NOIRLab, Astronomy Grad Network, Crunch, Society of Physics Students, Black Diamond, Cornell Catholic Community, NAU Newman Center, St. Joseph's, Our Lady of Lourdes, Assumption of the Blessed Virgin Mary, Cornell University, Northern Arizona University, California Institute of Technology

To the angels and saints who always kept me in their prayers, thank you!

St. Thomas Aquinas, St. Nicholas of Myra, St. Dominic, St. Michael, St. Raphael, St. Jude the Apostle, St. Roche, St. Gertrude of Nivelles, St. Francis of Assisi, St. Drogo of Sebourg

Holy Mary, Mother of God

Thank you for being my greatest advocate, my queen and my mother, and echoing my prayers to our Lord.

Jesus Christ, God the Father, and the Holy Spirit

Through your grace I have accomplished great things. I can never thank you enough for the countless blessings you've given me. Thank you for the many people you placed along my path, some of whom are mentioned above. Thank you for answering my prayers. Thank you for your love. Thank you for the incredible life that you gave me through your salvation. Thank you, thank you, thank you.

Table of Contents

Title	
Copyright	
Abstract	
Biographical Sketch	iii
Dedication	iv
Acknowledgements	v
Chapter 1: Introduction and Organization of Dissertation	1
1.1 Titan	5
1.2 Pluto	9
Thesis Organization	12
Chapter 2: The Development of Haze	16
1. Introduction	16
2. Data Reduction	20
2.1 MVIC Data	20
2.2. Phase Curves	23
3. Modelling	26
3.1. Radiative Transfer	26
3.2. Grid Search and Statistics	27
3.3 Size distribution	28
3.4. Population Types	31
3.4.1 Monodisperse and Log-Normal	32
3.4.2 Bimodal	34
3.4.3 Power-Law	35
3.4.4 Trimodal	40
4. Results	43
4.1. Three Regime of Populations	43
4.2 Fractal Dimensions	45
4.3 Growth Mechanics and Implications	48
5. Summary and Conclusions	53
Chapter 3: The Circulation Patterns of Atmosphere	56
1. Introduction:	56
1.1. The Equatorial Annulus	61
1.2. The North Polar Annulus	62
1.3. The South Polar Annulus	62
2. Data/Methods	63

2.1. Data Correction and Mosaicking	63
2.2. Identifying the Annuli Through Transects	64
2.3. Altitude from Spectra/Spectraltimetry	67
3. Results & Seasonality	72
3.1. Secondary Annuli	72
3.2. When do we see the annuli?	73
3.3. Changes during Cassini	76
3.4. The tilted pole	78
4. Discussion	82
4.1. Detailed Explanation of the Spectra	82
4.1.1. 300-500nm	82
4.1.2. 500-700nm	83
4.1.3. 700-2000nm	83
4.2. Origin and Evolution of the Annuli	85
4.2.1. Formation of the North Polar Annulus	85
4.2.2. Evolution of the North Polar Annulus	86
4.2.3. Evolution of the Equatorial Annulus	87
4.2.4. Formation of the Equatorial Annulus	88
4.3. Using the Annuli to Track the Stratosphere	89
4.3.1. The Tilt of Titan's Stratosphere	89
4.3.2. Testing Rotation Rates	91
5. Conclusion	92
Chapter 4: The Compositional Diversity of Surfaces	96
1. Introduction:	96
2. Data/Methods	99
2.1. Data Correction and Mosaicking	99
2.2. Spectral Clustering	103
2.3. Spectral Analysis	108
3. Results	113
3.1. Spectral Units	113
3.2. Sequences and Pathways	114
3.3. Delta-Spectra	116
4. Discussion	119
4.1. Distribution of Units	119
4.2. Interpretation of the Spectral Gradient	123
5. Conclusion	127
Chapter 5: Summary and Future Work	129
Summary	130

Future Work	131
Appendices	134
Appendix A. Data Processing	134
Appendix B. Off Disk Glow Correction	135
Appendix C. Error	137
Appendix D. Radiative Transfer	137
Appendix E. Phase Function	140
Appendix F: VIMS-Vis Destriping	141
Appendix Figures	143
References	162

Chapter 1: Introduction and Organization of Dissertation

The icy-worlds of the solar system are moons and dwarf planets which are composed of significant amounts of volatile material, either on the surface or in the interior (Figure 1). The first observations of this type of world were first described in Galilei 1610 with the observations of Europa and Ganymede. With Voyager 1 and 2's grand tours of the solar system, we acquired our first high spatial resolution observations of these worlds at a wide range of phase angles. We have found that icy-worlds are geologically complex and diverse, as much or more so than their silicate rich relatives. Several icy-worlds also have atmospheres with intricate weather systems and seasonal patterns. By studying icy-worlds we can investigate planetary processes in disparate environments, allowing us to better understand the links between composition, environment, and physical process. Perhaps the most compelling feature of icy-worlds is their potential to harbor



Figure1 Montage of icy worlds with the Earth's moon shown for scale, courtesy of Emily Lakdawalla/Planetary Society. For satellites labeled in blue there are geophysical measurements implying the presence of a subsurface ocean (Figure from Nimmo & Papalardo 2016).

life. These worlds are rich in organics and many have oceans of water tens to hundreds of kilometers below their icy crusts. Some of these ocean-worlds have oceans that are in direct contact with rocky cores, potentially mimicking environments on Earth (such as the mid-Atlantic ridge) where life may have started. Through our exploration of these worlds, we are furthering our search for the key to understanding the emergence of life.

In this dissertation I describe my investigations into the two icy-worlds most recently targeted by spacecraft missions; Titan (Cassini 2004-2017) and Pluto (New Horizons 2015). Both of these worlds have diverse geologies, evidence of recent/ongoing processes, and complex atmospheres with seasonal circulation patterns and active photochemistry. By studying the spectrophotometric properties of these worlds I have produced insights into their evolution and ongoing processes. These insights develop our knowledge of icy-worlds in general, which in turn expands our understanding of planetary science. I accomplish this through comparative planetology, whereby different natural processes and systems are studied by their effects and phenomena on and between multiple bodies. This is possible given the frequency of common features across the solar system including clouds, haze, impact craters, mountains, dunes, lakes, rivers, deltas, tectonic features like cracks and rifts, and endogenic features like volcanos and geysers. In this dissertation I draw conclusions about the processes that shape icy-worlds by comparing these and other features which appear on multiple bodies.

Spectrophotometry is a portmanteau of spectroscopy and photometry; it is the science where we measure the brightness of radiated light at different wavelengths. The way that light is scattered is dependent on the properties of the scattering object or medium. Laboratory measurements and theory form the foundation for understanding how light is scattered, and provides references we can use to identify the nature and properties of objects we cannot

investigate physically. This is the underlying principle of remote sensing, where we detect and monitor the physical characteristics of an area by measuring its reflected and emitted radiation at a distance. In this dissertation I demonstrate how I have used radiative transfer, spectra and phase curves to uncover the evidence which informs my science.

Radiative transfer is the physical phenomenon of energy transfer in the form of electromagnetic radiation. The propagation of radiation through a medium is affected by absorption, emission, and scattering processes. For planetary science, the most commonly invoked radiative transfer equation is the bidirectional reflectance distribution function (BRDF). This is a function of four real variables that defines how light is reflected at an opaque surface. In this dissertation I will also present the limb scatter technique which dictates the transfer of light in an optically thin environment as viewed from a tangent position. A material is opaque, transparent, or optically thick or thin, based on the optical depth, τ , which is the natural logarithm of the ratio of incident to transmitted radiant power through a material. A medium becomes opaque at $\tau=1$; we say a medium is optically thin if $\tau \ll 1$. The reflectance spectrum of a material shows how strongly certain wavelength of light are scattered or absorbed. The strength of the scattering or absorption of incident light is dependent on the composition and structure of the material, as well as the thermal, magnetic, and relativistic environment the material is in.

The phase curve describes the brightness of a scattering target subject to a known illumination geometry, denoted by the phase angle, θ . The phase angle is the angle formed between the incident vector and the emission vector. The incident vector starts at the illumination source, usually the Sun, and ends at the target, while the emission vector starts at the observer, either a spacecraft or telescope, and ends at the target. The phase angle, θ , is defined as

$$\theta = \cos^{-1}(\cos(i) \cos(e) + \sin(i) \sin(e) \cos(\psi)) \quad \text{Eq.1}$$

where i is the incidence angle, which is formed between the incident vector and the normal vector of the target, e is the emission angle, and ψ is the azimuthal angle, which is the angle between the projection of the incidence and emission vectors onto the horizontal plane defined by the normal vector. Depending on the field, the scattering angle α is sometimes used in place of θ where $\alpha = 180^\circ - \theta$. Throughout this thesis I use the phase angle θ . The area under the phase curve describes the intensity of all photons scattered from a single point. Depending on the physical properties of the material the light can be scattered diffusely (i.e. matte finishes) or specularly (i.e. a mirror) with most scattering events falling between these two extremes. The most commonly used photometric function in planetary science used to describe the scattering properties of a solid surface is the Hapke function:

$$R(\mu_0, \mu, g) = \frac{\omega_0}{4\pi} \frac{\mu_0}{\mu_0 + \mu} \{ [1 + B(g)]P(g) + H(\mu_0)H(\mu) - 1 \} S(\theta) \quad \text{Eq.2}$$

where μ_0 , μ are the cosines of the incidence (μ_0) and emergence (μ) angles, $B(g)$ is the backscattering function, $H(\mu)$ is the multiple scattering function, $S(\theta)$ is the function for macroscopic roughness, $P(g)$ is the phase function [Hakpe 1981]. Within these functions are the six ‘‘Hapke parameters’’ which describe the physical properties of a solid surface. These include the single scattering albedo, ω_0 , the opposition surge, h , the strength of the opposition surge, B_0 , the phase function, g or P_{11} , and the macroscopic roughness, θ .

1.1 Titan

Table 1

Orbital and physical characteristics of Titan, Pluto, Earth, and the Moon

	Titan	Pluto	Earth	Moon
<i>Mass (10^{20} kg)</i>	1346	130.3	59720	734.2
<i>Radius (km)</i>	2575	1188	6371	1737
<i>Mean Density (kg/m^3)</i>	1880	1854	5520	3344
<i>Gravity (g)</i>	0.14	0.06	1.00	0.17
<i>Visual Geometric Albedo</i>	0.22	0.52	0.37	0.14
<i>Rotation Period (Earth days)</i>	15.95	6.39	365.25	27.32
<i>Orbital Period (Earth years)*</i>	29.46	247.9	1.00	1.00
<i>Solar Semi-Major Axis (AU)*</i>	9.58	39.48	1.00	1.00
<i>Eccentricity*</i>	0.06	0.24	0.02	0.02
<i>Axial Tilt to Ecliptic</i>	26.73°	122.5°	23.44°	1.54°
<i>Inclination to Ecliptic</i>	2.49°	17.16°	0.00°	5.10°

* Values are for system barycenter

I first learned about Titan because I didn't do my homework in my senior year high school science class. To not fail the class, the teacher gave me the chance to write a report on a science paper, and since he knew I like astronomy he recommended I read the then recently published *The Moon That Would Be a Planet* by [Lorenz & Sotin 2010](#). This dissertation, where I can share all that I've learned about the world I fell in love with, is the realization of dream over a decade old.

Titan is the largest moon of Saturn first described in [Huygens 1659](#). In Table 1 I detail the orbital and physical characteristics of Titan and Pluto, as well Earth and the Moon for comparison. Since first visited by Pioneer 11 and Voyager 1&2, Titan has experienced one and half years. Our longest continuous observation of Titan with a spacecraft was from 2004 to 2017 with the Cassini spacecraft which observed Titan for roughly half its year, starting a little after winter solstice (the planetocentric longitude of the Sun from Saturn of, $L_s \approx 295^\circ$) and ending around summer solstice in the north ($L_s \approx 90^\circ$). The *Cassini-Huygens* mission consisted of the Cassini spacecraft and the Huygens probe.

The *Cassini-Huygens* mission consisted of the Cassini spacecraft and the Huygens probe. The mission was a joint operation of NASA, ESA, and ASI, with each organization providing equipment and expertise. On board Cassini was a variety in situ instrument to investigate fields, particles, and waves and remote sensing instrument capable of observing most of the spectrum from the extreme ultraviolet (~50 nm) to the far infrared (1 mm). From near to far the remote sensing instruments are the, Ultraviolet Imaging Spectrograph (UVIS), Visible and Infrared Mapping Spectrometer (VIMS), Imaging Science Subsystem (ISS), and Composite Infrared Spectrometer (CIRS). Cassini also carried a radar suite capable of active and passive sensing of microwave radiation (2.2 cm) which had the explicit mission objective to view Titan's surface through its atmosphere. The Huygens probe was also explicitly tasked with investigated the surface of Titan through insertion and in situ exploration. The Huygens probe parachuted through Titan's atmosphere on January 14th, 2005. Onboard it carried the Huygens Atmospheric Structure Instrument (HASI), Doppler Wind Experiment (DWE), Descent Imager/Spectral Radiometer (DISR), Gas Chromatograph Mass Spectrometer (GC/MS), Aerosol Collector and Pyrolyser (ACP), and Surface Science Package (SSP). The Huygens probe provided our only images of Titan's surface at resolutions better then 100m, reaching as low as sub centimeter scale. The Huygens probe also produced the "Huygens atmospheric profile" which is the point of reference for many radiative transfer and atmospheric models of Titan ([Fulchignoni et al. 2005](#)).

Titan is the only dense, nitrogen-rich atmosphere in the Solar System aside from Earth's. Titan's atmospheric temperate vs pressure is structured in the same way as Earths, with a troposphere, stratosphere, mesosphere, thermosphere and all the associated inversion layers ([Fulchignoni et al. 2005](#)). In the troposphere the atmosphere is roughly 5% methane (CH₄), 94% nitrogen (N₂) and 1% hydrogen and trace chemicals [[Broadfoot et al. 1981](#); [Hanel et al. 1981](#);

[Strobel & Shemansky 1982](#); [Strobel et al. 1993](#); [Vervack et al. 2004](#)], with a pressure of 1.5 bars and temperature of about 94 to 96 K. The temperature and pressure of Titan's troposphere is near the triple point for CH₄. This results in a methane cycle similar to the water cycle on Earth. As such, Titan is the only other body in the solar system with standing bodies of liquid in the form of lakes, seas, and rivers full of methane and ethane (C₂H₆). The thick atmosphere and active fluvial cycle results in erosion and sediment transport which shapes the surface of Titan into landforms similar to Earth.

Higher in the atmosphere, in the thermosphere, high energy photons and charged particles disassociate CH₄ and N₂ [[Yung et al. 1984](#); [Lavvas et al. 2008a, 2008b](#)]. The products of this photolysis recombine in a cascading series with one another in to form long chain hydrocarbons, polycyclic aromatic hydrocarbons (PAH), and nitriles [[Lebonnois et al. 2002](#)]. As these recombination products drift down through the atmosphere they clump together to form larger fractal aggregates particles, which take the form of haze [[Cabane et al. 1993](#); [Rannou et al. 2003](#); [Tomasko et al. 2008](#)]. Organic haze is one of the common features between icy worlds with any atmospheres. I discuss in Chapter 1 the formation of haze at Pluto and report evidence which substantiates the claim that Titan and Pluto's hazes are similar. Titan's haze is predominantly located in the stratosphere [[Catling & Kasting 2017](#)]. Noteworthy haze features include a globally extensive thin layer of detached haze (the detached haze layer; [[Smith et al. 1981](#); [Rages & Pollack 1983](#); [Rannou 2000](#); [Teanby et al. 2009](#); [West et al. 2018](#); [Seignovert et al. 2021](#)]), a hemispheric asymmetry in brightness (the north–south asymmetry; [[Sromovsky et al. 1981](#); [Smith et al. 1982](#); [Tomasko & Smith 1982](#)]), and polar hoods that occur during local winter (i.e., the north and south polar hoods; [Lorenz et al. 1997](#); [West et al. 2016](#); [Le Mouélic et al. 2018](#); [Seignovert et al. 2021](#); [Penteado et al. 2010](#)). In Chapter 2 I will discuss stratospheric haze bands formed by Titan's unique

seasonal circulation patterns. The stratospheric haze bands have been observed previously, but my work describes for the first time the link between the various haze bands and traces their appearance across half a Titan year. In my work I also discuss my discovery of four smaller haze bands present at mid-latitudes.

Titan does not have circulation cells in the same way we do on Earth, instead the troposphere vacillates between a global circulation cell in the summer and winter, and two symmetric cells that converge at the equator during fall and spring. This is produced by Saturn's obliquity (the angle of the rotation axis from the ecliptic, 29.7°) which causes the meridional circulation to be asymmetric about the equator and to reverse semiannually (Lebonnois et al. 2012; Teanby et al. 2012). The flow rises in the summer polar region and descends in winter polar regions. As the cells redistribute the heat in Titan's atmosphere, it also vertically transports gases and aerosols to high altitudes, transports them horizontally across the globe, and carries them back down to lower altitudes. During the fall and spring seasons, the single pole-to-pole cell splits into two symmetric cells, where the atmosphere ascends at the equator and descends at each of the poles (Mitchell et al. 2006; Tokano 2011; Newman et al. 2016; Lora et al. 2019; Battalio et al. 2022). Titan's stratosphere is also super rotating, which means the stratosphere is spinning faster than the solid body of Titan. The results of several global circulation models show that the super rotation is in agreement with the Gierasch–Rossow–Williams (GRW) mechanism for producing superrotations (Hörst 2017). In the GRW mechanism, angular momentum is transported to higher altitudes and then poleward by mean meridional circulation and is transported down and to the equator by barotropic waves generated by instabilities on the edges of the high-latitude jets (Gierasch 1975; Rossow & Williams 1979; Hourdin et al. 1995; Lebonnois et al. 2014). Analysis of the stratospheric super rotation by the Cassini Composite Infrared Spectrometer (CIRS)

revealed the stratosphere to be tilted 4° with respect to the solid-body rotation axis (Achterberg et al. 2008). In Chapter 2 I will discuss how we use the stratospheric haze bands to track the orientation of the stratosphere. I then discuss how the orientation of the stratosphere as a function of time/season informs us about the origin of the stratospheric tilt.

Titan's haze falls out of the atmosphere and settles on the surface as a meters thick coating. The haze is also the original source of material for the dunes at Titan's equator [Lorenz et al. 2008]. The haze particles however, are on the order of $1 \mu\text{m}$ while the sand dune particles are on the order of hundreds of microns. Several mechanisms have been suggested to explain the growth in particle size including sintering, lithification and erosion, flocculation, and evaporation [Barnes et al. 2015]. Given a lack of evidence for a fluvial environment at the equator and the inability for dune material to survive transport from the poles to the equator the leading theories are sintering and lithification and erosion [Charnay et al., 2015; Malaska et al., 2016; Yu et al. 2018; Brossier et al., 2018; Solomonidou et al., 2018]. Sintering is the process of forming a solid mass of material by heat or pressure without melting it to the point of liquefaction. Lithification is the process in which sediments compact under pressure, expel fluids, and gradually become solid rock. In this scenario methane rain and haze form temporary crusts on the surfaces at the equator which are then quickly eroded away by aeolian processes [Barnes et al. 2015]. Titan's dune fields are one of its most distinct features spectrally and morphologically. In Chapter 3 I discuss the spectral characteristics of the dunes and discuss how they relate to the surrounding terrain.

1.2 Pluto

I was finishing my first year of grad school when New Horizons flew by Pluto and a few months before, the Dawn spacecraft entered into orbit around Ceres. If I had been asked at the time what we would see, I would have said that Ceres was going to be very diverse and Pluto was going

to be old, heavily cratered, and otherwise featureless. We now know that those predictions could not have been more incorrect. These missions were my first time as a professional astronomer that I experienced the highest resolution observation of a world jump by several orders of, revolutionizing our understanding of a world. I imagine I must have felt what those astronomers that witnessed Mariner's first observations of Mars or Pioneer's observation of Saturn's ring must have felt. I think this was the first time I fully internalized that there is still so much to discover and that I was now at the forefront of planetary science and exploration.

Pluto was first observed from Lowell observatory by Clyde Tombaugh in 1930 [Tombaugh 1930]. On 2015 July 14, the New Horizons spacecraft flew within 12,500 km of Pluto's surface providing the first high spatial scale observations of Pluto over a wide range of phase angles. These observations revealed the Pluto has a surface with diverse geologic landforms and an atmosphere with haze and ongoing photochemistry.

New Horizons was the second mission to launch as a part of NASA's New Frontiers initiative. New Horizons used Jupiter to slingshot itself out towards Pluto. While flying by New Horizons was able to take high resolution images of Jupiter and all four Galilean satellites, including observing a 300 km high eruption of the volcano Tvashtar on Io in real time. On board new horizons were a series of in situ and remote sensing instruments including; Long-Range Reconnaissance Imager (LORRI), Pluto Exploration Remote Sensing Investigation (PERSI) which contained Alice (an ultraviolet imaging spectrometer) and Ralph (a telescope and two cameras), MVIC (Multispectral Visible Imaging Camera), a visible-light CCD imager with broadband and color channels; and LEISA (Linear Etalon Imaging Spectral Array), a near-infrared imaging spectrometer, and Radio Science Experiment (REX). After it's encounter with the Pluto system,

New Horizons went on to observe Arrokoth, a contact binary Kuiper belt object which is the farthest object in the solar system to ever be visited by a spacecraft.

Pluto stands as the poster child for trans-Neptunian objects (TNOs) and Kuiper-belt objects (KBOs), and it is the gateway to understanding objects of this region. In this way Pluto becomes a point of comparison, or a reference points which allows us to extrapolate the high resolution observation of Pluto to the observation of other TNOs which is limited to albedo, color, spectral, and orbital analysis. Studying TNOs in general provides insight into the oldest, least processed bodies in the solar system and how objects like asteroid, centaurs, and comets relate to one another. It also helps us to understand how some moons like Triton and Phoebe may have come to be captured. By studying the composition, dynamics, and orbital parameters of these bodies (such as distance or resonance) we find evidence we can use to expand our understanding of solar system formation and planetary evolution. This information extends into terrestrial planetary science as well as the leading explanation for Earth's water is by delivery from TNOs (comets). A mystery still being solved is how Venus, Earth, and Mars, wound up three drastically different environments despite similar sizes and similar orbital distances. Understanding the history and complexity of the Kuiper belt (30 to 50 AU) and Oort cloud (2,000 to 200,000 AU) will provide evidence to solve questions of the inner solar system (< 2 AU).

Pluto is locked in synchronous orbit with its largest moon Charon. Crater density shows that Pluto has terrains of various ages. One of the younger areas is Sputnik Planitia. This is a large patch of bright exposed nitrogen ice antipodal to Charon. Topography suggests that Sputnik Planitia is an ancient impact crater. The nitrogen ice displays hexagonal patterns with small rocks in the crevices between hexagons. These hexagons are likely produced by internal convection. Surrounding Sputnik Planitia are a series of mountains. To the east is Tombaugh Regio and to the

south is Norgay Montes. Among Norgay Montes is a deep pit next to a series of mountains. This may be indicative of cryovolcanism on the surface. From Tombaugh Regio we can see what appears to be glaciers of solid nitrogen flowing into Sputnik Planitia. To the southwest of Sputnik Planitia is Cthulhu Regio. Cthulhu Regio has the highest crater density on Pluto and is a dark red color, indicative of old terrain covered in organic materials, possibly tholins.

Pluto has one of the thickest atmospheres among icy worlds. High phase angle observations revealed Pluto is surrounded by haze, whose color and phase functions are consistent with fractal aggregates. Pluto's atmosphere is divided into roughly 20 regularly spaced haze layers from 80 to 150 km high, which is likely the result of pressure waves created by airflow over Pluto's mountains. In Chapter 1 I will discuss how Pluto's haze is uniquely distributed in either a bimodal distribution or a power law distribution, with high amounts of small particles, a substantial amount of large particles, and a paucity of intermediate size particles.

Thesis Organization

My dissertation will go from the top of the icy-worlds atmosphere moving down to the surface. I begin the dissertation by discussing the formation of haze at Pluto. Then I will discuss my observations of stratospheric haze bands at Titan, and what we can learn about circulation and seasonal patterns from the presence and location of these annuli. I will move onto the surface and discuss the spectral distinctness of Titan's equator and how I separated the equator into spectral units. From the spectral units and the patterns they form, I have found correlations between spectral units and geomorphologic units, as well as how the spectra changes across the equator. I will finish my dissertation by presenting the data correction techniques I developed to facilitate this research. In each chapter of my thesis I provide an introduction which goes into greater detail relevant for the topic discussed.

Chapter 2: The Development of Haze

The New Horizons spacecraft observed Pluto and Charon at solar phase angles between 16° to 169° . Herein, we use the Multispectral Visible Imaging Camera (*MVIC*) observations to construct multiwavelength phase curves of Pluto's atmosphere using the limb scatter technique. Observational artifacts and biases were removed by using Charon as a representative airless body. The size and distribution of the haze particles were constrained using a Titan fractal aggregate phase function [Tomasko et al. 2008]. We find that monodispersed and log-normal [Gao et al. 2017] populations cannot simultaneously describe the observed steep forward scattering, indicative of wavelength-scale particles, and the non-negligible back scattering indicative of particles much smaller than the wavelength. Instead, we find it necessary to use bimodal or power law distributions, especially below ~ 200 km, to properly describe *MVIC* observations. Above 200 km, where the atmosphere is isotropically scattering, a monodisperse, lognormal, or a bimodal/power law approximating a monodispersed population is able to fit the phase curves well. Compared to previously published distributions [e.g., Gao et al. 2017], we find that Pluto's atmosphere must contain haze particle number densities an order of magnitude greater for small (~ 10 nm) and large ($\sim 1\mu\text{m}$) radii, and relatively fewer intermediate sizes (~ 100 nm). These conclusions support a lower aggregate aerosol growth rate than Gao et al. 2017, indicating a higher charge to radius ratio upwards of $60e^-/\mu\text{m}$. In order to generate large particles with a lower growth rate, the atmosphere must also have a lower sedimentation velocity ($< \sim 0.01\text{m/s}$ at 200km), which is possible with a fractal dimension less than 2.

Chapter 3: The Circulation Patterns of Atmospheres

We analyzed *Cassini* data to derive the nature and evolution of circumglobal annuli observed in the stratosphere of Titan, Saturn's largest moon. The annuli were observed between

2004 and 2017 in data acquired by the Visual and Infrared Mapping Spectrometer (VIMS) onboard the *Cassini* spacecraft. We observed a North Polar Annulus (NPA), an Equatorial Annulus (EQA) and several secondary annuli. Pre-Cassini telescopic observations by HST and Keck reported an atmospheric feature consistent with the presence of a South Polar Annulus (SPA) between 1999-2001, although this feature was not observed by *Cassini*. Relative to the atmosphere near the annuli, they appear dark at 300-500nm and bright in methane absorption channels such as the ones at 900nm and 1150nm. The stratosphere seems to rotate around the north pole. Alternatively, it seems to rotate about a point offset from solid body rotation axis by a few degrees; this point in turn rotates around the solid body rotation axis.

Chapter 4: The Compositional Diversity of Surfaces

We use hyperspectral-imaging observations from the Visual and Infrared Mapping Spectrometer (VIMS) to identify the spectral characteristics of Titan's equator. Our dataset is several orders of magnitude larger than previous studies as we use all VIMS observations between -30° and 30°N with incidence and emission angles less than 75°, and a pixel spatial scale of 200km or less; we validate our dataset by reproducing the results of Griffith et al 2019. We interpret the distribution, size, shape, and patterns/sequences of spectrally distinct features to infer aspects of landform formation, composition, and evolution. We use vector quantization, dimension reduction, principal component analysis, and the Monte Carlo method to organize our dataset, identify features, and validate their significance. Using 32 wavelengths, we identify 16 spectrally distinct surface areas distributed across the equator. These spectral units occur in distinct sequences indicating that there is a discrete number of prominent spectral pathways. We find that 99.7% of the change in spectra between spectral units can be explained by 5 delta-spectra. We compare the five delta-spectra to the USGS spectral library to identify candidates for the change

in compositions across the equator. We find evidence among the delta-spectra for changes in abundance of water-ice, acetylene, benzene, alkane species, and Titan haze. We discuss the significance of both the pathways and delta-spectra, including their distribution, frequency, and size, and what they suggest about formation and evolution processes.

Chapter 5: Summary and Future Work

Throughout my candidacy I have had the opportunity to collaborate with dozens of scientists, work on developing new spacecraft missions, and mentor brilliant students. This dissertation presented my contributions to planetary science and to the study of icy-worlds. It also represents the starting line for my next journey and all the science I look forward to finding.

Appendix: Novel Techniques for Observational Planetary Science

In each project I achieve my science objectives through the development and applications of novel data reduction and analysis techniques. I present my corrections to; 1) reduce the effect of scattering from haze (the manifold technique); 2) remove instrumental off disk glow from MVIC; 3) remove striping from the VIMS-Vis detector.

Chapter 2: The Development of Haze

Pluto's Haze Abundance and Size Distribution from Limb Scatter Observations by MVIC

N. W. Kutsop, A. G. Hayes, B. J. Buratti, P. M. Corlies, K. Ennico, S. Fan, R. Gladstone, P. Helfenstein, J. D. Hofgartner, M. Hicks, M. Lemmon, J. I. Lunine, J. Moore, C. B. Olkin, A. H. Parker, S. A. Stern, H. A. Weaver, L. A. Young, and the New Horizons Science Team

Planetary Science Journal, June 2021, <https://doi.org/10.3847/PSJ/abdcaf>

1. Introduction

Pluto has long been known to have a seasonally varying atmosphere [Elliot et al. 2003; Sicardy et al. 2003]. On July 14, 2015, the New Horizons spacecraft flew within 12,500 km of Pluto's surface revealing the extent of its unique haze. [Stern et al. 2015; Gladstone et al. 2016]. Pluto's haze is optically thin, globally distributed, and extends to altitudes of >200 km with a scale height between 30-50km [Gladstone et al. 2016]. Below 80 km, up to 20 distinct layers between 1 km to 10 km thick, are observed over vast expanses of the globe [Cheng et al. 2017]. Unfortunately, observational constraints force us to bin our data into 20 km wide altitude bins, so individual haze layers are not resolved in the present analysis. Pluto has been mapped using the Hubble Space Telescope, but this was at a single phase angle ($<1^\circ$) and with a spatial resolution of 600km [Stern et al. 1997; Buie et al. 2010], whereas the New Horizons flyby has provided the first observations of Pluto over a range of phase angles (15° - 170°) and at spatial resolutions less than <1 km/pixel. In this work we use images acquired by New Horizon's Multispectral Visual and Infrared Camera (MVIC; Reuter et al. 2008) to generate calibrated phase curves of Pluto's atmosphere. We then use these phase curves to constrain the size and distribution of Pluto's haze particles using a fractal aggregate phase function.

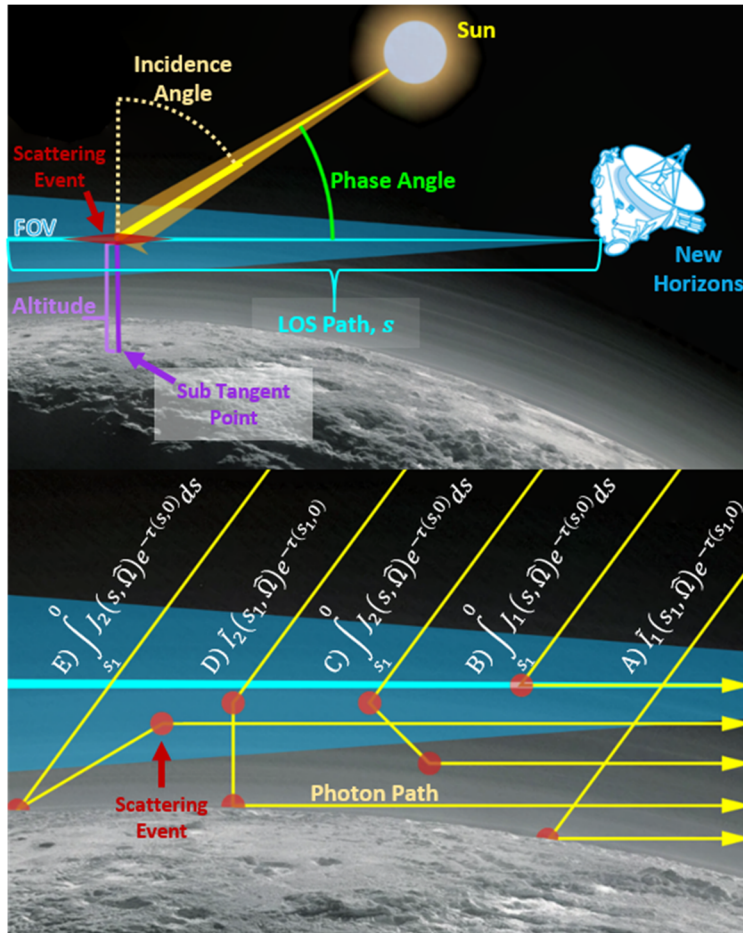


Figure 2 (A, Top) Schematic of the limb scatter technique relevant to observations of Pluto. Single scattering occurs all along the LOS path, s , but is dominated by scattering at the tangent point; the extent of the red area indicates where along the LOS the scattering signal is originating. (B, Bottom) Illustration of photons paths (yellow) as they experience up to the second order scattering events (red). The MVIC pixel field of view is in blue. New Horizons wireframe credit: NASA

High phase angle images indicate the atmosphere is strongly forward scattering. This indicates particles with a size parameter of $x \geq 1$, where $x = 2\pi a/\lambda$, a is the effective radius of the haze particle and λ is the wavelength of the incident light (for visible light in the range of 400-700nm this would necessitate a radius of, $a > \sim 100\text{nm}$). MVIC color composite images, however, reveal that the atmosphere is also very blue ($\frac{I/F \text{ Red}}{I/F \text{ Blue}} \approx .5$ at a phase angle of 18° , see Figure 5), indicative of particles where $x \ll 1$ (for visible light it would require a radius of, $a \approx 10\text{nm}$) [Gladstone & Young 2019]. This suggests that particles are fractal aggregates, similar to those formed at Titan [Gladstone et al. 2016]. UV solar occultation observations by the *Alice* instrument

[Young et al. 2018] show that the gaseous part of Pluto's atmosphere bears similarities in composition to those of Titan and Triton, with N₂, CH₄, C₂H₂, C₂H₄, and C₂H₆ present. Ground-based observations acquired by the Atacama Large Millimeter/submillimeter Array (*ALMA*) additionally confirm the presence of CO and HCN [Lara et al. 1997; Summers et al. 1997; Krasnopolsky & Cruikshank 1999; Wong et al. 2015; Lellouch et al. 2017]. Far and extreme ultraviolet photons drive photodissociation and photoionization of these constituents. At Titan, photolysis produces the monomers and other precursors which then combine and grow as they descend through the atmosphere [Lavvas et al. 2013]. The same process is expected to happen at Pluto, though with a different charged particle environment due to the lack of a thermosphere, exposure to the bare solar wind, and lack of a strong magnetospheric radiation component from a nearby giant planet. Previous work, based on photolysis models, suggest aggregates in Pluto's atmosphere have a fractal dimension, D_f , of 1.5-2.75 and are composed of 10-20 nm monomers [Gao et al. 2017; Lavvas et al. 2013]. Monomer abundance is bounded by the photolysis rates of CH₄ and N₂, which represent the primary limiting factors in haze production. The vertical haze scattering optical depth is currently only ~ 0.004 [Bertrand & Forget 2017]. Assuming an average radius of $\sim 0.2 \mu\text{m}$, the haze density near Pluto's surface is $\sim 0.8 \text{ particles/cm}^3$, or a column mass of $8 \times 10^{-8} \text{ g/cm}^2$.

We use the limb scatter technique, used extensively for remote sensing of Earth's atmosphere [Cunnold et al. 1973; Flittner et al. 2000; McPeters et al. 2000; Murtagh et al. 2002, Rault 2005; Degenstein et al. 2009; McLinden et al. 2012; Normand et al. 2013] to perform the radiative transfer necessary to model phase curves of Pluto's atmosphere, as more familiar bidirectional reflection equations [Hakpe 1981; Liou 2002] are inappropriate for our viewing geometries. As can be seen in Figure 2a, limb scattering occurs when sunlight enter Pluto's

atmosphere, undergoes one or more scattering events between the atmosphere and surface, and then enters the line of sight (LOS) vector between *MVIC* and Pluto [McLinden et al. 2012]. The tangent altitude is the height measured at the point along the LOS vector which is closest to the surface. The line between the tangent point and the sub-tangent point on the surface is parallel to the surface normal. Scattering into the LOS vector occurs throughout the atmosphere. For an optically thin atmosphere ($\tau \ll 1$, where τ is the optical depth), scattering into the LOS vector is dominated by the single scattering contribution from the tangent point. [Normand et al. 2013].

The phase curve describes the brightness of a scattering target subject to a known illumination geometry, denoted by the phase angle, θ . The phase angle is the angle formed between the incident vector and the emission vector. The incident vector starts at the illumination source, in our case the Sun, and ends at the target, Pluto's haze, while the emission vector starts at the observer, *MVIC* and *New Horizons*, and ends at the target. The phase angle, θ , is defined as

$$\theta = \cos^{-1}(\cos(i) \cos(e) + \sin(i) \sin(e) \cos(\psi)) \quad \text{Eq. 3}$$

where i is the incidence angle, which is formed between the incident vector and the normal vector of the target, e is the emission angle, and ψ is the azimuthal angle, which is the angle between the projection of the incidence and emission vectors onto the horizontal plane defined by the normal vector. Depending on the field, the scattering angle α is sometimes used in place of θ where $\alpha = 180^\circ - \theta$. In this work we use the phase angle θ .

The scattering phase function is the first element of the scattering phase matrix, P_{11} . In order to be consistent with work that utilizes multiple components of the phase matrix, we will use the notation, P_{11} to describe our phase functions. The phase function is normalized such that

$$\frac{1}{4\pi} \int_0^{2\pi} \int_0^\pi P_{11}(\lambda, \theta) \sin \theta d\theta d\psi = 1 \quad \text{Eq. 4}$$

Table 1
List of MVIC Observations of Pluto Used in This Study

Image Title	Time	Targets in FOV	Distance (1000 km)	Phase	Res (km)	SSC Lon	SSC Lat
299127622	2015 Jul 13 T21:08:41	PL/CH	726.68	16°15	14.31	-178°15	42°78
299147977	2015 Jul 14 T02:47:54	PL/CH	446.19	16°82	8.8	169°36	41°89
299162512	2015 Jul 14 T06:50:12	PL/CH	246.05	18°24	4.85	161°4	41°23
299176432	2015 Jul 14 T10:42:29	CH	72.19*	38°63*	1.44*	-12°38*	25°17*
299178092	2015 Jul 14 T11:10:52	PL	33.08	38°85	0.66	168°05	25°98
299193157	2015 Jul 14 T15:20:58	PL	175.3	169°36	3.47	-46°7	-45°96
299206942	2015 Jul 14 T19:10:41	PL/CH	364.82	167°06	7.19	-53°13	-44°78
299235612	2015 Jul 15 T03:08:33	PL/CH	759.41	165°96	14.94	-70°67	-43°98

Table 1: Each of the images were captured in the 4 color CCDs. As each CCD is stored in an independent file, each file has a preface relating to the file extensions in Table 1, i.e., XXX_sci.fit would be mc0_XXX_sci.fit, mc1_XXX_sci.fit, etc. All data, i.e., phase, resolution, etc., are given for Pluto, except for those marked with an asterisk, which are given for Charon.

The phase function is the probability that the radiation propagating in a given direction is scattered into an elementary solid angle making an angle θ with the incident direction [Sharma 2018]. It is typical to assume that a particle scatters symmetrically in the azimuthal direction [Sharma 2018], leaving the phase angle as the sole descriptor for the directionality of the scattering event.

2. Data Reduction

2.1 MVIC Data

MVIC uses one of the two feeds of the Ralph telescope, a 75 mm aperture f/8.7 system with an effective focal length of ~658 mm (Reuter et al. 2006). MVIC consists of seven independent Charged-Couple Device (CCD) arrays bonded to a single substrate. Six of the 5024 x 32 pixel CCD arrays are operated in Time Delay Integration (TDI) mode. In this mode the parallel transfer rate of each row is synched to the relative motion of the image across the detector's surface. TDI increases the effective integration time by 32X, substantially increasing image Signal to Noise Ratio (SNR). Of the six TDI arrays, there are two panchromatic/unfiltered (MP1, MP2) arrays for broadband high SNR imaging and four arrays with color filters in the red, blue, near-infrared, and methane windows (MC0, MC1, MC2, MC3). The seventh CCD is a panchromatic

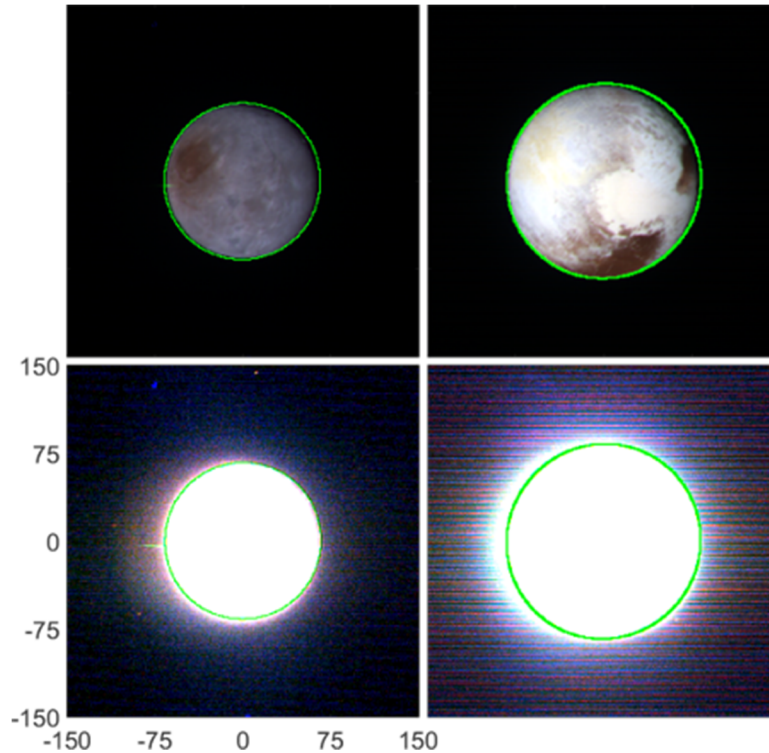


Figure 3 RGB images of Charon (Left) made from observation taken during 0299147977 and Pluto (Right) made from observation taken during 0299127622 , where the red, green, and blue channels are MVIC NIR, MVIC RED, and MVIC BLUE, respectively. In each image the green circle denotes the actual limb of Charon or Pluto (Top) Channels linearly scaled independently from min = median (I/F Space) to max = max (I/F Pluto). (Bottom) Channels linearly scaled independently from min = median (I/F Space) to max = min (I/F Charon)

frame transfer array with 5024×128 pixels (MPF), primarily provided for optical navigation. In all 7 frames, the first and last 12 pixels in each row are not optically active. The raw and calibrated data are available through the PDS [Stern 2007]. A detailed explanation of our data processing is provided in Appendix A.

We use data only from the Red, Blue, and NIR filters, which have pivot wavelengths of 620nm, 475nm, and 878nm, respectively. We ignore the panchromatic filters as we are investigating the spectral characteristics of Pluto's haze. We ignore the CH₄ filter (pivot wavelength of 885nm) because it is a narrow wavelength filter with low SNR that is encompassed by the wavelength range of the broader NIR filter. Furthermore, we only use images taken with an average pixel scale across Pluto's disk of less than 15 km/pixel. This produces the data set in Table 1, acquired within ~ 30 hours of closest approach. Images outside this range cover a redundant

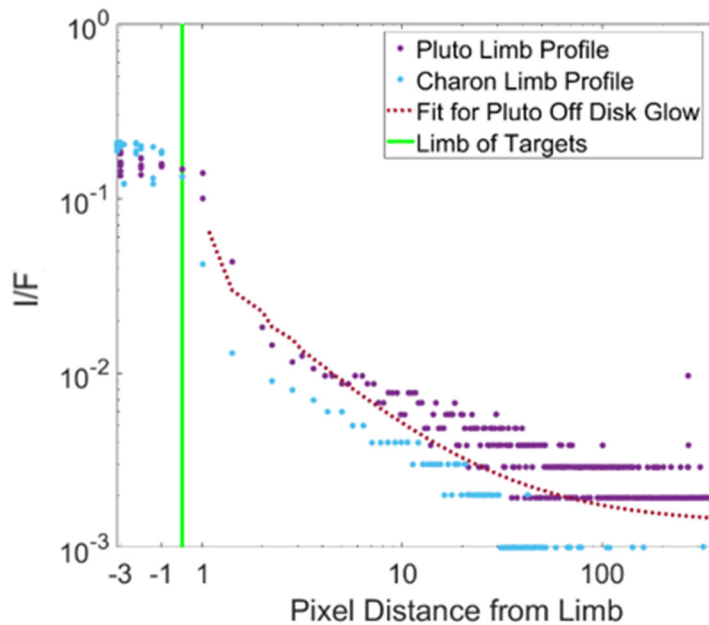


Figure 4: MVIC Red limb scatter profiles of Charon taken from sequence 0299147977 and of Pluto taken from sequence 0299127622. The observations were chosen such that they have nearly equal phase angle, 16.82° and 16.15°, and the targets have similar angular diameter, 0.15° and 0.19°. The limb profiles were chosen such that the incidence angle of the sub-tangent points were nearly identical, 79.80° and 79.85°, and the weighted average limb brightness were nearly identical, $I/F = 0.1513$ and 0.1515 . The fit, shown by the red dotted line, was generated for Pluto’s limb scatter profile using Eq. 6 and the values for MVIC Red in Appx. Table 1.

range of phase angles but have pixels that are too large to probe distinct altitudes in Pluto’s atmosphere.

These lower resolution images are also more susceptible to “off-disk glow”. This off-disk glow, is an instrument effect, similar to stray light seen in the Long Range Reconnaissance Imager (LORRI) [Cheng et al. 2017], This effect can be seen more than 100 pixels away from the disk, equating to more than 500 km in Appx.e images (Figure 3). To account for this glow, we follow a similar strategy as in Cheng et al. 2017, whereby we use the airless (i.e., presumably hazeless) body of Charon [Stern et al. 2017] to model and remove the effect. Figure 4 highlights our fit to the data and provides a comparison with Pluto’s off disk profile. Our technique is detailed in Appendix B.

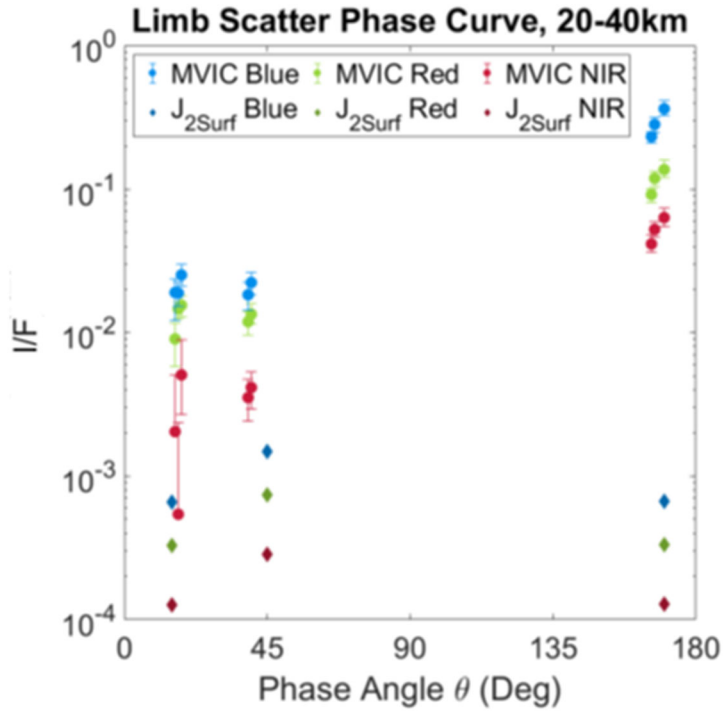


Figure 5: Median phase curve observed between 20-40km. Error bars represent the 15th and 85th percentile of the distribution of values within the altitude and phase bins. The diamonds are upper limit of the amount of secondary scattering, J_2 , from Sun \rightarrow Surface \rightarrow Atmosphere \rightarrow MVIC.

We present the uncertainty in I/F as the bounds occurring at the 15th and 85th percentile of the pixels in each bin (Appx. Table 3). The 15th and 85th percentile range is equivalent to the bounds at 1 standard deviation, σ , greater and less than the mean or median for a normal distribution. The variance in our data in a single bin is typically not normally distributed so the standard deviation is not appropriate for describing our variance. This variability in our binned data, $\sim 25\%$ and dependent on filter (Appx. Tables 2&3), is substantially greater than the 3% propagated error described in Appendix C. As such we do not consider the propagated error, but we present our determination of the propagated error above for the sake of completeness in Appendix C.

2.2. Phase Curves

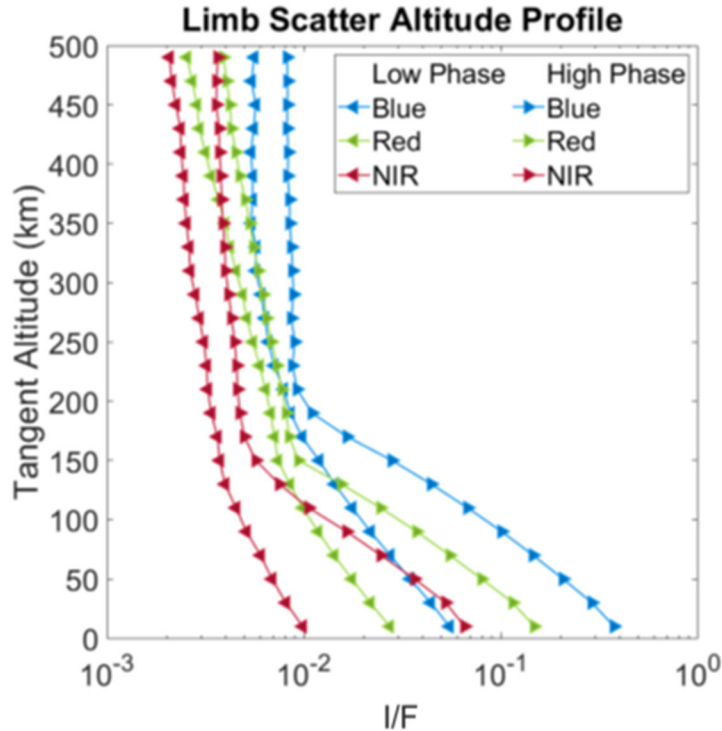


Figure 6 Approximate high phase angle ($\sim 165^\circ - 170^\circ$) and low phase angle ($\sim 16^\circ - 18^\circ$) components of MVIC Red, Blue, and NIR phase curves for each altitude bin.

We have produced phase curves for Pluto from 0-500km, in 20km wide altitude bins, at 8 solar phase angles of $16^\circ, 17^\circ, 18^\circ, 39^\circ, 40^\circ, 166^\circ, 167^\circ$, and 170° , in three colors, MVIC Blue, MVIC Red, and MVIC NIR. Representative values for the phase curves can be found in the Appx. Tables 2 and 3. Figure 5 shows an example of our phase curve at 20-40 km in all three wavelengths. Figure 6 shows the relative change of the high phase and low phase component of the phase curves as a function of altitude.

The phase curves in the lower atmosphere are strongly forward-scattering in all three filters. At 0-20km the forward scattered component is an order of magnitude higher than the back scattered component in all three filters. A convenient parameter for describing phase curves and phase functions is the asymmetry parameter, often denoted as g [Henye & Greenstein 1941]. g is defined as the first moment of the phase function and quantizes the degree of anisotropy in the scattering from -1 to 1, where $g = 1$ is fully forward scattering (typified by Mie scattering), $g = 0$

is isotropic (typified by Rayleigh scattering), and $g = -1$ is fully backscattering (typified by geometric scattering). We approximate g by fitting a simple monodisperse phase function (3.4.1 Monodisperse and Log-Normal) to the phase curves and finding the first moment [Liou 2002; Eq 3.4.9b]. From 0-40km we find the atmosphere to have a range of g from $\sim .6$ in the NIR filter to $\sim .7$ in the Blue filter. Regardless of scatterer type or distribution, this suggests that the haze is characterized by particles scattering in the Mie regime, where the size parameter $x \geq 1$. Given the wavelength range of the three MVIC filters, the haze in the lower atmosphere must be characterized by particles on the order of 100 nm, consistent with other forward scattering measurements [Gladstone et al. 2019; Gao et al. 2017].

As altitude increases, the I/F at all phase angles for the three filters decreases and they become less forward scattering (Figure 6). From 0-60km g decreases slowly while the total intensity decreases mostly uniformly across the 8 phase angles suggesting that the characteristic particle size is not changing very much, while the total abundance decreases uniformly. This implies that from 0-60km aerosol growth has largely ceased, preferential destruction or fallout of particular particles is not occurring, and all scatterer populations are uniformly increasing as they descend to the surface. From 60 - 200km g decreases rapidly, as the intensity at $\theta = 40^\circ, 41^\circ, 166^\circ, 167^\circ, 169^\circ$ decreases much faster than the intensity at $\theta = 16^\circ, 17^\circ, 18^\circ$. This is consistent with the characteristic particle size decreasing rapidly from 60 – 200km. The difference in the rate of change for the scattering anisotropy from 0-60km and 60-200km can be seen in Figure 6 through the linear decrease of the low phase angle component and the roughly exponential decrease of the high phase component.

The phase curves for the three filters all approach isotropic scattering in the upper atmosphere. The NIR and Red filter turn isotropic at 150km while the Blue filter becomes isotropic

just below 200km. This is consistent with the characteristic particle size entering the Rayleigh scattering regime for the NIR and Red filters at 150km, while the particles are large enough compared to the wavelength range for the Blue filter (475nm) that they are in the Mie scattering regime until 200km. If we take the transition from Rayleigh to Mie Scattering as $X = 0.2$, [Wiacek et al. 2013] then this would suggest that the characteristic particle size is $\sim 30nm$ at 150km and $\sim 15nm$ at 200km. This is about as small as the fractal aggregate haze particles can be if formed of monomers with spherical radii of 5-10nm [Gao et al. 2017]. Given this and the constant mild decrease in I/F for the phase curves in all three filters, it is likely that minimal aerosol growth occurs between 200-500km while the total abundance of particles grows steadily.

3. Modelling

3.1. Radiative Transfer

A full radiative transfer description of scattering from Pluto's limb would include ray tracing through spherical shells and account for multiple scattering [Bourassa et al. 2008]. These multiple scattering events are illustrated in Figure 2b. As none of our observations intersect the surface of Pluto we ignore all scattering between the surface and MVIC (Sun→surface→MVIC, Figure 2b A & Sun→atmosphere→surface→MVIC, Figure 2b D). Results from Fan et al. In Prep found that the upper limit of contribution from secondary scattering initiated by the ground (Sun→surface→atmosphere→MVIC, Figure 2b E) accounts for less than 10% of the observed radiance at the wavelength of the three MVIC filters used herein (Figure 5). For this reason, we ignore secondary scattering initiated by the ground and the higher order multiple scattering. We also ignore secondary (and multiple) scattering initiated by the atmosphere, (Sun→atmosphere→atmosphere→MVIC, Figure 2b C).

We determined the magnitude of the scattering due to Pluto's primary gaseous components, N₂ and CH₄, using the particle number density described in Young et al. 2018 and the Rayleigh scattering phase function. At 370 nm, where laboratory data for N₂ and CH₄ cross sections exists, we find that the Rayleigh scattering at the surface (0 km) due to N₂ is $I/F \approx 10^{-3}$, while Rayleigh scattering due to CH₄ is $I/F \approx 10^{-7}$. Given that Rayleigh scattering intensity approximates as $I \propto 1/\lambda^4$, the intensity at 370nm is 3 times stronger than for our Blue filter pivot wavelength of 492 nm. This also means Rayleigh scattering is even further reduced in the Red and NIR filters.

As described in detail in Appendix D, we ignore all scattering from Pluto except single scattering from Pluto's haze, which gives us

$$I/F(s_T, \lambda) = N_{Aerosol}(s_T) \sigma_{Aerosol}(s_T, \lambda) P_{11Aerosol}(s_T, \theta, \lambda) \Delta s_T \quad \text{Eq. 5}$$

3.2. Grid Search and Statistics

Our goal is to find a phase function that matches the observed limb scatter phase curves at all three wavelengths simultaneously at each altitude bin, for all altitude bins. Between them, we are looking to match the phase angle dependence, relative brightness difference between high and low phase, and slope $d(I/F(\lambda))/d\theta$. To do this we used an R^2 grid search where each element of the grid is

$$R^2 = 1 - \frac{SSE}{SST} \quad \text{Eq. 6.}$$

Here SSE is sum of squared error (Appx.etimes called the sum of squares of residuals) and SST is the total sum of squares, each given by

$$SSE = \sum_{k=1}^c \left(I/F_{obs}(\lambda, \theta_k) - N(s_T) \sigma(s_T, \lambda) P_{11}(\lambda, s_T, \theta_k) \right)^2 \quad \text{Eq. 7}$$

$$SST = \sum_{k=1}^c \left(I/F_{obs}(\lambda, \theta_k) - \overline{I/F_{obs}(\lambda, \theta_k)} \right)^2 \quad \text{Eq. 8}$$

where C is the total number of phase angles in our phase curves, k is each point in both the observed phase curve $I/F_{obs}(\theta)$ and the phase function $P_{11}(\theta)$. Our objective is the distribution and abundance of the scattering population, which are the driving aspect of the shape of the modeled phase curve. Because $N(s_T)\sigma(s_T, \lambda)$ are independent of phase angle under the assumption that the aerosols are randomly oriented, we replace them in Eq.7 with a scaling factor defined as

$$S_F = N(s_T)\sigma(s_T, \lambda) = \frac{1}{C} \sum_{k=1}^C \frac{I/F_{obs}(\lambda, \theta_k)}{P_{11}(\lambda, s_T, \theta_k)} \quad \text{Eq. 9}$$

R^2 ideally has a range of 0-1, with a value closer to 1 indicating that a greater proportion of variance is accounted for by the model and the model more accurately predicts the data. $R^2 \leq 0$, indicates the mean of the data, i.e. a horizontal line, provides a better fit to the data than the model. Negative R^2 are possible but typically occur for equations that do not contain a constant term.

We plot our data using the median and report the variation with the 15th and 85th percentile value. We conduct our fitting routines however using a Monte Carlo (MC) simulation with at least 320 runs to draw our phase curve values for each wavelength from the distribution of pixels in each of the altitude and phase bins. For each MC run, we redo our grid search and locate the best fit parameters. At the end we determine our best fit parameters by taking the average of the MC runs and report our uncertainty with the 15th and 85th percentile value for each fit parameter.

3.3 Size distribution

Background information about phase functions and the choices we made is provided in Appendix E. Phase functions produced by a distribution of particles sizes characterized by the differential particle radius number density distribution, $n(r)$, are found by integrating the phase function over all particle sizes (R.G. Grainger 2012),

$$P_{11}(\lambda, s_T, \theta) = a_{UV} \frac{1}{\beta_s} \int_{r_{min}}^{r_{max}} \sigma_s(\lambda, r, s_T) P_{11,Individual}(\lambda, s_T, r, \theta) n(r, s_T) dr \quad \text{Eq. 10}$$

$$\beta_{s,e}(\lambda, s_T) = a_{UV} \int_{r_{min}}^{r_{max}} \sigma_{s,e}(\lambda, r, s_T) n(r, s_T) dr \quad \text{Eq. 11}$$

$$n(r) = \frac{dN_p(r)}{dr} \quad \text{Eq. 12}$$

where $N_p(r)$ is the number of particles with radii between r and $r + dr$, σ_s and σ_e are the scattering and extinction cross section of the particle, and r is the effective particle radius. a_{UV} is the normalization constant necessary to find the total number of particles N_0 and match extinction coefficient observations made by the *New Horizons Alice* UV spectrometer determined by

$$a_{UV} = \frac{\beta_{eYoung18}(s_T)}{\int_{r_{min}}^{r_{max}} \sigma_e(165nm, r, s_T) n(r, s_T) dr} \quad \text{Eq. 11}$$

$\beta_{eYoung18}(s_T)$ is the extinction coefficient of the haze observed by *Alice* during solar occultation of Pluto at the tangent altitude of s_T [Young et al. 2018; Appendix B]. In order to do this, we needed to extrapolate the complex index of refraction from Ramirez et al. 2002, from 200nm to 165nm (the wavelength of the *Alice* occultation observations); we did so linearly. Note that from here on, P_{11} will refer to the phase function produced by a distribution of scatters, while $P_{11,Individual}$ will refer to the phase function produced by a single scatter of characteristic size between r and $r + dr$.

The total number of particles per unit volume, N_0 , is given by

$$N_0 = a_{UV} \int_{r_{min}}^{r_{max}} n(r) dr \quad \text{Eq. 14}$$

The scattering cross section are [Gao et al. 2017]

$$\sigma_{s,e} = Q_{s,e} \pi r_m^2 \quad \text{Eq. 15}$$

for spheres, and

$$\sigma_{s,e} = Q_{s,e}\pi \left(r_m N_m^{1/3} \right)^2 \quad \text{Eq. 16}$$

for fractal aggregates. $Q_{s,e}$ are the scattering and extinction efficiency respectively. The effective particle radius for a spherical particle is simply the radius of the sphere, whereas for a fractal aggregate the effective radius, R_f , is given by

$$R_f = r_m N_m^{1/D_f} \quad \text{Eq. 17}$$

where r_m is the radius of a monomer, N_m is the number of monomers in a fractal aggregate, and D_f is the fractal dimension. For fractal aggregate distributions, we assumed a particle size range between 2 monomers ($R_{min} = r_m 2^{1/D_f}$) to $R_{max} = 1\mu m$. The minimum size ensures that the particle is actually an aggregate and not a single monomer. The maximum size was initially chosen based on the upper range of [Gao et al. 2017](#). Testing of larger R_{max} , up to $1mm$, revealed that the particular slope of the high phase component of the phase curves necessitates that there be a dramatic lack of particles larger $1\mu m$ (Figure 11). This will be discussed in more detail in 3.4. Populations Type.

We also assume that the fractal dimension is $D_f = 2$. This is because only a fractal dimension of $D_f = 2$, was rigorously tested for [Tomasko et al. 2008](#). Unpublished results from further testing suggest that the code can produce accurate phase function for $1.5 < D_f < 2.5$. However, they may also produce physically irrelevant albedos and/or polarization values [[Email communications with M. Lemmon 2020](#)]. As will be discussed in 3.4. Populations Type, we investigated this range of D_f as the fractal dimension is an important parameter controlling the fallout time of the haze.

We assume that monomers maintain a constant size after formation and through fractal aggregation; as such we fix r_m as a constant for all altitude bins. The final P_{11} must fit the phase

curves of all three MVIC filters. Throughout our tests we found that modeled phase functions with different r_m values matched the observed phase curves equally well for all $r_m \leq 10nm$, while the quality of the fits diminished as r_m increased for $r_m > 10nm$. As will be discussed below we found that the $10nm$ monomer fractal aggregate distribution from [Gao et al. 2017](#), produced phase functions which matched our phase curve better than the $5nm$ monomer fractal aggregate, the $10nm$ spherical, and the $5nm$ spherical distributions from [Gao et al. 2017](#). Given this and our other test, we assumed that $r_m = 10nm$. We will discuss in [Section 4.1 Fractal Dimension](#) different monomer sizes as relevant to the fractal dimension D_f .

3.4. Population Types

We tested several particle population types including monodisperse, log normal, bimodal, and power law, which are defined in their relevant sections. For each population type, we tested the phase function produced by every pertinent variation of size and distribution of the particles (Eq.9, $S_F P_{11}(\lambda, s_T, \theta_k)$) against the observed I/F phase (Eq.9, $I/F_{obs}(\lambda, \theta_k)$). At each altitude bin, and for each population type we identified the combination of size and distribution that produced phase functions which best matched the observed phase curves by finding which one had the highest R^2 value ([3.2. Grid Search and Statistics](#)), and verified each by graphic interpretation. We then compared the different populations against one another to determine which were relevant to Pluto's atmosphere.

We will refer to three distributions as small, intermediate, and large size scatterers. This loose distinction is useful for referencing the distributions in terms of which population category is responsible for a particular aspect of the phase curve. While not strictly in the traditional parameter size cutoff [[Wiacek et al. 2017](#)] we define these groups as Rayleigh size scatterers,

$R_f(Ray) \approx 10 - 100nm$, intermediate size scatterers, $R_f(Int) \approx 100 - 500nm$, and Mie size scatterers, $R_f(Mie) \approx 500nm - 1\mu m$.

3.4.1 Monodisperse and Log-Normal

A monodispersed population is characterized by a single particle size. A log-normal distribution is given by

$$n_{LN}(R_f) = e^{\mu_{R_f} + \sigma_{R_f} R_f} \quad \text{Eq. 18}$$

Where μ_{R_f} is the mean and σ_{R_f} is the standard deviation of the natural logarithm of the effective radius, R_f . [Gao et al. 2017](#) determined $n(r)$ as functions of altitude and particle radius for spherical and fractal aggregate particle composed of monomers with r_m of 5nm and 10nm using the 1D Community Aerosol and Radiation Model for Atmospheres (CARMA). We found that the log-normal distributions produced by [Gao et al. 2017](#) were unable to simultaneously fit the steep forward scattering component and the non-negligible back scatter component present in Pluto's atmosphere from 0-200km (Figure 7). As expected, a monodisperse population of scatterers was similarly unable to match the shape and slope of the phase curves (Figure 7).

Of the distributions modeled by [Gao et al. 2017](#), we found that the 10nm fractal aggregate population best matched our phase curves, being able to match the difference in magnitude between high phase and low phase. This is likely because below 150km the 10nm distribution has the widest particle size standard deviation σ_{R_f} , where the appropriate $R_f(Mie)$ and $R_f(Ray)$ are in enough abundance to produce phase functions with the right order of magnitude difference between the high phase and low phase. Because the 10nm fractal aggregate fit better than any other distribution, and because our many tests on all the other population types revealed that $r_m \leq 10nm$ produce phase functions with nearly identical quality of fits, we use $r_m = 10nm$ for all populations going forward.

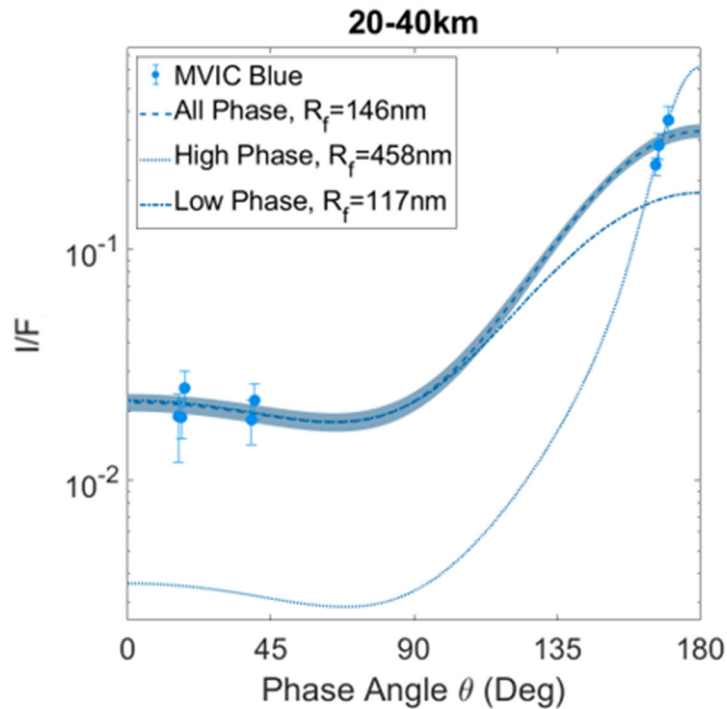


Figure 7 Phase functions produced by a best fit distribution of monodisperse scatterers with $r_m = 10$ nm and $D_f = 2$ for the 20-40km altitude bin for the MVIC Blue filter. Dashed line, best fit phase function for brightness at phase angles $16^\circ, 17^\circ, 18^\circ, 39^\circ, 40^\circ, 166^\circ, 167^\circ$, and 170° . The shaded blue area around the dashed line indicates the 15th and 85th percentile of phase functions which fit the distribution of I/F in each phase bin from the Monte Carlo run. Dotted line, best fit phase function for brightness at high phase angles of $166^\circ, 167^\circ$, and 170° . Dot Dash line, best fit phase function for brightness at low phase angles of $16^\circ, 17^\circ, 18^\circ, 39^\circ$, and 40° .

The problem remains however that there is not the correct disparity in abundance between the $R_f(Mie)$ and $R_f(Ray)$ to produce the appropriate slope at high phase angles. These distributions fail because the uniquely steep forward scattering component necessitates large fractal aggregate scatterers. Large $R_f(Mie)$ with the appropriate slope, have low phase angle components with at least two orders of magnitude lower I/F , which is not what we observe (Figure 5). Conversely, to produce the low phase component, which at most is only one order of magnitude lower than the high phase component (0-60km, Figure 6), requires smaller sized $R_f(Ray)$ scatterers. These $R_f(Ray)$ however scatter more isotropically and are unable to produce the steep slope at high phase. To demonstrate this, we found best fit phase functions for only the high phase component of our phase curves, $\theta > 90^\circ$, and low phase component of our phase curve, $\theta < 90^\circ$. Figure

7 demonstrates the need for a population of diverse particles by showing the best-fit results for the Blue filter. While not depicted in Figure 7, the same is true for the MVIC Red and MVIC NIR filters. Figure 7 shows that the best-fit using monodisperse aerosols is unable to reproduce the observations in the three MVIC filters.

We also investigated other log normal distribution by modifying the mean effective radius, μ_{R_f} , and the standard deviation σ_{R_f} of the [Gao et al. 2017](#) distribution. No amount of manipulation was able to produce a size distribution with a phase function to match the shape of our phase curves, appreciably better than the unmodified distributions from [Gao et al. 2017](#).

3.4.2 Bimodal

The bimodal distribution is a population characterized by two scatterers, $R_f(Big)$ and $R_f(Small)$, with arbitrary weights, $w(Big)$ and $w(Small)$ that summed to one. We utilize the conversions from [Grainger 2017](#) for integration of discrete particle sizes to a summation of weights. We found that the bimodal population was able to match the shape and slope of the phase curves very well at all altitude bins (Figure 8 a-c). From 0-180km the $R_f(Big)$ is between 500nm and 1 μ m ($R_f(Mie)$) while $R_f(Small)$ is between 20-100nm ($\sim R_f(Ray)$). From 0- 200km, the small particles are at least 3 orders of magnitude more heavily weighted than the large scatterers ($w(Small) = .99, w(Big) = .01$).

Above 200km the weights start to deviate randomly and vary from a uniform distribution ($w(Small) = .5, w(Big) = .5$) to $R_f(Small)$ being weighted four orders of magnitude more than $R_f(Big)$ ($w(Small) = .999, w(Big) = .001$). At this altitude range however, the size of $R_f(Big)$ and $R_f(Small)$ are very close to one another and are both in the $R_f(Ray)$ size range. This indicates that above 200km the population is very similar to a monodisperse population characterized by particles small enough to scatter isotropically at all wavelengths, as seen in Figure 6.

In Appx. Table 4B we include the best fit parameters for the size of the particles, the weights, and the approximation on total number of particles the weights suggest given the scattering cross section of the particles. We approximate N with

$$N_{B,M,S} = \frac{a_{UV}W_{B,M,S}}{\pi \left(r_m N_m^{\frac{1}{3}} \right)^2} \text{ Eq. 19}$$

3.4.3 Power-Law

We describe $n(R_f)$ using a power law distribution where

$$n_{PL}(R_f) = a_{UV}R_f^{-b} \text{ Eq. 20}$$

where b is the power law exponent.

As can be seen in Figure 8 a-c, the power law matches the shape and slope of the phase curves nearly as well as the bimodal distribution. In fact, a deep dive into the data reveals that more often than not, size and abundance of the bimodal distribution will intersect the two points on the power law. The key difference between the two type is the presence of $R_f(Int)$ in the power law distribution, while the bimodal distribution essentially sets this abundance to zero. This indicates that $R_f(Int)$ are not a defining factor of our phase curves.

The power law exponent is at its lowest at 20-40km, where $b = 3.5$. This is the most equally distributed of the power law populations and still there are 5 orders of magnitude more scatterers with size $R_f(Ray)$ than $R_f(Mie)$. As we move to higher altitudes, b steadily increases, indicating a bigger disparity between $R_f(Ray)$ and $R_f(Mie)$. The power law becomes steepest, $b \approx 6$, at 200km where the atmosphere transitions to isotropically scattering. This is the same altitude we saw the bimodal population begin to approximate a monodisperse population. This again suggests that above 200km, the atmosphere is dominated almost entirely by small isotropically scattering particles.

As a side note, the very steep and dramatic change in the power law exponent at 180 & 200km, likely comes about from low signal and low SNR observations, which were not removed as they were not yet negative. These skewed the grid searches to try and fit such implausibly dim observations. Further investigation revealed that power law exponents of $b \approx 5.5$ (the approximate mean of b at 160km and 220km) produced phase functions with similar R^2 values and matched the shape of the phase curves equally well upon inspection.

Population Comparison 20-40km

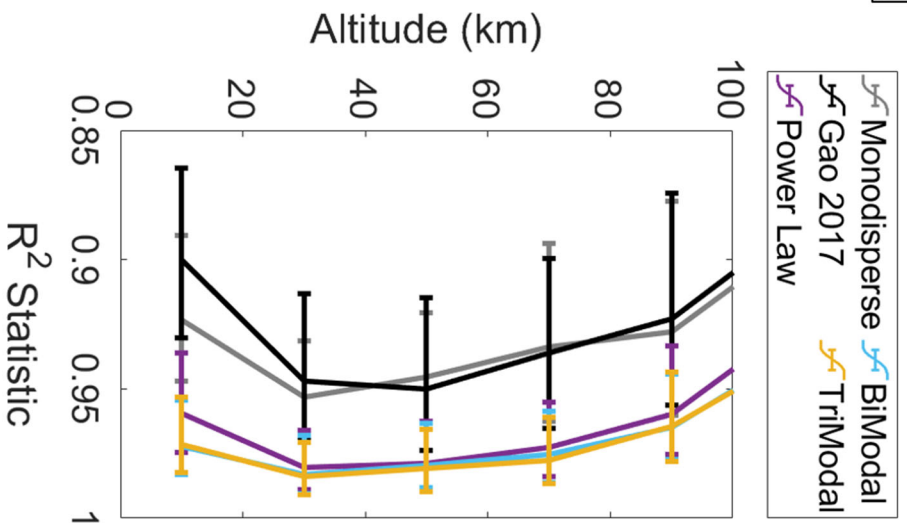
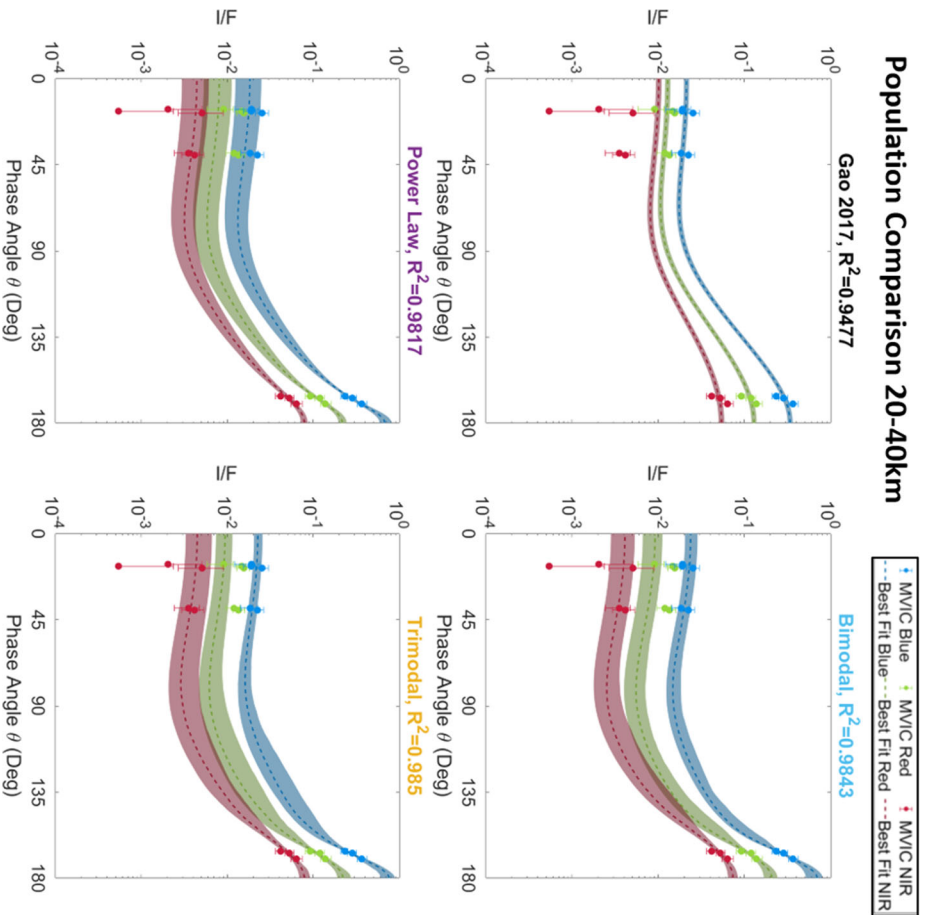


Figure 8a: LEFT) Best fit phase function are produced for the power law, bimodal, trimodal, and monodisperse distributions and compared against the phase functions produced by the distribution in Gao et al. 2017. Our observations from MVIC Red, Blue and NIR filters are presented as filled circles with error bars representing the variation in the data bins. All populations are generated with $r_m = 10$ nm and $D_j = 2$ for the 20-40km altitude bin. The dashed lines are the median (i.e. best fit) of the modelled phase functions while the shaded area around the dashed lines indicates their 15th and 85th percentile. The phase functions we modeled fit the observed phase curves well while the log normal from Gao does not fit well. RIGHT) R^2 values showing the how well the models(lines) fit the data(circles) in the figures to the left, at each altitude bin from 0-100 km, where 1 is the best score. Error bars show the 15th and 85th percentile of the score. The R^2 shows that the log normal has as much difficulty fitting as a monodisperse while the other populations match well.

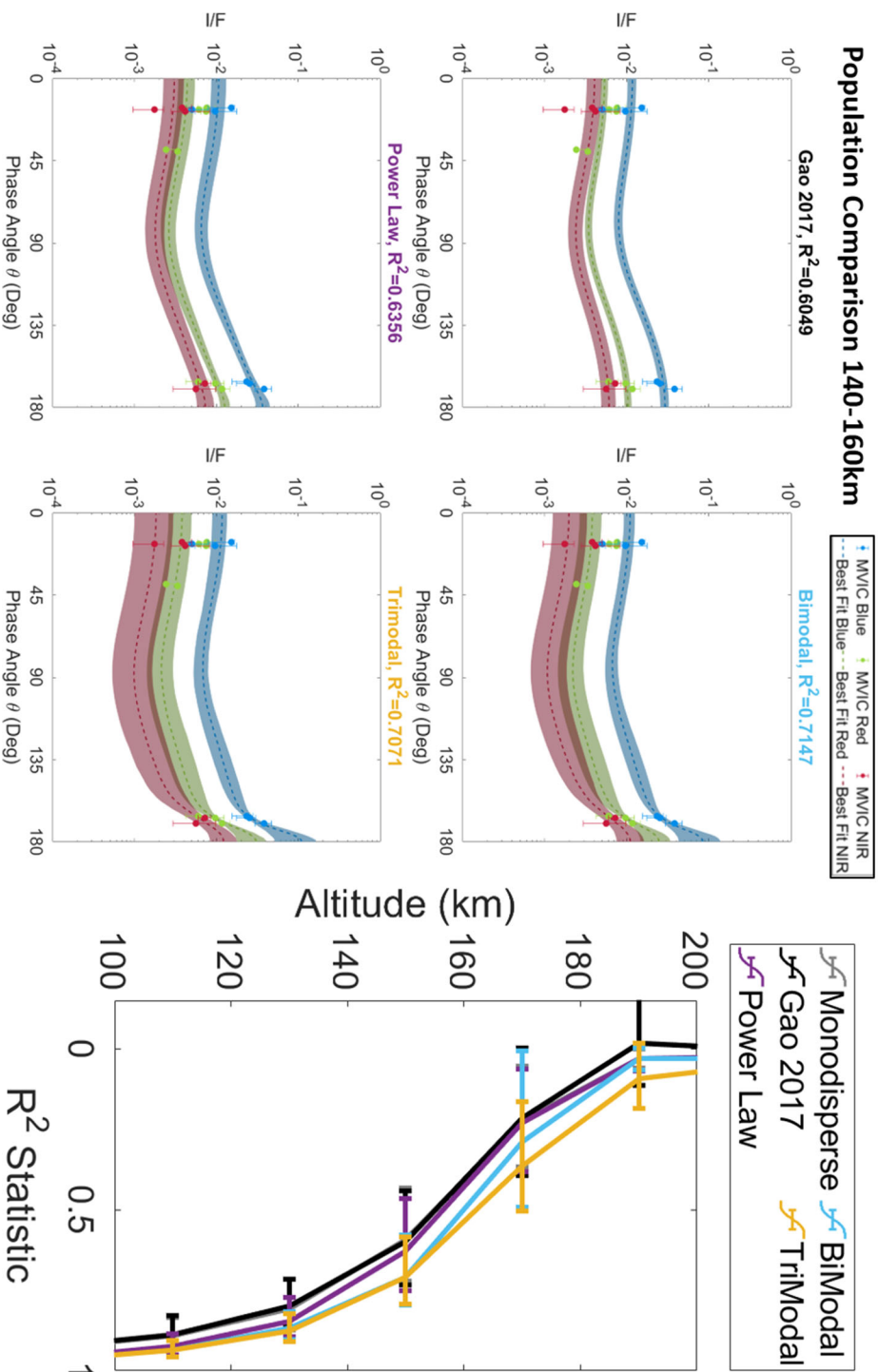


Figure 8b: LEFT) Best fit phase function are produced for the power law, bimodal, trimodal, and monodisperse distributions and compared against the phase functions produced by the distribution in Gao et al. 2017. Our observations from MVIC Red, Blue and NIR filters are presented as filled circles with 15th and 85th percentile error bars representing the variation in the data bins. All populations are generated with $r_m = 10$ nm and $D_f = 2$ for the 140-160km altitude bin. The dashed lines indicate the median (i.e. best fit) of the modelled phase functions while the shaded area around the dashed lines indicates their 15th and 85th percentile. As the altitude increases it becomes more difficult for the power law to match the steep high phase component. The bimodal and trimodal do not have this problem. RIGHT) R^2 values showing how well the models (lines) fit the data (circles) in the figures to the left, at each altitude bin from 0-100 km, where 1 is the best score. Error bars show the 15th and 85th percentile of the score. As the altitude increases the bimodal and trimodal appear to fit the data the best.

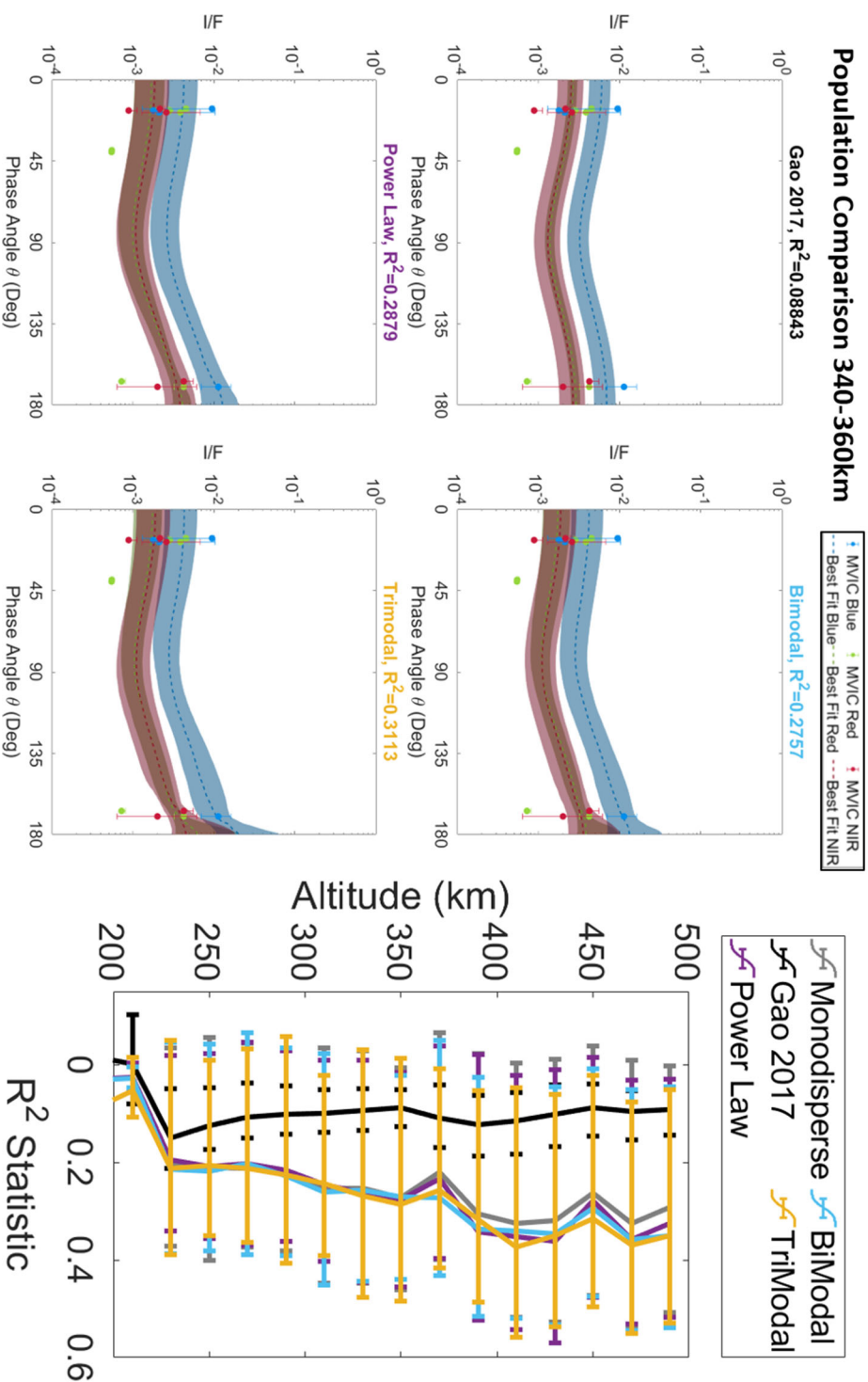


Figure 8c: LEFT) Best fit phase function are produced for the power law, bimodal, trimodal, and monodisperse distributions and compared against the phase functions produced by the distribution in Gao et al. 2017. Our observations from MVIC Red, Blue and NIR filters are presented as filled circles with 15th and 85th percentile error bars representing the variation in the data bins. All populations are generated with $r_m = 10$ nm and $D_f = 2$ for the 340-360km altitude bin. The dashed lines are the median (i.e. best fit) of the modelled phase functions while the shaded area around the dashed lines indicates their 15th and 85th percentile. All of the modeled phase functions appear to fit the observations equally well. RIGHT) R^2 values showing the how well the models(lines) fit the data(circles) in the figures to the left, at each altitude bin from 0-100 km, where 1 is the best score. Error bars show the 15th and 85th percentile of the score. The R^2 for all the populations modeled in this study are nearly identical, suggesting that at this altitude all of the distributions are all approximating a monodisperse population.

3.4.4 Trimodal

The bimodal and power law distributions suggest the same story for the relative abundance of $R_f(Ray)$ and $R_f(Mie)$. They imply a different story for $R_f(Int)$ however, where the bimodal imposes a complete absence and the power law imposes that $R_f(Int)$ is at the average of the logarithmic abundances for $R_f(Ray)$ and $R_f(Mie)$. To try and determine the importance of $R_f(Int)$, we investigated a trimodal distribution. Similar to the bimodal distribution, the trimodal distribution is characterized by three scatterers, $R_f(Big)$, $R_f(Med)$, and $R_f(Small)$, with arbitrary weights, $w(Big)$, $w(Med)$, $w(Small)$ that summed to one. These weights are converted to physical abundances using Eq.18. All together the trimodal distribution resulted in a six dimensional grid search with 214305 unique combinations and corresponding phase functions. Unlike the other distributions, we investigated all of them by sorting them using their R^2 value to see if a pattern emerged suggesting any principal components or important characteristic. This resulted in a distribution of R^2 with a discernable mean and deviation. We defined our “best fit” parameter and phase functions as those with an R^2 above 99.7th percentile.

The best fit trimodal parameters all had an $R_f(Int)$ abundance consistent with either a bimodal distribution or a power law. This means it is not possible to immediately remove the degeneracy between power law and bimodal. As can be seen in the difference between the bimodal and power law phase curves in Figure 8, $R_f(Int)$ controls the shape of the phase function in the range where we lack color observations ($40^\circ < \theta < 165^\circ$). This does reveal however that $R_f(Int)$ must have a relative abundance compared to $R_f(Ray)$ that is less than the abundance predicted by a power law. As with the power law and the bimodal distributions, we also saw that for all altitude bins, the most abundant populations of scatterers must lie in $R_f(Ray)$. This is not seen in the monodisperse or log-normal distributions which have a μ_{R_f} at $R_f(Int)$ in the lowest altitude bins.

Here they can match the difference between the low and high phase angle brightness but not simultaneously with the high phase angle slope (Figures 7 and 8).

As can be seen in the values of Appx. Table 4C, the $R_f(Med)$ in all altitude bins was very close in value to either $R_f(Small)$ or $R_f(Big)$; in fact they were the next available value, being as close as possible to either $R_f(Small)$ or $R_f(Big)$ as the grid search would allow. This would seem to indicate that the trimodal distribution is trying to approximate a bimodal one rather than a power law. While this is plausible, it should be viewed with skepticism as we do not have the phase coverage where $R_f(Med)$ being distinctly set apart from $R_f(Small)$ or $R_f(Big)$ would make a difference in the fits.

The trimodal investigation also revealed that while the size and abundance of the scatterer at $R_f(Ray)$ was mostly consistent there was Appx.e variability and multiple combination of size or abundance that would fit the phase curves well. This however was not the case for the scatterers at $R_f(Mie)$ where every single one of our best fits had the same size and abundance. For example, at 20-40km, it was crucial that the trimodal fit contain a scatterer with $R_f \approx 750nm$ and $w = .01$ ($N = 491972$). Whether this particle was represented by $R_f(Med)$ or $R_f(Big)$ was not critical, so long as one of them had this particle size at this particular abundance. We saw the same behavior for the rest of the altitude bins. This is likely due to the slope at high phase angles which is strongly controlled by the size of particles at $R_f(Mie)$, while the difference between the high and low phase components requires a finely controlled abundance of particles at $R_f(Mie)$.

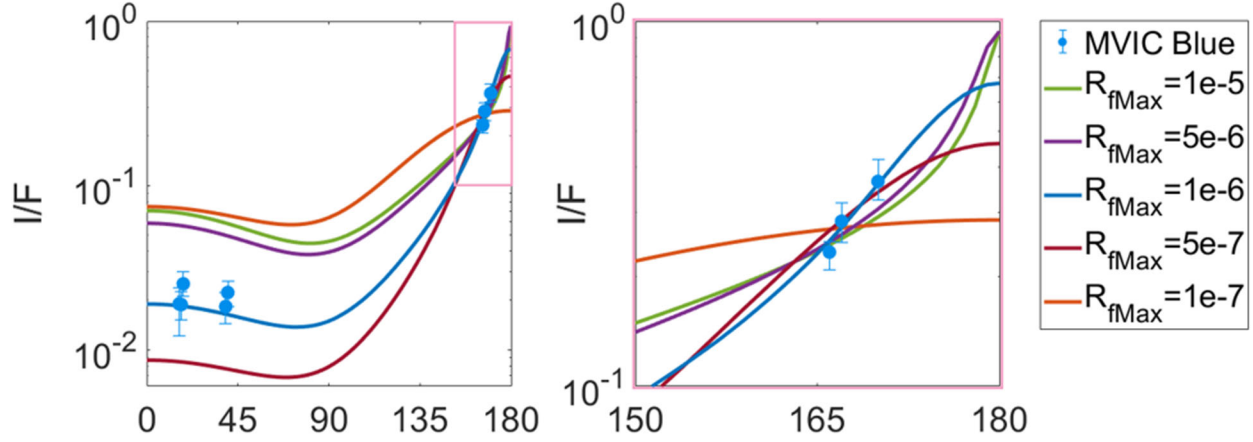


Figure 9 Phase functions produced by a best fit distribution of power law scatterers with $r_m = 10$ nm and $D_f = 2$ for the 20-40km altitude bin for the MVIC Blue filter. For each fit we vary the maximum R_f meaning no larger particles are considered in the fits, essentially setting their abundance to zero. Each phase function has a different power law exponent, b , which produces the best possible fit (highest R^2 value) for the range of R_f . The minimum size is set at two monomers large i.e. $R_f = r_m 2^{1/D_f} = 14.14$ nm (Left) Full phase range showing the relative change in high and low phase components. (Right) Zoom in of the high phase showing the change in slope from variable R_f .

As noted above, occasionally $R_f(Med)$ would occupy this crucial particle size at $R_f(Mie)$.

In these cases $R_f(Big)$ always diverged from a power law in size and abundance so that $R_f(Big)$ was less abundant than a power law would predict. Of these best fits that had $R_f(Med)$ occupying the crucial spot, the best of the best had $R_f(Big)$ occupying a size and abundance close to $R_f(Med)$, indicating more strongly that there is a dramatic decrease in the abundance of scatterers larger than the crucial particle size. This means that while we cannot definitively say whether the distributions follow a bimodal or power law at $R_f(Int)$, we can say that for scatterers larger than the scatterer size responsible for producing the slope at high phase angles, there must be a precipitous decline in abundance. This can be further confirmed by adjusting the particle range tested for the power law. We initially set $R_{fMax} = 1\mu m$ to be consistent with the modeling done by Gao et al. 2017. By adjusting R_{fMax} for the power law distribution, which unlike the bimodal and trimodal is a continuous distribution, we saw that the phase functions dramatically change in the shape of their slope at high phase angles and/or the difference in brightness between high and low phase angles (Figure 9). This all means that it is necessary to have a specific maximum particle

size at the right abundance, and then have an extreme paucity of larger particles even if it means a discontinuity in the particle abundance distribution. An in depth exploration of maximum particle size actually reveals that the best maximum particle size is $R_{fMax} = 1.4\mu m$. We did not use this value in our analysis however, because the increase in goodness of fit was minor and $R_{fMax} = 1\mu m$ is easier to compare across the other distribution types.

4. Results

4.1. Three Regime of Populations

Our results from the population investigation supports the empirical analysis of the high and low phase angle brightness done in 2.2. Phase Curves. From 500-200km, the atmosphere can be characterized by a tightly distributed population of scatterers at $R_f(Ray)$. In this altitude range photolysis is still taking place [[Bertrand and Forget 2017](#)].

From 200-60km, the atmosphere is characterized by two dominant populations of scatterers. The first is a population at $R_f(Ray)$ several orders of magnitude more abundant than any other population. The second is a population at $R_f(Mie)$, which is much less abundant but still crucial, as it is required to produce the appropriate phase functions. As can be seen in Appx. Table 4 B and C in the first few columns, the size of the fractal aggregates remains roughly the same for this altitude range. Here the minimum particle size is about 30 – 50nm and the maximum particle size, which was referred to as the crucial particle in Section 3.4.4 Trimodal, is about 500 – 750nm. While the particle sizes remain the same, the abundances for both increase inversely with altitude, in line with the occultation measurements made by *Alice* [[Young et al. 2018](#)]. In order for the lower 200km to be characterized by a bimodal distribution following this pattern, the scatterers at $R_f(Mie)$ would need to grow in abundance independently of $R_f(Int)$. It is difficult to imagine a mechanism that would preferentially produce only $R_f(Mie)$ scatterers at all altitude bins. That

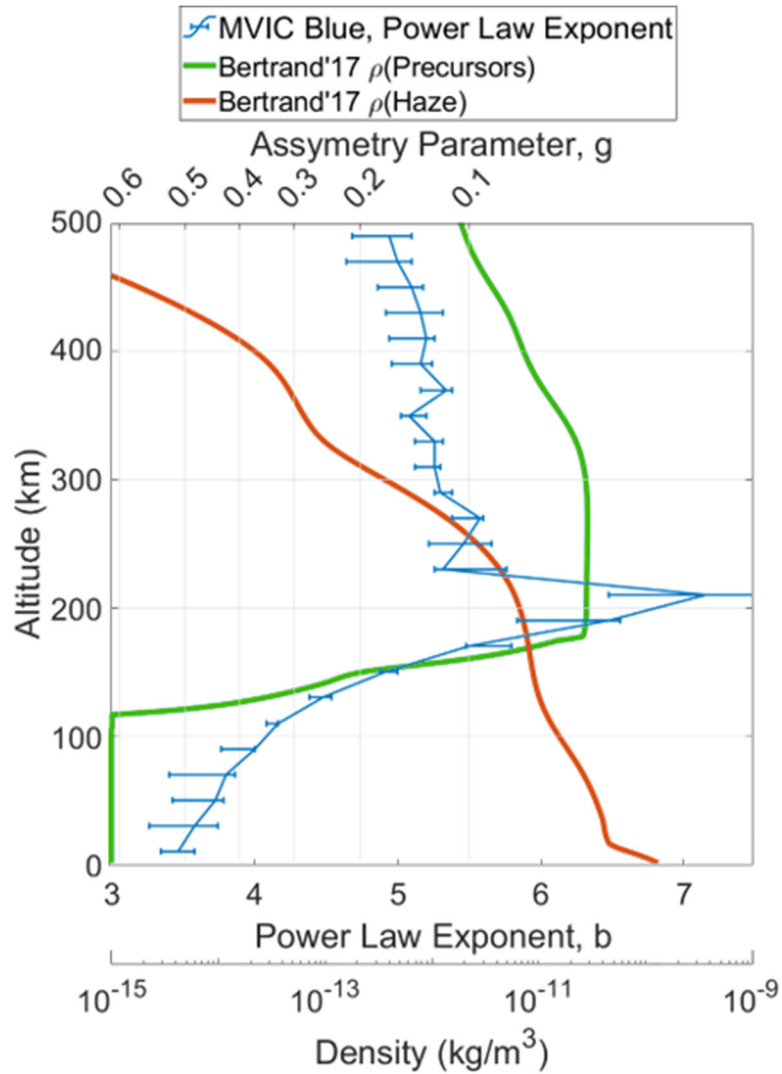


Figure 10 The best fit power law exponents as a function of altitude for $D_f = 2.0$, $r_m = 10 \text{ nm}$ (Blue). The upper x-axis shows the asymmetry parameter, g , for a phase function produced at MVIC Blue wavelengths by a fractal aggregate with the aforementioned fractal dimension and monomer size. (Green) The mass density of precursor material produced by photolysis predicted by Bertrand and Forget 2017. (Orange) The mass density of haze produced through aerosol growth of photolyzed material predicted by Bertrand and Forget 2017

being said the phase curves and R^2 value in Figure 8 clearly show that bimodal and trimodal populations, with their paucity of $R_f(Int)$, are better able to fit the phase curves and especially the steep slope at high phase angles.

As can be seen in Figure 10, the power law exponent steadily decreases until 60km where it begins to turn over and then increases in the lowest altitude bin 0-20km. A similar trend is seen in the parameters for the bimodal and trimodal distributions and indicates that the abundance

disparity between $R_f(Ray)$ and $R_f(Mie)$ steadily decreases from 200-60km, but starting at 60km, this disparity stops decreasing and briefly shows signs of increasing. This is the same altitude range where a dramatic change in temperature was observed by the *REX* instrument and ground-based stellar occultations [Sicardy et al. 2016; Hinson et al. 2017].

These three regions of aerosol growth (0-60km, 60-200km, and 200-500km) seem to occur at roughly the same altitudes where the number density of acetylene (C_2H_2), ethylene (C_2H_4), ethane (C_2H_6), hydrogen cyanide (HCN) and the temperature all experience dramatic slope changes [Lellouch et al. 2017; Young et al. 2018]. This indicates that either the processes controlling the abundance of these gasses also controls the growth rate of the aerosols, or that these gaseous components are directly responsible for aerosol growth via condensation. These regions also coincide with the termination of photolysis at ~ 200 km [Bertrand & Forget 2017] and a dramatic shift in the abundance of haze precursor material and haze (Figure 10).

4.2 Fractal Dimensions

We have until now assumed a fractal dimension of $D_f = 2$ for all the distributions for consistency with Tomasko et al. 2008 and Gao et al. 2017. However, D_f plays an important role in determining the porosity of the fractal aggregate which in turn dictates the sedimentation velocity, the cross-sectional area, and the coagulation rate. For all the distribution types discussed in Section 3.4 Population Types we investigated $D_f = 1.5, 2, 2.5$, while keeping all other parameters as they were originally described.

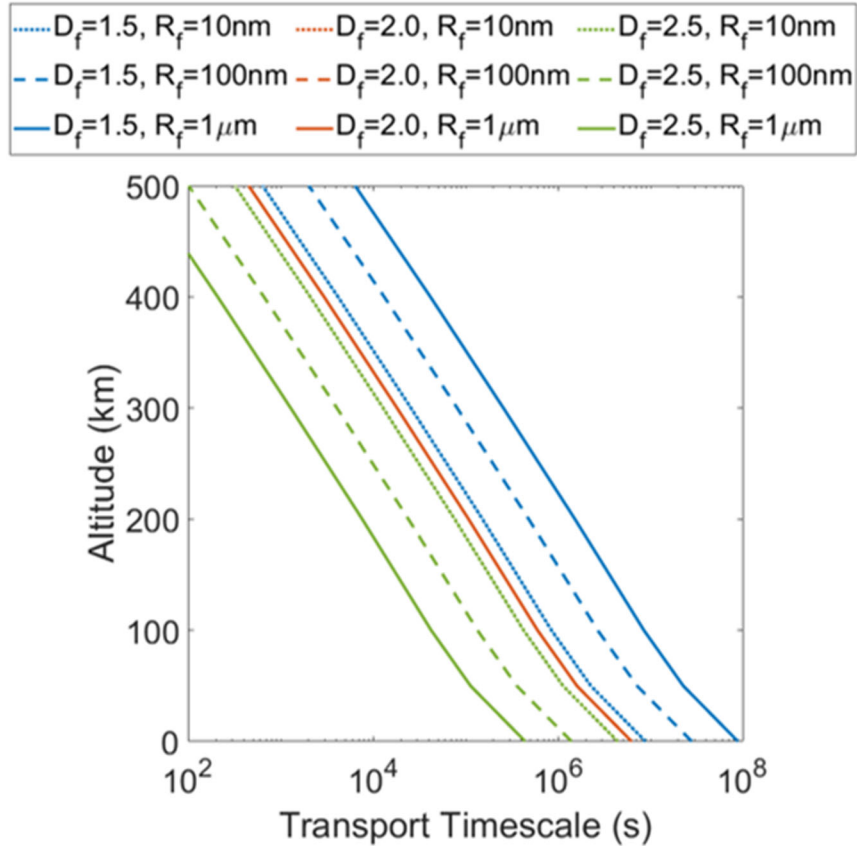


Figure 11 Sedimentation velocities of aerosols in Pluto's atmosphere for varying fractal dimension (D_f) and particle size (R_f)

A lower D_f results in lower sedimentation speed (Figure 11), increasing the time particles have to interact with one another and potentially grow, either through condensation or agglomeration. Although the model is not rigorously tested for a fractal dimension other than 2, as noted above, it will accurately show the difference between the monomer phase function and the aggregate. That is, a lower D_f will lead to a less compact aggregate, and that will show in the forward scattering.

While the model does account for interference effects within the fractal aggregate, it is also partially parameterized, and may therefore fail to accurately predict polarization and albedo values for aggregates with large numbers of monomers, especially when $D_f > 2$. As we are focused exclusively on the shape of the phase function, these shortcomings are not important. Future work

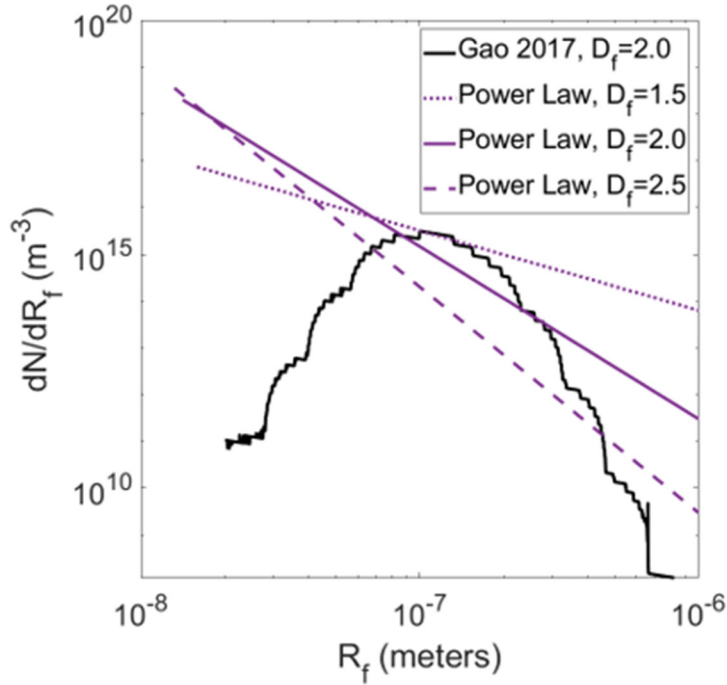


Figure 12 Comparison of cross section of fractal aggregate number densities for the 20-40km altitude bin from Gao et al. 2017 (Black) and the power law distributions (Purple) (Dotted) $D_f = 1.5, b = 1.703$ (Solid) $D_f = 2.0, b = 3.687$ (Dash) $D_f = 2.5, b = 4.830$

however should be done to ensure that phase functions with $D_f \neq 2$, that fit the observed phase curves are physically possible [Email communications with M. Lemmon 2020].

Changing the fractal dimension did not affect the quality of the fits nor the R^2 value in any appreciable way. For the bimodal and trimodal distributions, the best fit sizes for R_f also remained the same. As can be seen in Figure 12 for the power law distribution at 20-40km however, changing the fractal dimension resulted in a change in the relative abundance disparity between $R_f(Ray)$ and $R_f(Mie)$ and the total abundance $n(R_f)$. This is because the fractal dimension directly affects the extinction cross section, σ_e , where a larger D_f results in a larger σ_e . As we normalize our size distribution equations using Eq.13 and the *Alice* UV extinction coefficient, β_{Young} , we require that a decrease in σ_e must be compensated by an increase in the particle abundance, and vice versa. The biggest compensation occurred for the $R_f(Mie)$ scatterers, where at 20-40km we observed an

abundance difference of four orders of magnitude between $D_f = 1.5$ and $D_f = 2.5$. Meanwhile the $R_f(Ray)$ abundance only changed by about one order of magnitude over the fractal dimensions. This is likely due to a more significant change occurring in σ_e for larger scatterers than smaller ones. For all D_f tested, we noticed the same transitions at the same altitude discussed in [Section 4.1 Three Regime of Populations](#) for all population types.

4.3 Growth Mechanics and Implications

The abundance of $R_f(Ray)$ seen in the bimodal and power law distributions suggests that the coagulation rate is lower than that predicted by [Gao et al. 2017](#). This may be due to the haze having a higher charge to particle radius ratio, e^-/R_f . [Figure 5 \(top\)](#) of [Gao et al. 2017](#) shows variations in the particle size distribution 1.6 km above the surface of Pluto with changes in the particle charge to radius ratio, given in $e^-/\mu m$. They report a charge to particle radius ratio of $30 e^-/\mu m$, which produces a distribution of fractal aggregate in agreement with the retrieved mean particle size ($\sim 0.1-0.2\mu m$) from the forward scattering measurements [[Gladstone et al. 2016](#)], which is 2–4 times that obtained from observations of Titan aerosols [[Lavvas et al. 2010](#); [Larson et al. 2014](#)]. Following the pattern seen in their [Figure 5](#), and drawing a correlation to the high $R_f(Ray)$ abundances in our power law and bimodal distributions, we suggest that the haze has an $e^-/R_f \geq 60e^-/\mu m$. This is further supported by [Figure 5 \(bottom\)](#) of [Gao et al. 2017](#) which shows profiles of extinction coefficients, β_e ([Gao et al. 2017](#) uses α), corresponding to the particle charge to radius ratios of [Figure 5 \(top\)](#). While it reveals that β_e is not significantly perturbed when the charge to radius ratio is varied, it is also obvious that a higher e^-/R_f results in a lower extinction coefficient below 150km. While the profiles of β_e nearly match the observed β_e from the *Alice* UV solar occultations, they overestimate β_e below 150km, even for the largest charge to

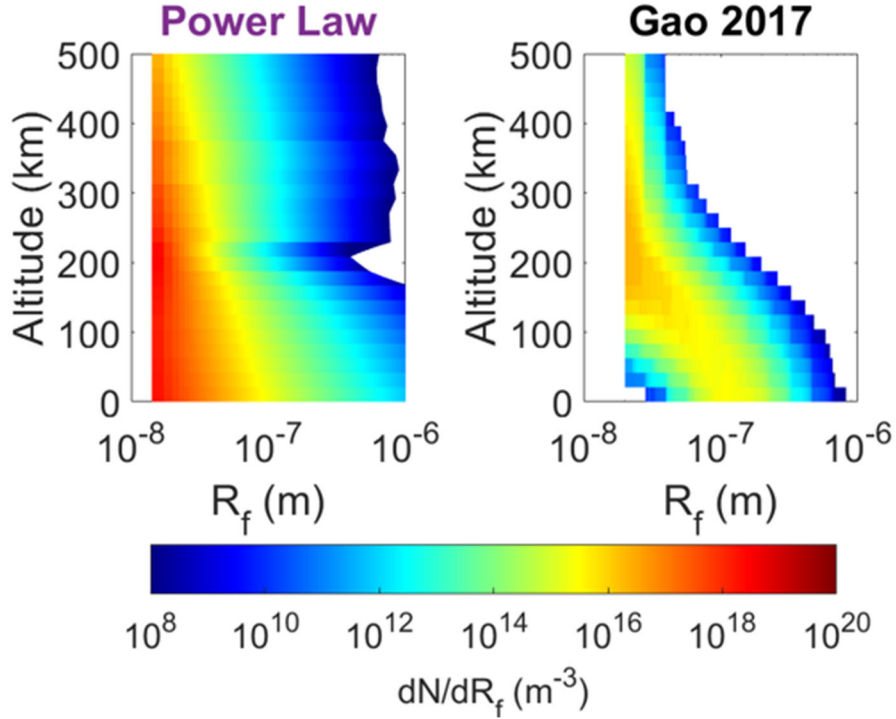


Figure 13: Number densities of particles as a function of altitude. Both are for fractal aggregates with $D_f = 2$, and $r_m = 10\text{nm}$. (Left) Best fit power law distribution. (Right) Gao et al. 2017 distribution

particles radius ratio tested by Gao et al. 2017, $e^-/R_f = 60e^-/\mu\text{m}$. Figure 5 (bottom) suggests that in order to match β_e below 150km, e^-/R_f must be greater than or equal to $60e^-/\mu\text{m}$.

In Gao et al. 2017 Figure 5 (top), the population distributions with a high e^-/R_f have a high abundance of scatterers at $R_f(\text{Ray})$, but a complete absence of $R_f(\text{Mie})$ scatterers. As we have shown in Figures 8, 12, and 13, it is necessary have an abundance of $R_f(\text{Mie})$ scatterers greater than the abundance predicted by Gao et al. 2017, in order to simultaneously match the difference in brightness between high and low phase, the slope at high phase, and β_e observed using *Alice*. This means that while a lower coagulation rate is necessary (possibly through an increased e^-/R_f), there must also be a mechanism which allows the aerosol to grow in size to $R_f(\text{Mie})$ and to a sufficient abundance to match the shape of β_e . One possibility is decreasing the sedimentation velocity of the haze by decreasing the fractal dimension. Using the sedimentation velocity equations from Gao et al. 2017 we show in Figure 11, that aerosols of $R_f \geq 100\text{ nm}$ and

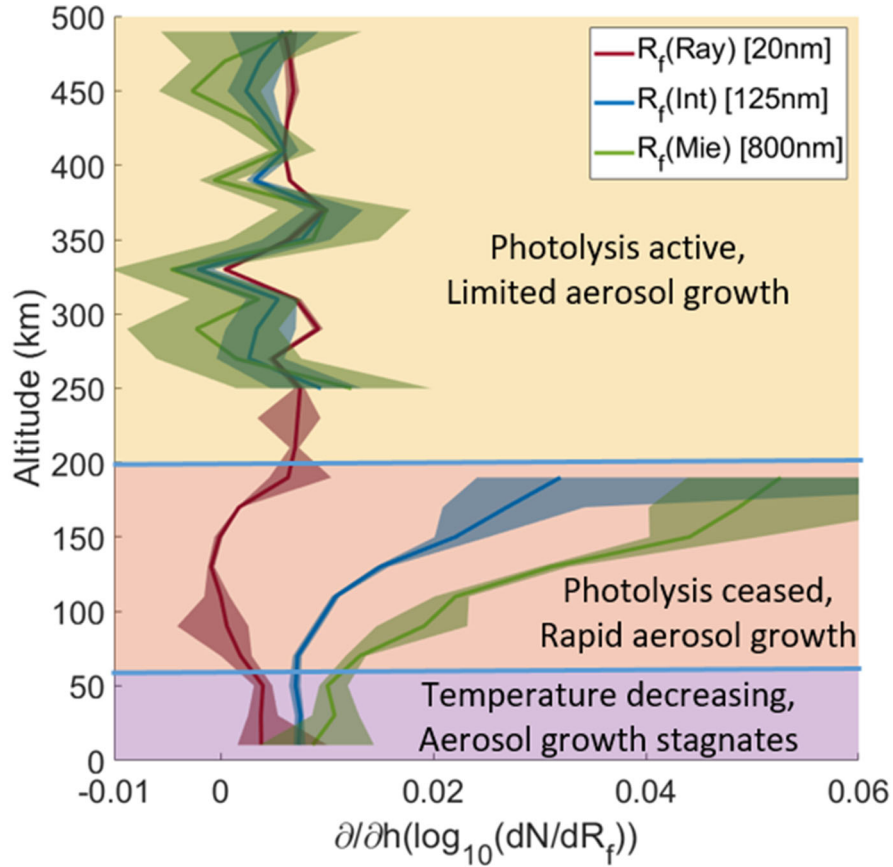


Figure 14 Log abundance gradient for characteristic particle sizes of the best fit power law distribution in Figure 12. We omit the 200-220 and 220-240 altitude bins for $R_f(\text{Int})$ and $R_f(\text{Mie})$ as their solutions are unconstrained. The yellow, orange, and purple regions denote the three regimes of aerosol growth. Yellow, 500-200km, here photolysis is active and little aerosol growth occurs. Orange, photolysis has ceased and aerosol rapidly grow and increase in abundance. Purple, the temperature drops and aerosol growth decreases precipitously, all sizes increase in abundance at the same rate.

$D_f = 1.5$, descend through the atmosphere an order of magnitude slower than aerosols with $D_f = 2$. This decrease in velocity gives the aerosols more time to coagulate and form larger particles, even with the larger e^-/R_f .

In order to describe the observed phase curves, there must be $R_f(\text{Ray})$ present throughout the entire atmosphere in high abundance and there must be $R_f(\text{Mie})$ particles orders of magnitude more abundant than determined by Gao et al. 2017 (Figure 12 & 13). Without a more complete phase curve we are unable to determine the necessary amount of $R_f(\text{Int})$, though we can place upper and lower limits on the abundance. We were able to determine that the abundance of

$R_f(Int)$, must be less than or about equal to what would come from a power law distribution. Without a mechanism that preferentially destroys or removes $R_f(Int)$, we can also assume that the abundance of $R_f(Int)$ must be greater than or about equal to the abundance of $R_f(Mie)$ that would come from a bimodal distribution. It is however possible that such a mechanism does exist to preferentially remove $R_f(Int)$, which point to our distribution being bimodal rather than a power law. This will require further modeling outside the scope of this paper.

The distribution and growth pattern of the aerosols could be indicative of three regimes of aerosol growth, controlled respectively by condensation, UV photolysis, and temperature. Figures 6, 11 and 13 all demonstrate areas where the growth rate and primary population type changes at ~ 60 km, and ~ 200 km. These transitions are highlighted in Figure 14, which shows the logarithmic change in abundance as altitude decreases for three particle sizes at the characteristic sizes of $R_f(Ray)$, $R_f(Int)$, and $R_f(Mie)$. From 500 to 200km, all three particle sizes experience little increase in abundance, with the smallest particles experiencing the greatest abundance increase, and the largest experiencing the least. This indicates that there is little growth of aerosols growth. From 200 to 60 km, the large particles begin to rapidly increase in abundance, while the small particles stop increasing in abundance and reach stagnation at ~ 150 km. This indicates that larger particles are starting to grow from the smaller particles, and use the small particles as fast as they can be delivered from above. Then from 60 – 0 km, all three particle size converge and increase in abundance at the same rate. This, along with the return to small particles increasing in abundance, suggests that aerosol growth has largely ceased. 200km in Pluto's atmosphere has been shown to be the altitude of peak condensation of acetylene (C_2H_2), ethylene (C_2H_4), ethane (C_2H_6) through heterogeneous nucleation [Wong et al. 2017]. As Wong et al. 2017 state, above 400 km, there are too few aerosols for condensation to be important, and below 200 km, the temperature is

too high to allow condensation. We point out that [Wong et al. 2017](#) shows that condensation occurs from 500-200km, and abruptly terminates at 200km. A similar trend at these altitudes occurs with the peak and termination of CH₄ photolysis ([Bertrand & Forget 2017 Figures 2,3 and 4](#)). [Bertrand & Forget 2017](#) attribute CH₄ photolysis to the production of haze precursor material, which steadily increases from 500km accelerating as it peaks at 200km, before, completely terminating just below 200km. In addition to and as a consequence of “C₂H_x” condensation and UV photolysis of CH₄ to make precursors, the temperature in Pluto’s atmosphere experiences several transitions of its own, as observed using *REX* and *Alice* [[Hinson et al. 2017](#); [Young et al. 2018](#)].

These three aspects of Pluto’s atmosphere follow the same path as the population distributions. It begins with a mostly monodisperse population giving rise to isotropic scattering, before rapidly evolving into disparate populations with an abundance of $R_f(Ray)$ and the presence of a maximum particle size of 500-750nm. From this we suggest that aerosol growth is limited above 200km, and produces mostly precursor material at $R_f(Ray)$. Where this haze nucleation and condensation is occurring, the temperature in Pluto’s atmosphere is roughly constant around 70K. At 200km the spike in precursor production and condensation should lead to the formation of an abundance of aerosols mostly at $R_f(Ray)$ but at other sizes as well. Below 200km, where the condensation and photolysis has ceased, the temperature begins to increase from ~70K at ~300km to ~110K at ~40km. In this more kinetically active environment, free from condensation, the haze particles rapidly interact to form larger particles through fractal coagulation. The coagulation rate is such that $R_f(Mie)$ increase in abundance about five orders of magnitude between 200km-50km. In this same range the $R_f(Ray)$ particles barely increase one order of magnitude, showing that the coagulation rate of particles is slightly less than the production rate of precursor material (Figure 14). This temperature controlled coagulation is further supported by

the observation in Figure 14 that at 60km the coagulation rate starts to diminish and all populations uniformly increase right before the surface. This is consistent with the temperature inversion observed using *REX* and *Alice* occurring at the boundary surface layer [Young et al. 2018]. Here the temperature first approaches an inflection at $\sim 110\text{K}$, before rapidly cooling to $\sim 40\text{K}$ at the surface. In this kinetically less active environment we would expect the aerosols to cease interactions and proceed to fallout.

These hypotheses suggest possible formation mechanism for the bimodal or power law distributions that must be present to produce the phase curves observed by *MVIC*. Further microphysical haze and general circulation modeling however, will need to be conducted to test these the assertions. Additionally, more complete radiative transfer limb scatter analyses, which could include multiple instruments that are able to fill the phase coverage gap, will be needed to break the degeneracy of a bimodal or power law distribution. Breaking this degeneracy will favor one formation mechanism over another.

5. Summary and Conclusions

The main results of this work are:

- 1) We have characterized and removed an instrumental bias which added spurious brightness far off the disks of Charon and Pluto. This off disk glow accounts for up to 30% of the observed brightness in the lower atmosphere and greatly distorts the shape of the phase curves, particularly in the back scatter regime.
- 2) We have produced phase curves of Pluto's atmosphere from *MVIC* observations using the limb scatter technique. These observations were corrected for the above described off disk glow. The phase curves were produced for the *MVIC* RED (pivot wavelength of $620\mu\text{m}$), *MVIC* BLUE (475nm), and *MVIC* NIR (878nm) filters. Our dataset covered an altitude

range of 0-500km as well as low and high solar phase angle of 16.15° to 18.24°, 38.85°, and 165.96° to 169.36°. For this work we binned all the data which matched our sub selection criteria, as described in Section 2.2. Data Processing, into 20 km wide altitude bins and one-degree wide phase bins. This produced the dataset in Appx. Tables 2 and 3.

- 3) The phase curves show that Pluto's lower atmosphere (<200km) is strongly forward scattering, indicative of a population of scattering particles in the Mie regime, which means the size of the particles is approximately equal to the wavelength of light. In the lower atmosphere there is a non-negligible amount of back scatter. This indicates that there must be a distribution of particles, as the phase functions produced by only the aforementioned Mie particles, have nearly no back scatter component. As such there must be an additional population of small size scatterers, which occupy the Rayleigh regime and are much smaller than the wavelength of light. In the upper atmosphere (>200km) the scattering becomes nearly isotropic. This suggests that between the upper atmosphere and the lower atmosphere there is the rapid accumulation or growth of large size scatterers.
- 4) We modeled the phase functions produced by a monodisperse, bimodal, trimodal, lognormal, and power law distribution of particles. Our results confirmed the empirical analysis of the phase curves: that a distribution of particles characterized by an abundance of small size scatterers $R_f < 50nm$ (99%), and a non-negligible amount of large scatterers ($100nm < R_f < 1\mu m$) (1%) which specifically include a crucial particle size of 500-700nm are able to fit the phase curves observed below 200km. Above 200km, these populations all approximated a monodisperse population with a characteristic particle size where Rayleigh scattering dominates ($R_f(Ray) \approx 10 - 100nm$). Without color observations over the complete range of phase angles, we cannot determine the abundance

of intermediate sized scatterers ($R_f(Int) \approx 100 - 500nm$), though it must be less than or equal to the abundance of $R_f(Int)$ from a power law and greater than or equal to the abundance of large aerosols scattering in the Mie regime ($R_f(Mie) \approx 500nm - 1\mu m$) from a bimodal distribution.

- 5) In order to achieve aerosol population distributions with great abundance disparities between Rayleigh sized scatters ($R_f(Ray) \approx 10 - 100nm$) and Mie sized scatters ($R_f(Mie) \approx 500nm - 1\mu m$), the atmosphere needs to produce large $R_f(Mie)$ scatterers while not eliminating the smaller $R_f(Ray)$. This can be accomplished by increasing the charge to radius ratio to prevent removal of smaller scatterers, while reducing the sedimentation velocity to allow these more coagulation resistant particles an opportunity to form large scatterers. The sedimentation velocity can be reduced for larger and larger particles with a fractal dimension less than two.

Chapter 3: The Circulation Patterns of Atmosphere

Titan Stratospheric Haze Bands Observed in Cassini VIMS as Tracers of Meridional Circulation

N. W. Kutsop, A. G. Hayes, P. M. Corlies, S. Le Mouélic, J. I. Lunine, C. A. Nixon, P. Rannou, S. Rodriguez, M. T. Roman, C. Sotin, T. Tokano, and The Cassini VIMS Team

Planetary Science Journal, May 2022, <https://doi.org/10.3847/PSJ/ac582d>

1. Introduction:

Titan has a thick organic haze that obscures its surface at visible and infrared wavelengths, and is produced through the dissociation of CH₄ and N₂ by UV light and charged particles [Yung et al. 1984; Lavvas et al. 2008a; Lavvas et al. 2008b]. Noteworthy haze features include a globally extensive thin layer of detached haze (the Detached Haze Layer)[Smith et al. 1981; Rages & Pollack 1983; Rannou et al. 2002; Teanby et al. 2009d; West et al. 2018; Seignovert et al. 2021]; a hemispheric asymmetry in brightness (the North-South Asymmetry) [Sromovsky et al. 1981, Smith et al. 1982; Tomasko & Smith 1982], and polar hoods that occur during local winter (i.e. the North and South Polar Hoods) [West et al. 2016; Seignovert et al. 2021; Le Mouélic et al. 2018; Lorenz et al. 1997b; Penteado et al. 2010b]. Tracking the distribution and evolution of Titan's haze is a key tool for studying Titan's atmospheric photochemistry, dynamics, and circulation. Herein, we describe circumglobal bands, or annuli (Figure 15 & 16), in Titan's atmosphere using observations from *Cassini's* Visual and Infrared Mapping Spectrometer (VIMS) and discuss their relevance to the nature of Titan's stratosphere and circulation in general. We also used the Cassini Imaging Science Subsystem (ISS) to investigate links between the annuli seen in VIMS and clouds detected by ISS [Turtle et al 2018] (Figure 16).

Circumglobal bands have been previously identified in Titan's atmosphere. Like the north-south asymmetry, these have been observed to be dark at wavelengths shorter than 600 nm and

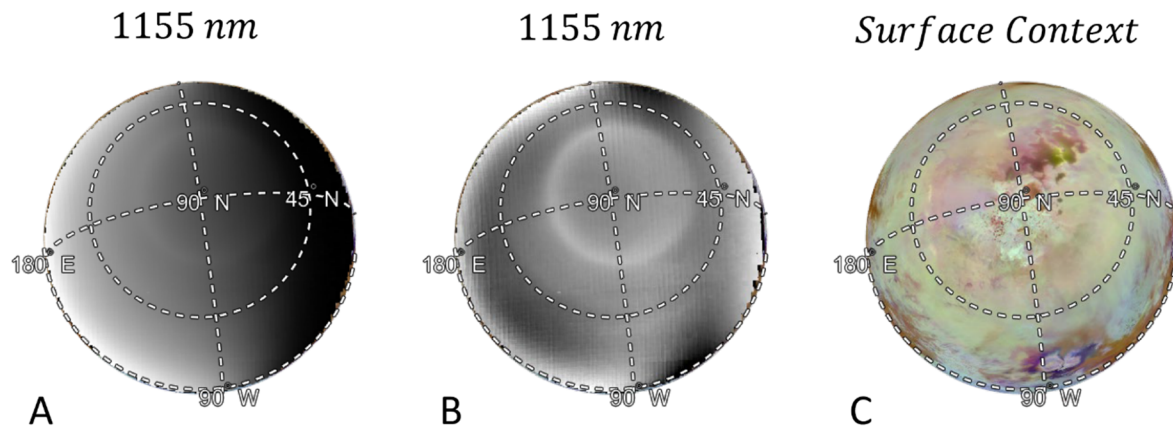


Figure 15: Orthographic mosaics of T096, 2013-12-01, LS = 51.2o (A) 1155nm mosaic, (B) 1155nm mosaic with manifold correction. (C) Context using VIMS-ISS map [Seignovert, et al., 2019]

bright in methane absorption channels such as those at 900nm and 1150nm. North polar atmospheric bands have been previously observed [Smith et al. 1982; Griffith et al 2008; Jennings et al. 2015; Le Mouélic et al. 2018] and the North Polar Annulus (NPA) has likely been observed before [Sromovsky et al. 1981; Rannou et al. 2012; Le Mouélic et al. 2012], but not with the morphology and spectral characteristics we report for the first time, which were only possible with near nadir observations of the north pole taken around 2014. The Equatorial Annulus (EQA) has been previously identified in other works, either directly or indirectly [Roman et al 2009; de Kok et al 2010a]. A South Polar Annulus (SPA) was observed in Titan's south polar region by Keck and HST [Roe et al 2002; Lorenz et al 2001c] prior to *Cassini's* arrival at Saturn. Throughout the course of the *Cassini* mission, we did not observe the south polar annulus seen previously.

Circumglobal atmospheric bands are found on all solar system bodies with a substantial atmosphere and are valuable observables for investigating a variety of planetary processes. On Earth and Venus these bands are found in the jet streams which can be observed by tracking clouds or infrared radiance [Horinouchi et al. 2017]. These jets reveal the location of meridional convergence zones and can be used to understand the pattern of zonal circulation. Annular modes of variability have recently been identified in the atmospheres of Mars and Titan [Battalio and Lora

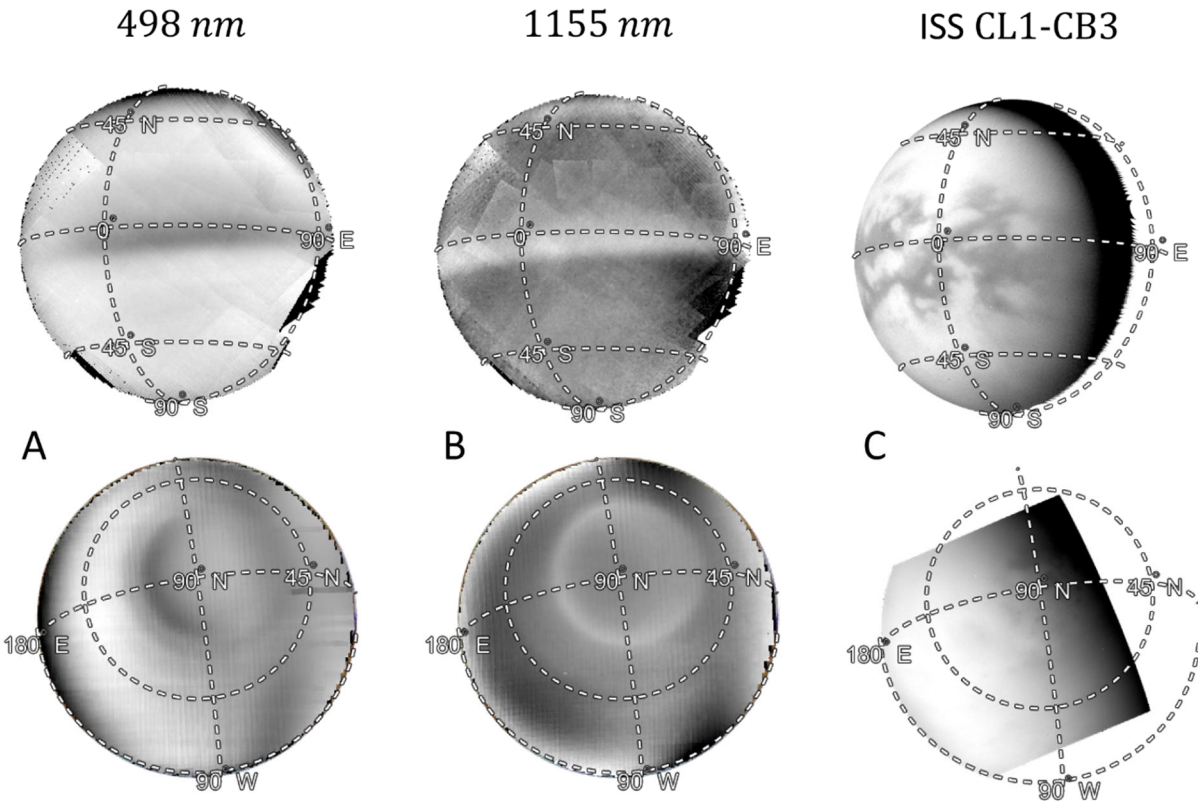


Figure 16: (Top) T061, 2009-08-25, $L_s = .49^\circ$, (Bottom) T096, 2013-12-01, $L_s = 51.2^\circ$. (A) 494nm mosaic with manifold correction, (B) 1155nm mosaic with manifold correction. (C) ISS NAC observations taken during the same respective flyby. Both are taken with filters CL1 and CB3 with an effective wavelength of 938.03 nm [Knowles 2016]. Image names are (top) N1630071434_1 (bottom) N1764434226_1

2021]. Annular modes such as these, explain much of the internal variability of Titan's troposphere as simulated in a global circulation model (GCM). The gas giants (Jupiter and Saturn) and the ice giants (Uranus and Neptune) all display patterns of planetary banding, with regions of different temperatures, composition, aerosol properties and dynamics separated by strong meridional and vertical gradients in the zonal (i.e., east-west) winds [Fletcher et al. 2020]. Auroras are particularly bright bands found on the giant planets, Earth, Mars, and Ganymede. Auroras at Ganymede reveal that the largest moon of the solar system has an internal ocean [Saur et al. 2014]. Jupiter's auroras are used as evidence in explaining why the gas giant's upper atmosphere is much hotter than expected from sunlight alone. Spectroscopic observations of these bands from Keck II suggest that the excess heat is produced by the redistribution of auroral energy [O'Donoghue et al. 2021].

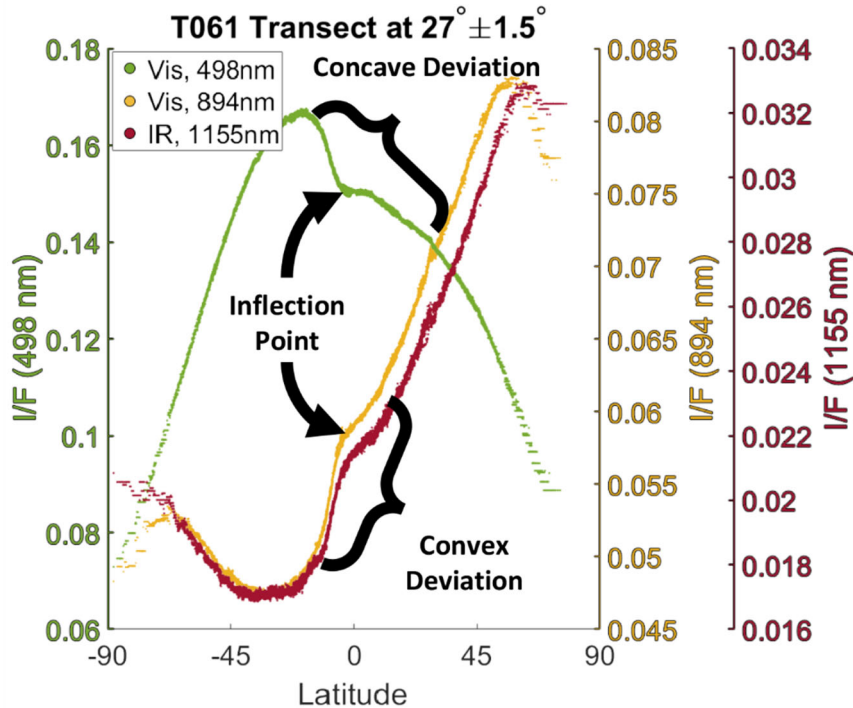


Figure 17: Transect of pixels from mosaic of T61 flyby [2009-08-25] (See Figure 16). The deviation in each of the three curves is attributed to the equatorial annulus (EQA). The inflection point of each deviation is attributed to the center of the annulus and the Gaussian tails on either side of the inflection point is the uncertainty in locating the annulus. The north-south asymmetry appears as the smooth parabolic curve between the hemispheres. The equatorial annulus adds a sharp deviation in the curve, without which the north-south asymmetry would appear as a gradient between the hemispheres, rather than the asymmetry we see.

Observations of Titan show that the stratosphere is super-rotating with wind speeds of ~ 200 m/s [Flasar and Achterberg 2009]. Several Titan GCMs are able to reproduce the super-rotation, though not always with wind speeds matching observations. The results of these GCMs are in agreement with the Gierasch-Rossow-Williams (GRW) mechanism for producing super-rotations [Horst 2017]. In the GWR mechanism, angular momentum is transported to higher altitudes and then poleward by mean meridional circulation and is transported down and to the equator by barotropic waves generated by instabilities on the edges of the high-latitude jets [Hourdin et al. 1995; Lebonnois et al. 2014; Gierasch 1975; Rossow & Williams 1979].

Analysis of the stratospheric super-rotation by the Cassini Composite Infrared Spectrometer (CIRS), revealed the stratosphere to be tilted 4° with respect to the solid body rotation axis [Achterberg et al. 2008]. Multiple observations of the tilt showed that it was directed 76° west of

the subsolar longitude. Further observations using CIRS suggest that the tilt is not fixed in a solar reference frame, but rather fixed in an inertial reference frame [[Achterberg et al. 2011](#)]. The tilt has been confirmed by multiple follow up investigations using composition and tracking atmospheric features [[Achterberg et al. 2008](#); [Roman et al. 2009](#); [Teanby et al. 2010b](#); [West et al. 2016](#)].

While mechanisms that explain the tilt and its relationship with super-rotation have been put forth [[Achterberg et al. 2008](#); [Tokano 2010a](#)], there remains a lack of consensus. Achterberg et al 2008 proposed that the tilt, by feedback between the circulation and the heating, facilitates the vertical transport of angular momentum to balance the heat flow and insolation at low latitudes. [Tokano 2010](#) proposed that the tilt is the result of thermal tides and is only possible if atmospheric waves perturb the circulation. With the annuli, we are able to produce a time series set of measurements of the tilt, and its azimuthal offset, throughout the *Cassini* mission (2004-2017), which provides an important database that can be used for future modeling of the origin and evolutions of the tilt, the super-rotation of the middle atmosphere, and the link between them.

Saturn's eccentricity (0.055) and obliquity (26.7°) dictate the variation in the amount and location of haze production throughout a Titan year. The obliquity also causes the meridional circulation to be asymmetric about the equator and to reverse semi-annually [[Teanby et al. 2012](#); [Lebonnois et al. 2012a](#)]. The flow rises in the summer polar region and descends in winter polar regions. As the cells redistribute the heat in Titan's atmosphere, it also vertically transports gasses and aerosols to high altitudes, transports them horizontally across the globe, and carries them back down to lower altitudes. During the fall and spring seasons, the single pole-to-pole cell splits into two symmetric cells where the atmosphere ascends at the equator and descends at each of the poles [[Mitchell et al. 2006](#); [Tokano 2011](#); [Newman et al. 2016](#); [Lora et al. 2019](#); [Battalio et al. 2021](#)].

We discuss in *Section 4* the apparent correlation of the annuli presence and location with the predicted meridional circulation cell cycle.

1.1. The Equatorial Annulus

The EQA occurs at the boundary of the north-south asymmetry [Roman et al. 2009, de Kok et al. 2010]. The north-south asymmetry is a feature of Titan's atmosphere where one hemisphere is darker than the other; which hemisphere is darker varies as a function of time and the degree of contrast varies with wavelength. The north-south asymmetry was first observed in 1980-11-11 in Voyager 1 observations (and retrospectively observed in Pioneer 11 observations, 1979-08-31), and has since been observed continuously by ground-based telescopes, HST, and *Cassini* [Smith et al. 1981; Sromovsky et al. 1981; Caldwell et al. 1992]. Previous analysis of ISS data from 2004-2007 indicates that the EQA/north-south asymmetry was present at around 80 km altitude with an axial tilt of $3.8^\circ \pm 0.9$ relative to the spin axis, with the vector directed $79^\circ \pm 24^\circ$ to the west of the subsolar longitude [Roman et al. 2009]. A height of 80 km, with possible additional contributions between 50 and 150 km, was also inferred for the EQA from *Cassini* VIMS [de Kok et al. 2010a], while CIRS measurements of HCN indicated the hemispheric asymmetry extended to at least 125 km [Teanby et al 2010b]. In images of scattered light, the EQA helps to exaggerate the difference between the hemispheres (Figure 17). The variability in altitude estimations above can be attributed to the variety of instruments used, changes in the EQA over time, and targets accessed, i.e. the HCN used by Teanby et al 2010b may be a part of the EQA but at an altitude different from the haze in the north-south asymmetry used by Roman et al. 2009.

The EQA is one of the few features observed at visible wavelengths that has been observed between Titan years, as the EQA can be inferred from observations of the north-south asymmetry

seen by Pioneer 11 (September 1979, [Tomasko & Smith 1982](#)), Voyager 1 (November 1980, [Sromovsky et al. 1981](#)), and Voyager 2 (August 1981, [Smith et al. 1982](#)).

1.2. The North Polar Annulus

The NPA is, on average, spectrally and morphologically identical to the EQA. The spectra, size, and position of the NPA change more profoundly than the EQA, which we discuss in *Section 4.2*. Because more than half of the NPA can be seen in a single observation and there are multiple observations with the same illumination geometry taken close in time to one another, we are capable of triangulating the NPA (*Section 2.4*). We use the vector normal to the plane of the modeled ellipses to describe its tilt with respect to the rotation axis of Titan's solid body (θ_{NP}), its axial precession west of the subsolar longitude (ϕ_{Sol}), and its declinations in an inertial reference frame.

1.3. The South Polar Annulus

The SPA was not observed in the *Cassini* data, due to the timing of the event. The SPA appeared as a weak dark ring using the Hubble Space Telescope (HST) at 336 nm (HST Wide Field and Planetary Camera filter F336W) [[Lorenz et al 2001c](#)] and a bright collar using Keck II at 1158 nm and 1702 nm (W.M. Keck II KCAM and SCAM, filters J1158 and H1702) [[Roe et al 2002](#)] around 60°S latitude and centered on the south pole from 1999 to 2001. [Lorenz et al. 2001c](#) concluded that at least some of the material responsible for this feature must be at altitudes of above 150km. [Roe et al 2002](#) used the presence of the SPA in the J1158 Keck filter to conclude that SPA must be at or above 40 to 50 km altitude. Both [Roe et al. 2002](#) and [Lorenz et al. 2001c](#) note the similarity of the SPA they observed with the dark northern collar observed by Voyager 2 around the north pole and suggested that the SPA has a seasonal origin. The altitude difference between [Roe et al. 2002](#) and [Lorenz et al. 2001c](#) can be attributed to the different wavelengths used to interpret the altitude (i.e. 336 nm vs 1702 nm).

2. Data/Methods

Our processing workflow starts with the publicly available VIMS data set on the Planetary Data System (PDS) [Le Mouélic et al 2019; https://pds-imaging.jpl.nasa.gov/data/cassini/cassini_orbiter/covims_0001/data/]. VIMS consisted of two imaging spectrometers; a visual detector (VIMS-Vis) with 96 channels between .35 and 1.05 μm and an infrared detector (VIMS-IR) with 256 spectroscopic channels between 0.89 and 5.13 μm [Brown et al. 2004]. The absorption and scattering by methane, nitrogen, and haze means that some channels in VIMS can see the surface, while for other channels the atmosphere is completely opaque [Corlies et al 2021]. For every pixel, we determined the viewing geometry and location information using the SPICE toolkit from NAIF [Acton et al 2017].

2.1. Data Correction and Mosaicking

We created super-sampled mosaic images of Titan for ingress and egress observations of each flyby, weighting higher spatial resolution pixels more in the mosaicking. We rasterized the pixels to a spatial resolution of 5 km² and calculated the weighted average of all individual image pixels that filled each pixel of the mosaic. The primary constraints on data incorporated into the mosaics was a pixel scale of less than 250 km and a change in the phase angle, θ , of less than 3°. This means closest approach observations, with their rapidly changing viewing geometry, were not used.

VIMS image cubes from the Vis detector have stripes of varying brightness at each sample running across the lines. The stripes are due to offsets of about one hundred DN introduced by the readout electronics on the signal [Filacchione et al 2007]. We developed a destriping routine described in *Appx. F. Destriping VIMS-Vis* which we applied to every VIMS-Vis image cube.

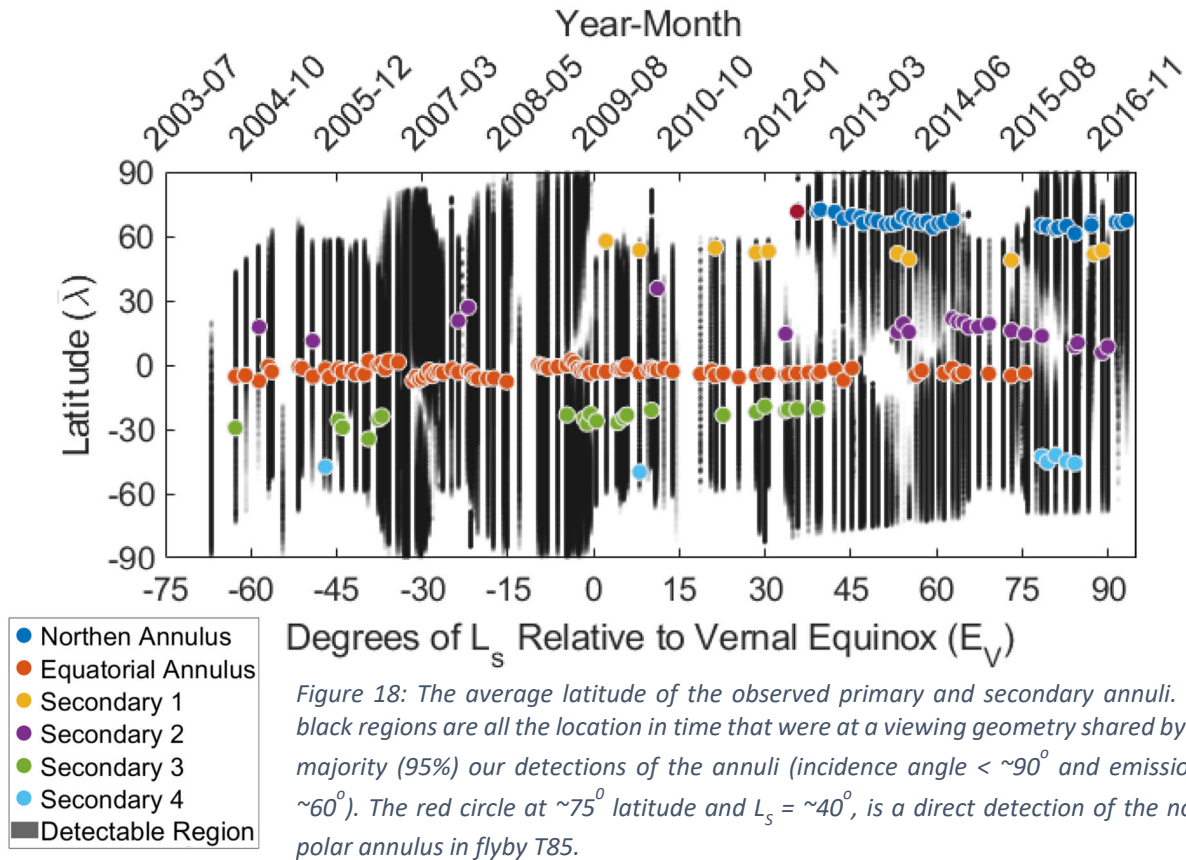


Figure 18: The average latitude of the observed primary and secondary annuli. The black regions are all the location in time that were at a viewing geometry shared by the majority (95%) our detections of the annuli (incidence angle $< \sim 90^\circ$ and emission $< \sim 60^\circ$). The red circle at $\sim 75^\circ$ latitude and $L_s = \sim 40^\circ$, is a direct detection of the north polar annulus in flyby T85.

We leverage Titan’s smoothly scattering atmosphere to improve contrast in the image cubes and increase spectral clarity (see *Appx. G. Manifold Correction Technique*). Manifold corrections were applied to all image cubes from both detectors, although we only used the manifold corrected data for making mosaics and examining images (Figures 15 & 16). Data used for spectral analysis, like the transects discussed below, have no corrections applied except the VIMS Radiometric Calibration, RC19 [Clark et al 2018], which is applied to all VIMS PDS data and the destriping applied to VIMS-Vis.

2.2. Identifying the Annuli Through Transects

Taking a north-south transect of the pixels in a mosaic at a single longitude and over all latitudes produces a curve of brightness for the queried wavelengths and longitudes (Figure 17).

In these meridional transects the band can be seen as a deviation in the normally smooth and featureless curves. For wavelengths where the annuli are darker than the surrounding atmosphere, the deviation is concave, while for wavelengths where the band is bright, the deviation is convex.

We used the transects to determine the presence and location of the annuli. We propose that the center of the annulus is at the inflection point for the observed deviations, and that the width of the annulus is where the deviation returns to the smooth path. The annuli in general appear darkest at ~ 500 nm and brightest at ~ 1150 nm, and are also very bright at ~ 900 nm. We use these three channels to investigate the annuli because they show the greatest contrast and span both the VIMS-Vis and VIMS-IR detectors. Using both detectors to identify the annuli is necessary for redundancy because occasionally one detector will have bad data. We took transects of each flyby on the ingress and egress hemisphere, every 10° of longitude (i.e. 60° , 70° , 80° , etc.) and spanning all visible latitudes. This produced a dataset of 4829 transects, and each of these were examined to determine if deviations matching the ones associated with the annuli were present.

We created a dataset of annuli detections with information on the viewing geometry, coordinates, and time of observation by analyzing the transects. Transects were analyzed manually in a random order (randomizing over both flyby and longitude) to prevent unintentionally biasing our search to patterns seen when looking at consecutive longitudes in the same flyby. We then reorganized our data and displayed those detections over the appropriate flyby mosaics. With the context of the mosaics we found that our initial search results produced many false positives. These false positives were caused by several sources, including the north polar hood, the south polar vortex, observation of the limb at irregular angles, and seams between VIMS image cubes [Kelland et al. 2018, Le Mouélic et al. 2018]. We identified and removed these false positives by reinvestigating each transect, this time in flyby and longitude order, as well as viewing the relevant mosaics.

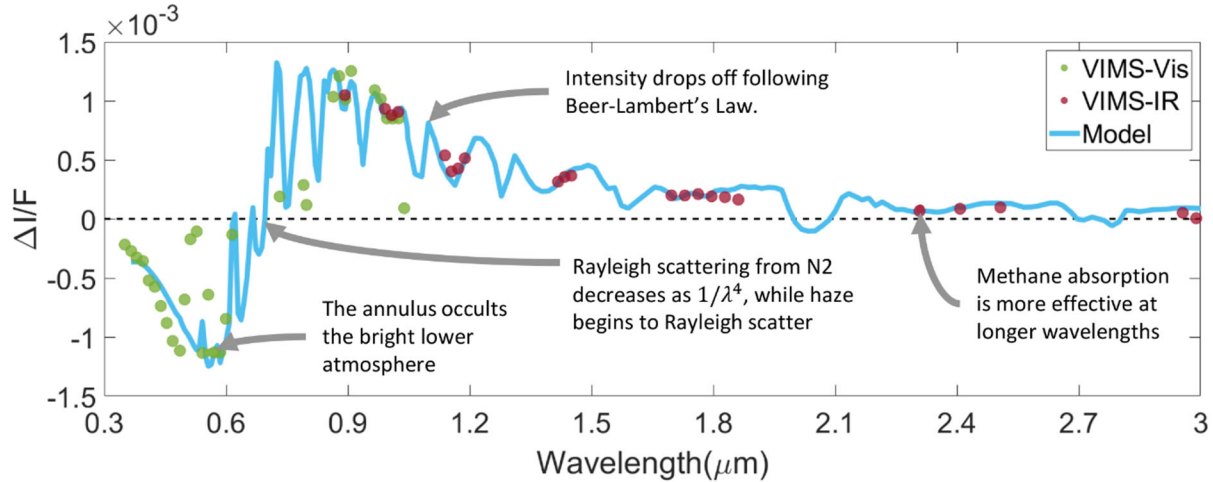


Figure 19: Averaged differential spectrum of the equatorial annulus (EQA) from $L_s = 345^\circ$ to 15° (flybys T044-T072). The differential spectra shown in the cyan curve is produced from the difference between a model spectrum with typical haze abundance, and model spectra where the haze abundance is increased at 100-130 km by 10%.

We further refined and expanded our detections by explicitly looking for patterns in the location of the inflection point between the transects that correlated to features that had the morphology of the annuli. This is the dataset we use for tracking the annuli over the course of the Cassini mission and producing the sinusoidal fits and triangulated models. Our final dataset contained 552 transects for the NPA and 686 transects for the EQA, and a total of 256 transects for the four secondary annuli. Figure 18 shows our range of detections through the average latitude of the annuli. Information on the location timing and aspects such as tilt of the averages of our transects is provided in Appx. Table 5.

We use the transects to acquire spectra of the annuli. The spectrum of the annuli has no distinguishing features when compared to spectra taken from pixels located just north or south of the annuli (Appx. Figure 5). This suggests that the annulus is compositionally indistinct from the rest of the atmosphere and that observed brightness differences are the result of a local increase in haze optical depth. Instead of a typical VIMS spectrum, we investigated the differential spectrum of the annuli, $\Delta I/F$. Using the transects we identify the northern and southern edge of the annuli, i.e. where the smooth featureless atmosphere transitions to the deviation of the annuli and back

again. We use these bounds to remove the deviation from the curve, and we then interpolate the data spanning the resulting hole. We use a straight line (first degree polynomial) to interpolate the data. We have investigated using a second and third degree polynomial, as well as splines, and the results are very similar. We therefore use the straight line, as anything more complicated is not justifiable. The differential spectrum is then the maximum difference between the deviation and the interpolated data. Figure 19 shows the average differential spectrum of the T061 EQA. This is a good representative of the EQA and NPA spectra, except for early and late spectra of the NPA which we discuss in *Section 4.2*.

2.3. Altitude from Spectra/Spectraltimetry

We estimated the altitude of the annuli using spectraltimetry. Features entrained in an absorbing medium will become visible at different pressure levels dependent on the wavelengths. Using superposition, we can infer the shape and altitude/depth of a feature by its appearance in the spectra. This technique has already been used extensively at Titan for measuring the height of clouds using observations from Cassini and ground-based telescopes [Brown et al. 2002; Le Mouélic et al. 2012a; Ádámkóvics et al. 2016a; Corlies et al. 2021]. As methane is the primary absorber in Titan’s atmosphere at IR wavelengths, we used a methane opacity profile from Rannou et al. 2016 to estimate the altitude of the EQA and the NPA. We calculated the altitude where the atmosphere becomes opaque in two ways. First, we determined the altitude, H , where the sum of the weighted (with Gauss coefficients) effective optical depth (following Pollack and McKay, 1985) calculated with four k-correlated coefficients where $\tau(z) = \sum_{i=1}^4 w_i \tau_i(z)$ is equal to 1 [Goody et al. 1989]; this is the dotted green curve in Figure 20. Second, we determined the average H as the weighted altitude (with Gauss coefficients) $H = \sum_{i=1}^4 w_i H_i$ calculated from the altitudes

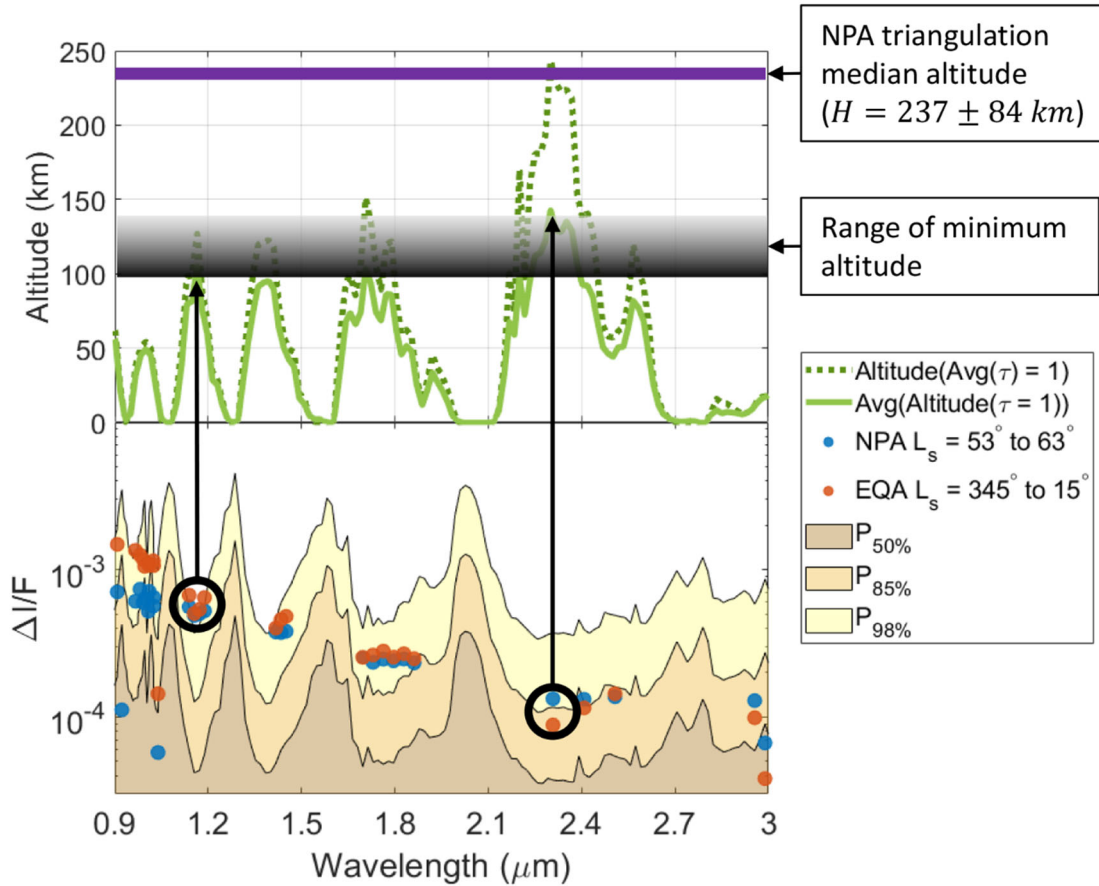


Figure 20: The averaged differential spectra of the north polar annulus (NPA; blue) and the equatorial annulus (EQA; orange) from $L_s = 55^\circ$ to 65° and $L_s = 345^\circ$ to 15° respectively. The purple line indicates the average median altitude of Model A and Model B from our triangulation efforts of the NPA, Section 3.5. The green curves show the modeled altitudes where the atmosphere is opaque when averaged over the different terms of the k -correlated description. Solid green curve, the altitudes where the average column opacity is equal to 1. Dashed green curve, the average altitude where the column opacity is 1. Yellow, gold, and brown, are the 50th, 85th, and 98th percentile values of the difference between neighboring pixels across all flybys. Features in the differential spectra are significant if they are outside these bounds. The grey area shows the range of expected minimum altitudes based on the detection at $\sim 1.2 \mu\text{m}$ with $> P_{98\%}$ and the detection at $\sim 2.3 \mu\text{m}$ with $\approx P_{85\%}$

H_i where the effective $\tau_i(z)$ are equal to 1; this is the solid green curve in Figure 20. We believe that the second method is more appropriate for spectraltimetry.

In order to determine the altitude of a feature, we must first determine if the difference of the feature from the rest of the observation is significant. To determine the significance of a feature we used a similar approach outlined in [McCord et al. 2008](#) and the references therein. We found the $\Delta I/F$ between neighboring pixels in our mosaics and determined their n^{th} percentile values,

$P_{n\%}$. We found that our 125 mosaics all had similar $P_{n\%}$ values and so we opted to use the average across all mosaics, $\bar{P}_{n\%}$. We suggest that a feature, i , is significant (meaning its $\Delta I/F$ is outside the range of $\Delta I/F$ between neighboring pixels which come about via noise) if $\Delta I/F(i) > \bar{P}_{98\%}(\Delta I/F)$. A feature with $\Delta I/F(i) > \bar{P}_{85\%}(\Delta I/F)$ is considered to be a positive detection as well, but it is considered with scrutiny. We chose $\bar{P}_{85\%}$ and $\bar{P}_{98\%}$ as these percentiles represents a statistical significance similar to 1σ and 2σ respectively for normal and non-normal distributions. As can be seen in Figure 20, the differential spectra of the annuli is significant from the background up to the methane absorption channels between around $\sim 1.4 \mu m$. At these wavelengths Titan is essentially opaque, at ~ 100 km. At the next series of absorption channels between around $2.4 \mu m$, the differential brightness falls within $\bar{P}_{85\%}$, suggesting an upper limit of the minimum height of ~ 130 km. Regardless of how bright annuli are at other wavelengths, they all fail our criteria beyond $2.6 \mu m$. In images of the annulus at these wavelengths, it is very difficult to discern the annulus from the rest of the atmosphere. By $3.0 \mu m$ it becomes difficult to interpret the spectraltimetry. We suggest that this is not due to the annulus being below a certain opaque altitude, but rather because of the low SNR at these wavelengths due to lack of solar illumination and because the scattering intensity has diminished following Beer-Lambert's law. Titan's stratosphere is between ~ 50 km and ~ 300 km, while the main haze layer is between ~ 100 km and $\sim 400/500$ km [Hörst 2017]. Depending on the flyby, the differential spectrum of the NPA is identical to the EQA, and so we can conclude that it is at the same altitude for part of a Titan year. In *Section 4.2*, we will discuss the altitude implications of the change in differential spectra of the NPA.

2.4. Altitude from Triangulation

We triangulate the location of the north polar annulus by finding the intersection between multiple observations of the annulus at different times with similar illumination geometries. We

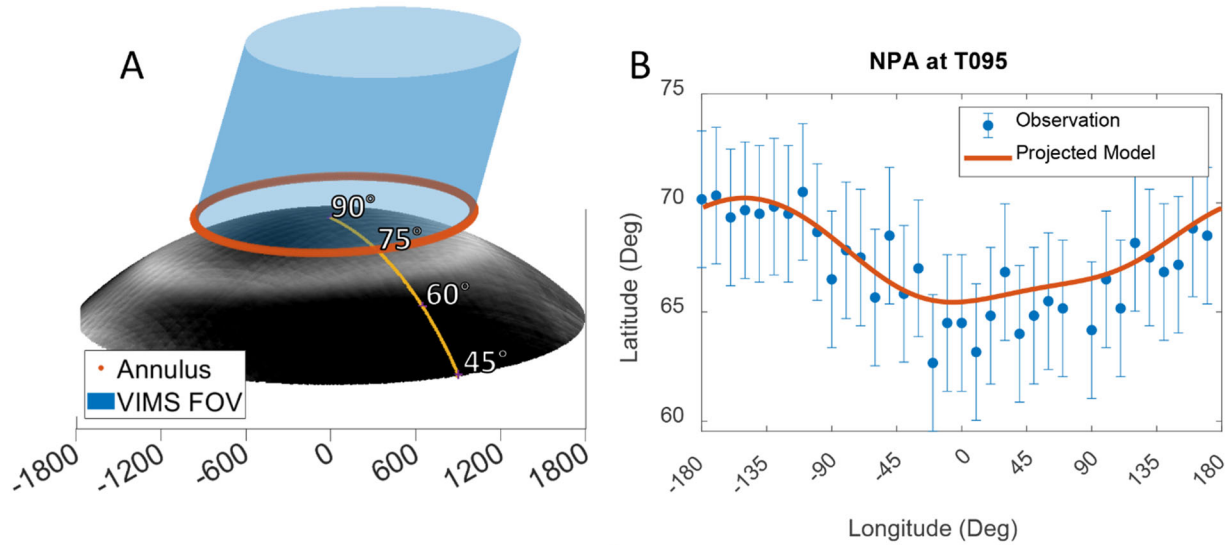


Figure 21: T095, 2013-10-14, $L_S = 49.7^\circ$ (Left, A), Our triangulated model of the north polar annulus (NPA; orange) and the contemporaneous VIMS observation (black and white) projected onto Titan as seen from the side. (Right, B) The projection of the modeled annulus onto Titan (orange) fitting our observation of the annulus (blue) in Lat-Lon space.

produced two models where the opposite hemisphere was illuminated between the two groups. The first used observations from flybys T092 to T096 ($L_S = 46.71^\circ$ to $L_S = 51.2^\circ$), and the second used observations from flybys T103 to T107 ($L_S = 58.37^\circ$ to $L_S = 62.79^\circ$). These produced modeled annuli which we refer to as Model A and Model B respectively.

The true/physical location of the annuli exists along a cone connecting the observations of the annuli with *Cassini* (Figure 21A). We used the location of the inflection points on the transects to define one point on a vector extending from the position of *Cassini* at the time of observations of the transect to and through the annulus. We interpolated between the inflection points using a sinusoidal fit. This produced a higher density vector field to find intersections between cones. The width of the deviation of the transects and the longitudinal bin width of the transects produce uncertainty in the location of the center of the annuli. To compensate for this, we performed a Monte Carlo simulation with 75 runs, where we randomly varied the location of our interpolated points by half of the average latitudinal width of all transect deviations (3 degrees), and by the longitudinal separation between interpolated points (2 degrees). In each run of the Monte Carlo

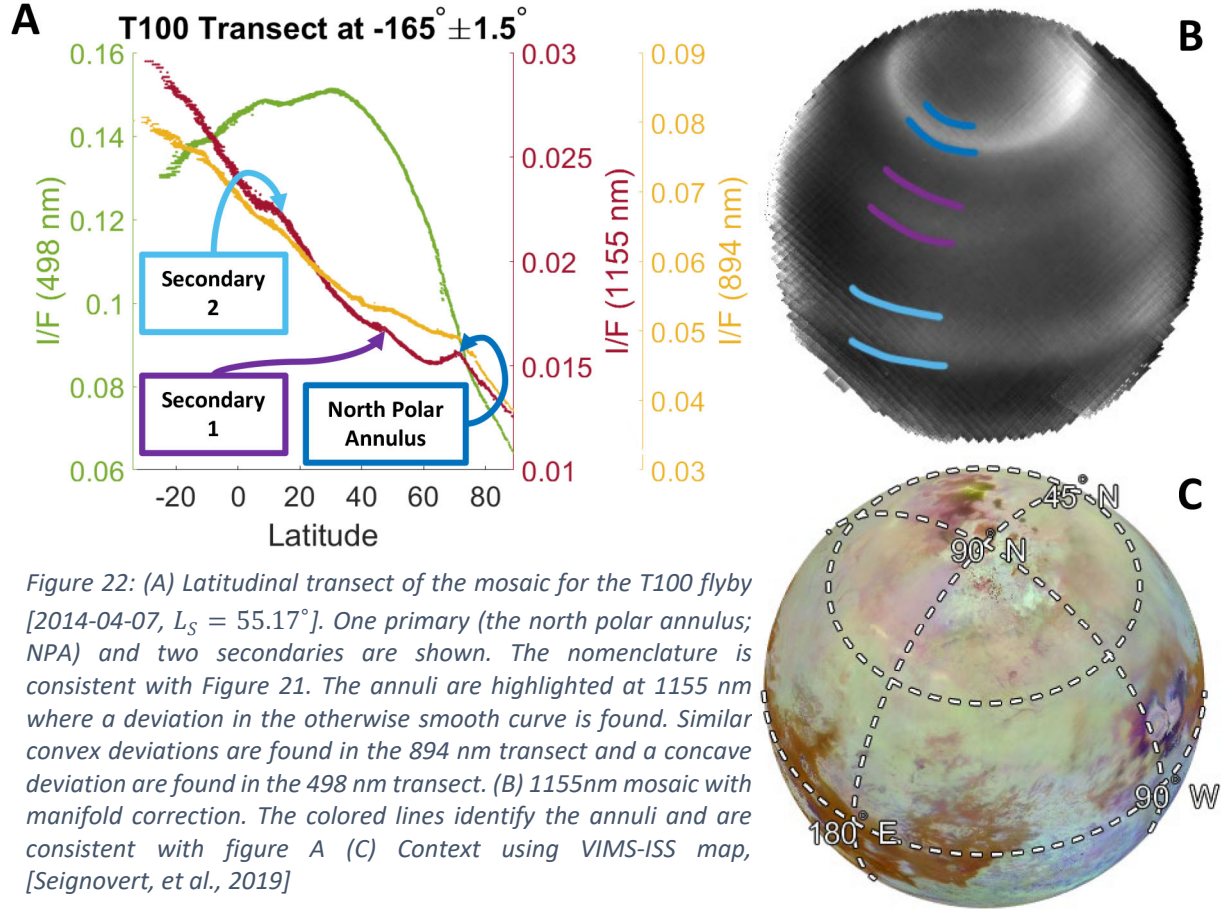


Figure 22: (A) Latitudinal transect of the mosaic for the T100 flyby [2014-04-07, $L_S = 55.17^\circ$]. One primary (the north polar annulus; NPA) and two secondaries are shown. The nomenclature is consistent with Figure 21. The annuli are highlighted at 1155 nm where a deviation in the otherwise smooth curve is found. Similar convex deviations are found in the 894 nm transect and a concave deviation are found in the 498 nm transect. (B) 1155nm mosaic with manifold correction. The colored lines identify the annuli and are consistent with figure A (C) Context using VIMS-ISS map, [Seignovert, et al., 2019]

simulation, we found the closest point between any and all two vectors from multiple flybys in a longitude bin of two degrees width.

For each flyby where we detected the NPA, we projected our modeled annuli onto Titan from the perspective of Cassini (Figure 21B). We then used the chi-square goodness of fit statistic to determine how well our model matched our observations. The chi-square goodness of fit statistic is given by

$$\chi^2 = \sum_{i=1}^N \frac{(\phi_i - F(\lambda_i))^2}{\sigma^2} \quad \text{Eq.21}$$

where ϕ is the latitude of the projected annuli, λ is longitude of the projected annuli, F is the function for the expected latitude, and σ^2 is the variance related to the measurement error for ϕ .

As we expected, we saw a lower goodness of fit to our observations the farther in time a flyby was

from either Model A's group (T092 to T096), or Model B's group (T103 to T107) suggesting that the annulus changes over time. We used a grid search, to investigate what changes were necessary in order to match the annulus we predicted with our observations. We varied several parameters including tilt and altitude, but most of these could be neglected. The two significant parameters we varied were the radius of the ellipse (preserving the eccentricity) from -250 km to +250 km; and the direction of the annulus's normal vector with respect to the subsolar longitude from -180° to +180°. Changing the radius of the annulus also changed the altitude.

3. Results & Seasonality

The annuli appear roughly sinusoidal in latitude-longitude space (Figure 21) and, similar to [Roman et al 2009](#), we use a sinusoidal fit to determine the tilt with respect to the rotation axis of Titan's solid body (θ_{NP}), the axial precession west of the subsolar longitude (ϕ_{Sol}), and the average latitude ($\bar{\lambda}$). The average values from our sinusoidal fits coefficients (with 95% confidence bounds) to the EQA over all our observations are, $\theta_{NP} = 2.78 \pm 1.63^\circ$; $\phi_{Sol} = 110.27 \pm 54^\circ$; $\bar{\lambda} = -3.13 \pm 2.09^\circ$. The average values for the sinusoidal fit coefficients of the NPA (with 95% confidence bounds) over all our observations are, $\theta = 2.05 \pm 1.27^\circ$; $\phi_{Sol} = 162.38 \pm 85.83^\circ$; $\bar{\lambda} = 66.39 \pm 2.01^\circ$. Our results for determining the altitude of the EQA and the NPA suggest that the annuli are at least 100km in altitude which puts our findings in line with [Lorenz et al. 2001c](#).

3.1. Secondary Annuli

We found 4 secondary annuli (Figure 22). We have grouped them together based on common latitude ranges (Figure 18). These features are nearly identical to the primary annuli spectrally and morphologically, the difference being that they are less intense and distinct. Secondary Annuli 2 and 3 (using the nomenclature from Figure 18) occur within 30 degrees of the equator and sometimes both secondary annuli and the equatorial annuli can be seen together. Secondary Annuli 1

and 4 occur at roughly 55°N and 55°S. It is interesting that we see the southern secondary annuli so low in latitude, while not observing the SPA. It is possible that the secondary annuli have less of a seasonal dependence in a similar way to the EQA while the SPA and the NPA are seasonal features. The secondary annuli are more sporadic than the primary annuli. This could be due to a more sensitive viewing geometry requirement. Alternatively, it may indicate that the increase in haze is especially low and that the variation in abundance can vary enough to make the secondary annuli detectable or not between observations.

3.2. When do we see the annuli?

In Figure 18, we plot the location of the mean latitude against the time of the observation in units of degrees of planetocentric longitude of the sun relative to vernal equinox, L_S . The observations of the annuli are grouped largely by their mean latitude and perception of repeat observations. We found that the presence of the annuli is not correlated with the presence of tropospheric clouds, as can be seen in Figure 16C.

The annuli are seen over a wide range of viewing geometries. But a closer inspection of each observation reveals the vast majority (95%) occur at incidence angles, i , between 9° and 91°, and at emission angles, e , between ~4° and ~57°. We mapped where VIMS observed Titan within these ranges, suggesting that if an annulus was in the area when these observations were taken, there would be a higher probability of detection. In Figure 18 gaps in the detection of the annuli, in particular the EQA starting at $L_S = 45.21^\circ$ and the NPA starting at $L_S = 63.77^\circ$, correlate well to the areas we suggest would not show an annulus, whether it is present or not.

We see the EQA during the entirety of the *Cassini* mission, and secondary annuli for essentially the same length of time. Our earliest observation of the NPA comes from flyby T085 [2012-07-24, $L_S = 35.61^\circ$] where the annulus can be seen as solitary arc extending off the disk of

Titan (Figure 18 red dot), and we first see the NPA as the band on the disk of Titan in flyby T087, [2012-11-13, $L_S = 39.16^\circ$]. This is the same time that *Cassini* begins its inclined series of orbits to focus on Titan's north polar region. It is therefore difficult to determine whether the NPA is a seasonal feature brought about by the increase in insolation or if the NPA is always present and we simply lacked the ability to observe it. The absence of the SPA gives us a clue in breaking the degeneracy, leading to our preferred hypothesis that the NPA is a seasonal feature.

We know that the SPA was observed prior to *Cassini's* arrival. Yet despite the existence of south polar observations with good resolution and good viewing geometry (e.g. -32.1° to $0^\circ L_S$ relative to vernal equinox), we did not observe the SPA. From this we conclude that the SPA is absent due to the changes in season. It was predicted by [Roe et al. 2002](#) that the SPA would vanish as summer moved towards autumn in the southern hemisphere. Titan's stratosphere has already been shown to be periodic as the north-south asymmetry switches between either hemisphere being bright or dark. We propose that the NPA is similarly periodically symmetric to the SPA. Since the SPA is seasonal, and we also see the NPA change with the seasons as discussed below, we propose that the NPA appears according to the season. We suggest that if the NPA was present before our earliest detections, it was not significantly earlier on a seasonal timescale.

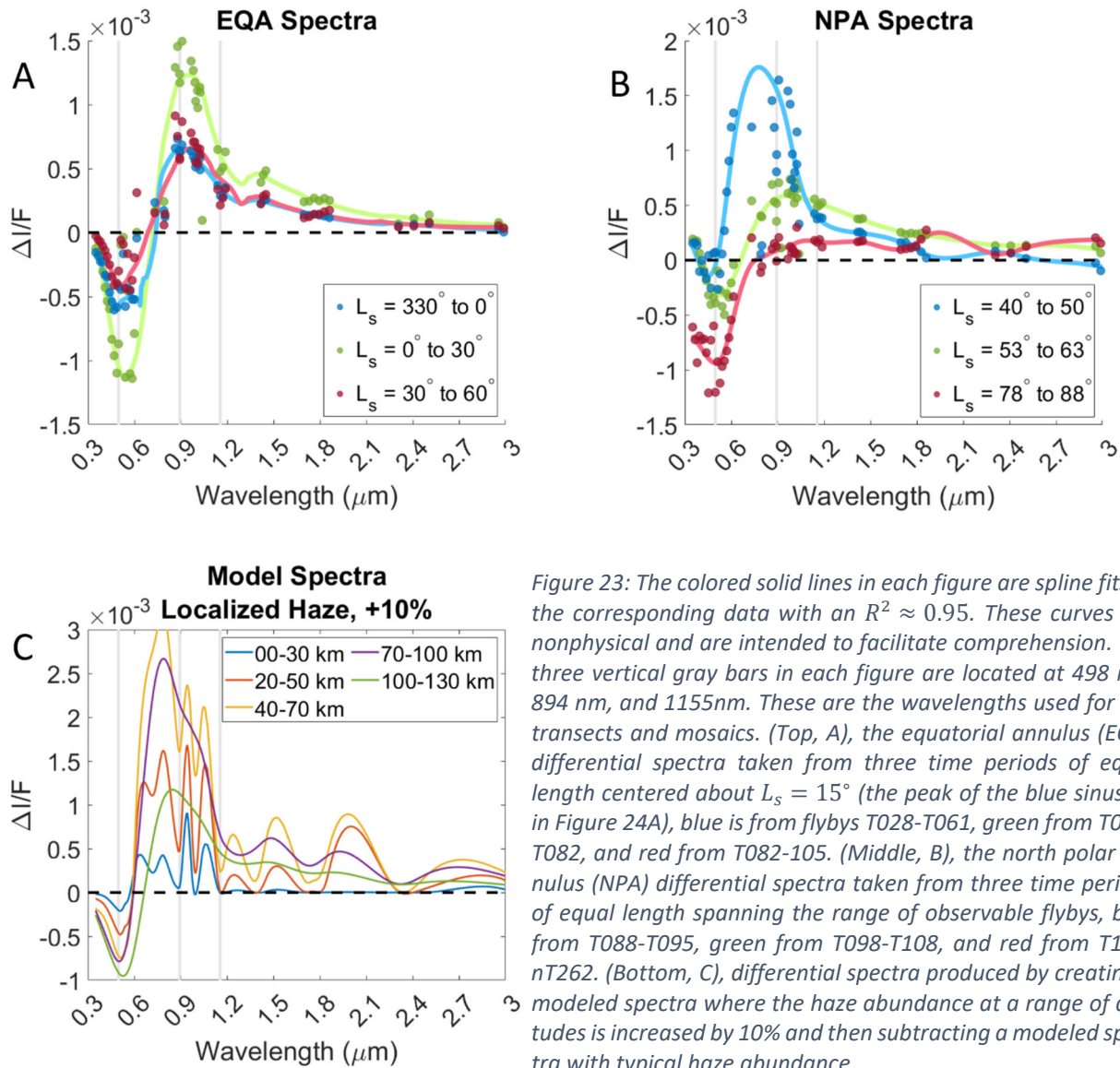


Figure 23: The colored solid lines in each figure are spline fits to the corresponding data with an $R^2 \approx 0.95$. These curves are nonphysical and are intended to facilitate comprehension. The three vertical gray bars in each figure are located at 498 nm, 894 nm, and 1155 nm. These are the wavelengths used for our transects and mosaics. (Top, A), the equatorial annulus (EQA) differential spectra taken from three time periods of equal length centered about $L_s = 15^\circ$ (the peak of the blue sinusoid in Figure 24A), blue is from flybys T028-T061, green from T061-T082, and red from T082-105. (Middle, B), the north polar annulus (NPA) differential spectra taken from three time periods of equal length spanning the range of observable flybys, blue from T088-T095, green from T098-T108, and red from T119-T262. (Bottom, C), differential spectra produced by creating a modeled spectra where the haze abundance at a range of altitudes is increased by 10% and then subtracting a modeled spectra with typical haze abundance.

If we assume that the SPA has a similar seasonal timescale to the NPA, and given our detection of the NPA range from 2012-07-24 to 2017-09-11 ($L_s = 39.17^\circ$ to 93.3°), then we could expect the SPA to be present as early as January 1998 and as late as March 2003 ($L_s \approx 220^\circ$ to 280°). If we continue to extrapolate we should expect to see the SPA again starting around February 2027. If, however, Earth-based observations of Titan are taken before 2027 and the SPA is observed, this would imply that the NPA should have been visible as early as December 2006 ($L_s = 315.29^\circ$), or *Cassini* flyby T021. As this is not the case, an observation of the SPA before

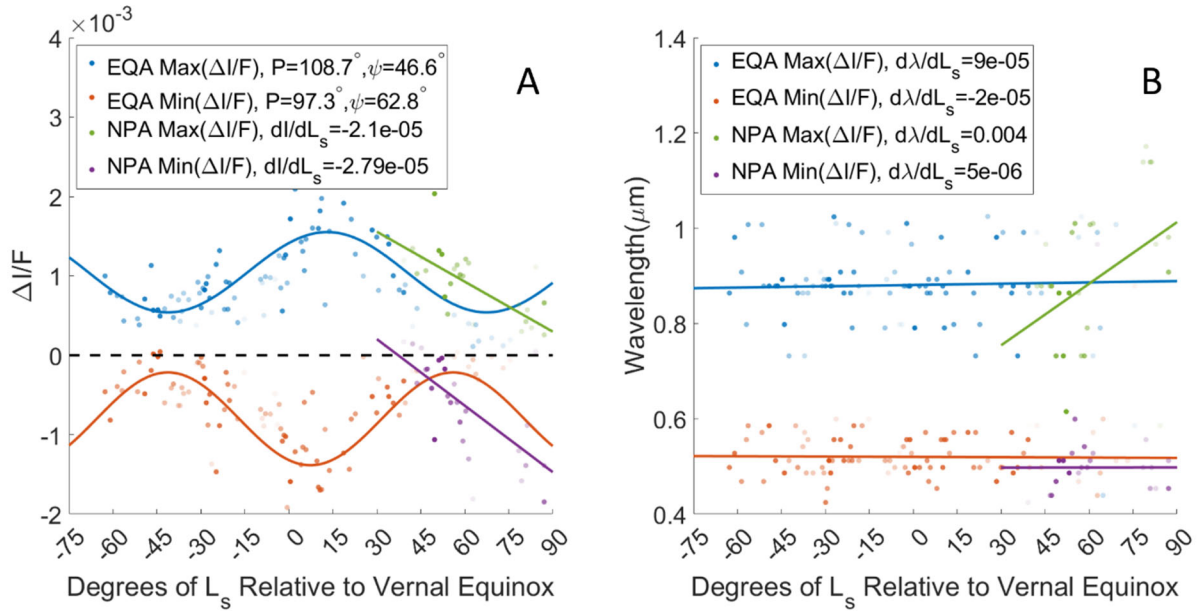


Figure 24: (Left, A) Blue, maximum value of $\Delta I/F$ of the equatorial annulus (EQA) differential spectrum. Orange, minimum value of $\Delta I/F$ of the EQA differential spectrum. Green, maximum value of $\Delta I/F$ of the north polar annulus (NPA) differential spectrum. Purple, minimum value of $\Delta I/F$ of the NPA differential spectrum. (Right, B) Blue, the wavelength of the maximum $\Delta I/F$ of the EQA differential spectrum. Orange, the wavelength of the minimum $\Delta I/F$ of the EQA differential spectrum. Green, the wavelength of the maximum $\Delta I/F$ of the NPA differential spectrum. Purple, the wavelength of the minimum $\Delta I/F$ of the NPA differential spectrum. The opacity of the data points correlates to the relative weight of the data. Data is weighted according to the number of transect detections. For details on the curves, see Appx Table 6.

2027 would imply that the southern stratosphere does not mirror the northern stratosphere. This might be unsurprising as asymmetries are already observed between the atmosphere of the north/south hemispheres, such as the lag in the expected onset of methane clouds in the north following equinox [Rodriguez et al. 2009; Rodriguez et al. 2011; Turtle et al. 2018].

3.3. Changes during Cassini

The differential spectra of the EQA and NPA change as the season progresses (Figure 23 & 10). The shape of the differential spectrum of the EQA remains the same as evidenced by the positions of the peak brightness and darkness in Figure 23a. The amplitude however changes a great deal and has a very symmetric pattern, with the peak amplitude centered about ten degrees after the vernal equinox (Figure 24a). The nature of the spectral changes for the NPA is different from that of the EQA. The entire spectrum of the NPA becomes darker as we approach summer

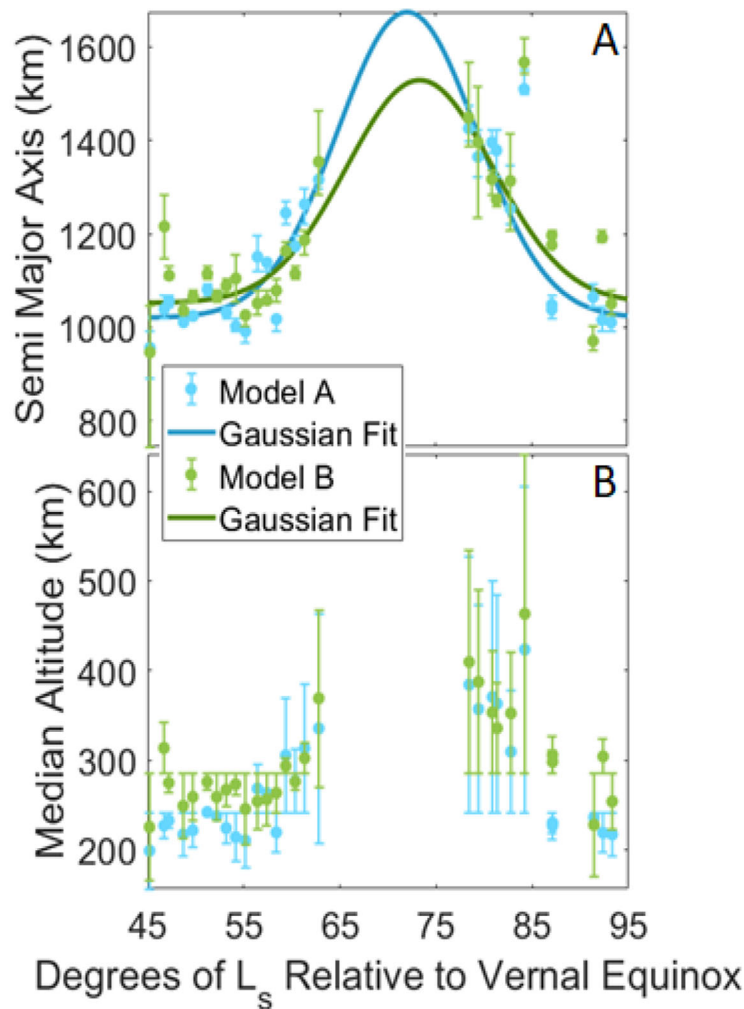


Figure 25: Both figures show the results of the chi-square minimization routine to determine the change in parameters of the north polar annulus (NPA). Model A was constructed using flybys T094 to T098 and Model B was constructed with flybys T101 to T105. (Top, A) Semi-major axis of the NPA as a function of L_s . The curves are Gaussian fits, with (Bottom, B) Median altitude of the NPA vs L_s . The change in altitude is a product of the change in semi major axis.

solstice. The bright part of the spectrum moves red-wards while the dark component shows a small shift to bluer wavelengths (Figure 23b & 24b).

Our triangulated models indicate that the semi-major axis of the NPA increases as Titan approaches northern summer potentially reaching a maximum size of about 1500 km around $L_s = 72^\circ$ (Figure 25a). This may be due to the meridional circulation transporting the haze which had been lofted by the onset of the pole-to-pole circulation cell, towards the south pole. As the annulus increases in radius it also increases in altitude, assuming a constant tilt (Figure 25b). This may imply that the change in altitude we suggest based on the changing spectra of the NPA, is caused

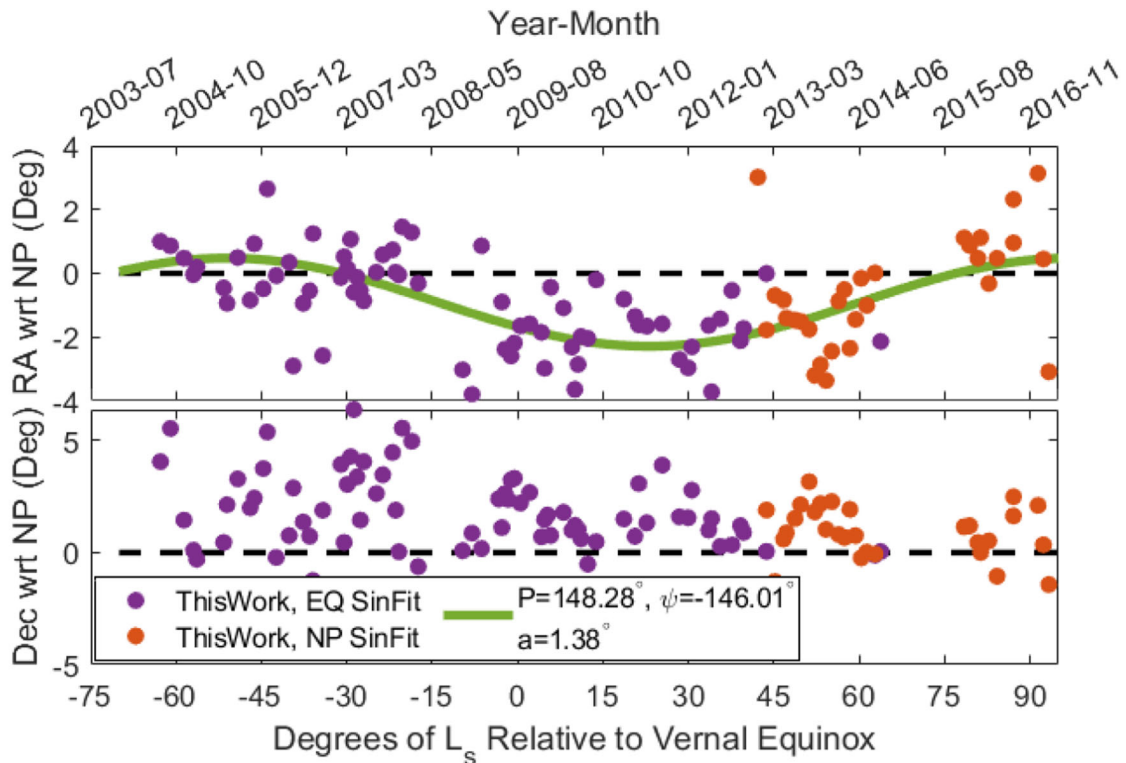


Figure 26: (Top) The right ascension offset of the normal vector of the annuli from the solid body rotation axis in an inertial reference frame (ICRF). The right ascension of Titan’s solid body rotation axis is $RA = 39.48^\circ$ [Stiles et al., 2008]. The green sinusoid through the flyby has a goodness of fit metric of $R^2 = 0.411$. (Bottom) The declination offset of the normal vector of the annuli from the solid body rotation axis in an inertial reference frame (ICRF). The declination of Titan’s solid body rotation axis is $RA = 83.43^\circ$ [Stiles et al., 2008].

by the NPA increasing in size, rather than the NPA being lofted higher itself. After $L_s = 72^\circ$, the size of the annulus seems to decrease, returning to its original size just before summer solstice.

3.4. The tilted pole

In a review of open questions at Titan following *Cassini*, Nixon et al 2018 asks: “*Is the [azimuthal and tilt offset of the stratosphere] fixed in magnitude and direction, or does it wander on seasonal or longer time scales?*” In Figures 26, 27, & 28 we show the change in the tilt and the offset as a function of time in solar and inertial reference frames. We note that the data for the EQA and NPA are contiguous but not continuous; however, where appropriate we analyzed and interpreted the data as if it was one continuous set.

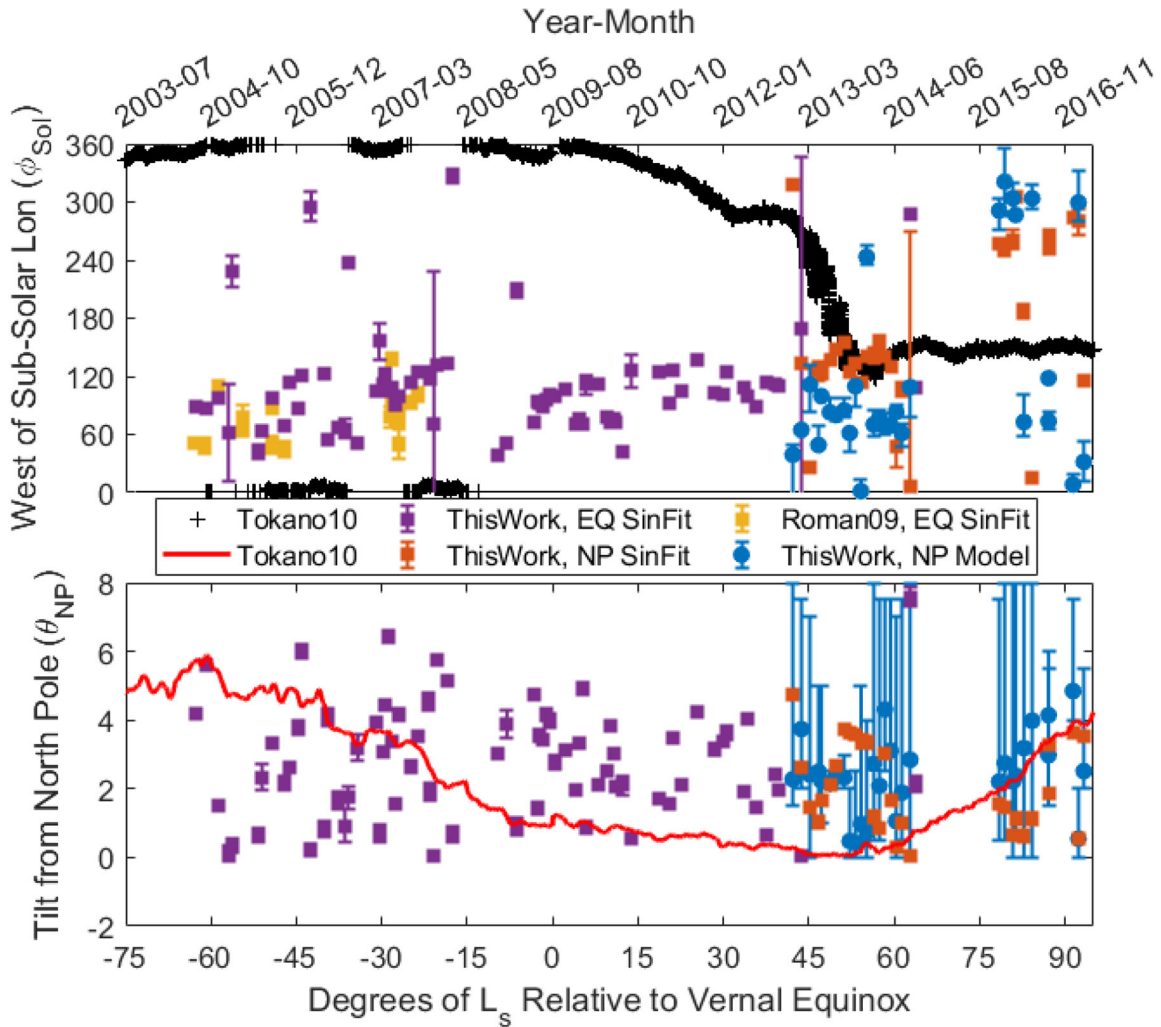


Figure 27: (Top) Western azimuthal offset of the normal vector of the annulus from the subsolar vector. The yellow squares are taken from Roman 2009 Table 2 Column 6. The black crosses are taken from Tokano 2010 Figure 20B. (Bottom) Magnitude of the polar offset of the normal vector of the annulus from the solid body rotation axis (North Pole). The red Line is taken from Tokano 2010 Figure 19A.

Achterberg et al. 2011 suggested a longer time base of stratospheric tilt offset may reveal the offset to be fixed in an inertial (star-fixed) reference frame. We determined the right ascension and declination difference between the normal vector of the annulus and the Titan solid body rotation axis [Stiles et al. 2008] aligned to the X-axis of the International Celestial Reference Frame (ICRF) [Charlot et al. 2020]. In Figure 26, we see that instead of being fixed, it appears that the stratospheric tilt offset in an inertial frame is a function of the Titan season. We modeled the oscillation of the right ascension of the stratosphere about the north pole ϕ_{NPRA} , as a function of L_s

$$\phi_{NPRA}(L_s) = \phi + M \sin\left(\left(360 \frac{L_s}{P} + \psi\right) \frac{2\pi}{360}\right) \quad \text{Eq. 22}$$

where ϕ is an offset in right ascension of the north pole of Titan, M is the amplitude, P is the period, and ψ is the phase shift. We used the bisquare weights method to minimize the influence of outliers. We found that the coefficients (with 95th percentile bounds) for the EQA and NPA combined are $\phi = -0.9071^\circ \pm 0.38^\circ$, $M = 1.38^\circ \pm 0.35^\circ$, $P = 148.3^\circ \pm 36.3^\circ$, and $\psi = -146^\circ \pm 18.5^\circ$. The curve in Figure 26 fits our data with an $R^2 = 0.411$.

Additionally, we find that the tilt offset in a solar reference frame (i.e. the subsolar longitude) is also a function of the season (Figure 27). We assume that the stratosphere is a triaxial ellipsoid, although hemispheric asymmetries of the atmospheric angular momentum (AAM) are possible and perhaps necessary to explain our observations [Tokano 2010a]. Since each group can be characterized by a first-degree polynomial and considering both would require a more complicated model, for now we will describe their progression separately. We find that the EQA rotation axis precesses westward at a rate $d\phi_{sol}/dt = 0.21 \pm .23(+W^\circ/L_s)$, with a starting point at vernal equinox $\phi_{sol}(0) = 99.22 \pm 7.51^\circ$. We find that the NPA rotation axis precesses westward at a rate $d\phi_{sol}/dt = 3.85 \pm .99(+W^\circ/L_s)$, with a starting point at vernal equinox $\phi_{sol}(0) = -71.3 \pm 66.41$. This contradicts the prediction from Tokano 2010 showing a time series of the angular distance from the subsolar longitude which moves eastward as the season progresses (Figure 27).

Tokano 2010a explains the movement of the equatorial AAM as a result of the seasonal reversal of the meridional circulation. The reversal of the meridional circulation cell causes a simultaneous change in the components AAM_x and AAM_y, which manifests itself as a 180° shift of the tilt. Tokano 2010a did not emphasize that AAM_x and AAM_y also depend on the zonal wind u . If u is very large (as is the case in Titan's stratosphere), a sign change of v may have little

influence on AAM_x and AAM_y according to Eq. 1 and 2 of Tokano 2010. From a comparison with [Achterberg et al. 2008](#), the zonal wind in the stratosphere produced by Tokano's GCM is too weak and this could bias the seasonal variation in the AAM tilt angle. It is probable that the weight of v of the equatorial AAM is too large relative to that of u . An additional reason may be an underestimation of the axial component of AAM, AAM_z, in the calculation of the tilt angle by [Tokano 2010a](#). According to [Tokano and Neubauer 2005](#) AAM_z strongly varies with season due to seasonal reversal of the zonal wind direction in the lower troposphere. However, since the stratospheric super-rotation in their GCM is greatly underestimated, it is likely that the seasonal variation in AAM_z relative to the annual-mean AAM_z is too large. In reality, the mean AAM_z may be much larger while its seasonal variation due to tropospheric winds remains unchanged. This implies that the lack of a systematic seasonal tilt angle of the stratosphere in the observational data is evidence of the relative seasonal invariance of the axial AAM due to perennial stratospheric super-rotation. Our results however, do seem to match [Tokano 2010a](#)'s predictions for the NPA between 40 and 60 degrees past the vernal equinox. This might indicate that the GCM from [Tokano 2010a](#) could predict the rotation of the stratosphere by using observations such as those presented in this work to further constrain the model.

[Tokano 2010a](#) shows in his Figure 18 that the tilt of the stratosphere with respect to the North Pole should vary from 0 to 8 degrees biannually with the maximum tilt peaking around 30 degrees of planetocentric longitude of the Sun after summer and winter solstice. We find that the tilt of the EPA and NPA stay within the bounds predicted by [Tokano 2010a](#), but with much greater variability (Figure 27). We found a weak correlation between the variability and differences in the longitudinal extent of some of our observations, which may indicate inaccuracies in our tilt estimations. The upper limit of our tilt measurements follows the same path predicted by [Tokano](#)

2010a, decreasing at the same rate between -60 and 65 degrees relative to the vernal equinox. That the rate of change predicted by Tokano 2010a is consistent with what was observed over the *Cassini* mission indicates that the forces which change the tilt were accurately modeled.

4. **Discussion**

We propose that the annuli are features of enhanced aerosols that are corralled/confined by gradients in the winds, or at least mark locations where aerosols are in a stable quasi-equilibrium for an extended time period. Given their location, circumglobal nature, and seasonal behavior, we suggest that the annuli are caused by the meridional cell circulations, with different mechanisms for the NPA and EQA, respectively.

4.1. **Detailed Explanation of the Spectra**

4.1.1. *300-500nm*

The difference spectrum is negative for wavelengths shorter than ~ 700 nm, indicating that the annuli are darker than the surrounding atmosphere (Figure 19). The local darkening could be produced by multiple scattering in a higher optical depth environment removing net-outbound photons, or by absorption of inbound photons which never get a chance to scatter from the low altitude gasses. Rayleigh scattering is the dominant mechanism of scattering by particles much smaller than the wavelength of light ($x = 2\pi r/\lambda \ll 1$, for particles of radius r and wavelength λ) and has an intensity dependence of $I \propto 1/\lambda^4$. In the lower atmosphere scattering by gaseous nitrogen and methane dominate; since both have a kinetic radius of $r \approx 0.2nm$, the lower atmosphere is highly backscattering. The annuli however, if predominantly made of haze particles, will have effective radii around 1.0 to 2.0 μm [Lavvas et al 2010], which leads to aerosol/particle scattering at these wavelengths with only a small backscatter component (in the limit of spherical particles this is Mie scattering). Outbound photons scattered by the gasses which interact with the

annuli must contend with a higher optical depth, which is not encountered outside the annuli. Alternatively, the haze or a companion species may have absorption features around 500 nm. In this scenario photons are absorbed more effectively in the higher optical depth environment of the annuli, producing the contrast we observe.

To test this hypothesis, we use a model that predicts the photometry in UV and visible (e.g., [Rannou et al. 2016]). This model is tuned to fit Titan's spectra near the equator, as observed in a near nadir viewing (e.g. spectra from VIMS observation CM_1477457253_1 in flyby TA). We then successively increase by 10% the haze opacity in different layers in order to assess the effect of this change on the outgoing intensity relative to the reference model, producing a modeled differential spectrum. As can be seen in Figure 19, an increase of 10% haze opacity at 100-130 km produces a differential spectra nearly identical to the averaged differential spectra of the EQA from 345°-15° Ls. A more complete radiative transfer model is needed to determine if the mechanism of obscuration only arises from an increase in haze opacity at a specific altitude or if changes in scattering and absorption properties are also needed to explain the data in fine detail.

4.1.2. 500-700nm

Beginning with 500 nm and progressing red-wards, the brightness of the annulus starts to increase (Figure 19). Nitrogen and methane move further into the Rayleigh scattering regime but the intensity from the lower atmosphere, optically thick because of these gases, decreases as $I \propto 1/\lambda^4$. Meanwhile the haze moves towards Rayleigh scattering, which leads to an increase in its backscatter component. Together, this means that the brightness from the lower atmosphere decreases while the brightness at the top of the annulus increases. The increased optical depth of the annuli produces more backscattering than the rest of haze throughout the atmosphere. The higher altitude also presents a shorter two-way path through the atmosphere, reducing multiple scattering

events which could remove the photons from the beam of VIMS. The increase in localized backscatter and the reduction of multiple scattering leads to the annuli being brighter than the surrounding atmosphere.

4.1.3. 700-2000nm

The backscatter component of weak-particle/aerosol scattering is not particularly intense owing to the lower extinction efficiency of the relatively small scatterers. The extra brightness produced by the annuli is therefore lost in the brightness produced by the highly reflective surface. Not only is the surface brightness ($I/F \approx 10^{-1}$) two to three orders of magnitude greater than the $\Delta I/F$ for the annuli ($\sim 10^{-3}$), but the surface is much more variegated than the atmosphere making the detection of the small difference between the annuli and the rest of Titan very difficult. Instead we utilize the methane absorption channels, including ~ 900 nm and ~ 1150 nm used for our detections. The majority of photons are absorbed at these wavelengths. Those that are not absorbed are scattered by the haze. As before, the increased optical depth at a higher altitude increases backscatter and reduces multiple scattering, producing a localized bright feature.

At longer wavelengths, several complementary effects produce a slow drop off in differential brightness. Primarily, the intensity of the scattered light drops off as $1 - e^{-\lambda}$ following Beer-Lambert's Law. Additionally, the longer wavelength methane absorption channels are more effective, requiring a lower density of methane to achieve opaqueness. This means that the atmosphere becomes opaque at higher altitudes as wavelength increases. At ~ 2.4 μm the annulus becomes indiscernible from the rest of the atmosphere. The atmosphere becomes essentially opaque at ~ 100 km at 1.2 μm and at ~ 130 km for ~ 2.4 μm , suggesting that the annulus has a minimum altitude of 100-130 km. Altitude constraints for the NPA and EQA are discussed further in the next section.

Finally, solar intensity drops off at longer wavelengths, leading to a signal-to-noise ratio so low that it is not possible to discern the annulus in the images or the deviation in the transects.

4.2. Origin and Evolution of the Annuli

4.2.1. Formation of the North Polar Annulus

The NPA occurs at the boundary where the north polar hood was seen until it dissipated during Titan's spring [[Le Mouélic et al 2012a](#)]. At that time, a bright ring of haze and mist whose opacity smoothly rises from about 51° to 68°N was seen by VIMS bordering the north polar hood [[Griffith et al. 2008](#)]. While this band is not spectrally or morphologically consistent with our observation of the NPA, it is circumglobal at certain wavelengths and was estimated to be at about 40 km of altitude according to radiative transfer modeling. This band is evidence of the potential for haze to build up at the border of the north polar hood. When the north polar hood began to break up, this band did not immediately dissipate, leaving behind a zone clear of haze and clouds near the pole [[Le Mouélic et al 2012a](#); [Rannou et al. 2012](#)]

We propose that the NPA is another manifestation of haze collecting at the mixing boundary encircling the north polar hood. In this scenario, haze is produced in the summer hemisphere and transported to the winter hemisphere. This process forms a polar hood [[Rannou et al. 2004](#); [Larson et al. 2015](#)] and gradually builds up an annulus at the boundary of a polar jet or a sharp change in the polar vertical velocities. Titan's polar hoods contain high concentrations of ethane which is consistent with their location above the arctic circle [[Mayo & Samuelson 2005](#)]. The polar annuli, however, exist equatorward of the arctic circle and may not be able to maintain condensed ethane aerosols. As spring comes to the north, the ethane begins to deplete from the polar hoods, entraining accumulated haze with it. Because the polar annuli lack ethane, they persist longer, until they are eventually transported away by the summer meridional circulation.

We also investigated whether the NPA (and the other annuli) could be explained by methane clouds, as nearly global arcs of cloud have been observed with ISS and VIMS [Turtle et al 2018]. We find that there is no obvious correlation between the presence of clouds and the presence of the annuli. In Figure 16C, we see that the annuli are present while no clouds are visible. We have also seen that the presence, location, and morphology of clouds when seen by VIMS or ISS does not correlate with the presence, location, or morphology of the annuli. We suggest that the annuli and clouds seen in Turtle et al 2018 may be related by the same (or a similar) mechanism which acts to corral them into global circular features.

4.2.2. Evolution of the North Polar Annulus

The differential spectrum of the NPA changes as Titan moves further towards northern summer. We see that the entire spectrum gets darker and the bright component shifts redwards (Figure 23B and 24). We note the similarities between the differential spectra of the NPA over time (Figure 23B), and the modeled differential spectra where the haze abundance is increased at several altitudes (Figure 23C). As the altitude of the modeled differential spectra increases, the dark component short of 700 nm decreases while shifting spectrally very little. We see the same behavior in the NPA differential spectrum over time. The dark components of the differential spectra of the NPA at $L_S = 40^\circ - 50^\circ$, $L_S = 53^\circ - 63^\circ$, and $L_S = 78^\circ - 88^\circ$ most closely resemble the dark components of the modeled differential spectra at 0 - 30 km, 20 - 50 km, and 100 - 130 km, respectively. We propose that these similarities are indicative of the NPA increasing in altitude as the season progresses. The bright component of the modeled differential spectra also shows some similarities to the observed spectra, but not as much as the dark component. A more complete radiative transfer model is needed to fully quantify how the spectra of the NPA changes in the way that it does.

This scenario is consistent with the expected change in the meridional circulation [Battalio et al. 2021]. As spring turns to summer, the two meridional circulation cells which converge in an upwelling event at the equator transition to a single cell, which rises in the north and subsides in the south [Tokano 2011]. We propose that haze originally transported to the north polar hood during the winter and spring months is lofted higher by the summer upwelling at the north. It is possible that the band observed at the boundary of the north polar hood did not simply dissipate, but rather moves to higher altitudes while also changing in abundance, size, fractal dimension, and/or single scattering albedo.

The increase in the semi-major axis of the NPA in Figure 25 may be related to variations in the polar temperature. As the temperature gradient decreases during summer, the weakening strength of the jet and polar vortex could result in larger amplitude waves dipping further south [Newman et al. 2011; Lora et al. 2015; Lora et al. 2019] This could also lead to an increase in the ellipticity of the annuli. Determining the ellipticity of the annuli requires additional terms in the sinusoidal function, which must await constraint by higher resolution observations than are currently available. Alternatively, as upwelling at the north pole peaks at summer solstice, the increase in velocity may act to move the bounds of NPA farther south. It could also be indicative of the upwelling moving to lower latitudes. This could be a sign of how Titan moves from pole-to-pole circulation at solstice to equator-to-pole circulation at the equinoxes.

4.2.3. Evolution of the Equatorial Annulus

We proposed in *Section 4.1*, that the dark component of the annuli's differential spectra (shorter than 600 nm) is produced by the haze in the annulus obscuring the bright Rayleigh scattering from the lower atmosphere. If the haze in the annulus is more abundant, it will have a higher

optical depth, which will make it more efficient at blocking the illumination from below. Meanwhile, the bright component of the differential spectra (near IR) of the annuli is produced by the scattering from the top of the annuli. Once again more haze in the annuli leads to a higher optical depth, which facilitates more back scattering.

We propose that the dark and bright components of the EQA spectra in Figures 23A and 24 change intensity in unison from a change of optical depth. The change in optical depth is due to changing haze abundances as a function of season. The EQA is at its brightest and darkest around the vernal equinox. From this we infer that the haze at the equator increases until it reaches a maximum abundance in the annuli around the vernal equinox, and then begins to decrease. It appears that the EQA becomes least distinguishable from the rest of the atmosphere around the summer and winter solstices. This suggests that the haze abundance in the EQA is similar to the rest of the stratosphere.

4.2.4. Formation of the Equatorial Annulus

If the haze abundance is responsible for the change in intensity of the EQA, then the haze reaches its maximum abundance at the vernal equinox, which coincides with the circulation pattern of upwelling at the equator from the equator-to-pole meridional circulation cell circulation. We suggest that the haze becomes suspended at the convergence of the north and south cells. As the circulation transitions from equator-to-pole to pole-to-pole, the haze which had been accumulating and suspended begins to disperse. What is curious, however, is that we do not see the equatorial annulus go away; rather it persists all the way up to and including at summer solstice. This might suggest that some part of the haze which had been built up during fall remained at the equator. Perhaps this is because of some area of quiescence brought about by gravity or pressure waves, or

maybe the circulation in the middle stratosphere is just not effective. In this case horizontal circulation may happen in the troposphere and near the stratopause, flowing in opposite directions, while the center of the stratosphere remains unmixed and undisturbed.

4.3. Using the Annuli to Track the Stratosphere

Given their altitude ($> \sim 130$ km), the annuli are tracers of Titan's zonal stratospheric super-rotation and seasonal meridional circulations, as well as the orientation of the stratosphere with respect to the solid body. The annuli can be observed from Earth-based observatories, allowing us to extend the understanding of the stratosphere and meridional circulation a full Titan year. The distribution of secondary annuli bears a resemblance to zonal wind patterns produced by barotropic waves in Titan's stratosphere based on shallow water modeling [Luz & Hourdin 2003]. The secondary annuli may offer accessible observables of Titan's barotropic waves.

4.3.1. The Tilt of Titan's Stratosphere

The tilt of Titan's atmosphere, relative to the tilt of the solid surface, is one of the remaining questions left open after the end of the *Cassini* mission [Nixon et al. 2018]. The mechanism of the tilt and super-rotation of Titan's stratosphere are not well understood. Tokano 2010a proposes that the tilt is the result of thermal tides and is only possible if atmospheric waves perturb the circulation. From Figure 27 we see that the observed temporal variation in the azimuthal offset of the normal vector of the annulus from the subsolar vector does not follow the path predicted by Tokano 2010a. The most likely explanation is that the weak zonal wind in his GCM affects all three components of AAM in such a way that the azimuth of the tilt turns out to be wrong most of the time. Another possible explanation is that the tilt is not directly responding to thermal tides unlike the assertion by Tokano 2010a. Tokano 2010a discarded the possibility of mixed Rossby-gravity waves as a cause of westward migration of the tilt because the super-rotating winds in the upper

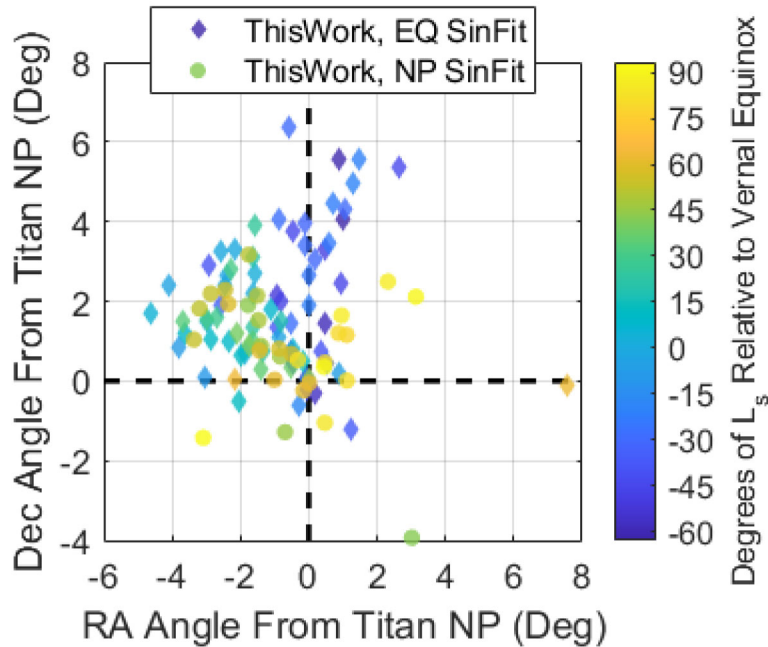


Figure 28: The right ascension and the declination offset of the normal vector of the annuli from the solid body rotation axis. Diamonds are data from the equatorial annulus (EQA) and circles are data from the north polar annulus (NPA). The colors correspond to the time of observation.

stratosphere should turn the phase speed of such waves relative to the surface to eastward. However, it is worth mentioning that [Battalio and Lora 2021b](#) predicted the presence of mixed Rossby-gravity waves and equatorial Rossby waves in their GCM. Therefore, the likelihood that Rossby waves affect the precession of the tilt of the annuli cannot be fully dismissed. [Achterberg et al 2008](#) proposes that the tilt facilitates the vertical transport of angular momentum to balance the heat flow and insolation at low latitudes by feedback between the circulation and the heating. Our results

The azimuthal position of the stratosphere shows some correlation with the subsolar longitude. We suggest that the orientation and position of the stratosphere are strongly correlated with the seasons when examined in an inertial reference frame (Figures 26 & 28). There is some indication that the stratosphere reorientates itself throughout the year around a centroid offset by a few degrees from the north polar axis. Assuming this is correct, we suggest that the centroid about

which the stratosphere reorientates itself, is itself rotating around the north polar axis. In this scenario the centroid is a seasonal feature (Figure 26 Top), while the stratosphere around the centroid may be an orbital or diurnal feature with a much shorter period (Figure 26 Bottom). We suggest that our dataset supports the proposed mechanism for the tilt suggested in [Achterberg et al. 2008](#).

In Figure 26 we see how the azimuthal position of the stratospheric tilt (the angle in the XY plane) is oriented with respect to the north polar axis in an inertial (star-fixed) reference frame. The tilt follows a sinusoid, with a maximum deflection of about 2° degrees clockwise at $L_s \approx 25^\circ$. We propose that this sinusoid indicates that the orientation of the stratosphere is dependent on the season rather than on the solar position. We propose that the stratosphere rotates around the north polar axis in response to the subsolar latitude and true anomaly. These results support and expand on the interpretation of [Achterberg et al. 2011](#), which suggested that the stratosphere is fixed in an inertial reference frame. These results imply that the mechanism for the tilt proposed in [Achterberg et al. 2008](#) are seasonally dependent and reorientation at different azimuthal angles facilitates this process or is a product of the process. Additionally in Figure 28, the points seem to cluster around the $RA = -2^\circ$ and $Dec = 2^\circ$ suggesting that the stratosphere rotates around an axis offset from the north polar axis. The three peaks in Figure 26 Bottom between -15 and 60 degrees relative to the vernal equinox might indicate that this axis is orbiting around the north polar axis and is presenting itself in our data as a second order waveform.

4.3.2. Testing Rotation Rates

The large difference in the rotation rate of the EQA and the NPA ($0.14 \pm .4$ vs $3.35 \pm .54$) would suggest that the equatorial and polar stratosphere rotate independently of one another. GCMs show that the different latitudes experience different zonal wind velocities in the stratosphere [[Newman et al. 2011](#); [Lebonnois et al. 2012a](#); [Lora et al 2015a](#)]. The simulations show,

however, that the peak wind speed is in the winter hemisphere, with the slowest speed experienced in the summer hemisphere. We suspect that the EQA and NPA precession rates are not decoupled. In Figure 27 Top we can see that from -60 to 10 degrees relative to vernal equinox, the EQA does not precess. Then from 10 to 40 degrees after the vernal equinox, the precession rate of the EQA accelerates. If the EQA precession rate were to remain on its course after $L_s = 40^\circ$ we might expect it to look exactly like the precession rate of the NPA. We therefore suggest that the EQA and NPA precess together at the same rate. Furthermore, we suggest that the EQA and NPA are nearly parallel with each other and move in lock step. A more detailed investigation of nearly contemporaneous observations of the EQA and NPA will be needed to verify this hypothesis.

5. Conclusion

The North Polar Annulus (NPA), the Equatorial Annulus (EQA) and the South Polar Annulus (SPA) are stratospheric seasonal features that provide insight into the Titan's circulation mechanisms and patterns. The annuli are unique among Titan features in their refined morphology (as compared to the polar hoods and the north-south asymmetry), their predictability (as compared to clouds), and their scale, which allows for Earth-based observations. From the differential spectra of the annuli, we conclude that the annuli are areas of increased haze. Using spectraltimetric techniques, we determined the minimum altitude of the annuli to be between 100-130 km. Triangulation of the NPA is consistent with the spectraltimetry with a modeled median altitude of $H = 217 \pm 2$ km. We tracked the EQA and the NPA over the course of the Cassini mission and investigated their changes in position and spectra.

The annuli are easily observable features that can be used to track the evolution of Titan's stratosphere on seasonal and yearly timescales. The annuli have already been observed with Keck [Roe et al 2002] and with an expected spatial resolution of 200km, and a spectral range of 600 to

2300nm, the annuli should be readily observable with JWST [Nixon et al 2016]. The timing and position of the annuli are controlled by Titan's circulation, and dynamic and chemical mixing boundaries. An understanding of the annuli, including how they form and what they are made of, provides insight into the driving forces that control Titan's stratosphere.

The EQA is visible for the entirety of the *Cassini* mission. The spectra of the EQA increases in absolute contrast to a maximum of about 10 degrees of L_S after the vernal equinox. We suggest that this is evidence of the haze increasing in abundance in the EQA as Titan approaches the vernal equinox. We propose that the EQA is formed by upwelling at the equator where the north and south equator-to-pole meridional circulation cells converge around the vernal equinox. When the meridional circulation cells transition to a single pole-to-pole cell, most of the haze accumulated at the equator is transported poleward. Given the continuous observation of the EQA we propose that some haze must remain in the middle stratosphere where wind speeds are possibly low and meridional circulation is stagnant. This is supported by the meridional stream functions shown in Figure 7 of Lebonnois et al 2012a. We see that at $L_S = 123.8^\circ$ (the nearest time to summer solstice) the meridional circulation crosses the equator at ~ 300 km. Meanwhile, in the lower stratosphere near 100 km, the meridional circulation is limited to a small cell spanning 20°S and 20°N . In this area we might expect that this small cell continuously circulates any haze that had been lofted during the convergence events seen at $L_S = 8.9^\circ$ and 179.3° .

We did not observe the SPA despite many opportunities where the viewing geometry would have allowed detection. Because it was detected in 1999-2001, but not during the *Cassini* mission, we propose that the SPA is a seasonal feature. Thus, if we assume that the polar stratospheres and the circulation are mostly symmetric between the hemispheres, then we can also assume the NPA is a seasonal feature.

The NPA becomes detectable about 35 degrees of L_s after the vernal equinox and remains present up to the end of the *Cassini* mission. The spectra of the NPA is nominally identical to the EQA, but it changes in ways the EQA does not. The darkening of the spectra of the NPA is consistent with our models that suggests that the altitude of the NPA is increasing throughout our observations. The NPA shares its morphology and location with several other north polar features including the north polar hood. The timing/sequence of the other polar features and the NPA leads us to suggest that the NPA is haze which was on the border of the north polar hood. As the north pole enters summer the ethane in the north polar hood falls out carrying the haze along with it, leaving the NPA as remnant haze occupying the stratosphere on the arctic circle.

An important result of this work is the tracking of the tilt and azimuthal offset of the annuli, and by extension the stratosphere. We found that the tilt of the stratosphere is in the range predicted by [Tokano 2010a](#), but does not follow any distinct pattern. We found that the azimuthal position of the stratosphere does not match the prediction from [Tokano 2010a](#). The azimuthal position of the stratosphere shows some correlation with the subsolar longitude. We suggest that the orientation and position of the stratosphere are strongly correlated with the seasons when examined in an inertial reference frame (Figures 26 & 28). There is some indication that the stratosphere reorients itself throughout the year around a centroid offset by a few degrees from the north polar axis. Assuming this is correct, we suggest that the centroid about which the stratosphere reorients itself, is itself rotating around the north polar axis. In this scenario the centroid is a seasonal feature (Figure 26 Top), while the stratosphere around the centroid may be an orbital or diurnal feature with a much shorter period (Figure 26 Bottom). We suggest that our dataset supports the proposed mechanism for the tilt suggested in [Achterberg et al. 2008](#).

In order to analyze the annuli, we developed 1) a mosaicking routine with aspects of sub-pixel super resolution, 2) a technique for correcting the striping in the VIMS-Vis dataset, and 3) an empirical technique for improving the contrast in a Titan observation. Any data used in this work or any of the above described techniques can be made available by contacting the first author.

Chapter 4: The Compositional Diversity of Surfaces

Investigating the Spectral Diversity of Titan's Equatorial Region from Patterns Identified in the Cassini VIMS Dataset

N. Katsop, A. G. Hayes, C. Sotin, J. L. Lunine, K. Lawrence, S Le Mouélic, S. Rodriguez, S. P. D. Birch, P. M. Corlies, J. Madden, J. Soderblom

Icarus, Submitted

1. Introduction:

The Visual and Infrared Mapping Spectrometer (VIMS, [Brown et al. 2004]) acquired hyperspectral observations in the 350 – 5100 nm wavelength range of Saturn's moon, Titan, from 2004 (near Winter Solstice) to 2017 (near Summer Solstice). In this work, we utilize the entire VIMS dataset to investigate the spectral variability of Titan's equatorial region (-30N to 30N), with a goal of identifying repeating spatial patterns and documenting compositional diversity. Our specific objectives are to identify areas of common composition and determine paths of evolution based on proximity and morphologic correlations. We focus our attention on the areas identified by previous studies, which used subsets of the VIMS data set [Griffith et al. 2019; Soderblom et al. 2007] to identify regions as water-ice rich, to both validate and expand upon previous results by bringing the entirety of the VIMS dataset to bear.

Titan's surface has landforms morphologically similar to Earth's, though they exist in a chemically and environmentally disparate state. Those landforms are expected to form and evolve atop a thick (~100-150 km) water-ice crust, based on Titan's bulk density and the ubiquitous presence of water-ice in the outer solar system. Most of that water-ice surface, however, is covered by other materials that are hard to uniquely identify, in part because the surface is obscured by Titan's thick atmosphere of methane, nitrogen, and organic haze [Veverka 1973; McKay 1996]. To overcome this, the Cassini spacecraft, operating from 2004 - 2017, carried the RADAR suite

[Elachi et al. 2004]. In addition, the Imaging Science Subsystem (ISS) [Porco et al. 2004], and the Visual and Infrared Mapping Spectrometer (VIMS) [Brown et al. 2004] demonstrated that they could penetrate Titan's thick atmosphere. These instruments have been used to characterize the geomorphology of Titan's surface [Birch et al. 2014; Schoenfeld et al. 2021; Lopes et al. 2020; Malaska et al. 2016] as well as the composition via reflectance spectra and dielectric permittivity [Wye et al. 2007; Poggiali et al. 2020]. In this work we use the VIMS instrument to investigate the patterns of spectral features seen at the equator to describe the processes and evolution of the area.

Titan is a spectrally diverse surface which has been canonically modeled using a handful of spectrally distinct units. These include water ice, water–ammonia ice and other water ice mixtures, liquid methane and ethane, evaporites, acetylene, benzene, CO₂ frost, organic materials such as nitriles, alkynes, alkanes, aromatic ring compounds, and organic polymers related to laboratory tholins [Lopes et al. 2016; Griffith et al.; 2003; Negrao et al.; 2006; Barnes et al.; 2007a; Soderblom et al.; 2007; McCord et al.; 2008; Hirtzig et al.; 2013; Singh et al. 2016; Cordier et al. 2016; Griffith et al. 2019; Czaplinski et al. 2020; Mackenzie et al. 2016]. These spectrally diverse features show strong correlations with RADAR-derived morphological units, signifying a link between formation/evolution and composition [Schoenfeld et al. 2021; Langhans 2012; Williams et al. 2011; Barnes et al. 2008]. One VIMS feature which has garnered significant attention in the existing literature is the “VIMS dark blue” unit [Soderblom et al. 2007]. The blue unit is so called because of its blue appearance in RGB images produced using the methane windows at 2.0, 1.6, and 1.3 μm respectively. In these synthetic color images, the blue unit exhibits a higher reflectance at 1.3 μm and lower reflectance at 2.0 and 1.6 μm . The spectral slope of the blue unit is similar to that of water-ice, so this unit is most commonly attributed to areas with an observable fraction of exposed water-ice.

Water-ice has been proposed to be at least partially exposed in several locations across the equator. This includes the rims and ejecta of impact craters [Neish et al. 2015], at the mouths of dendritic channels [Soderblom et al. 2007], mountains and hummocky terrain [Malaska et al. 2016], in the uppermost layers of the midlatitude alluvial fans, undifferentiated plains, and labyrinth terrains [Solomonidou et al. 2020], and in a long “ice corridor” extending more than 6000 km [Griffith et al. 2019]. The presence of exposed water-ice on Titan’ surface, however remains contentious and different studies conflict with one another about the terrain that should be ice poor/rich or organic poor/rich [Neish et al. 2015; Werynski et al. 2019; Malaska et al. 2016; Solomimondou et al. 2020]. In this work we avoid interpreting the spectra of features as being indicative or counter-indicative of absolute composition, such as water-ice rich/poor. This is because we are only able to capture a partial spectrum of the surface, which furthermore is contaminated by atmospheric scattering. We instead discuss relative abundances with regard to the spectra, discuss the change in spectra between features, and discuss correlations between our observation and the proposed locations of water-ice.

Titan’s equatorial geology is primarily characterized by dunes, hummocks, mountains, labyrinthic terrain, and plains [Malaska et al. 2016; Lopes et al. 2020; Schoenfeld et al. 2021]. The broad array of surface spectral features seen in VIMS which are associated with RADAR SAR observations and topography indicate a vibrant geologic environment with evidence for pluvial, fluvial, aeolian, tectonic, cryovolcanic, exogenic, and karstic processes [Hayes et al. 2016]. Plains dominate the midlatitudes, which transition to dunes closer to the equator. Impact craters excavate these sites and are filled in by sedimentary processes. At the resolution provided by Cassini, the distribution of units appears roughly symmetric between the northern and southern hemispheres. This all suggests that sedimentary, fluvial, and erosion processes are latitudinally dependent and

symmetric between the hemispheres. Several features at the equator have been associated with cryovolcanism, but this remains a contentious topic [Lopes et al. 2013].

In this paper we discuss the composition and evolution of Titan’s equator through inferences gleaned from repeating patterns of spectral units. We first describe our dataset, followed by a discussion of the techniques developed to remove atmospheric contributions and increase the contrast within an image as well as the efficacy of combining and comparing multiple observations. We next discuss our methodology for determining clusters of similar composition across the equator and between select features. We finish by discussing and interpreting the patterns of composition observed and propose possible paths of geologic evolution.

2. Data/Methods

Our processing workflow starts with the publicly available VIMS data set on the Planetary Data System (PDS) [Le Mouélic et al. 2019; https://pds-imaging.jpl.nasa.gov/data/cassini/cassini_orbiter/covims_0001/data/]. VIMS consisted of two imaging spectrometers; a visual detector (VIMS-Vis) with 96 channels between .35 and 1.05 μm and an infrared detector (VIMS-IR) with 256 spectroscopic channels between 0.89 and 5.13 μm [Brown et al. 2004]. The absorption and scattering by methane, nitrogen, and haze means that some channels in VIMS can see the surface, while for other channels the atmosphere is completely opaque [Corlies et al. 2021]. For every pixel, we determined the viewing geometry and location information using the SPICE toolkit from NAIF [Acton et al. 2018].

2.1. Data Correction and Mosaicking

We created super-sampled mosaic images of Titan for ingress and egress observations of each flyby, weighting higher spatial resolution pixels more in the mosaicking. We rasterized the pixels to a spatial resolution of 5 km^2 and calculated the weighted average of all individual image

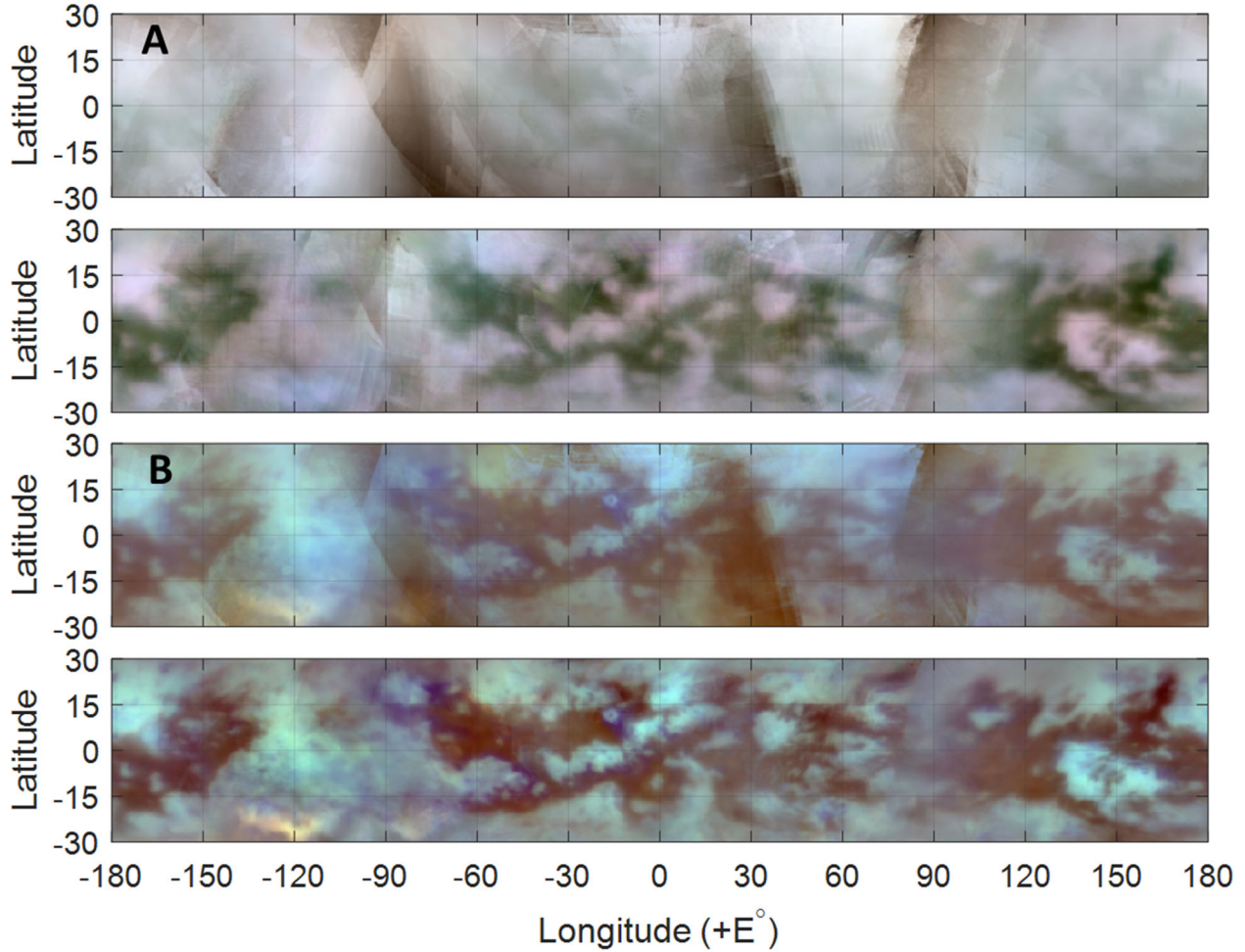


Figure 29 (A) : Equirectangular projection of our data in RGB at $0.929 \pm .004 \mu\text{m}$, $0.834 \pm .004 \mu\text{m}$, $0.827 \pm .004 \mu\text{m}$ respectively, (Top) Data without atmospheric correction. (Bottom) Data with atmospheric corrections (B) Equirectangular projection of our data in RGB at $5.03 \pm .08 \mu\text{m}$, $2.03 \pm .03 \mu\text{m}$, $1.28 \pm .01 \mu\text{m}$ respectively. (Top) Data without atmospheric correction. (Bottom) Data with atmospheric corrections

pixels that filled each pixel of the mosaic. The primary constraints on data incorporated into the mosaics was a pixel scale of less than 250 km and a change in the phase angle, θ , of less than 3° . This means closest approach observations, with their rapidly changing viewing geometry, were not used.

VIMS image cubes from the Vis detector have stripes of varying brightness at each sample running across the lines. The stripes are due to offsets of about one hundred DN introduced by the readout electronics on the signal [Filacchione et al. 2007]. We developed a destriping routine described in Kutsop et al. 2022 which we applied to every VIMS-Vis image cube. We leverage

Titan's smoothly scattering atmosphere to improve contrast in the image cubes and increase spectral clarity via the manifold technique described in Kutsop et al. 2022. Manifold corrections were applied to all image cubes from both detectors.

Methane absorption and scattering by haze results in only $\sim 48^1$ channels spread throughout the full 352 channels available to VIMS that can effectively observe the surface. Within these surface channels, absorption and scattering by gas and haze alter the spectra of Titan's surface as observed by VIMS. Of these we used 32 channels in our analysis; 5 visual and 27 infrared². We ignored the other ~ 16 channels because they were either heavily contaminated by atmospheric scattering (i.e. $< 750\text{nm}$) or the channels were redundant (i.e. the gradient between two channels is low) and including them would increase computational time without adding new information (i.e. $> 5\mu\text{m}$).

We then collect every pixel from our flybys into one searchable dataset of equally spaced points on a sphere [Thomson 1906]. We create a Thomson sphere with 51 million points where the points are about 4.5 km apart [Semechko 2022]. We can then constrain our data by viewing geometry, resolution, time, and location. For this work we limited our data to latitudes of -30° to 30°N , incidence and emission angles less than 75° , and a pixel spatial scale of 200km or less. We then reproject this data into an equirectangular map (Figure 29) and combine any overlapping pixels by first finding the median resolution, m_r , and then taking the median brightness of the pixels with resolutions less than m_r .

¹Whether a channel sees the surface is often a subjective matter. We believe that these include 644, 651, 688, 695, 747, 754, 820, 827, 835, 930, 937, 944, 1046, 925, 942, 1057, 1073, 1090, 1270, 1286, 1532, 1549, 1565, 1582, 1598, 1993, 2010, 2026, 2043, 2059, 2689, 2706, 2773, 2789, 2806, 4929, 4946, 4963, 4980, 4997, 5014, 5031, 5048, 5064, 5081, 5098, 5115 nanometers.

² The 32 wavelengths used in this research are 827, 835, 930, 937, 944, 942, 1057, 1073, 1090, 1270, 1286, 1532, 1549, 1565, 1582, 1598, 1993, 2010, 2026, 2043, 2059, 2689, 2706, 2773, 2789, 2806, 4946, 4980, 5014, 5048, 5081, 5115 nanometers

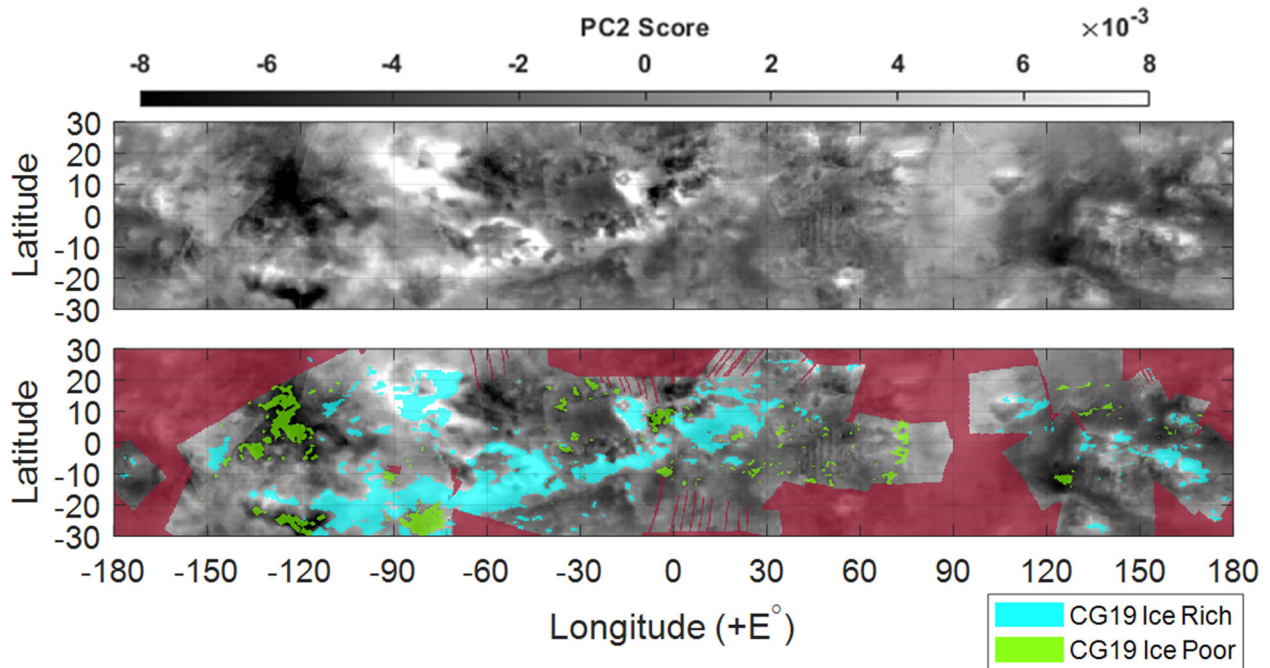


Figure 30 (Top) Equirectangular projection of the second principal component score for our data. (Bottom) Equirectangular projection of the second principal component score for our data with blue and green polygons indicating areas from Griffith et al 2019 identified as ice rich and ice poor respectively. The red polygons indicate areas not observed in Griffith et al 2019.

We validate our dataset by reproducing the results of Griffith et al. 2019. In their work, they use principal component analysis (PCA) to identify the maximum variance at the equator at 1.1, 1.3, 1.6 and 2.0 μm . A blue slope has been commonly invoked as evidence for water-ice on Titan [Clark et al. 2010], though other compounds, like some hydrocarbons such as acetylene, have similar blue slopes. In Griffith et al. 2019 they associate water-ice with absorption features at 1.6 and 2.0 μm in the second principal component found for the majority of their VIMS cubes. Using the second (or in one case the third) principal component they identified areas on Titan's equator which could be water-ice-rich/organic-poor or water-ice-poor/organic-rich.

We extract the pixels from our Tomson sphere and create an equirectangular map. In accordance with Griffith et al. 2019, we use 4 channels; the 1.1, 1.3, 1.6, and 2.0 μm . We find the principal components in our data, and we find that the second principal component matches the description of the second principal from Griffith et al. 2019. In Figure 30, we show a map of the

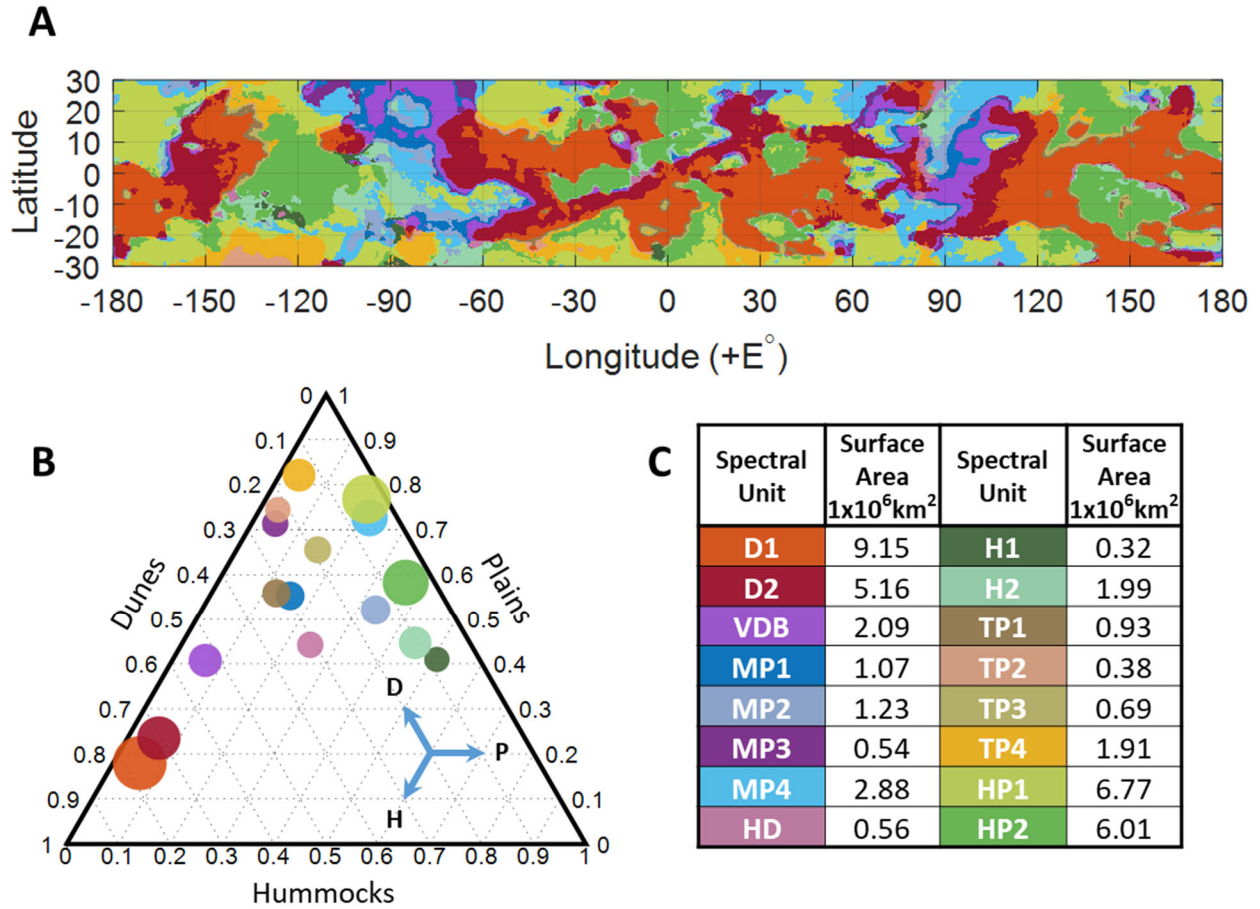


Figure 31 (A) Equirectangular projection of our data clustered into 16 spectrally distinct units as determined through our Monte Carlo k-means clustering algorithm. Each color represent a different unit. The colors of each unit are chosen so as to maximize the correlation with the spectra, i.e. red areas have a redder spectral slope, blue areas have a bluer spectral slope. (B) Distribution of spectral units according to geomorphologic units determined by Lopes et al 2020. The three arrows in the lower right indicate how the graph should be read, i.e. the center of the arrows is 20% dunes, 20% plains, and 60% hummocks. (C) Surface area coverage for each spectral unit.

value of the second principal component. The areas that are found to have a high score of the principal component (i.e. bright at 1.1 and 1.3 μm and dark at 1.6 and 2 μm) correlate closely with the areas identified in Griffith et al., 2019 as water-ice rich. We also find that the areas with a large negative score (i.e. bright at 1.6 and 2.0 μm and dark at 1.1 and 1.3 μm), correlate closely with the areas identified as organic-rich by Griffith et al., 2019. We show that our dataset is able to reproduce the results of Griffith et al. 2019.

2.2. Spectral Clustering

We use k-means clustering to identify spectrally distinct units. We use our equirectangular map where each point of latitude and longitude has a corrected spectrum of 32 channels. K-means clustering separates the data into k clusters by iteratively solving for the cluster centroids which minimize the distance between members of a cluster and the centroid [Vassilvitskii 2007]. The efficacy of k-means clustering is improved by first reprojecting the spectra into the principal component space using PCA [Liu et al. 2015]. We found the most reproducible cluster centroids by conducting our k-means clustering inside a Monte Carlo simulation with 500 runs. Each Monte Carlo initiates with random starting centroids and each iteration of centroid solutions carries a random element [Galton 1894]. Our final cluster centroids are then the average of all the runs.

Using the common techniques for determining the statistical significance of the number of k-clusters, we find that the “optimum” is 2 clusters; the dunes and non-dunes. Instead we choose to separate our data into 16 clusters (Figure 31). This is based on the variance explained by the addition of multiple components. The variance of a dataset is the eigenvalues of the covariance of the components, which regardless of how many components, always sums to one. In the bottom right of Figure 32 we show the variance explained by 28, 24, 20 and 16 components. As can be seen, all the cumulative sum curves go asymptotic at around 16 components, signifying that the addition of further components does not significantly explain more of the variance. In each case 16 components explains about 99.95% of the variance. 16 is also half of the spectral channels that we used and ensures that we are not oversampling. In Figure 31A we see that the 16 units correlate to areas of spectral diversity with distinct morphologies reasonable for the area (instead of one or two pixels, as might be the case if we were sampling noise). By distinct morphologies reasonable for the area, we mean, for example that crater rims visible in RADAR or ISS appeared as closed

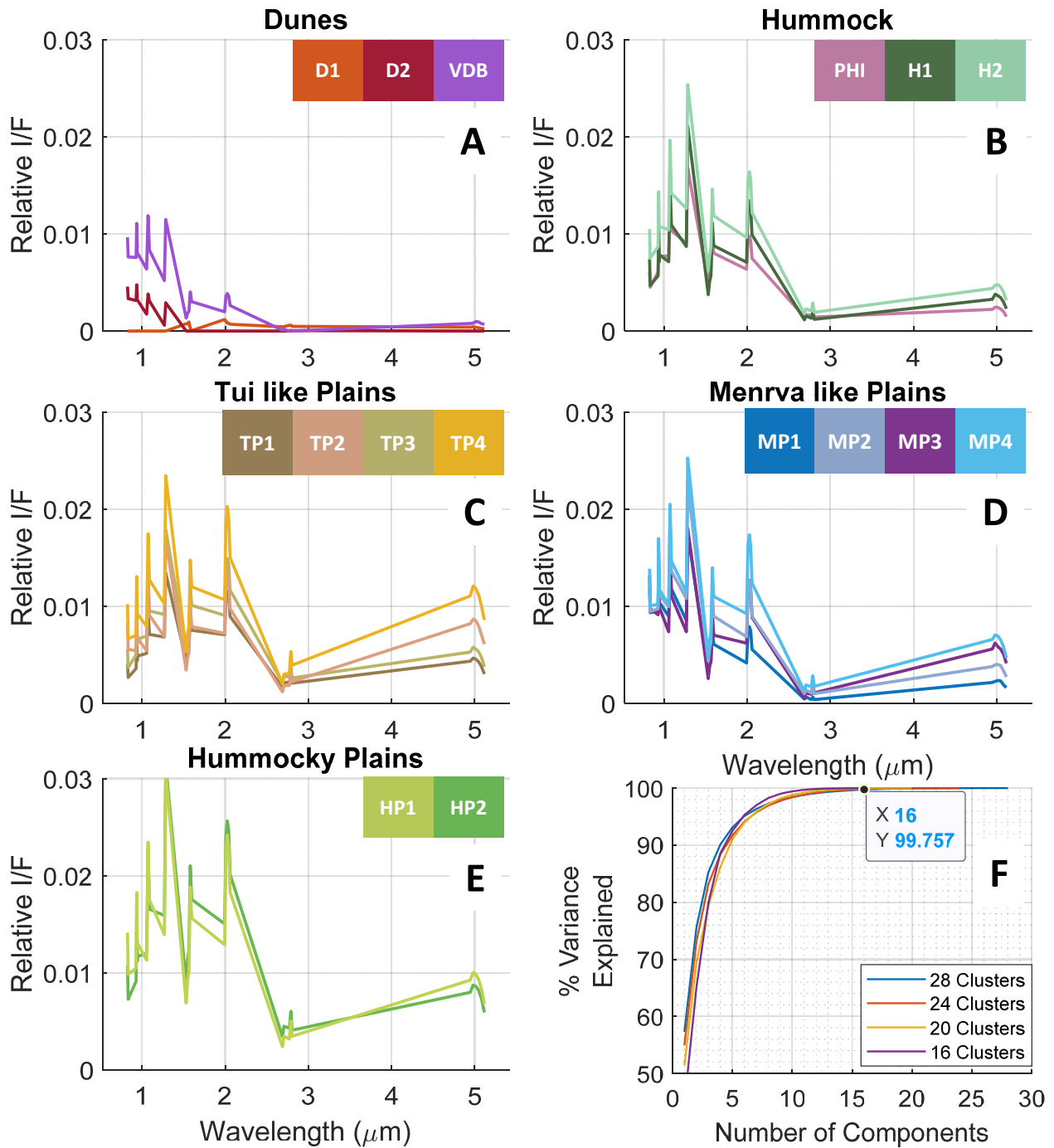


Figure 32(A-E) Relative spectra for 16 spectral units grouped according to association with geomorphologic units and prevailing patterns. The spectra is adjusted so the minimum spectra is 0. (F) Cumulative sum curves of the variance explained by each component for a series of increasing k-clusters.

circles in maps we constructed of the spectral units. The spectra of each cluster centroid are shown in Figure 32.

	D1	D2	VDB	MP1	MP2	MP3	MP4	PHI	H1	H2	TP1	TP2	TP3	TP4	HP1	HP2
D1		2	5.3	7.6	9.3	9	11	7	8	10	7	9.3	9.5	10	10	10
D2	1.8		3.6	6.3	8.5	8.2	9.9	7	8	9	7	8.6	9	9.3	9.8	9.3
VDB	5.3	4		3.6	6.8	5.8	8.6	5	6	8	6.8	6.9	7.8	7.3	8.8	8.3
MP1	7.6	6	3.6		4.1	4	6.9	5	5	6	7.1	6.9	8	6.5	8	7.7
MP2	9.3	9	6.8	4.1		3.7	4.4	5	4	4	6.5	6.7	7.1	5.5	6.6	6.5
MP3	9	8	5.8	4	3.7		5.3	6	5	6	6.3	4.9	7.4	6	7.1	7
MP4	11	10	8.6	6.9	4.4	5.3		8	7	3	7.9	6.4	6.6	4.2	3.8	4.4
PHI	7.4	7	5	4.6	5.2	6	7.8		3	6	4.2	5.2	5.3	5.5	8.3	7.8
H1	8.3	8	6	5.2	4	4.9	6.5	3		5	4.9	4.4	4.9	5.1	7.9	7.4
H2	9.7	9	7.8	6.4	3.8	5.9	2.8	6	5		7	7	5.3	3.8	4.5	4.3
TP1	7	7	6.8	7.1	6.5	6.3	7.9	4	5	7		4.4	4.6	6.8	8.3	8.1
TP2	9.3	9	6.9	6.9	6.7	4.9	6.4	5	4	7	4.4		4.5	4.9	6.8	6.7
TP3	9.5	9	7.8	8	7.1	7.4	6.6	5	5	5	4.6	4.5		4.4	6.6	6.2
TP4	10	9	7.3	6.5	5.5	6	4.2	6	5	4	6.8	4.9	4.4		3.1	3.4
HP1	10	10	8.8	8	6.6	7.1	3.8	8	8	5	8.3	6.8	6.6	3.1		1.7
HP2	10	9	8.3	7.7	6.5	7	4.4	8	7	4	8.1	6.7	6.2	3.4	1.7	

Table 2 The number of standard deviations necessary for the $32n$ -hyperellipsoids of the spectra for each spectral unit to intersect.

To further demonstrate the separability and appropriateness of our clusters, we developed a metric in which we reproject the spectra of the pixels in the clusters as 32-dimensional ellipsoids. This technique is inspired by the silhouette method [Rousseeuw 1987]. The silhouette method measures how close a data point is to its own cluster centroid (cohesion) compared to the next closest cluster centroid (separation). Our metric uses the same philosophy of cohesion vs separation but uses the standard deviation of any two clusters to simultaneously determine the distinction of two clusters. In our metric, the centers of these ellipsoids are the cluster centroids. The length of the axes is the standard deviation of all pixel's spectra within a cluster. We suggest that the number of standard deviations necessary until the ellipsoids intersect is directly related to their uniqueness. In Table 2 we show the number of standard deviations needed before an ellipsoid intersects a partner.

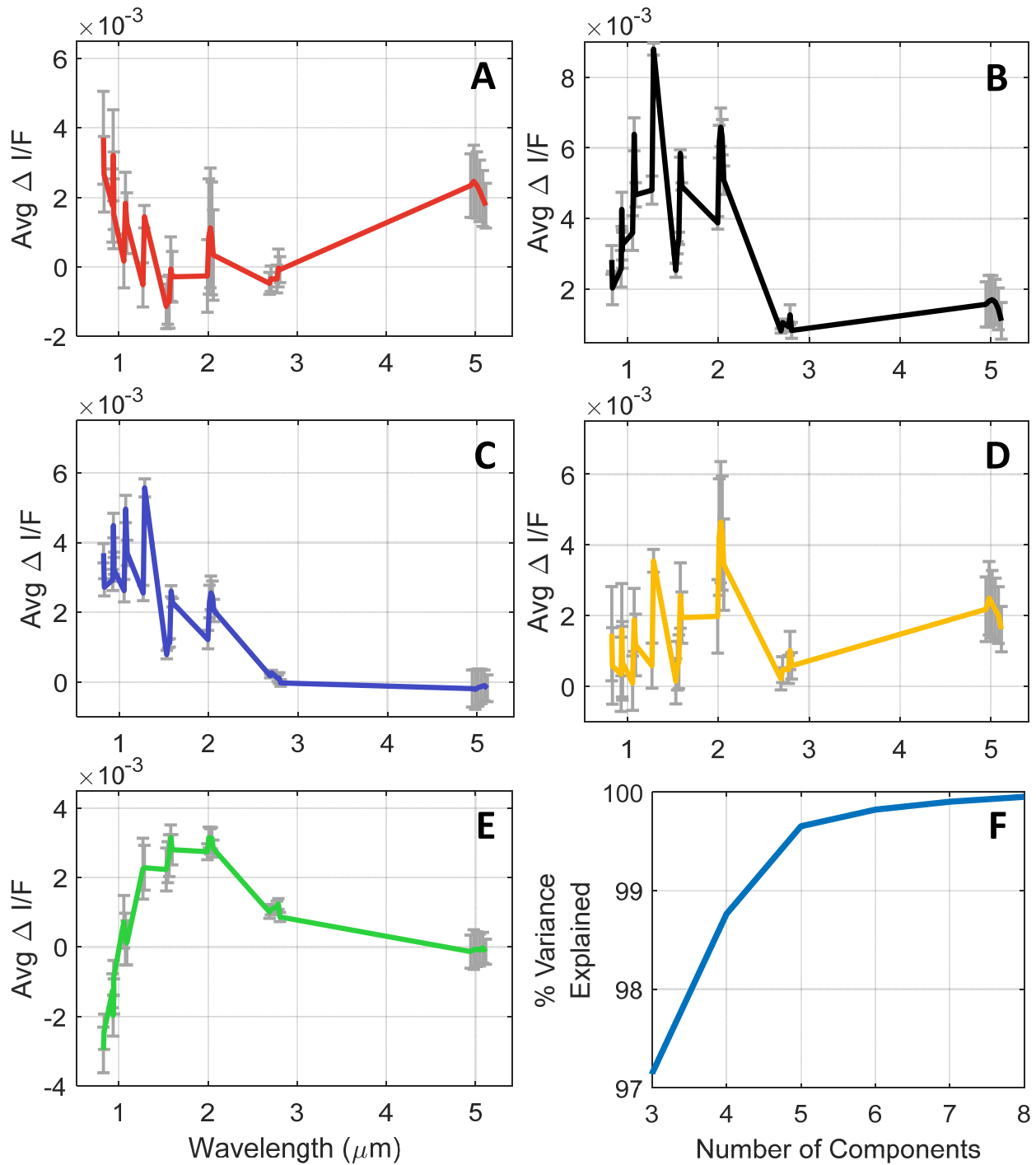


Figure 33 (A-E) Five distinct delta-spectra which account for the majority of variance seen in between pairs of spectral units (Figure 31). Grey error bars are one standard deviation about the mean. (F) The variance explained by the addition of spectral components. Not shown is the variance explained by one or two components, which are 61% and 82% respectively.

We also determine which spectral units share a boundary with one another. Of the boundaries we only keep the bounded pairs which account for a cumulative sum of 95% of the

perimeter of either unit. We find the differential spectra between bounded pairs, and using another k-means clustering procedure with 20,000 Monte Carlo runs, determine that the change in composition can be characterized with five delta-spectra, as shown in Figure 33. As before, each Monte Carlo initiates with random starting centroids and each iteration of centroid solutions carries a random element [Galton 1894]. With five delta-spectra we can explain 99.7% of the variance seen in the spectral gradient across the surface. In Figure 33 we display the cumulative sum of the delta-spectra, which shows that the addition of further delta-spectra accounts for a marginal increase in representation of the variance.

We categorize each of our spectral units by identifying which of the six geomorphologic units mapped by Lopes et al. 2020 the majority of the spectral unit is in. We categorize each of our spectral units by identifying which of the six geomorphologic units mapped by Lopes et al. 2020 the majority of the spectral unit is in. We find that our spectral units can be categorized into three geomorphological groups (dunes, hummocks, and plains). Figure 31B shows the relative occurrence of the spectral units within the morphologic units.

In addition to categorizing the spectral units using the geomorphologic unit, we characterize the geomorphologic units using the spectral units. To do this we determine the areal coverage of the spectral units within the boundaries of each geomorphologic unit. We then characterize each geomorphologic unit by the spectral units with a cumulative areal coverage of at least 68% (greater than one standard deviation).

2.3. Spectral Analysis

We also determine the spectral gradient across the surface with

$$\nabla F = \partial F / \partial \lambda^i + \partial F / \partial \phi^j, \text{ EQ1}$$

where λ is the latitude and ϕ is the longitude. We use our equirectangular map where each point of latitude and longitude has a corrected spectrum of 32 channels. In Figure 34A we present an equirectangular projection of the differential spectra (Eq, 1). The spectral gradient map is clustered according to the lowest spectral angle between the data and the five delta-spectra that explain the observed spectral changes (Figure 33). In Figure 34A, the purer the color, the smaller the angle is between the differential spectra and the associated delta-spectral vector. White indicates that the angle between the differential spectra and the delta-spectra is equal for 2 or more delta-spectra, i.e. the differential spectra can suitably match one or another delta-spectral vector.

If we assume that the change in composition between spectral units is linear then the delta-spectra from Figure 33 would be a representation of the compositional change from one unit to another. To that end, we compared our delta-spectra with the USGS spectral library, which has a dataset specifically convolved for VIMS. We determined the spectral angle between the library and our delta-spectra using each available spectral channel. Many of the spectra in the library are missing reflectance values at one or more of the 32 wavelengths we use. In these cases we only use our $\Delta I/F$ values at wavelengths where data is available in the library spectra for our comparisons. On average, we were able to use about 22 spectral channels in our comparisons.

The USGS spectral library contains ~2500 spectra, in groups of “Artificial Material”, “Vegetation”, “Minerals”, “Soils and Mixtures”, “Coatings”, “Liquids”, and “Organic Compounds”. We only expect the last two categories to be relevant to material on Titan, and so we primarily focus our comparisons on these two. We highlight material from the “Liquid” and “Organic Compound” groups by shading the cells of our results in Table 3 with blue and orange respectively.

"Red"		θ	σ
1	Red Coated Algae Water RCAW1	21.24	0.78
2	Melting snow mSnw09 (slush)	28.07	0.68
3	Melting snow mSnw14 (slush)	28.13	0.68
H2O	H2O-Ice GDS136 77	40.54	0.85
"Green"		θ	σ
1	Phenazine SA-P13207	14.81	0.75
2	Antipyrine SA-A5882 85K	15.88	0.66
3	Phenazine SA-P13207 85K	16.8	0.71
H2O	H2O-Ice GDS136 77	86.75	1.03
"Blue"		θ	σ
1	Acetylene MTG 80K	16.07	1.14
2	Tannic Acid SA-403040	16.43	1.07
3	Indole SA-I3408 75K	17.01	1.04
H2O	H2O-Ice GDS136 77	30.91	1.41
"Black"		θ	σ
1	Phenylacetylene SA117706 85K	23.23	2.79
2	Propyne SA-295493 Frost 80K	23.88	3.02
3	Indole SA-I3408	23.97	2.97
H2O	H2O-Ice GDS136 77	51.59	4.26
"Yellow"		θ	σ
1	Butane Camco frost 78K	27.73	1.97
2	Pentane SA-76878 fine fr86K	28.23	1.95
3	Violanthrone79 SA-641790	31.46	2.14
H2O	H2O-Ice GDS136 77	68.95	2.89

Table 3 The materials from the USGS Spectral Library Chapters L and O with the smallest spectral angle with respect to the delta spectra (Figure 33). Material highlighted in blue and orange are from the "Liquid" and "Organic Compound" groups respectively.

We compared each of the five delta-spectras against the library in a Monte Carlo simulation with 100,000 runs. Each run we adjusted the delta-spectra with a random normal distribution about the standard deviations shown by the error bars in Figure 33. After each run we noted the ten materials with the lowest spectral angle. At the end we found the mean and standard deviation of

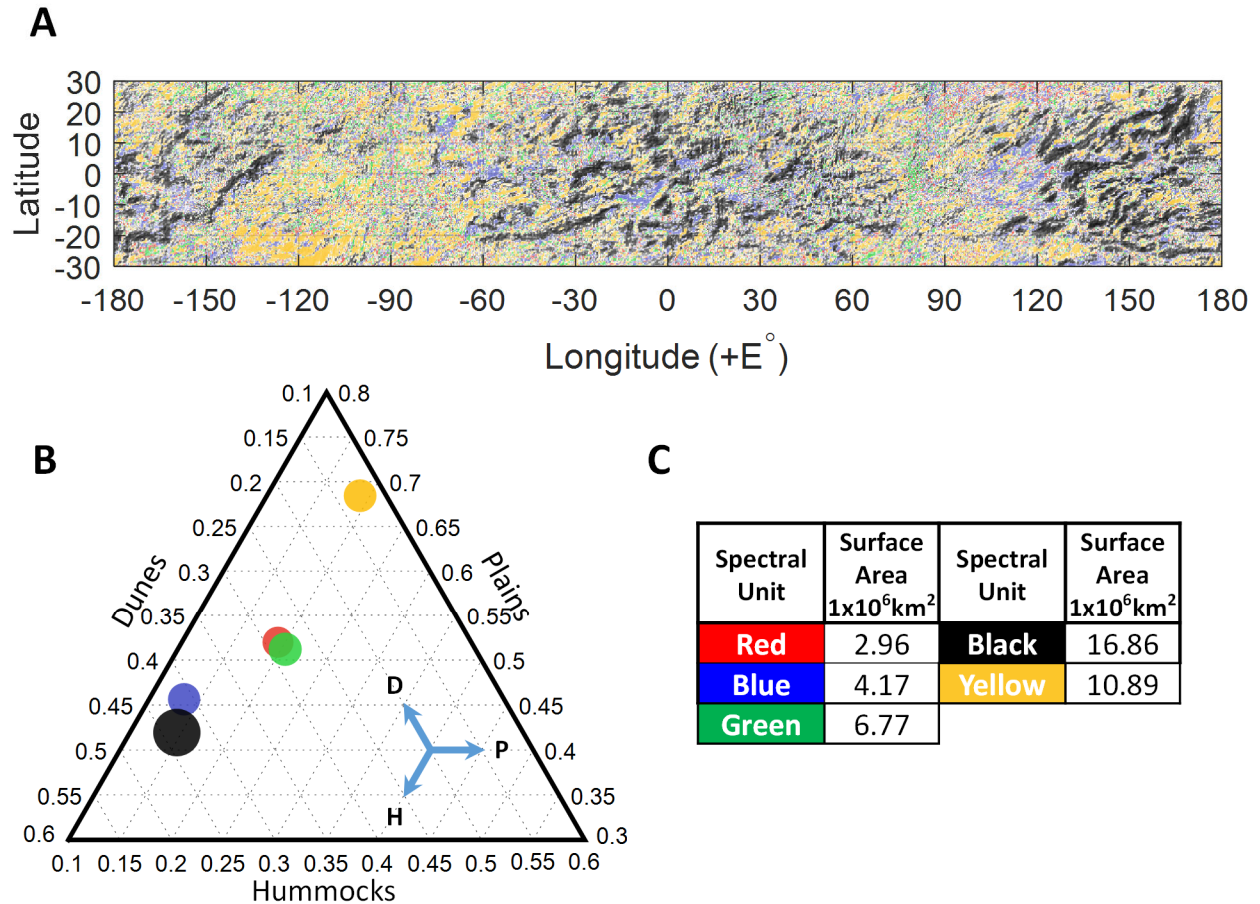


Figure 34 (A) Equirectangular projection of the spectral gradient clustered using the delta-spectra (Figure 33). (B) Distribution of the spectral gradients associated with the delta-spectra according to geomorphologic units determined by Lopes et al 2020. The three arrows in the lower right indicate how the graph should be read, i.e. the center of the arrows is 20% dunes, 40% plains, and 40% hummocks. (C) Surface area coverage for each area associated with the delta-spectra.

the spectral angle for each of the materials that were in the top ten more than once. From this distribution we found the three materials with the lowest average spectral angle (Table 2). Because water-ice is so frequently invoked to explain spectral features, we separately kept track of the spectral angle between each of the five delta-spectra and water-ice. We ran the water-ice comparison through the same Monte Carlo simulation as before and reported the average spectral angle and the standard deviation in Table 3.

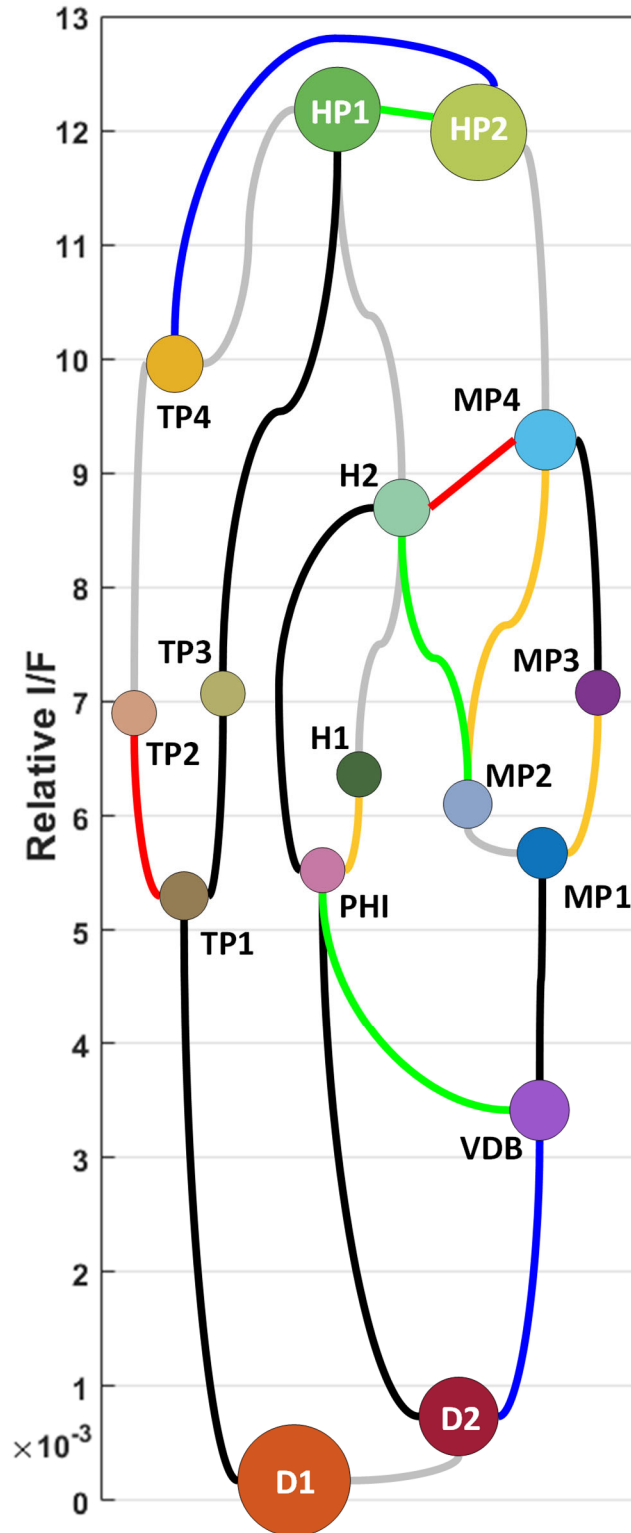


Figure 35 Network diagram showing the connection between pairs of units. The arrows move in the direction of increasing intensity (dimmest units at the top, brightest units at the bottom). The size of the markers represents the relative areal coverage of each unit Figure(31). The color of the vectors indicate that the change in spectra from one unit to the next is almost the same as the respective delta-spectra (Figure 32), Gray arrows indicate that the change in spectra requires 2 or more spectra linearly mixed in order to make a match.

3. Results

3.1. Spectral Units

As we show in Figures 30 and 31, areas identified in previous studies as potentially ice-rich correlate with several of our spectral units; in particular units **D2**, **VDB**, and **MP1**. We propose that these three units, by virtue of spatial correlation, are compositionally similar to the ice corridor identified by Griffith et al. 2019 and the *VIMS* dark blue areas first identified by Soderblom et al. 2007. These spectral units have a greater spatial coverage than the ice corridor or the areas identified as *VIMS* dark blue, suggesting that they are more expansive than previously reported. We propose that the reason these new areas are detected in our work is because: 1) we use the entire *VIMS* dataset which constitutes full global coverage and 2) our analysis uses 32 wavelengths (instead of 4 [Griffith et al. 2019] or 3 [Soderblom et al. 2007]) over a broader and fuller spectral range².

Three of our spectral units, **D1**, **D2**, and **VDB**, are found almost exclusively in the “dunes”, two of our spectral units, **H1**, **H2**, are predominantly in the “hummock”, and ten spectral units represent the “plains”. By examining Figure 31 and 35 we see that the ten “plains” units appear in recurring sequences and patterns allowing us to divide them into three sub-groups. The first is the “Menrva” plains (**MP1-4**) subgroup, named as such because Menrva Crater accounts for the largest single patch of these units. The second is the “Tui” plains (**TP1-4**) subgroup, named as such because Tui Regio accounts for the largest single patch of these units. The third is the “hummocky” plains (**HP1-2**) subgroup, named as such because these units, while mostly in the plains, also make up a significant portion of the hummocks.

There is one additional spectral cluster not accounted for, which we refer to as the “Plains Hummock Isolate” feature or **PHI**. By areal coverage, this unit is primarily found in the plains

(~45%) and has the least coverage in the hummocks (~25%). **PHI** however, appears almost exclusively in sequences involving **H1** and **H2** and is usually completely surrounded by one or the other hummock unit. When **PHI** is not surrounded by **H1** or **H2**, it is predominantly in contact with the dunes correlated with the ice-corridor, **VDB** and **D2**. When **PHI** is part of the sequence involving **VDB** or **D2**, the sequence continues only to **H2** and never directly to **H1**. Given its isolation from any other plains units and strong association with the hummock units, we categorize **PHI** with the hummock units.

3.2. Sequences and Pathways

In Figure 35 we show a connection diagram illustrating the transition between our spectral units. Each pair of nodes with a line in between them are in contact with or share a boundary with one another. We see that there are multiple, yet discrete, paths from one unit to another. Some units, however, have no direct paths between them (e.g. **D1** and **HP2**). The diagram is situated so that the units with a darker average spectrum are at the bottom and those with a brighter average spectrum are at the top.

We determined the differential spectra between the units in Figure 35 and compared their spectra to the five delta-spectra in Figure 32. To compare, we first calculate the spectral angle between the sample (spectra between nodes) and the test vectors (five delta-spectra). Then we find the first and second minimum angles. Our point of comparison, a , is then

$$a = \tan(1)/\tan(2) \text{ EQ2}$$

where a ranges from 0 to 1. We propose that the differential spectra between the nodes closely resembles one of the five delta-spectra for $a < .5$ and $1 < 15$ (note that for this particular dataset the second condition is redundant). The color of the lines indicate which of the delta-spectra most

closely resembles the difference between the units. Gray lines indicate that the differential spectra does not meet our criteria.

We see in Figure 35 that there are essentially two paths to move from the darkest unit, **D1**, to the brightest unit, **HP2**. The first and shortest path moves directly from **D1**, into the Tui-like plains subgroup, and then to **HP1** and **HP2**. In addition to the regions from Figure 31A, we see this same path occurring on the northern and western expanses of the boundary between the plains and the dunes (e.g. around 0N -30E)]; specifically, we most commonly see the sequences **D1** → **TP1** → **TP3** → **H1** (**D1** → \ → **H1**) or **D1** → **TP1** → **TP2** → **TP4** → **H2** (**D1** → \ → **H2**) in Figure 31A. The **D1** → \ → **H2** sequence stands in contrast to the **D1** → \ → **H1** sequence in its predominant morphology and relatively limited occurrence. In Figure 31A we typically see the **D1** → \ → **H1** sequence as a thin ridge between the dunes and the plains (e.g. -30E 0N, -135E 0N, and 135E 17N). The **D1** → \ → **H2** sequence does not show this morphology and is typically seen as a broad expanse (e.g. -45E 12N, and -45E -21N.) We see the **D1** → \ → **H1** pattern around smaller outcroppings of non-dune material (e.g. [-10N;0E] and [0N;165E] , and [-20N;0E]). Other noteworthy features with similar patterns include Sotra Patera, Mohini Fluctus, Shikoku Fluctus, and Selk Crater. We note that on this path, the dunes do not transition from the darkest **D1** to the lighter **D2** or **VDB**, both of which are spatially correlated with the ice corridor.

The second path moves from **D1** through **D2** and **VDB**. From **D2** and **VDB**, the path splits again into either the Menrva-like plains or the hummock units. The first branch is exclusively an offshoot of **VDB** into the Menrva-like plains; the most common sequence being **D1** → **D2** → **VDB** → **MP1** → **MP2** → **MP4** (**D1** → \ → **MP4**). In addition to Sinlap and Menrva Craters, we see this sequence of units on the southern and eastern expanses of the boundary between the

hummocks/plains and the dunes, in the western Xanadu flow feature [Wall et al. 2009; Lopes et al. 2013], and in a large crescent shaped area north of Hotei Regio. We also see in Figure 31A that these Menrva-like plains are preferentially distributed on the trailing and leading hemispheres, between -120E and -60E, and between 60E and 120E.

The second branch from **D2** and **VDB** moves into **PHI**. On the other end there is a single route moving from **H2** into the crater units. When **PHI** transitions from **VDB** or **D2** the sequence continues directly to **H2**; this sequence is **VDB/D2 → PHI → H2**. When **PHI** is in contact with **H1** it is part of a sequence as **H2 → H1 → PHI**, at which point PHI becomes isolated within **H1**. The **H2 → H1 → PHI** sequence is small and uniquely isolated from the other units and sequences. The largest single patch of this sequence is west of Eir Macula near -125E and -15N. Comparing this location in *SAR* and *ISS* images does not reveal features with which the patch can obviously or immediately be associated.

3.3. Delta-Spectra

The difference between bounded pairs of spectral units is the spectra of the change in composition if we assume linear mixing. We find that 99.7% of the variance of the differential spectra between bounded pairs can be explained by five components. The five components are referred to as delta-spectra and are named “red”, “green”, “blue”, “black” and “yellow”. The names correspond to the spectra which most closely resembles its namesake (i.e. blue is bright at shorter wavelengths, red is bright at longer wavelengths).

Blue: The “blue” delta-spectrum has the bluest slope of the five delta-spectra. The spectrum is mostly characterized by an increase in reflectivity at visible and short IR wavelengths, with essentially no change at five μm . By comparing Figures 31 and 34, we see that the “blue” delta spectra is most closely associated with the **D1 → \ → MP4** sequence. In particular, we

observe that **D2** → **VDB**, which is spatially correlated with the ice corridor and the *VIMS* dark blue, have large patches of spectral gradient consistent with the “blue” delta-spectrum. The only other pair we see with this “blue” delta-spectrum is **TP4** → **HP2**. In our comparison with the USGS spectra, we see that the “blue” delta-spectrum is most spectrally similar to acetylene at 80K. As we discuss in Section 4.2, the “blue” delta-spectrum matches water-ice more closely than any of the other delta-spectra.

Black: The other major transition from the dunes to the plains is consistent with the “black” delta spectra. Of the five delta-spectra, the black delta-spectra covers the largest surface area. It also represents the largest and most numerous patches of consistent spectral gradient. The “black” delta-spectrum has the most neutral spectral slope of the five delta-spectra and may be most indicative of albedo variations. The large patches of the “black” delta-spectrum are most consistent with the **D1** → **W** → **H1** sequence. We also see that the trailing and leading hemispheres of the equator are noticeably lacking in large patches of the “black” delta-spectrum. In our comparison between the delta-spectra and the USGS spectral library, we find that the “black” delta-spectrum is most consistent with phenylacetylene at 80K.

Green: The “green” delta-spectrum is characterized by an increase of reflectivity at 2 μm and a decrease of reflectivity at short wavelengths; of the five delta-spectras it is the only one which has a significant negative component. The “green” delta-spectrum does not show any large areas of consistent spectral gradient like the other delta-spectra. The “green” delta-spectrum is the most closely associated with the hummocks, which is reflected in Figure 35, where the pairs of units with a green transition are those moving into the hummock group (**VDB** → **PHI** and **MP2** → **H2**) and within the hummocky plains (**HP1** → **HP2**). In our comparison between the delta-spectra and the USGS spectral library, we find that the “green” delta-spectrum is most consistent with

phenazine ($C_{12}H_8N_2$) and antipyrine ($C_{11}H_{12}N_2O$) more commonly known as phenazone. Both are composed of a benzene ring and two nitrogen atoms, with additional components.

Red: Figure 34B suggests that the “red” delta-spectrum is homogeneously distributed amongst all three geomorphologic features. In Figure 34A we notice that there is one region with numerous small patches all closely packed together, in the area of 90E to 130E and 25N to 30N. This area has no name but it is north of Belet, west of Aura Undae, and south of Uanui Virgae. Although unnamed, this area appears morphologically distinct from the rest of the equator, with its thin wisps of plains and dunes. As such we dub this area the Kasure Undae, given their resemblance to the brush technique in Japanese calligraphy. In Figure 31A, this area correlates to what appears to be the largest contiguous patch of **MP4**. Besides the general distribution of this **MP4** across the trailing and leading hemispheres, we see the next largest patch of **MP4** in the center of Menrva Crater. In Figure 35 there are few changes between the spectral units which are associated with the “red” delta-spectrum

All three of the closest matching spectra from the USGS spectral library are consistent with H_2O . This is almost certainly due to the severe blue slope 827 nm to 1532 nm. Given however, that the surface temperature of Titan is around 180K below the freezing point of water, there is no reason to believe that there would be any liquid water anywhere. The analysis of the “red” delta spectra serves as an example of the precarious nature of determining composition based on slopes, broad similarities, or a few spectral channels.

Yellow: We see in Figure 34A that the regios (Hotei Regio and Tui Regio) have large contiguous expanses of spectral gradient associated with the “yellow” delta-spectrum. There are additional large patches near Eir Macula, Ksa Crater, Tishtrya Virga, and west of Afekan. Of the five delta-spectra, the “yellow” delta spectra is unique as it is the most isolated in regards to the

geomorphologic units. In the ternary plot of Figure 34, about 68% of the “yellow” delta-spectrum is found in the plains while only 19% is in the hummocks and 13% is in the dunes. In Figure 35 we see this supported by the companions with a change in spectra associated with the “yellow” delta-spectrum; two of which are intra-plane transitions (**MP1** → **MP3**, **MP2** → **MP4**) or a transition between the plane hummock isolate and the hummocks (**PHI** → **H1**). In our comparison between the delta-spectra and the USGS spectral library, we find that the “yellow” delta-spectrum is most consistent with butane (C₄H₁₀) and pentane (C₅H₁₂), both of which are alkanes.

4. Discussion

4.1. Distribution of Units

In general, spectral units spatially correlate to geomorphologic units (Figure 31). There are, however, examples of spectral units transcending geomorphologic boundaries. This can partially be explained by the lower spatial scale of the *VIMS* dataset in comparison to the *SAR* and *ISS* data used to map the geomorphologic units. This does not, however, explain the broad distribution of units like **HP2** (40% hummocks & 60% plains over 6 million km²). When spectral units cross morphologic boundaries, we are likely looking at Titan’s sediment transport pathways at work. Erosional and or depositional products can be transported across and between geomorphic units. This can indicate superposition of new material or chemical alterations which transcend boundaries. On the other hand, we do not see only one or two distinct spectral units, which would be expected by an undisturbed uniform covering, i.e. global snowfall a la Antarctica. If we accept that the equator is covered by some material, then it must be true that the equator is covered and cleaned non-uniformly in space and time.

Lopes+2020 Units	% of Equator/km ² (Surface Area)	Spectral Units	Coverage (% of GeoUnit)	Coverage (km ²)
Plains	47.30% 1.97x10 ⁷ km ²	HP1	26.5%	5.22x10 ⁶
		HP2	17.2%	3.39x10 ⁶
		MP4	10.5%	2.07x10 ⁶
		D1	8%	1.58x10 ⁶
		TP4	7.7%	1.52x10 ⁶
Dunes	34.3% 1.43x10 ⁷ km ²	D1	48.9%	6.99x10 ⁶
		D2	25.4%	3.6x10 ⁶
Hummock	17.10% 7.11x10 ⁶ km ²	HP2	30.5%	2.17x10 ⁶
		HP1	19.1%	1.36x10 ⁶
		H2	12.2%	8.67x10 ⁵
		MP4	9.1%	6.47x10 ⁵
Craters	0.80% 3.22x10 ⁵ km ²	MP2	15.2%	4.89x10 ⁴
		H2	14%	4.51x10 ⁴
		D1	13.6%	4.38x10 ⁴
		MP4	10.9%	3.51x10 ⁴
		HP2	8.6%	2.77x10 ⁴
		MP1	8.1%	2.61x10 ⁴
Lakes (Dry)	0.50% 1.93x10 ⁵ km ²	TP4	52.7%	1.02x10 ⁵
		HP1	13.7%	2.64x10 ⁴
		MP4	10.6%	2.05x10 ⁴
Labyrinth	0.10% 4.67x10 ⁴ km ²	HP1	43.4%	2.03x10 ⁴
		H1	19.7%	9200
		MP4	7.7%	3600

Table 4: Areal distribution of spectral units amongst the six geomorphologic units from Lopes et al 2020. The table shows the spectral units which account for at least one standard deviation of the total coverage of the geomorphologic unit.

The spectrum and morphology of the dunes however, is closely related. We see in Figure 31 that Units **D1** and **D2** are noticeably isolated from the other spectral units. This is supported by Table 4, where we see that the dunes are the only self consistent unit, where the majority of the coverage is accounted for by the spectral units found mostly in the dunes. This indicates a unique relationship between the spectra and the morphology of the dunes, not shared by any other spectral units or geomorphologic units. The fact that the dunes are spectrally distinct from other

morphologies (e.g., hummocks and/or plains) suggests that they are not simply the direct erosional remnants of those morphologies and that dune material is further processed during its evolution.

We note in Table 4 that **MP4** is found in significant quantities in all of the geomorphologic features, save for the dunes. This is the only spectral unit found in significant quantities in all the units, though its areal coverage is only the 5th largest. We also see in Table 2 that **MP4** is the most spectrally distinct unit in comparison to the dunes, and in Figure 31B that **MP4** has essentially no presence in the dunes (72% plains, 23% hummock, 5% dunes). **MP4** may therefore be an example of plains uncontaminated by any dunes. If **MP4** is topographically high, then this could indicate a limit to the mobility of the dunes. If **MP4** is particularly young, as we might expect given its association with craters, then this could indicate the age and mobility of the dunes.

D2, **VDB**, and **MP1** correlate with spectrally distinct areas attributed to water-ice [Griffith et al. 2019]. In Griffith et al. 2019, the authors point to the observation that the margins between high bright terrain and dunes, aside from the Sotra-to-Aaru strip, do not reveal water-ice. By associating the Sotra-to-Aaru strip and Menrva with **D2**, **VDB**, and **MP1**, we observe that the materials associated with the “ice corridor” are more expansive and specifically occurs in more margins between high bright terrain and dunes. The increase in areal coverage suggests that the subsurface layers across the equator are more homogeneous than previously proposed in Griffith et al. 2019. The asymmetric distribution of these units around Quivira also challenges this proposition as the north and south sides of Quivira are only separated by about 5° latitude or about 225km. Furthermore we have no reason to expect a radically different topography one the north vs south side of Quivira, suggesting that the discrepancy is not due to topographic differences. Based on our results we suggest that the subsurface layers are mostly homogeneous, and rather it is the degree of dune coverage which affects the perceived composition. The discrepancy in dune

coverage could be due to preferential wind patterns, where at least one mode is known to come from the southwest (Ewing et al. 2014).

We see in Table 2 that of the 16 units, two pairs of units have a low degree of spectral separability as determined by the intersection of the spectral hyperellipsoids; these being **D1** and **D2**, and **HP1** and **HP2**. From this we can infer that roughly 14 to 16 spectral units is an appropriate minimum decomposition of Titan's equatorial spectra. We can see that these same four units are the most spectrally distinct between the groups (i.e. the dunes are very spectrally distinct from the plains). The areal coverages of **D1**, **D2**, **HP1**, and **HP2**, are 22%, 12%, 14%, and 16% of the equatorial surface area, respectively. This means that, spectrally, Titan's equator is about one third dunes, one third undifferentiated plains, while the remaining third is composed of the 12 most spectrally distinct units. We propose that this reflects the gross structure of the equator where the hummocky plains form the Titanian bedrock, the dunes sit atop the bedrock and are sourced exclusively from fallout, and the spectrally diverse terrain represents areas of localized compositional changes. We propose that **HP1** and **HP2** can be spectrally similar while covering a large range of morphologies as the bedrock is mechanically modified by impacts and erosion. A large portion of the spectrally diverse terrain is likely represented by areas of variable dune coverage as we transition between units. The remaining spectrally diverse terrain is where we might expect to find more dynamic processes such as drainage networks, cryovolcanic activity, and chemical processing.

From the pattern of connections in Figure 35, and the placement of the nodes in Figure 31B, we notice a symmetry among the ten of the plains units above the .5 line in Figure 31B. Each of these units has a counterpart which appears in the same configuration to the other units; the pair combinations are **MP1&TP1**, **MP3&TP2**, **MP2&TP4**, **MP4&TP3**, **HP1&HP2**. In the table of

Figure 31C, we see that these counterparts have very similar coverage. In Figure 31B we see that these counterpart units share a similar distribution amongst the geomorphologic units. In Figure 35 we see that the counterparts have a similar average brightness. We also see that sequences between pairs of counter parts are nearly identical (i.e. **MP1 → MP3/MP2** and **TP1 → TP2/TP3**), with the major deviation being the paths to the hummock units. This could imply that there are distinct compositions associated with the same morphologies, which would support the argument in Griffith et al. 2019 of the presence of subsurface layers with variable compositions across Titan’s equator.

4.2. Interpretation of the Spectral Gradient

The gradient of the spectra of our equirectangular maps (Figure 29) describes the change in spectra from one discrete space (25km²) to another. We compare the spectral gradient of the surface with the five delta-spectra to understand the gross changes across the surface (Figure 34A). By then comparing the five delta-spectra to the USGS spectral library we can begin to investigate how the composition of the surface changes across the equator.

Blue: Of the five delta-spectra, the “blue” delta-spectrum is the most consistent with H₂O-Ice at 77K (Table 2). The “blue” delta-spectrum being similar with water-ice is consistent with the identification of the “ice-corridor” and the “VIMS dark-blue” features both being water-ice. From Figure 34B, we see that the “blue” delta-spectrum is equally distributed across both plains and dunes and acts as transitions between the two.

The correlation between the “blue” delta-spectrum patches and the spectral units associated with the ice corridor may indicate exposure of water-ice through the expansion of interdunes. It could also indicate that the plains are eroding into the dunes and the erosion products are mostly water-ice, although observational evidence such as microwave radiometry suggests the plains are

predominantly organic in composition. While the leading theory holds that the hummocks are eroding into the dunes, we see the most contiguous compositional change between the dunes and the plains in the forms of the “blue” and “black” delta-spectrum (Figure 34B). An issue with this explanation is that we see an asymmetric distribution of the blue compositional units across narrow terrain such as Quivara. This would imply a preferential southern erosion from Quivara to the dunes.

The interdune explanation does not explain the “blue” transition from the Tui-like plains units into the hummocky plains. This implies that the changes similar to the “blue” delta-spectrum are consistent with a compositional change rather than a change in exposure of underlying bedrock. One explanation for this is that the Tui and Menrva-like plains are compositionally similar to one another and compositionally distinct from the hummocky plains. Given their association with the dunes, the Menrva-like plains may seem compositionally distinct due to the presence of dunes and interdunes.

Black: Change in spectra via the “black” delta spectra are the most common. As variance in albedo is often the first principal component in any spectral PCA, this lends evidence that the “black” delta-spectrum may be indicative of albedo change. Patches of the “black” delta spectra make up the majority of transitions between the dunes and the plains. These are those areas not associated with the ice-corridor but rather the Tui-like plains.

Of the top 3 compositional comparison candidates in Table 3, we note that phenylacetylene (C_8H_6) and indole (C_8H_7N) are composed of a benzene ring while phenylacetylene and propyne (C_3H_4) are alkynes. From this we can assume that the “black” delta-spectrum is some change in line with hydrocarbons, be it compositional, albedo, or some other photometric property.

Green: The “green” delta spectra is unlike the other four. It is the only one with a significant negative component, it is the only one that is smooth, and it has the lowest variance. The “green” delta-spectrum has a very steep short wavelength component, increasing in brightness as it moves redward. Past this steep slope, we see that the spectrum has a smooth almost exponential decay, from a peak at $\sim 2 \mu\text{m}$ to a minimum at $5 \mu\text{m}$. A similar spectral shape is seen in the stratosphere in areas of localized increased haze abundance [Kutsop et al. 2022].

In Figure 34B, we see that the distribution of “green” delta-spectra is unique in comparison to the other four. Unlike the other four there are no areas of large contiguous patches (like the “blue”, “black” and “yellow” delta-spectrum) nor is there a large obvious area of many small patches (like the “red” delta spectra). Instead the “green” delta spectra seems to be homogeneously distributed across the surface. This is supported by the ternary diagram where we see that the “green” delta-spectrum is the uniformly distributed of the five delta-spectra (51% plains, 29% dunes, 20% hummocks). In Figure 35 we see that the “green” delta spectra is limited to transitions involving plains and hummocks (**VDB** \rightarrow **PHI**, **MP2** \rightarrow **H2**, and **HP1** \rightarrow **HP2**). From topographic models of Titan, we see that there is roughly one kilometer of relief from the lowest to the highest features [Lorenz et al. 2013; Corlies et al. 2017]. Hummocks by definition are associated with hills and mountains, making them topographic deviations of increased elevation amongst the surrounding area. We propose, given its resemblance to haze, its spatial distribution, and its associated with hummocks and plains, that the “green” delta spectra is associated with change in haze abundance or characteristics. One explanation for this could be the difference in altitude. In this scenario the higher altitude exposes the surface to a lower density of haze, and the sudden transition (given the nature of hummocks) produces a noticeable change in composition. Alternatively, the transition from the plains to the hummocks may produce a sharp deviation in the

prevailing wind patterns, thereby lofting recently deposited haze and increasing the haze abundance in the local area.

Red: The “red” delta-spectrum, like the “green”, is quite unique in comparison with the other four. The spectrum simultaneously has the steepest blue slope and red slope. Of the five delta-spectras it shows the largest increase in reflectivity at 5 μm . The “red” delta-spectrum seems almost the inverse or counterpart of the “green” delta spectra. Given its singular association with the previously unnamed Kasure Undae, which is a unique morphologic feature at the equator, we can assume that the “red” delta-spectrum is morphologically driven.

Yellow: The largest patches of contiguous “yellow” delta-spectrum are spatially correlated with Tui and Hotei Regio. These regions have been proposed as possible cryovolcanic sites [Barnes et al. 2006; Nelson et al. 2009a; Wall et al. 2009; Lopes et al. 2013] and paleolake beds covered in evaporitic deposits [Moore and Howard 2010; Barnes et al. 2011; MacKenzie et al. 2016]. Simulations show that butane and acetylene are good candidates for species that could compose the surface of evaporites [Cordier et al. 2016]. This is exactly in line with our comparison to the USGS spectral library which shows the “yellow” delta-spectrum most closely resembles butane frost at 78K. This strongly supports the interpretation that Tui and Hotei Regio have at one point been a lacustrine feature which no longer exists and has left behind evaporitic material. If true, then the “yellow” delta-spectrum can be used diagnostically to identify other paleolake features.

The “yellow” delta-spectrum being associated with evaporitic material and spatially isolated to gradients within the plains could be significant in interpreting the evolution of Titan’s plains. One possibility is that in Titan’s distant past, liquid could have been far more prevalent, even approaching the point of global coverage [Lunine et al. 1983]. In such a scenario, as the ocean

receded the entire surface could become covered in a thin layer of butane evaporites. As time progresses many areas are modified chemically or covered by dunes, but some areas maintain the veneer of the ancient evaporites. Another explanation could be that evaporitic deposition occurs more readily and with less starting fluid than is currently predicted. In this scenario, small pools of liquid form in the plains which rapidly recede and leave behind a thin veneer, like hard water stains on a countertop produced by even a drop of municipal water left to evaporate. Such pools do not form so readily in the dunes or hummocks where we might expect higher porosity and steeper slopes respectively. Several other features like virgae and craters account for the remaining large patches of “yellow” delta-spectrum. This could indicate that these virgae and craters were once home to lakes and are now covered in evaporite material.

5. Conclusion

In this work:

1. We developed image and atmospheric corrections which make short-and-mid-wavelength VIMS observations available for spatial analysis. We have validated our dataset by reproducing the results from Griffith et al. 2019, which use higher heritage techniques. We propose that the “ice corridor” identified by Griffith et al. 2019 is more expansive than previously suggested. This expansion then challenges the proposition made in Griffith et al.. 2019 that the narrow expanse of the ice corridor is indicative of variable composition in Titan’s subsurface layer.
2. We used PCA and k -means clustering to analyze Titan equatorial spectra in 32 dimensions. We find that roughly 99.5% of the spectral variance of the equator can be explained by breaking up the surface into about 16 spectrally distinct units. Further analysis using the hyper-ellipsoids shows that the equator could be broken into as few as 14 spectral units.

3. We analyzed the distribution of spectral units and identified common spatial sequences that are found across the equator. We also find that, as expected, there are some strong correlations between spectra and geomorphology, which likely indicates a link between composition and process. This is particularly true for the dunes. We also find that many spectral units transcend geomorphologic boundaries suggesting that we are observing some form of sediment transport moving material between units with potentially dissimilar compositions or morphology. This could include such scenarios as aerosol being deposited across a wide range of the surface, temporary lakes drying and leaving behind fresh evaporites, or dunes encroaching on plains at different rates dependent on prevailing wind patterns and local topography.
4. We identified which spectral units frequently share a boundary. We then determined the average change in spectra between these pairs of units. We used PCA to determine that the changes in spectra at geomorphic boundaries across the equator can be characterized by five delta-spectra. We then used *k*-means clustering to identify these five-delta spectra. We then found the spectral gradient of the surface across all 32 wavelengths, and then used spectral angle mapping to identify which areas of the spectral gradient most closely resemble the five delta-spectra.
5. We compare the delta-spectra to the USGS spectral library of “liquids” and “organic compounds”. Three of the five delta-spectras we propose an interpretation for in our analysis; the “blue”, “green”, and “yellow”. The “red” and “black” spectra, while compelling, require further analysis to comprehend their significance. We find that “blue” delta spectra, which is spatially correlated with the “ice corridor”, is spectrally similar to water-ice (spectral angle of $\sim 30^\circ$ (Table 2)). We note, however, that there is a closer match

between the “blue” delta-spectrum and acetylene ($\sim 15^\circ$). This result challenges the assertion that there are expanses of relatively pure water-ice at Titan’s equatorial latitudes. The “green” delta-spectrum has a shape reminiscent of increased haze and is homogeneously distributed across all geomorphologic features. The “yellow” delta-spectrum maps spatially to Hotei and Tui Regio, and is spectrally similar to butane frost and shows the largest change at 5 microns. This supports conclusions made by others that the Regios are potentially paleolakes with large expanses of 5-micron-bright evaporite material.

Chapter 5: Summary and Future Work

Summary

In this dissertation I have provided new insights into Titan and Pluto.

On Pluto, I utilized observation from the New Horizons spacecraft to generate multispectral phase curves of Pluto's atmosphere at discrete altitudes. From the phase curves I was able to constrain the size, particle size distribution, and fractal dimension of Pluto's haze. By combining this information with altitude and information on the composition and temperature of the atmosphere, I was able to draw conclusions about how Pluto's haze develops.

Like Pluto, Titan has organic haze produced by photolysis and composed of fractal aggregates. The distribution of this haze is determined by Titan's atmospheric circulation. Using Cassini observations, I was able to identify and track stratospheric haze bands on Titan over the course of half a Titan year. The occurrence, presence, morphology, and location of these bands were indicative of changes in Titan's stratospheric circulation. From this information I was able to provide evidence to support certain general circulation models and highlight the seasonal transport of haze between the hemispheres.

This haze eventually settles out of the atmosphere to cover the surface. The distribution patterns produced by the changes in circulation dictate the location and abundance of haze on the surface. By investigating the spectral diversity of the surface using visual and infrared observations, I am able to claim that the surface of Titan is not uniformly covered in a layer of haze, at least one not more than a few microns thick. Instead I find that Titan's surface, or at least its equator, is spectrally diverse and that this spectral diversity is closely linked to morphology. By investigating the patterns of spectral diverse terrain, determine the change in spectra between terrain units, and comparing the patterns to morphology and abundance, I am able to draw

conclusions about the evolution of Titan's equator.

The single conclusion which can be drawn from these insights is that icy-worlds are complex systems where, for example, photometric processes in the stratosphere affect the surface composition and structure which affects circulation in the troposphere which affects the distribution of stratospheric products, ad nauseam. To understand icy-worlds requires multidisciplinary efforts unique in astronomy and most closely related to the efforts of Earth science. The key difference between Earth and planetary science, is that we will never (at least not in my lifetime or even my grandkids) be able to explore the surface or atmospheres of these worlds with the intimacy that we can Earth. Compare for example the potential of a handful of rovers or even piloted space missions, to the efforts of tens to hundreds of thousands of geologists, who can stand in a waders and randomly pick up rocks to determine the sediment transport of a stream on an island in the middle of the Atlantic. This is why I chose to focus on the spectrophotometric properties of the icy worlds. We must utilize our toolsets to the maximum, and extract every bit of information from scattered light of these distant worlds.

Future Work

As I alluded to in my introduction, this thesis constitutes the end of one journey and the beginning of grand adventure. The datasets that I have cultivated will bear fruit for me, my mentees, and the planetary science community for the next decade. From the first harvest, will be several projects directed related to the work I have presented in this dissertation.

First, I am currently investigating the spectral separability at mid latitudes (-60N to -30N and 30N to 60N) and at the poles (-90N to -60 and 60 to 90). Through these efforts I will investigate and expound upon the spectral differences between the northern and southern variants of terrain, and between the equator, mid latitudes and poles. Further work is required at the equator to explain

several interesting patterns we observe. This includes: Why are most of the bluer spectral units, as shown in Figure 31A, located on the trailing and leading hemispheres between -120 and -60 and 60 to 120? Why is there a preferential distribution of **D1** → **W** → **MP4** on the southern side of Quivira and the eastern side of Xanadu and the southeastern side of Dlimun extending through Oahu Facula and on the western edge of Belet moving eastwards towards Adiri? Conversely why do we see that the **D1** → **W** → **H1** sequence is preferentially on the western side of Xanadu, the northern side of Quivira (i.e. south side of Fensal), the southside of Aztlan? It is also not obvious as to why the Tui-like plains do not transition regularly into the hummocks. Nor is it obvious as to why the Menvra-like plains, which are associated with the “ice corridor” and “VIMS dark blue” units, transition into the hummocks. Expanding the analysis to the mid-latitudes and poles will help to determine if these observed patterns are global in extent.

Tracking the distribution and evolution of Titan’s haze is a key tool for studying Titan’s atmospheric photochemistry, dynamics, and circulation. The presence and appearance of the annuli as a function of season can be used as a tracer to understand and test hypotheses for Titan’s circulation. Additionally, the shape and position of the annuli constrain Titan’s super rotating stratosphere and its offset from the spin axis. I have recently proposed to use the Quad-camera, Wave-front-sensing, Six-wavelength-channel Speckle Interferometer (QWSSI) on the Lowell Discovery Telescope (LDT) to observe Titan’s stratosphere. The 880 nm or 1200 nm channels on the QWSSI are appropriate for observing the stratosphere and the annulus. Given the sensitivity and plate scale size of QWSSI [Clark et al 2020] I can observe Titan’s atmosphere with a scale size as small as ~60km per pixel. This is sufficient to detect the annuli and track seasonal changes in stratospheric circulation. With no orbital remote sensing platform currently planned to go to Saturn, and JWST time too precious for continuous monitoring programs, ground-based

observations will be key to tracking these features. These observations will also be highly complementary, establishing the temporal behavior on a global scale, and providing context for local in-situ observations of Titan's tropospheric circulation that will be made by the Dragonfly rotorcraft in the mid-2030's

In Chapter 2, I provided constraints from New Horizons data on the population type, abundances, and some physical properties of Pluto's aerosols. There are several objectives I would like to address to expand upon this work. First, a full phase curve from 0-180° is needed to determine the abundance of ($R_f(Int) \approx 100 - 500nm$) and break the degeneracy between a power law, bimodal, and trimodal distribution. This could be accomplished with the inclusion of images from the panchromatic filters or other instruments (i.e. LORRI) or more flyby missions, but an orbiter would provide a more comprehensive and definitive data set. Secondly, microphysical models like CARMA, will need to consider these phase curves and distributions in future work. Results from rigorous modeling will help better understand the processes that lead to a bimodal or power law distribution. Future modeling will also explore the total charge that can build up on these particles and how they pass their charge onto other aerosol or gaseous components. Finally, tests of the Tomasko et al. 2008 fractal aggregate phase function for a fractal dimension not equal to two have not been verified or reviewed. Validation of other fractal dimensions should be done to increase confidence in these results.

Appendix A. Data Processing

All the images taken are in Flexible Image Transport System (FITS) format and readable with standard FITS viewers and software libraries. [Stern & Finley 2016]. For this work, the raw data is processed into level 2 calibrated products by removing the bias and flat-field pattern to convert pixel values from raw Data Number (DN) to calibrated DN [Peterson et al. 2007]. Level 2 calibrated products were provided directly from coauthor Buratti and were produced in September of 2017. Radiometric calibration coefficients, stored as keywords in the FITS header, are used to convert raw DN to physical reflectance values. Error estimates for each pixel are calculated assuming shot noise and measured detector parameters (e.g., read noise and Poisson noise from dark current) and an error array is constructed in a new extension of the FITS file. Finally, the SOC pipeline adds a data quality extension based on both scene complexity and instrumental factors. The data quality flag is set to zero if the data are clean and a nonzero value that represents potential issues. These include defects in reference calibration files, such as dead pixels, missing data, zero value pixel, DN not linear in regime of detector, or an unidentified error [Peterson et al. 2007].

We convert from the calibrated DN to physical reflectance units by following the procedures described in C.J. Howett et al. 2017. Navigation files were generated for each image using the Jet Propulsion Laboratory Navigation and Ancillary Information Facility's SPICE system/routines [Acton et al. 2018]. The SPICE system combines kernel files containing information on the spacecraft, camera orientation, planetary ephemerides and more with keywords in each image's FITS files such as time of observation, image size, and scan rate. Using the SPICE API, we determined which pixels should be on the disk as well as characteristics of the pixels on and off the disk such as geographic coordinates, tangential altitude, and viewing geometry (i, e, θ, ψ). For pixels off the disk we also determined the viewing geometry and geographic location of the sub-tangent point.

Due to pointing and absolute timing uncertainties the location of our disks predicted by SPICE and the actual location of Pluto's disk seen in the images were shifted by 1-10 pixels in line and/or sample. The same shift was seen for both Charon and Pluto in images that observed both simultaneously, suggesting that there is no internal timing error or rotational offset. To account for these random shifts, we manually adjusted the navigation files until the disk predicted by SPICE matched with the disk in the image to within 1 pixel radii.

Appendix B. Off Disk Glow Correction

There is an instrument effect, similar to stray light seen in the Long Range Reconnaissance Imager (LORRI) [Cheng et al. 2017], which causes spurious brightness far from the limb of the disk of Pluto. This effect can be seen more than 100 pixels away from the disk, equating to more than 500 km in some images. To account for this glow, we follow a similar strategy as in Cheng et al. 2017, whereby we use the airless (i.e., presumably hazeless) body of Charon [Stern et al. 2017] to model the effect. For each observation of Charon in the time frame of our investigation (Table 1), we locate each pixel on the solid limb and find which pixels off the disk are closest to each of those limb pixels, as shown in SOM Figure 1. Around the disk we now have brightness profiles dependent on solid limb brightness and distance. The solid limb brightness, I/F_L , is taken to be the weighted average of the nearest on-disk pixels to the solid limb pixel within a radius of four pixels. These weights are determined from the Gaussian profile of the point spread function [Reuter et al. 2017]. The distances of the pixels from the solid limb, D_L , is determined by the altitude of the center of the pixel divided by the difference in altitude between the highest altitude corner of the pixel and the lowest altitude corner of the pixel. Both Pluto and Charon cast shadows at photometric longitudes, Λ , for $|\Lambda| > 90^\circ$. This means that pixels with a subtangent-point of $i > 90^\circ$, will have a LOS through the atmosphere that is only partially illuminated. To ensure we are only using pixels whose LOS is totally illuminated, we limit ourselves to those with a subtangent-point $i < 90^\circ$.

We fit the Charon off disk brightness profile to be a two-dimensional function of the form:

$$I/F_{CH} \left(D_L, I/F_L, \lambda \right) = \frac{pD_L + a_1 e^{b_1 I/F_L} + c_1 e^{d_1 I/F_L}}{D_L + a_2 e^{b_2 I/F_L} + c_2 e^{d_2 I/F_L}} \quad \text{Eq. B1}$$

Figure 3 highlights our fit to the data and provides a comparison with Pluto's off disk profile. Best-fit coefficients, and their associated errors, can be found in SOM Table 1. We find that the magnitude of the removed off-disk glow is on the order of the variability we see in I/F , constituting a substantial fraction of the observed signal.

We limit our data for generating phase curves to observation of Pluto where Pluto's weighted limb brightness, I/F_L , is within the range of Charon's I/F_L . This procedure maximizes the efficacy of our fits though our functional form of Charon's off disk profiles allows us to apply this correction to any limb brightness value. We were not able to limit the data in this way from

the Blue filter because Pluto is much brighter in the blue than Charon. We also found that variations in the geographic location of the subtangent point coincided with brightness variations at all altitudes, ranging from a factor of 2 to an order of magnitude (SOM Figure 2). To limit the variation in the brightness profiles we constrained our data to subtangent points with an incidence angle of 75-85° and in the region of 35 - 50°N latitude and 80°W – 40°E longitude (SOM Figure 3).

Phase curves were generated by binning the data into 20 km high altitude bins. This ensures that we have at least several pixels in each altitude bin, even at our lowest spatial resolution. We only use pixels that have all four corners within the defined altitude bins. We choose our upper limit to be 500 km as this is the height where photolysis of methane takes place [Gladstone et al. 2019] and below this altitude aerosol growth begins [Gladstone et al. 2019]. Due to the nature of our Mie scattering code [Mätzler; C. 2002] we must round the phase angle of each pixel to the nearest whole integer. At closest approach this results in two phase angles, at 40° and 41°, so that each of our phase curves have a total of eight points. In the figures presented herein, the I/F is presented by the median of the I/F values of the pixels within the altitude bins and at the same phase angle. For our fitting routines, however, we use a Monte Carlo simulation with at least 320 runs to draw our phase curve values from the distribution of pixels in each of the altitude and phase bins.

Negative pixel values arise from level-1 calibrations (i.e. flat field corrections and dark current subtractions), and the Charon off disk subtraction. This means that some points in our phase curves have median I/F values below zero, especially in the NIR channel which has lowest SNR of our 3 filters. We excluded these observations from our phase curves, as their inclusion interfered with our fitting routines. Values that were excluded are noted in the SOM Tables 2 and 3 in red. Recall, however, that this is for the phase curve figures, for our fitting routines we use a 320 run Monte Carlo simulation to draw our phase curve values from the distribution of pixels in each of the altitude and phase bins.

Appendix C. Error

In addition to the primary data, each FITS files contains two extensions. The first extension is the 1σ standard deviation of each pixel in DN. The second extension is the data quality flags, which contain the error array, and the data quality array for the primary data. A full explanation of the various flags and error calculation is detailed in *New Horizons SOC to Instrument Pipeline*

ICD. Throughout this work we only include pixels where the data are flagged as good [Peterson et al. 2007].

Along with the random pixel error, a 1-3% error exists in the adjustment factor required to correct the observed count rates to the predicted count rates [Howett et al. 2017]. This adjustment factor was determined through comparison of photometry with well-calibrated stars observed inflight by all 7 MVIC CCDs. To calculate error, we combine Poisson photon noise for each pixel (uncertainty from dark current and bias is negligible) with a systematic multiple offset to account for each frame’s absolute calibration error. The calibration error is approximated by a Gaussian distribution with a standard deviation of 3%.

We present the uncertainty in I/F as the bounds occurring at the 15th and 85th percentile of the pixels in each bin (SOM Table 3). The 15th and 85th percentile range is equivalent to the bounds at 1 standard deviation, σ , greater and less than the mean or median for a normal distribution. The variance in our data in a single bin is typically not normally distributed so the standard deviation is not appropriate for describing our variance. This variability in our binned data, ~25% and dependent on filter (SOM Tables 2&3), is substantially greater than the 3% propagated error above. As such we do not consider the propagated error, but we present our determination of the propagated error above for the sake of completeness.

Appendix D. Radiative Transfer

A full radiative transfer description of scattering from Pluto’s limb would include ray tracing through spherical shells and account for multiple scattering [Bourassa et al. 2008]. This takes the form of the integral

$$I(\vec{r}_0, \hat{\Omega}) = \int_{s_1}^0 J(s, \hat{\Omega}) e^{-\tau(s,0)} ds + \tilde{I}(s_1, \hat{\Omega}) e^{-\tau(s_1,0)} \quad \text{Eq. D1}$$

which specifies the radiance, I , observed at location, \vec{r}_0 , in the propagation direction specified by the unit vector, $\hat{\Omega}$, along the LOS path, s . This is the integral of the scattered source term, J , plus the radiance at the end of the path, \tilde{I} , both attenuated along the path to the observer by the optical depth, τ . \tilde{I} is total radiance (direct, single scattered, multiple scattered) from the end point of the path, which is either space or the ground (Figure 1 bottom, A & D). As none of our observation intersect the surface of Pluto or the Sun, this term is zero and will not be discussed further.

The source term from scattering is

$$J(s, \hat{\Omega}) = \beta_s(s) \int_{4\pi} I(s, \hat{\Omega}') P_{11}(s, \theta) d\Omega' \quad \text{Eq. D2}$$

β_s is the scattering coefficient, P_{11} is the scattering phase function (Eq.2) and θ is the angle formed between incident and emergent vectors specified by the unit vectors $\hat{\Omega}'$ and $\hat{\Omega}$ respectively. J is the total scattering source term where the final scattering event occurs in the atmosphere. The integral is evaluated over all solid angles as multiple scattering can have its source from any direction, including the sun (Figure 1b, B), the ground (Figure 1b, E), and from all other scatterers in the atmosphere (Figure 1b, C). Because the solar beam is the only source of light for the first order scattering, the integral over all space that is required to evaluate the source term (Eq. 5) simplifies to

$$J_1(s, \hat{\Omega}) = \beta_s(s) F_{\odot}(\hat{\Omega}_0) e^{-\tau(\text{sun}, s)} P_{11}(s, \theta) \quad \text{Eq. D3}$$

where $F_{\odot}(\hat{\Omega}_0)$ is the incident solar flux density. Thus the total contribution to the radiance at any position \vec{r}_0 from a single scattering event is

$$I_1(\vec{r}_0, \hat{\Omega}) = F_{\odot}(\hat{\Omega}_0) \int_{s_1}^0 \beta_s(s) P_{11}(s, \theta) e^{-\tau(\text{sun}, s)} e^{-\tau(s, 0)} ds \quad \text{Eq. D4}$$

Multiple scattering ($i > 1$) that has its final scattering event in the atmosphere is

$$J_i(s, \hat{\Omega}) = \beta_s(s) \int_{4\pi} I_{i-1}(s, \hat{\Omega}') P_{11}(s, \theta) d\hat{\Omega}' \quad \text{Eq. D5}$$

We can then rewrite Eq. 4 as

$$I(\vec{r}_0, \hat{\Omega}) = \int_{s_1}^0 e^{-\tau(s, 0)} \sum_{i=1}^{\infty} J_i(s, \hat{\Omega}) ds \quad \text{Eq. D6}$$

In a dense atmosphere like Earth or Titan, multiple scattering contributes significantly to the total radiance; accounting for nearly half of the observed radiance at visible wavelength in the stratosphere, with the other half coming from single scattering (Bourassa et al. 2008 figures 3 & 11). On Pluto, however, results from [Fan et al. In Prep](#) found that the upper limit of contribution from secondary scattering initiated by the ground, $J_{2\text{surf}}$ (Sun→surface→atmosphere→MVIC, Figure 1b E) accounts for less than 10% of the observed radiance at the wavelength of the three MVIC filters used herein (Figure 4). Fan et al. determined the amount of secondary scatter for incident and emergent vectors along the specular plane, at altitudes from 0-200km for all phase angles, using the equations in Hapke (1981) and assuming isotropic scatterers for the surface

materials, a monodispersed population of scatterers, and a single scattering albedo ϖ_0 of .9 [Buratti et al. 2017] for all three filters. The amount of contribution is inversely proportional to the altitude and reaches the maximum for a phase angle of 90° . For the representative phase angle of our data, at 15° , 45° and 170° , the amount of secondary scattering predicted is always one to two orders of magnitude less than the observed I/F and, in all cases, is less than or equal to the brightness variability in our phase curves, $(\sigma I/F)$. For this reason we ignore J_{2Surf} and higher order multiple scattering terms. We also ignore secondary (and multiple) scattering initiated by the atmosphere, J_{2Atm} (Sun→atmosphere→atmosphere→MVIC, Figure 1b C). We note that J_{2Surf} is maximal at $\theta = 90^\circ$ and, at this geometry, is non-negligible and cannot be neglected.

The single scattering source term in Eq. 4 is integrated along the path s as single scattering occurs at all points along the LOS. In an optically thin atmosphere like Pluto's however, the integral in Eq. 4 is largely dominated by scattering from the tangent point, reducing Eq. 4 to [Normand et al. 2013],

$$I \approx \beta_s(s_T) F_\odot (\widehat{\Omega}_0) P_{11}(s_T, \theta) \Delta s_T \quad \text{Eq. D7}$$

where s_T , is the tangent point in Pluto's atmosphere (for our purposes s_T is the altitude) and Δs_T is the tangent point path length. Accounting for all components of Pluto's atmosphere Eq. 10 becomes,

$$\begin{aligned} I/F(\lambda) = [N_{Gas}(s_T) \sigma_{Gas}(s_T) P_{11Gas}(s_T, \theta) \\ + N_{Aerosol}(s_T) \sigma_{Aerosol}(s_T) P_{11Aerosol}(s_T, \theta)] \Delta s_T \quad \text{Eq. D8} \end{aligned}$$

where λ , is the pivot wavelength of our MVIC filters, $N(s_T)$ is the particle number density at s_T in units of per volume, σ is the scattering cross section in units of area.

The particle number density for Pluto's atmosphere was described in Young et al. 2018, based on a UV solar occultation from the *New Horizons Alice* instrument to measure the abundance of N_2 , CH_4 , C_2H_2 , C_2H_4 , C_2H_6 , and haze as function of altitude. They show that abundance in Pluto's atmosphere is dominated by N_2 with $10^{15} cm^{-3}$ and CH_4 with $10^{12} cm^{-3}$ at the surface. We determined the magnitude of the scattering due to Pluto's gaseous components using these abundance altitude profiles, scattering cross section for N_2 and CH_4 from experimental work [Sneep and Ubachs 2005, Wilmouth and Sayres 2019], and the Rayleigh scattering phase function of

$$P_{11} = \frac{3}{4} (1 + \cos^2(\alpha)) \quad \text{Eq. D9}$$

We determined the magnitude at 370 nm where laboratory data for N₂ and CH₄ cross sections exists. This is 122 nm shorter than our BLUE filter pivot wavelength and according to the Rayleigh scattering intensity approximation of $I \propto 1/\lambda^4$, the intensity at 370nm is 3 times stronger than at 492nm. Even at this wavelength we find that the Rayleigh scattering at the surface (0 km) due to N₂ is $I/F \approx 10^{-3}$, while Rayleigh scattering due to CH₄ is $I/F \approx 10^{-7}$. The mean variability for the MVIC Blue filter at 0-20km for all phase angles is $\approx 10^{-2}$. Given that these values for the UV wavelength and at the surface where n is at its largest, are at most an order of magnitude lower than the variability we see the MVIC Blue Filter, we can ignore the contribution from the gaseous components. This is even more the case for the Red and NIR filters where because $I \propto 1/\lambda^4$, the contribution from the gaseous components is almost nonexistent. Therefore Eq. 11 reduces to

$$I/F(s_T, \lambda) = N_{Aerosol}(s_T) \sigma_{Aerosol}(s_T, \lambda) P_{11Aerosol}(s_T, \theta, \lambda) \Delta s_T \quad \text{Eq. D10}$$

Appendix E. Phase Function

Many analytic and numerical techniques have been developed to solve for the scattering of electromagnetic waves by arbitrary scatterers (Sharma 2018). These exact solutions, however, can be complicated to implement and may have dubious analytic value when trying to diagnose a scatterer from a phase curve, especially if the phase curve is discontinuous or incomplete.

We investigated many relevant phase functions including Mie scattering, Henyey-Greenstein's phase function, various modification of both of Mie scattering and Henyey-Greenstein that more accurately approximate real scatterers, and models that handle extreme or niche situations [Henyey & Greenstein 1941; Cornette & Shanks 1992; Liu 1994, Draine 2003; Zhao et al. 2006; BenZvi et al. 2007; Aartsen et al. 2013]. Following this exploration, we decided to use the empirical phase function described by Tomasko et al. 2008 for scattering by a fractal aggregate composed of small monomers in Titan's atmosphere. Fractal aggregation is consistent with the color images of Pluto that show strong forward scattering by a predominantly blue atmosphere [Gladstone et al. 2016]. Titan's haze seems to be composed of fractal aggregates that form as a consequence of photolysis and coagulate as they travel through Titan's atmosphere (e.g. Lavvas et al. 2013, Gladstone et al. 2016; Cheng et al. 2017; Young et al. 2018); given the similarities in atmospheric composition this suggests that Pluto's haze may be as well.

The Tomasko et al. 2008 phase function uses the fractal dimension, D_f , number of monomers per aggregate, N , the complex index of refraction as input parameters, $m_r + i m_i$, and

the monomer size parameter, X_m , given by $X_m = 2\pi r_m / \lambda$, where r_m is the spherical radius of the monomers. The tested range for these parameters can be found in Table A1 of [Tomasko et al. 2008](#). As a part of this work, we constructed a Matlab implementation of the phase function described in the appendix of [Tomasko et al. 2008](#).

The composition, given by proxy through the complex index of refraction, does not change the phase angle brightness dependence, or shape, of our modeled phase curves. It does, however, change the scattering and extinction cross sections, σ_s and σ_e , the scattering and extinction coefficient, β_s and β_e , and the particle number density for particles of a radius r , $N(r)$ (Eq. 13), which all dictate the absolute brightness of our phase curves. As such we follow the lead of other authors [[Gao et al. 2017](#); [Young et al. 2018](#)] and assume that the haze has the same composition as Titan's haze. We use the complex index of refraction for Titan's haze from [Ramirez et al. 2002](#). The wavelength range covered by [Ramirez et al. 2002](#) ends at 200 nm. To use the abundance measurements made by the Alice instruments UV solar occultations (Section 3.3. Size distribution), it was necessary to linearly extrapolate the complex index of refraction from [Ramirez et al. 2002](#) to 165nm. We found the real and imaginary components of the Titan aerosol at 165nm to be $m_r = 1.6839$ and $m_i = 0.0166$.

Appendix F: VIMS-Vis Destriping

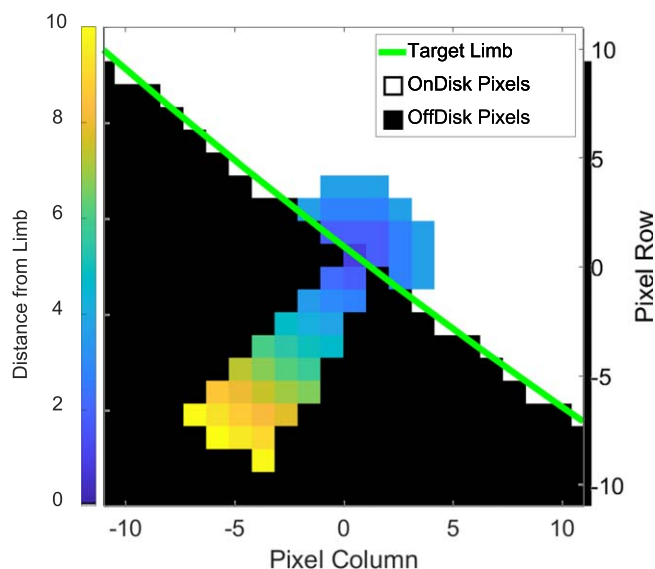
To remove the striping, we reconstruct what the offsets introduced by the readout electronics would have been. We first sample each line of data which runs perpendicular to the striping on the sample (Figure A.1). We apply a smoothing spline based on the LOESS (Appendix G) method to each line. We use a second degree polynomial to model the local regression and a span of $2/3$. The span is the fraction of the total number of data points used for calculating the smoothed value. We subtract the smoothed spline from the data and approximate the spikiness of the data from the stripes in the lines (Figure A.2). Stitching the lines back together, with each of their respective smoothed curves removed produces an approximation of the stripes (Figure A.3). We know that the offset applied is constant for each sample. We approximate this constant value by taking the median of data along the line dimension (Figure A.4). This gives us a single line of data, which we then expand to the original image size, producing a mask for the initial offset (Figure A.5). To destripe the data we subtract Figure A.5 from Figure A.1 to produce a VIMS image with greatly improved clarity.

Appendix G: Manifold Correction

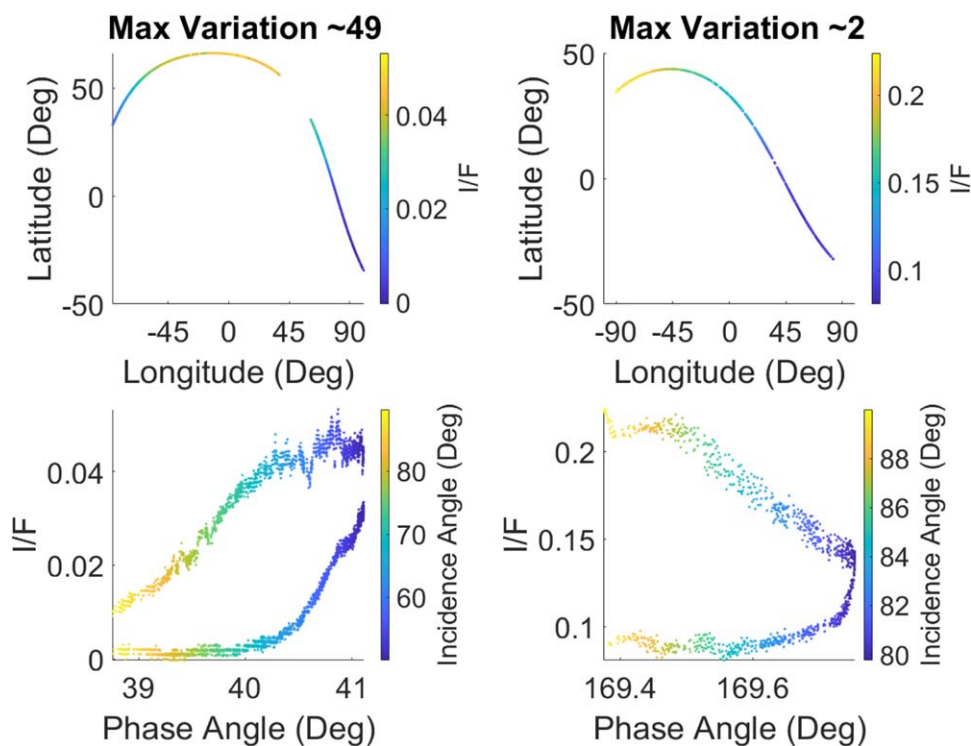
The goal of the manifold technique is to remove global scale brightness trends from our observations. We want to remove effects due to illumination geometry and scattering from the haze while preserving compositional and physical properties like grain size and roughness. The predicted brightness due to these effects resembles a curvy surface, which we call a “manifold”. To remove effects like viewing geometry and scattering from the VIMS data we subtract the manifold from the observations. This technique is analogous to flat-field corrections which are ubiquitous throughout astronomy.

First, we produce sub-pixel style super resolution mosaics and project them into an orthographic view. We have to produce a manifold for each channel in VIMS because the amount and type of scattering in the atmosphere varies with wavelength. For each channel we randomly sample one hundred pixels from the mosaic. We fit a locally estimated scatterplot smoothing function (LOESS) to the data points where the independent variables are the row and column location of the pixel in the mosaic, and the dependent variable is the pixel brightness. The LOESS method fits a low-degree polynomial to a subset of the data at each point in the range of the data set. The polynomial is fitted using weighted least squares, giving more weight to points near the point whose response is being estimated and less weight to points further away. [[Savitzky & Golay 1964](#); [Cleveland 1979](#)]. We then repeat this process one hundred times, each time selecting one hundred random pixels from the mosaic, for each channel. This produces one hundred manifolds which we take the average of to produce the final manifold.

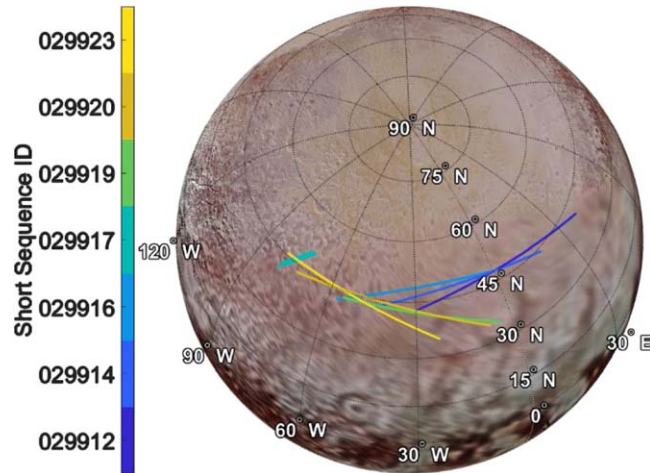
By sampling only one hundred pixels from our mosaic (which are at least 400,000 pixels in total), we nullify all small scale variations in data, like those caused by surface composition. The randomly sampled pixels will be separated by about 730km on average, which is twice as wide as Menrva Crater, one of the largest features on Titan’s surface. Doing this one hundred times through bootstrapping, provides a good estimate of the underlying parameters for the brightness trend on Titan. This technique is flexible in many ways including in the number of data points sampled, how many Monte-Carlo runs are made, the wavelengths corrected, and the polynomial degree and weighting of the LOESS function.



Appx Figure 1. An example of how the limb scatter profiles are acquired. The colored pixels off the disk all share the same nearest-limb pixel. These produce the limb scatter profiles and phase curves. The colored pixels on the disk are those that fall within a 3 pixel radius of the limb pixel. These and the limb pixel define the weighted average limb brightness.



Appx Figure 2. Variation in I/F , 5 pixel radii away from the limb of Pluto. The maximum brightness variation for each MVIC sequence is labeled at the top. (Left) Pixels taken from MVIC sequence 0299178092 (See Table 1). (Right) Pixels taken from MVIC sequence 0299193157 (See Table 1). (Top) Variation in brightness as a function of geographic location of the sub-tangent point. (Bottom) Variation in brightness as a function of viewing geometry.



Appx Figure 3. Location of sub-tangent points for our limb scatter profiles. The orthographic view is centered on the middle latitude and longitude of all the sub-tangent points, at 60.45°N and -32.12°E .

Appx Table 1

Best-Fit Coefficients for the Charon Off-disk Profile, Equation (B1), and the Associated 95% Confidence Bounds

MVIC Red		95% Confidence Bounds		MVIC Blue		95% Confidence Bounds	
Coefficients	Best Fit	Lower	Upper	Coefficients	Best Fit	Lower	Upper
p	0.00137	0.001353	0.001387	p	0.005522	0.00534	0.005704
a ₁	-0.9675	-2563	2561	a ₁	0.7243	-1.62E + 04	1.62E + 04
b ₁	-3.886	-567.5	559.7	b ₁	0.3689	-265.6	266.3
c ₁	1.02	-2561	2563	c ₁	-0.6917	-1.62E + 04	1.62E + 04
d ₁	-3.886	-538.6	530.8	d ₁	0.3692	-278	278.7
a ₂	10.46	-1.99E + 05	1.99E + 05	a ₂	1.76E-05	-3.18E-06	3.84E-05
b ₂	-18.98	-79.25	41.3	b ₂	27.19	23.37	31.01
c ₂	-4.794	-1.99E + 05	1.99E + 05	c ₂	1.934	1.784	2.084
d ₂	-18.97	-144.8	106.8	d ₂	-10.84	-11.24	-10.43
MVIC NIR		95% Confidence Bounds		MVIC CH ₄		95% Confidence Bounds	
Coefficients	Best Fit	Lower	Upper	Coefficients	Best Fit	Lower	Upper
p	-0.00096	-0.00097	-0.00095	p	-0.00181	-0.00183	-0.00178
a ₁	0.08538	0.08469	0.08607	a ₁	0.7961	-6695	6697
b ₁	-17.66	-17.76	-17.56	b ₁	-3.81	-141.6	134
c ₁	0.004379	0.004346	0.004411	c ₁	-0.6812	-6697	6695
d ₁	9.286	9.257	9.315	d ₁	-3.81	-165	157.3
a ₂	17.16	17.02	17.3	a ₂	5.861	5.82	5.902
b ₂	-34	-34.07	-33.93	b ₂	-13.33	-13.37	-13.29
c ₂	0.05112	0.05081	0.05144	c ₂	-4.56E-07	-9.13E-07	3.19E-10
d ₂	6.595	6.57	6.62	d ₂	36.83	33.33	40.33

		I/F, Uncorrected							I/F, Charon Corrected										
		Phase Angle (deg)							Phase Angle (deg)										
		16	17	18	39	40	166	167	170			16	17	18	39	40	166	167	170
Altitude (km)	MVIC Red	0-20	0.031333	0.037618	0.030677	0.020273	0.023096	0.133667	0.169932	0.207051	0-20	0.005927	0.019227	0.0186	0.016838	0.019815	0.107607	0.146532	0.192724
		20-40	0.023227	0.022238	0.021983	0.014456	0.015425	0.108562	0.128875	0.141864	20-40	0.009039	0.014639	0.015524	0.011914	0.013447	0.091753	0.119215	0.137186
		40-60	0.020244	0.018331	0.018139	0.009678	0.011576	0.076805	0.088621	0.097465	40-60	0.008997	0.012396	0.013358	0.007913	0.009697	0.064617	0.082444	0.094017
		60-80	0.017391	0.014503	0.015281	0.007738	0.008704	0.053827	0.060578	0.069281	60-80	0.008829	0.01044	0.011468	0.006	0.007049	0.044304	0.055607	0.066536
		80-100	0.016389	0.012557	0.013381	0.006772	0.006775	0.037447	0.043239	0.046753	80-100	0.008904	0.008924	0.010383	0.00509	0.00519	0.029606	0.039037	0.044273
		100-120	0.014473	0.011572	0.012402	0.005826	0.00581	0.025936	0.028891	0.031197	100-120	0.008341	0.007851	0.009339	0.004225	0.004246	0.019005	0.025303	0.028924
		120-140	0.013512	0.009669	0.010531	0.004864	0.005807	0.017301	0.019213	0.020522	120-140	0.008157	0.006814	0.008231	0.003314	0.004241	0.011139	0.015887	0.018458
		140-160	0.012547	0.008705	0.009583	0.003909	0.004863	0.011537	0.012549	0.013663	140-160	0.007608	0.006099	0.007452	0.00242	0.00334	0.005967	0.009628	0.011675
		160-180	0.011598	0.0082	0.009549	0.0039	0.003899	0.007678	0.007696	0.00976	160-180	0.007296	0.005569	0.007058	0.002378	0.002418	0.002383	0.004877	0.007845
		180-200	0.010635	0.007732	8.60E-03	0.002935	3.90E-03	4.80E-03	0.005748	0.007806	180-200	0.006987	0.005204	6.52E-03	0.001445	2.40E-03	1.67E-05	0.002929	0.005934
		200-220	0.010617	0.006772	0.008579	0.002938	0.002933	0.002887	0.003841	0.006827	200-220	0.006475	0.004499	0.006258	0.001456	0.001457	-0.00147	0.001252	0.005
		220-240	0.009663	0.006765	0.007647	0.002943	0.002938	0.001925	0.002885	0.006819	220-240	0.006612	0.004441	0.005664	0.00147	0.001473	-0.00212	0.000432	0.005014
		240-260	0.009649	0.005806	0.006703	0.002943	0.002941	0.001923	0.00288	0.005861	240-260	0.00586	0.003682	0.004835	0.001476	0.001487	-0.00197	0.000487	0.00413
		260-280	0.008689	0.005799	0.006691	0.002938	0.002943	0.001921	0.002879	0.005858	260-280	0.005317	0.003666	0.004815	0.001466	0.001488	-0.0019	0.000553	0.00414
		280-300	0.008685	0.005793	0.006684	0.001968	0.002943	0.001921	0.002878	0.005856	280-300	0.005238	0.003656	0.004662	0.000517	0.001488	-0.00176	0.000608	0.004157
		300-320	0.007728	0.004845	0.005742	0.001971	0.001966	0.000963	0.002877	0.005857	300-320	0.004907	0.002878	0.003962	0.000523	0.000528	-0.00236	0.000658	0.004178
		320-340	0.00772	0.00483	0.005736	0.001977	0.001968	0.000962	0.002875	0.005856	320-340	0.004573	0.002854	0.003958	0.000535	0.00053	-0.00228	0.000692	0.004191
	340-360	0.007719	0.00483	0.005731	0.001982	0.001974	0.000963	0.00287	0.005856	340-360	0.004484	0.002846	0.003832	0.000545	0.000545	-0.00222	0.000719	0.004207	
	360-380	0.00676	0.004828	0.004787	0.001988	0.00198	0.000963	0.00287	0.005855	360-380	0.003925	0.002826	0.003081	0.000554	0.000552	-0.00211	0.000758	0.00422	
	380-400	0.006754	3.87E-03	4.78E-03	0.001989	0.001987	0.000963	1.93E-03	0.005854	380-400	0.00372	2.01E-03	3.09E-03	0.000555	0.000563	-0.00203	-6.19E-05	0.004233	
	400-420	0.006754	3.87E-03	4.78E-03	0.001989	0.001989	0.000963	1.93E-03	0.005854	400-420	0.003775	2.00E-03	3.09E-03	-0.00042	0.000564	-0.00196	-3.33E-05	0.004245	
	420-440	0.005794	3.86E-03	4.78E-03	0.001988	0.001988	0.000962	1.93E-03	0.005855	420-440	0.003157	2.00E-03	3.00E-03	-0.0004	-0.00041	-0.00191	-1.42E-05	0.004258	
	440-460	0.005791	3.86E-03	4.78E-03	0.002014	0.002014	0.000963	1.92E-03	0.005856	440-460	0.003052	2.00E-03	2.19E-03	0.000586	-0.00042	-0.00181	7.26E-06	0.004267	
	460-480	0.005789	3.86E-03	4.78E-03	0.002012	0.002012	0.000963	1.92E-03	0.005856	460-480	0.003008	2.00E-03	2.19E-03	0.000591	0.000594	-0.00176	3.00E-05	0.004278	
	480-500	0.005789	2.91E-03	3.82E-03	0.002008	0.002015	0.000963	1.92E-03	0.005857	480-500	0.003055	1.16E-03	2.19E-03	0.000585	0.000594	-0.00172	4.70E-05	0.004286	
Altitude (km)	MVIC Blue	0-20	0.05072	0.055431	0.053491	0.040917	0.044922	0.312613	0.389651	0.525741	0-20	0.010961	0.022631	0.028331	0.030809	0.035956	0.2638	0.361231	0.525643
		20-40	0.038328	0.034375	0.03719	0.024728	0.028749	0.258928	0.298416	0.364365	20-40	0.019047	0.018883	0.025253	0.018376	0.022347	0.233165	0.283356	0.364229
		40-60	0.033814	0.029848	0.032832	0.016548	0.020547	0.187577	0.210983	0.256141	40-60	0.017848	0.015626	0.022311	0.010552	0.010455	0.16847	0.199371	0.255988
		60-80	0.029631	0.025528	0.028749	0.016447	0.016458	0.133621	0.146196	0.185511	60-80	0.017121	0.013235	0.019772	0.010507	0.010521	0.118328	0.135612	0.185048
		80-100	0.025552	0.02134	0.024689	0.012415	0.012411	0.097479	0.104131	0.125659	80-100	0.014906	0.011271	0.016559	0.00659	0.006579	0.08411	0.095228	0.125188
		100-120	0.025399	0.017097	0.020465	0.008309	0.008329	0.067687	0.070648	0.08649	100-120	0.015012	0.008248	0.01307	0.002547	0.00258	0.055749	0.062351	0.085859
		120-140	0.025343	0.017074	0.020576	0.004178	0.008301	0.046673	0.049507	0.056393	120-140	0.015228	0.00836	0.013247	-0.00153	0.00256	0.035685	0.041366	0.055917
		140-160	0.025244	0.012846	0.016575	0.004168	0.004172	0.033741	0.033029	0.038876	140-160	0.015178	0.005033	0.009602	-0.00153	-0.00153	0.02325	0.025268	0.03806
		160-180	0.021126	0.012816	0.016481	0.004166	0.004165	0.021157	0.020675	0.025963	160-180	0.012331	0.005027	0.009608	-0.00151	-0.00152	0.011313	0.013182	0.0253
		180-200	0.021091	0.012776	0.016456	0.004186	0.004163	0.01276	0.012442	0.02155	180-200	0.012414	0.00505	0.00971	-0.00148	-0.00151	0.003785	0.005223	0.020275
		200-220	0.021097	0.01279	0.016382	0.00419	0.004181	0.008496	0.008285	0.012759	200-220	0.012684	0.005156	0.009727	-0.00146	-0.00147	-0.00035	0.001189	0.016102
		220-240	0.021037	0.008564	0.0124	0.004199	0.004188	0.008443	0.004172	0.013003	220-240	0.012612	0.001489	0.005891	-0.00144	-0.00146	-0.00031	-0.00263	0.012524
		240-260	0.016925	0.008558	0.012384	0	0.004199	0.004257	0.004149	0.012988	240-260	0.009241	0.001528	0.005935	-0.00562	-0.00144	-0.00394	-0.00266	0.012221
		260-280	0.016931	0.008563	0.012358	0	0.004258	0.004148	0.012975	0.012975	260-280	0.009351	0.001598	0.005974	-0.00562	-0.00562	-0.008	-0.00259	0.012079
		280-300	0.01692	0.008558	0.012343	0.004244	0	0.004253	0.004144	0.012956	280-300	0.00932	0.00164	0.006008	-0.00137	-0.00562	-0.00373	-0.00251	0.011843
		300-320	0.016886	0.008558	0.012293	0.004263	0.004215	0.00425	0.004142	0.012954	300-320	0.009408	0.001696	0.006009	-0.00135	-0.0014	-0.00357	-0.00245	0.011746
		320-340	0.016873	0.008549	0.008302	0.004259	0.00426	0.00425	0.00414	0.012949	320-340	0.00948	0.001741	0.002103	-0.00134	-0.00135	-0.00335	-0.0024	0.011502
	340-360	0.016861	0.008538	0.008278	0	0.004262	0.00424	0.00414	0.012938	340-360	0.00941	0.001778	0.002108	-0.0056	-0.00134	-0.00339	-0.00234	0.011273	
	360-380	0.01276	0.004316	0.008271	0	0.004242	0.004132	0.012937	0.012937	360-380	0.005899	-0.002	0.002126	-0.00559	-0.0056	-0.00325	-0.0024	0.011172	
	380-400	0.012743	0.004294	0.008271	0	0.004242	0.00413	0.01292	0.01292	380-400	0.005913	-0.0021	0.002153	-0.00559	-0.00559	-0.00317	-0.00226	0.010984	
	400-420	0.012716	0.00429	0.008261	0	0.004244	0.004128	0.012926	0.012926	400-420	0.005852	-0.0021	0.002166	-0.00559	-0.00559	-0.00306	-0.00222	0.010936	
	420-440	0.012706	0.00429	0.008256	0	0.004248	0.004126	0.012924	0.012924	420-440	0.005836	-0.0021	0.002186	-0.00558	-0.00559	-0.00296			

		//F 15 th Percentile, Charon Corrected							//F, Charon Corrected										
		Phase Angle (deg)							Phase Angle (deg)										
		16	17	18	39	40	166	167	170			16	17	18	39	40	166	167	170
MVIC Red	Altitude (km)	0-20	0.002553	0.013312	0.012053	0.014628	0.017485	0.0101889	0.138149	0.171346	0-20	0.005927	0.019227	0.01186	0.016838	0.019815	0.107607	0.146532	0.192724
		20-40	0.005846	0.012523	0.012878	0.009679	0.011549	0.080679	0.103952	0.120598	20-40	0.009039	0.014639	0.015524	0.011914	0.013447	0.091753	0.119215	0.137186
		40-60	0.006887	0.011002	0.011402	0.006838	0.008754	0.0555	0.072963	0.080648	40-60	0.008997	0.012396	0.013358	0.007913	0.009697	0.064617	0.082444	0.094017
		60-80	0.00745	0.009427	0.010101	0.005033	0.006077	0.037098	0.049198	0.056803	60-80	0.008829	0.01044	0.011468	0.006	0.007049	0.044304	0.055607	0.066536
		80-100	0.006937	0.008203	0.008993	0.004158	0.005078	0.026203	0.033465	0.036476	80-100	0.008904	0.008924	0.010383	0.00509	0.00519	0.029606	0.039037	0.044273
		100-120	0.006084	0.007113	0.008005	0.003286	4.18E-03	0.016291	0.02141	0.024066	100-120	0.008341	0.007851	0.009339	0.004225	0.004246	0.019005	0.025303	0.028924
		120-140	0.006094	0.006365	0.007179	3.26E-03	0.003297	0.009153	0.013122	0.015484	120-140	0.008157	0.006814	0.008231	0.003314	0.004241	0.011139	0.015887	0.018458
		140-160	0.005874	0.005747	0.006422	2.35E-03	3.30E-03	0.004209	0.007645	0.009678	140-160	0.007608	0.006099	0.007452	0.00242	0.00334	0.005967	0.009628	0.011675
		160-180	0.005636	0.004993	0.006095	0.001409	2.37E-03	0.000709	0.00389	0.006813	160-180	0.007296	0.005569	0.007058	0.002378	0.002418	0.002383	0.004877	0.007845
		180-200	0.005312	0.004297	5.35E-03	1.42E-03	1.44E-03	-9.58E-04	0.002057	0.004933	180-200	0.006987	0.005204	6.52E-03	0.001445	2.40E-03	1.67E-05	0.002929	0.005934
		200-220	0.00447	0.004262	0.004742	1.43E-03	1.43E-03	-0.00243	0.000347	0.004015	200-220	0.006475	0.004499	0.006258	0.001456	0.001457	-0.00147	0.001252	0.005
		220-240	0.004544	0.003536	0.004513	1.45E-03	1.45E-03	-0.00262	3.48E-04	0.004041	220-240	0.00612	0.004441	0.005664	0.00147	0.001473	-0.00212	0.000432	0.005014
		240-260	0.003857	0.003488	0.003923	1.45E-03	1.46E-03	-0.00298	-0.00044	4.06E-03	240-260	0.00586	0.003682	0.004835	0.001476	0.001487	-0.00197	0.000487	0.00413
		260-280	0.003948	0.002776	0.003017	0.000494	1.47E-03	-0.00283	-0.00038	0.003168	260-280	0.005317	0.003666	0.004815	0.001466	0.001488	-0.00119	0.000553	0.00414
		280-300	0.003684	0.002697	0.003697	4.98E-04	0.000517	-0.00269	-0.00034	0.003182	280-300	0.005238	0.003656	0.004662	0.000517	0.001488	-0.00176	0.000608	0.004157
		300-320	0.003316	0.002723	0.002963	5.07E-04	5.09E-04	-0.00255	-0.00028	0.003197	300-320	0.004907	0.002878	0.003962	0.000523	0.000528	-0.00236	0.000568	0.004178
		320-340	0.003811	0.001917	0.002872	5.20E-04	5.12E-04	-0.00246	-0.00024	0.003214	320-340	0.004573	0.002854	0.003958	0.000535	0.00053	-0.00228	0.000692	0.004191
	340-360	0.002728	0.001915	0.002866	5.31E-04	5.27E-04	-2.32E-03	-0.00019	0.00323	340-360	0.004484	0.002846	0.003832	0.000545	0.000542	-0.00222	0.000719	0.004207	
	360-380	0.002722	0.001909	0.002114	5.38E-04	5.37E-04	-0.00224	-0.00015	0.003242	360-380	0.003925	0.002826	0.003081	0.000554	0.000552	-0.00211	0.000758	0.00422	
	380-400	0.002694	1.89E-03	2.02E-03	-0.00044	5.45E-04	-0.00215	-1.17E-04	0.003255	380-400	0.00372	2.01E-03	3.09E-03	0.000555	0.000563	-0.00203	-6.19E-05	0.004233	
	400-420	0.001984	1.12E-03	2.02E-03	-4.35E-04	-0.00042	-0.00206	-8.61E-05	0.003268	400-420	0.003775	2.00E-03	3.09E-03	-0.00042	0.000564	-0.00196	-3.33E-05	0.004245	
	420-440	0.001936	1.07E-03	2.01E-03	-4.26E-04	-4.28E-04	-1.98E-03	-5.78E-05	0.003278	420-440	0.003157	2.00E-03	3.00E-03	-0.0004	-0.00041	-0.00191	-1.42E-05	0.004258	
	440-460	0.002019	1.04E-03	2.02E-03	-0.00042	-4.25E-04	-0.00194	-3.36E-05	0.00329	440-460	0.003052	2.00E-03	2.19E-03	0.000586	-0.00041	-0.00181	7.26E-06	0.004267	
	460-480	0.00202	1.06E-03	2.02E-03	-0.00041	-0.00041	-0.00186	-3.95E-06	0.003299	460-480	0.003008	2.00E-03	2.19E-03	0.000591	0.000594	-0.00176	3.00E-05	0.004278	
	480-500	0.001213	1.06E-03	1.16E-03	-0.00042	-0.00041	-1.80E-03	1.20E-05	0.003307	480-500	0.003055	1.16E-03	2.19E-03	0.000585	0.000594	-0.00172	4.70E-05	0.004286	
MVIC Blue	Altitude (km)	0-20	-0.00137	0.014602	0.022857	0.025846	0.029958	0.246503	0.325956	0.461546	0-20	0.010961	0.022631	0.028331	0.030809	0.035956	0.2638	0.361231	0.525643
		20-40	0.012103	0.015253	0.021136	0.014366	0.018388	0.208809	0.247981	0.323889	20-40	0.019047	0.028883	0.025253	0.018376	0.022347	0.233165	0.283256	0.364229
		40-60	0.011954	0.01278	0.018322	0.010408	0.010404	0.148106	0.175789	0.223362	40-60	0.017848	0.015626	0.022311	0.010552	0.014455	0.16847	0.199371	0.255988
		60-80	0.012231	0.010196	0.015632	0.006503	0.006455	0.10382	0.119285	0.159734	60-80	0.017121	0.013235	0.019772	0.010507	0.010521	0.118328	0.136512	0.185048
		80-100	0.009748	0.007587	0.012449	0.002506	0.006493	0.07178	0.082435	0.107292	80-100	0.014906	0.011271	0.016559	0.006559	0.006579	0.08411	0.095228	0.125188
		100-120	0.010565	0.007687	0.009005	0.0025	0.002498	0.047667	0.053704	0.076222	100-120	0.015012	0.008248	0.01307	0.002547	0.00258	0.055749	0.062351	0.085859
		120-140	0.011	0.004413	0.009126	-0.00157	0.002514	0.03119	0.033385	0.050235	120-140	0.015228	0.00836	0.013247	-0.00153	0.00256	0.035685	0.041366	0.055917
		140-160	0.007867	0.004534	0.005444	-0.00155	-0.00155	0.015423	0.017499	0.029591	140-160	0.015178	0.005033	0.009602	-0.00153	-0.00153	0.02325	0.025268	0.03806
		160-180	0.007909	0.004552	0.005472	-0.00153	-0.00155	0.007206	0.009071	0.020566	160-180	0.012331	0.005027	0.009608	-0.00151	-0.00152	0.011313	0.013182	0.0253
		180-200	0.004528	0.001032	0.005573	-0.0015	-0.00153	-0.00045	0.001191	0.015896	180-200	0.012414	0.00505	0.009711	-0.00148	-0.00151	0.003785	0.005223	0.020275
		200-220	0.004567	0.001122	0.005644	-0.00147	-0.00149	-0.00454	-0.00288	0.011678	200-220	0.012684	0.005156	0.009727	-0.00146	-0.00147	-0.00035	0.001189	0.016102
		220-240	0.004684	0.001202	0.001753	-0.00563	-0.00147	-0.00454	-0.00285	0.011095	220-240	0.012612	0.001489	0.005891	-0.00144	-0.00146	-0.00031	-0.00263	0.012524
		240-260	0.004831	0.001301	0.001792	-0.00563	-0.00147	-0.00436	-0.00277	0.008005	240-260	0.009241	0.001528	0.005935	-0.00562	-0.00144	-0.00394	-0.00266	0.012221
		260-280	0.004991	0.001394	0.001844	-0.00562	-0.00563	-0.00806	-0.00268	0.007572	260-280	0.009351	0.001598	0.005974	-0.00562	-0.00562	-0.0038	-0.00259	0.012079
		280-300	0.005042	0.001469	0.001889	-0.00562	-0.00562	-0.00794	-0.00261	0.007379	280-300	0.00932	0.00164	0.006008	-0.00137	-0.00562	-0.00373	-0.00251	0.011843
		300-320	0.0012	-0.00234	0.00193	-0.00561	-0.00561	-0.00781	-0.00256	0.007192	300-320	0.009408	0.001696	0.006009	-0.00135	-0.0014	-0.00357	-0.00245	0.011746
		320-340	0.001389	-0.00246	0.001967	-0.0056	-0.00561	-0.00767	-0.0064	0.007091	320-340	0.00948	0.001741	0.002103	-0.00134	-0.00135	-0.00335	-0.0024	0.011502
	340-360	0.001298	-0.00238	0.001973	-0.0056	-0.0056	-0.0076	-0.00636	0.006967	340-360	0.00941	0.001778	0.002108	-0.0056	-0.00134	-0.00339	-0.00234	0.011273	
	360-380	0.001413	-0.00237	-0.00199	-0.0056	-0.0056	-0.00749	-0.00641	0.006941	360-380	0.005899	-0.002	0.002126	-0.00559	-0.0056	-0.00325	-0.0023	0.011172	
	380-400	0.001406	-0.00234	-0.00199	-0.00559	-0.0056	-0.00739	-0.00638	0.00681	380-400	0.005913	-0.0021	0.002153	-0.00559	-0.00559	-0.00317	-0.0026	0.010984	
	400-420	0.001468	-0.0023	-0.00195	-0.00559	-0.00559	-0.00731	-0.00633	0.006678	400-420	0.005852	-0.0021	0.002166	-0.00559	-0.00559	-0.00306	-0.00222	0.010936	
	420-440	0.001495	-0.00226	-0.00194	-0.00559	-0.00559	-0.00724	-0.00631	0.006686	420-440	0.005836	-0.0021	0.002186	-0.00558	-0.00559	-0.00296	-0.00219	0.010784	
	440-460	0.001544	-0.00222	-0.00192	-0.00558	-0.00558	-0.00716	-0.00626	0.006555	440-460	0.005856	-0.00209	0.002201	-0.00558	-0.00558	-0.00295	-0.00215	0.010705	
	460-480	0.001581	-0.00218	-0.0019	-0.00558	-0.00558	-0.0071	-0.00624	0.00652	460-480	0.005863	-0.00207	0.002222	-0.00558	-0.00558	-0.00285	-0.00212	0.010682	
	480-500	0.000194	-0.00214	-0.00188	-0.00558	-0.00558	-0.00703	-0.00621	0.006481	480-500	0.005934	-0.00204	0.00223	-0.00128	-0.00558	-0.00481	-0.00209	0.010599	
MVIC NIR	Altitude (km)	0-20	-0.01636	-															

Monodisperse						
Altitude [km]	R_f [m]	$S_f(\text{Red})$	$S_f(\text{Blue})$	$S_f(\text{NIR})$	N	R^2
0–20	1.52E-07	0.036009	0.072786	0.015108	2.74E + 08	0.865475
20–40	1.52E-07	0.028623	0.055318	0.009785	2.01E + 08	0.922079
40–60	1.46E-07	0.021802	0.041302	0.007731	1.59E + 08	0.924416
60–80	1.34E-07	0.016537	0.031749	0.005944	1.5E + 08	0.918738
80–100	1.22E-07	0.012712	0.024462	0.005011	1.41E + 08	0.904564
100–120	1.07E-07	0.009609	0.018049	0.004372	1.44E + 08	0.870422
120–140	8.99E-08	0.007206	0.014575	0.003304	1.82E + 08	0.784031
140–160	6.60E-08	0.005203	0.012029	0.00313	3.08E + 08	0.583708
160–180	4.85E-08	0.003771	0.008536	0.002592	5.69E + 08	0.217304
180–200	2.99E-08	0.002836	0.00632	0.002355	1.69E + 09	0.025136
200–220	1.41E-08	0.00275	0.005583	0.002191	1.1E + 10	0.025143
220–240	4.64E-08	0.002757	0.006506	0.002098	2.94E + 08	0.193508
240–260	4.25E-08	0.002524	0.005881	0.001984	2.37E + 08	0.180628
260–280	5.30E-08	0.00246	0.00582	0.001977	1.03E + 08	0.201255
280–300	4.64E-08	0.002202	0.005145	0.001932	1.23E + 08	0.176891
300–320	5.79E-08	0.002114	0.00505	0.001805	37617981	0.223527
320–340	5.79E-08	0.002007	0.004677	0.001788	37001751	0.207765
340–360	6.60E-08	0.002058	0.004389	0.001706	26888536	0.194362
360–380	5.07E-08	0.001775	0.005177	0.001673	28232173	0.212574
380–400	6.90E-08	0.002052	0.005483	0.001637	9800958	0.216517
400–420	6.05E-08	0.002151	0.004869	0.001553	10364015	0.23234
420–440	6.32E-08	0.002477	0.004797	0.001541	7039408	0.256974
440–460	5.54E-08	0.001614	0.004302	0.001533	7470849	0.20137
460–480	5.07E-08	0.001344	0.003901	0.001473	7113140	0.190098
480–500	7.88E-08	0.001442	0.00422	0.001403	1781873	0.181047

Note.

R_f : fractal aggregate the effective radius, Equation (15);
 S_f : scaling factor, Equation (7);
 N: the particle number density Equation (D8); and
 R^2 : goodness of fit metric, Equation (4).

Appx Table 4B

Parameters to Produce the Phase Functions which Best Fit the MVIC Phase Curves for a Bimodal Population

Bimodal										
Altitude [km]	R_f (Big) [m]	R_f (Small) [m]	w(Big)	w(Small)	$S_f(\text{Red})$	$S_f(\text{Blue})$	$S_f(\text{NIR})$	N(Big)	N(Small)	R^2
0–20	5.87E-07	3.14E-08	0.01	0.99	0.014665	0.038995	0.007094	2396096	1.18E + 10	0.970199
20–40	5.87E-07	3.14E-08	0.01	0.99	0.011658	0.031447	0.005614	1761078	8.65E + 09	0.982934
40–60	5.87E-07	1.41E-08	0.001	0.999	0.008936	0.025567	0.004195	486252.3	6.98E + 10	0.97895
60–80	5.87E-07	4.10E-08	0.01	0.99	0.007399	0.020903	0.003308	705113.8	2.43E + 09	0.977037
80–100	7.66E-07	6.98E-08	0.01	0.99	0.007092	0.020629	0.002947	206005.9	4.97E + 08	0.963088
100–120	5.87E-07	5.35E-08	0.01	0.99	0.004538	0.012833	0.001946	297976.8	7.19E + 08	0.935362
120–140	5.87E-07	2.41E-08	0.001	0.999	0.003693	0.011139	0.001459	80074.61	5.66E + 09	0.863065
140–160	1.00E-06	4.10E-08	0.001	0.999	0.003331	0.010305	0.001621	14561.47	1.03E + 09	0.696982
160–180	7.66E-07	4.10E-08	0.001	0.999	0.002358	0.006774	0.001564	17548.33	8.69E + 08	0.305135
180–200	1.85E-08	1.41E-08	0.001	0.999	0.002803	0.006339	0.00236	10244769	1.46E + 10	0.028246
200–220	3.14E-08	2.41E-08	0.5	0.5	0.002831	0.005553	0.00223	6.62E + 08	9.44E + 08	0.01608
220–240	5.35E-08	4.10E-08	0.5	0.5	0.002557	0.006879	0.002199	1.19E + 08	1.7E + 08	0.225045
240–260	5.35E-08	4.10E-08	0.5	0.5	0.002376	0.006417	0.002071	75948261	1.08E + 08	0.209769
260–280	5.35E-08	4.10E-08	0.5	0.5	0.002214	0.006112	0.002042	58600469	83565082	0.219741
280–300	2.64E-07	4.10E-08	0.001	0.999	0.00201	0.005419	0.001962	14104.42	1.69E + 08	0.203182
300–320	6.98E-08	5.35E-08	0.5	0.5	0.001865	0.005235	0.001942	13574660	19357653	0.256475
320–340	4.50E-07	4.10E-08	0.001	0.999	0.001567	0.004398	0.001699	3679.63	89636184	0.284104
340–360	2.64E-07	6.98E-08	0.001	0.999	0.001668	0.004569	0.001822	3956.358	23306650	0.281346
360–380	3.45E-07	4.10E-08	0.001	0.999	0.001609	0.005013	0.001689	2859.75	48852129	0.259635
380–400	1.55E-07	2.41E-08	0.01	0.99	0.001974	0.004097	0.001727	126341.7	1.5E + 08	0.352209
400–420	2.03E-07	5.35E-08	0.01	0.99	0.002115	0.004417	0.001744	23280.34	13590742	0.387014
420–440	2.03E-07	3.14E-08	0.01	0.99	0.001916	0.003592	0.001566	34572.32	41042138	0.37244
440–460	5.87E-07	4.10E-08	0.001	0.999	0.001175	0.003554	0.001324	464.1657	16124122	0.327138
460–480	4.50E-07	3.14E-08	0.001	0.999	0.00108	0.003594	0.00129	725.9001	25216212	0.380154
480–500	1.00E-06	6.98E-08	0.001	0.999	0.001122	0.00358	0.001336	68.19479	2368941	0.368415

Note.

R_f : fractal aggregate the effective radius, Equation (15);
 w: relative weight of aerosol population, Equation (16);
 S_f : scaling factor, Equation (7);
 N: the particle number density Equation (D8);
 R^2 : goodness of fit metric, Equation (4).

Appx Table 4C
Parameters to Produce the Phase Functions which Best Fit the MVIC Phase Curves for a Trimodal, Population

Trimodal													
Altitude [km]	R _f (Big) [m]	R _f (Med) [m]	R _f (Small) [m]	w(Big)	w(Med)	w(Small)	S _F (Red)	S _F (Blue)	S _F (NIR)	N(Big)	N(Med)	N(Small)	R ²
0–20	7.38E-07	5.44E-07	4.77E-08	0.003162	0.02846	0.968377	0.014487	0.03705	0.007165	284007.5	3834545	3.35E + 09	0.971118
20–40	7.38E-07	5.44E-07	6.47E-08	0.01	0.021623	0.968377	0.013793	0.036613	0.006511	491971.6	1595853	1.22E + 09	0.983568
40–60	1.00E-06	5.44E-07	6.47E-08	0.001	0.030623	0.968377	0.01039	0.027322	0.005062	23808.93	1640844	8.87E + 08	0.980958
60–80	7.38E-07	8.77E-08	1.92E-08	0.003162	0.096838	0.9	0.008341	0.023634	0.003572	318289.9	1.67E + 08	1.18E + 10	0.977289
80–100	7.38E-07	8.77E-08	3.52E-08	0.01	0.683772	0.306228	0.007464	0.019963	0.003252	213129.6	2.49E + 08	3.77E + 08	0.965165
100–120	7.38E-07	6.47E-08	1.41E-08	0.003162	0.313065	0.683772	0.004675	0.013982	0.001881	143157.1	3.64E + 08	6.03E + 09	0.936028
120–140	7.38E-07	4.77E-08	1.41E-08	0.003162	0.9	0.096838	0.003773	0.011395	0.001429	75771.35	8.3E + 08	4.52E + 08	0.874405
140–160	1.00E-06	4.77E-08	3.52E-08	0.001	0.315228	0.683772	0.003242	0.010099	0.001553	15453.53	2.81E + 08	9.15E + 08	0.716832
160–180	1.00E-06	1.92E-08	1.41E-08	6.84E-05	3.16E-05	0.9999	0.002221	0.006979	0.00121	4217.254	380151.7	1.8E + 10	0.352303
180–200	1.00E-06	1.92E-08	1.41E-08	2.16E-05	1.00E-05	0.999968	0.002353	0.005816	0.001801	1078.118	97183.68	1.46E + 10	0.082479
200–220	7.38E-07	1.92E-08	1.41E-08	2.85E-05	3.16E-06	0.999968	0.002408	0.005113	0.001788	1598.359	23074.33	1.09E + 10	0.048872
220–240	1.00E-06	4.77E-08	3.52E-08	1.00E-05	0.683772	0.316218	0.002585	0.006974	0.002117	52.9123	2.09E + 08	1.45E + 08	0.22099
240–260	6.47E-08	4.77E-08	3.52E-08	0	0.9	0.1	0.002367	0.006372	0.002114	0	1.63E + 08	27091177	0.19855
260–280	1.00E-06	4.77E-08	2.60E-08	0.0001	0.316128	0.683772	0.002066	0.005718	0.001834	382.7242	69849429	3.4E + 08	0.235189
280–300	7.38E-07	6.47E-08	4.77E-08	0.000316	0.315912	0.683772	0.001893	0.005188	0.001831	816.4107	20922115	67934907	0.226059
300–320	7.38E-07	4.01E-07	6.47E-08	0.000684	0.000316	0.999	0.001607	0.00453	0.001696	749.8482	780.4494	28103396	0.222952
320–340	7.38E-07	4.77E-08	3.52E-08	0.000684	0.999	0.000316	0.001493	0.004435	0.001547	1068.926	60100021	28539.78	0.276822
340–360	7.38E-07	6.47E-08	4.77E-08	0.000684	0.999	0.000316	0.001546	0.004368	0.001665	749.3151	28083418	13336.01	0.304334
360–380	5.44E-07	6.47E-08	4.77E-08	0.001	0.099	0.9	0.001457	0.004547	0.001603	1219.61	2064649	28157551	0.226554
380–400	4.01E-07	2.96E-07	1.41E-08	0	0.000316	0.999684	0.001791	0.004172	0.001528	0	4154.839	7.58E + 08	0.373723
400–420	2.96E-07	3.52E-08	1.41E-08	0.003162	0.9	0.096838	0.001835	0.003737	0.001491	8283.566	40313440	14644556	0.352354
420–440	1.61E-07	4.77E-08	3.52E-08	0.031623	0.9	0.068377	0.002151	0.003838	0.001718	84524.74	12184061	1388681	0.331279
440–460	7.38E-07	6.47E-08	4.77E-08	0.001	0.099	0.9	0.001193	0.003714	0.001367	268.96	683052.9	9315434	0.323804
460–480	5.44E-07	1.92E-08	1.41E-08	0.000316	0.683772	0.315912	0.000832	0.002778	0.000947	433.5225	81185568	56269660	0.35653
480–500	5.44E-07	4.77E-08	3.52E-08	0.0009	0.0001	0.999	0.001032	0.003377	0.001283	327.6183	933.807	13994714	0.334011

Note.

R_f: fractal aggregate the effective radius, Equation (15);

w: relative weight of aerosol population, Equation (16);

S_F: scaling factor, Equation (7);

N: the particle number density Equation (D8);

R²: goodness of fit metric, Equation (4).

Appx Table 4D
Parameters to Produce the Phase Functions which Best Fit the MVIC Phase Curves for a Power-Law Population

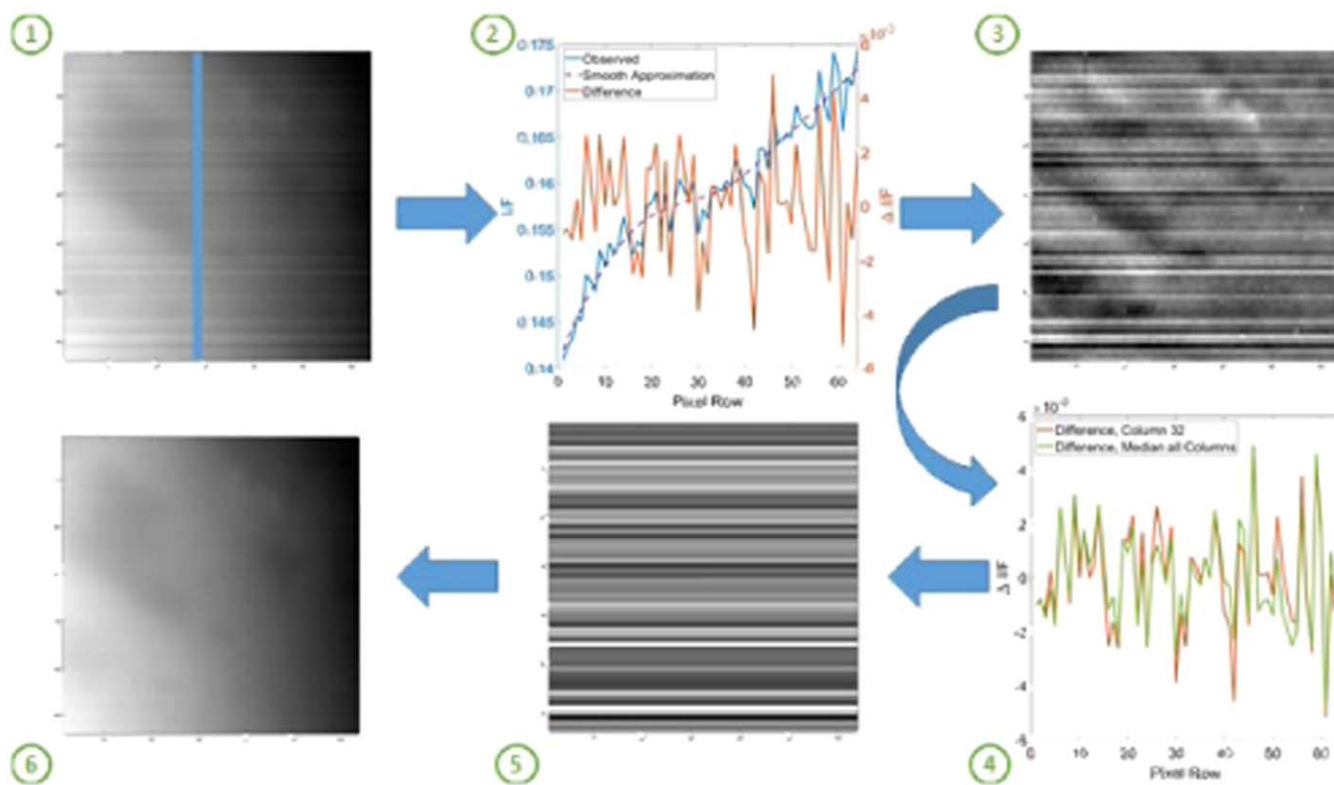
Power Law								
Altitude [km]	b	S _F (Red)	S _F (Blue)	S _F (NIR)	n(1000 nm) [dN/dR _r (m ⁻³)]	n(150 nm) [dN/dR _r (m ⁻³)]	n(20 nm) [dN/dR _r (m ⁻³)]	R ²
0–20	3.466934	0.016823	0.04117	0.008827	6.91817E + 11	4.97082E + 14	5.37E + 17	0.963392
20–40	3.587174	0.014669	0.034874	0.007572	3.87151E + 11	3.4945E + 14	4.81E + 17	0.98194
40–60	3.727455	0.011275	0.027459	0.005818	1.967E + 11	2.31679E + 14	4.23E + 17	0.980278
60–80	3.807615	0.008306	0.020624	0.004175	1.22414E + 11	1.67865E + 14	3.60E + 17	0.973282
80–100	4.008016	0.006664	0.016797	0.003267	54308378030	1.0892E + 14	3.50E + 17	0.96144
100–120	4.188377	0.005135	0.01317	0.002476	25271747507	6.87012E + 13	3.05E + 17	0.92517
120–140	4.488978	0.004348	0.011197	0.002019	7644424271	3.81815E + 13	3.24E + 17	0.846872
140–160	4.92986	0.0039	0.009948	0.002668	1353525568	1.56035E + 13	3.21E + 17	0.632401
160–180	5.571142	0.003325	0.008044	0.002532	148875526	4.97613E + 12	3.18E + 17	0.230534
180–200	6.472946	0.002751	0.006194	0.002364	1892664.504	4.92886E + 11	2.78E + 17	0.020131
200–220	6.352705	0.002811	0.00541	0.002192	131735.5651	1.07328E + 11	2.04E + 17	0.00439
220–240	5.611222	0.002392	0.006347	0.002048	23933249.89	1.36215E + 12	1.53E + 17	0.210957
240–260	5.511022	0.00216	0.005863	0.001966	22314450.88	1.05016E + 12	9.64E + 16	0.200411
260–280	5.551102	0.00205	0.005551	0.001927	21579137	9.06086E + 11	7.37E + 16	0.203209
280–300	5.450902	0.001887	0.005145	0.001881	41452521.47	1.14568E + 12	5.97E + 16	0.213684
300–320	5.230461	0.001639	0.004564	0.001732	34915845.81	7.68188E + 11	3.14E + 16	0.260886
320–340	5.130261	0.00149	0.004282	0.001697	57114140.77	9.62964E + 11	2.97E + 16	0.26324
340–360	5.190381	0.001511	0.004061	0.001652	43351634.9	8.50975E + 11	3.09E + 16	0.265182
360–380	5.450902	0.001598	0.0049	0.001753	13919520.93	3.56545E + 11	1.72E + 16	0.265825
380–400	5.150301	0.00192	0.00431	0.001609	20394183.22	3.71018E + 11	1.24E + 16	0.370224
400–420	5.130261	0.001969	0.004113	0.001556	13387976.11	2.62801E + 11	9.53E + 15	0.364456
420–440	5.03006	0.001963	0.003742	0.001483	11749872.2	2.13758E + 11	7.15E + 15	0.379081
440–460	5.07014	0.001228	0.003596	0.001526	8294692.629	1.56747E + 11	5.46E + 15	0.295896
460–480	4.9499	0.001087	0.003334	0.001338	8407436.282	1.36464E + 11	4.04E + 15	0.333832
480–500	4.92986	0.001051	0.003214	0.001376	11293481.8	1.35236E + 11	2.90E + 15	0.332972

Note.

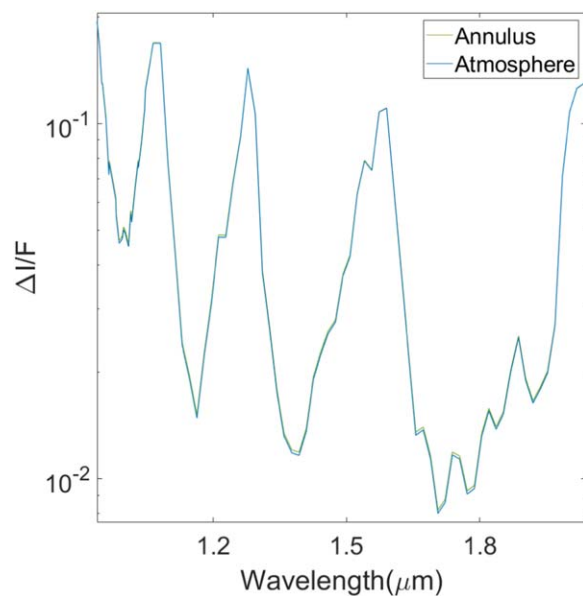
b: power law exponent; S_F: scaling factor, Equation (7);

n: the differential particle radius number density distribution, Equation (10);

R²: goodness of fit metric, Equation (4).



Appx. Figure 4. Schematic showing the VIMS destripping routine described in Appendix A.



Appx Figure 5. Zoom-in of the modeled atmospheric spectra and the modeled annulus spectra from Figure 3. The difference between the two spectra is less than the line width at certain wavelengths.

Appx. Table 5
 Details of Every Detection of the Annuli

Flyby	Rev	CA UTC	CA Altitude (km)	CA Ephemeris Time	Planetocentric Longitude of the Sun (L_S)	Average Incidence (deg)	Average Emission (deg)	Average Phase (deg)	Central Longitude (deg)	Average Latitude (deg)	Average Pixel Scale (km^2)	Tilt from North Pole (deg)	Prime Meridian Offset (deg, E+)	Subsolar Longitude Offset (deg, E+)	# of Longitude Bins
<i>North Polar</i>															
T079	TI158	2011-12-13T20:11:23	3 583.241 3	377 079 149.2	28.41	54.69	68.8	19.26	160.27	66.96	77.37				1
T087	TI174	2012-11-13T10:22:08	973.650 52	406074195	39.17	86.21	49.6	131.11	-54.23	65.28	82.11				4
T088	TI175	2012-11-29T08:56:59	1 014.693 4	407 451 486.1	39.66	82.54	43.81	126.19	-68.06	68.85	109.08				2
T089	TI181	2013-02-17T01:56:35	1 978.042 3	414338262	42.19	84.54	35.21	117	-46.05	71.35	157.9	4.76	-148.86	42.8	11
T090	TI185	2013-04-05T21:43:30	1 400.076 1	418 470 277.6	43.7	86.63	37.13	108.86	-36.78	67.95	59.31	2.63	36.93	-133.18	17
T091	TI190	2013-05-23T17:32:55	970.052 55	422 602 441.7	45.21	63.7	45.17	105.01	-113.93	69.63	120.39	1.45	145.81	-26.03	8
T092	TI194	2013-07-10T13:21:47	963.786 73	426 734 573.9	46.7	76.96	29.5	97.53	-73.07	68.79	100.32	1.04	48.07	-125.51	17
T093	TI195	2013-07-26T11:56:22	1 399.697 9	428111849	47.2	81.42	20.11	90.41	-49.04	66.1	61.42	1.64	52.23	-121.96	25
T094	TI197	2013-09-12T07:43:56	1 396.765 3	432243903	48.71	72.86	21.35	83.1	-44.12	67.57	44.02	2.13	38.62	-137.35	28
T095	TI198	2013-10-14T04:56:27	960.758 29	434998654	49.7	63.33	36.86	76.56	95.32	67	86.54	2.67	30.1	-147.04	35
T096	TI199	2013-12-01T00:41:19	1 400.035 4	439 130 545.8	51.19	61.83	23.53	66.13	-77.15	65.5	43.51	3.73	24.2	-154.76	36
T097	TI200	2014-01-01T21:59:41	1 399.810 4	441885648	52.18	62.89	19.95	59.94	-92.06	65.69	78.62	3.61	55.66	-124.39	36
T098	TI201	2014-02-02T19:12:38	1 235.470 6	444640425	53.17	71.86	34.72	51.74	-34.07	66.41	98.89	3.59	48.03	-133.19	36
T099	TI202	2014-03-06T16:26:47	1 499.789 9	447395274	54.16	60.41	29.14	43.04	-66.15	69.17	134.98	3.38	68.39	-113.99	22
T100	TI203	2014-04-07T13:41:14	963.449 34	450150141	55.16	61.96	38.6	34.27	-51.81	68.04	58.05	3.35	42.69	-140.85	28
T101	TI204	2014-05-17T16:12:15	2 991.882 4	453615202	56.4	87.01	29.86	109.5	99.55	66.71	110.8	1.19	-142.66	-142.04	11
T102	TI205	2014-06-18T13:28:25	3 658.690 5	456370172	57.39	84.11	34.45	104.14	70.52	66.15	79.78	0.85	-152.88	-153.39	17
T103	TI206	2014-07-20T10:40:58	5 103.283 1	459 124 925.1	58.38	74.41	37.43	99.95	30.52	66.73	83.72	3.03	-138.85	-140.55	24
T104	TI207	2014-08-21T08:09:09	964.103 3	461880616	59.36	77.77	31.85	103.26	95.2	64.14	44.64	1.65	-127.36	-130.01	17

Appx. Table 5
(Continued)

Flyby	Rev	CA UTC	CA Altitude (km)	CA Ephemeris Time	Planetocentric Longitude of the Sun (L_S)	Average Incidence (deg)	Average Emission (deg)	Average Phase (deg)	Central Longitude (deg)	Average Latitude (deg)	Average Pixel Scale (km ²)	Tilt from North Pole (deg)	Prime Meridian Offset (deg, E+)	Subsolar Longitude Offset (deg, E+)	# of Longitude Bins
T105	TI208	2014-09-22T05:23:19	1 401.501 6	464635466	60.34	62.97	42.2	110.48	59.9	65.89	39.78	0.28	-42.95	-46.78	18
T106	TI209	2014-10-24T02:40:30	1 013.168 4	467390497	61.32	82	42.51	119.77	112.2	66.38	60.52	1.02	-101.1	-106.05	13
T107	TI210	2014-12-10T22:26:35	980.572 19	471 522 462.4	62.79	94.3	35.54	125.85	153.02	67.83	89.29	0.06	-0.03	-6.83	5
T119	TI235	2016-05-06T16:54:37	969.201 5	515 825 744.7	78.42	83.96	42.9	121.75	104.13	65	54.45	1.58	70.48	103.41	10
T120	TI236	2016-06-07T14:06:17	974.555 42	518 580 444.9	79.39	85.08	34.14	114.78	110.67	64.5	71.57	1.47	78.43	110.11	8
T121	TI238	2016-07-25T09:58:23	975.407 36	522 712 770.8	80.84	82.05	36.62	112.29	97.54	63.17	64.4	0.66	69	98.88	16
T122	TI239	2016-08-10T08:30:53	1 698.358 2	524 089 920.8	81.34	88.69	29.92	111.84	106.87	63.95	143.08	1.13	25.46	54.66	11
T123	TI243	2016-09-27T04:16:59	1 775.659 2	528221887	82.77	67.77	45.93	112	61.43	64.83	69.29	0.62	146.1	173.41	8
T124	TI248	2016-11-13T23:55:56	1 585.323 9	532 353 423.8	84.21	64.59	49.77	112.65	50.88	61.26	107.16	1.15	-40.36	-15.05	5
nT261	TI261	2017-02-17T13:10:26	186 795.47	540 609 095.4	87.09	52.84	36.6	78.03	-66.31	66.57	109.41	1.87	88	107.36	14
nT262	TI262	2017-02-17T19:41:26	220 499.08	540 632 554.7	87.1	62.33	35.93	85.05	-22.58	65.17	133.8	3.3	69.19	94.66	25
nT283	TI283	2017-07-10T13:50:53	264 321.55	552 966 722.3	91.4	48.91	23.94	55.67	-15.45	66.54	155.08	3.63	73	76.7	19
nT288	TI288	2017-08-11T05:04:11	194 993.55	555 699 920.5	92.36	55.89	30.81	71.73	31.21	66.47	118.68	0.57	83.39	80.23	11
nT292	TI292	2017-09-11T19:04:49	119 734.92	558 428 758.2	93.3	69.87	29.57	84.68	-68.04	67.29	72.39	3.53	-103.57	-114.72	14
Flyby	Rev	CA UTC	CA Altitude (km)	CA Ephemeris Time	Planetocentric Longitude of the Sun (L_S)	Average Incidence (Deg)	Average Emission (Deg)	Average Phase (Deg)	Central Longitude (Deg)	Average Latitude (Deg)	Average Pixel Scale (km ²)	Tilt from North Pole (Deg)	Prime Meridian Offset (Deg, E+)	Subsolar Longitude Offset (Deg, E+)	# of Longitude Bins
<i>Equatorial</i>															
T00A	TI00A	2004-10-26T15:30:05	1 174.330 6	152076669	297.26	40.84	26.45	19.97	-127.87	-7.54	70.95	1.53	106.02	-98.09	8
T00B	TI00B	2004-12-13T11:38:15	1 192.669 9	156 209 959.6	299.03	44.16	20.53	56.83	-52.61	-0.53	56.37	0.12	-141.42	-61.56	6
T003	TI003	2005-02-15T06:57:53	1 578.974 6	161 722 737.3	301.4	33.54	24.86	13.25	-137.36	-5.31	46.56	4.19	110.84	-89.49	9
T004	TI005	2005-03-31T20:05:16	2 403.893 6	165 571 580.1	303.06	37.27	25.61	15.82	-140.4	-4.8	28.03	5.63	115.77	-86.38	10

Appx. Table 5
(Continued)

Flyby	Rev	CA UTC	CA Altitude (km)	CA Ephemeris Time	Planetocentric Longitude of the Sun (L_S)	Average Incidence (deg)	Average Emission (deg)	Average Phase (deg)	Central Longitude (deg)	Average Latitude (deg)	Average Pixel Scale (km ²)	Tilt from North Pole (deg)	Prime Meridian Offset (deg, E+)	Subsolar Longitude Offset (deg, E+)	# of Longitude Bins
T005	TI006	2005-04-16T19:07:16	1 359.185 5	166950500	303.65	54.11	23.32	57.12	-32.98	-3.1	28.12	0.35	51.89	131.46	8
T006	TI013	2005-08-22T08:53:38	3 660.731 8	177 972 881.9	308.36	48.76	23.57	52.66	-27.62	-0.9	41.36	0.65	-117.04	-42.08	7
T007	TI014	2005-09-07T04:01:28	83 235.56	179 337 751.7	308.95	47.63	24.07	51.93	-31.65	-1.42	74.69	2.34	-135.32	-64.31	8
T008	TI017	2005-10-28T04:15:25	1 352.876 1	183 744 988.8	310.81	32.39	24.59	23.54	-138.2	-5.36	65.17	3.34	120.95	-98.26	11
T009	TI019	2005-12-26T18:59:26	10 411.572	188895630	313.01	25	24.2	27.13	-42.06	-1.93	44.49	2.17	-113.75	-69.27	10
T010	TI020	2006-01-15T11:41:26	2 043.032 2	190 597 350.9	313.73	43.96	24.51	37.79	-151.46	-5.65	24.62	2.61	118.01	-113.56	11
T011	TI021	2006-02-27T08:25:18	1 812.311 4	194 300 783.6	315.29	29.83	25.75	18.17	-14.14	-1.86	112.98	3.79	-101.6	-86.97	13
T012	TI022	2006-03-19T00:05:55	1 949.351	195 998 820.6	316.02	51.77	24.99	65.01	-142.81	-3.17	32.31	6.01	141.32	-121.09	11
T013	TI023	2006-04-30T20:37:28	5 735.424 2	199 701 513.3	317.59	36.53	20.29	39.7	-10.78	-2.56	16.94	0.22	80.93	64.59	6
T014	TI024	2006-05-20T12:18:11	1 879.178 5	201399556	318.3	63.07	33.15	91.51	-119.98	-3.06	105.32				1
T015	TI025	2006-07-02T09:20:47	1 906.160 9	205 104 112.1	319.86	47.05	25.06	61.53	10.59	-4.36	93.78	0.84	-76.12	-122.92	6
T016	TI026	2006-07-22T00:25:26	950.385 67	206799991	320.6	52.87	30.76	59.39	2.03	1.9	79.66	4.1	-89.86	-54.3	7
T017	TI028	2006-09-07T20:16:51	999.713 19	210932276	322.33	46.94	23.72	62.92	7.47	0	47.34	1.66	-100.42	-66.74	5
T018	TI029	2006-09-23T18:58:48	960.198 92	212 309 993.5	322.92	35.17	41.28	64.49	-8.17	-4.97	73.94				4
T019	TI030	2006-10-09T17:30:07	980.047 47	213687072	323.5	46.57	40.81	65.03	5.44	-1.83	81.26	0.92	-98.11	-65.7	5
T020	TI031	2006-10-25T15:58:07	1 029.512 2	215063952	324.07	36.2	45.98	71.81	-4.31	1.87	74.86	1.75	90.75	122.4	5
T021	TI035	2006-12-12T11:41:31	1 000.284 7	219195756	325.81	58.62	34.79	67.41	21.76	1.3	95.85	3.2	-80.38	-50.71	5
T025	TI039	2007-02-22T07:24:34	86 205.694	225 401 139.6	328.38	24.79	55.63	69.36	126.85	-3.17	112.45				2
T026	TI040	2007-03-10T01:49:00	980.607 62	226763405	328.95	30.35	49.26	62	127.31	-5.45	68.68	3.95	50.28	-105.51	7
T027	TI041	2007-03-26T00:23:27	1 010.089 8	228 140 672.1	329.53	24.87	46.2	53.24	135.84	-6.95	115.47	0.7	0.02	-156.42	7
T028	TI042	2007-04-10T22:58:00	991.146 26	229 517 944.8	330.1	28.7	42.45	45.81	128.52	-6.15	74	3.05	45.75	-111.34	10
T029	TI043	2007-04-26T21:32:58	981.179 96	230895243	330.67	30.56	32.86	37.25	129.21	-4.42	89.58	4.43	34.81	-122.91	8

Appx. Table 5
(Continued)

Flyby	Rev	CA UTC	CA Altitude (km)	CA Ephemeris Time	Planetocentric Longitude of the Sun (L_S)	Average Incidence (deg)	Average Emission (deg)	Average Phase (deg)	Central Longitude (deg)	Average Latitude (deg)	Average Pixel Scale (km ²)	Tilt from North Pole (deg)	Prime Meridian Offset (deg, E+)	Subsolar Longitude Offset (deg, E+)	# of Longitude Bins
T030	TI044	2007-05-12T20:09:58	959.584 86	232272663	331.25	31.07	27.95	29.29	133.41	-2.6	82.7	6.44	54.11	-104.23	12
T031	TI045	2007-05-28T18:51:55	2 299.088 5	233 650 380.2	331.81	35.39	32.69	27.47	127.37	-4.86	29.45	3.4	50.88	-107.98	11
T032	TI046	2007-06-13T17:46:11	965.396 65	235028836	332.39	32.08	25.94	16.15	131.63	-3.3	58.83	1.56	68.97	-90.22	9
T033	TI047	2007-06-29T16:59:46	1 932.782 6	236408451	332.95	26.72	19.52	13.69	137.71	-3.14	23.28	4.17	60.02	-99.2	11
T034	TI048	2007-07-19T01:11:20	1 331.914 5	238 079 545.2	333.65	38.73	23.51	58.26	43.25	-1.15	25.18				3
T035	TI049	2007-08-31T06:32:36	3 324.615 5	241 814 020.8	335.19	26.82	17.15	26.87	159.3	-1.97	26.5	2.64	74.92	-113.88	10
T036	TI050	2007-10-02T04:42:43	973.489 1	244 572 228.1	336.33	35.94	26.9	32.54	134.06	-3.48	91.04	3.53	65.33	-123.77	10
T037	TI052	2007-11-19T00:47:25	999.652 91	248705310	338.03	36.22	16.89	40.66	142.73	-2.75	49.56	4.55	65.53	-125.14	8
T038	TI053	2007-12-05T00:06:50	1 298.834 1	250 085 274.9	338.59	31.41	19.37	44.55	158.82	-3.48	17.42	1.9	73.28	-117.31	9
T039	TI054	2007-12-20T22:57:55	969.950 23	251463540	339.17	46.04	32.55	50.13	134.06	-5.92	93.88	0.07	120.53	-70.43	8
T040	TI055	2008-01-05T21:30:19	1 014.118 2	252 840 684.6	339.72	38.06	21.11	55.98	156.25	-6.22	14.92	5.77	59.6	-132.02	9
T041	TI059	2008-02-22T17:32:07	999.872 23	256 973 591.9	341.42	46.94	35.5	66.19	139.27	-6.33	82.74	5.16	59.89	-133.31	7
T042	TI062	2008-03-25T14:27:48	999.447 82	259727333	342.54	53.8	23.75	72.98	141.59	-6.17	24.96	0.69	-132.47	32.88	7
T044	TI069	2008-05-28T08:24:32	1 399.989 7	265 235 137.1	344.79	44.41	51.07	89.45	146.68	0.1	105.68				3
T046	TI091	2008-11-03T17:35:23	1 105.099 8	279 005 787.9	350.33	51.51	44.65	81.13	-98.42	0.17	90.41	3.03	165.25	-38.85	6
T047	TI093	2008-11-19T15:56:28	1 023.290 7	280 382 252.9	350.89	49.5	45.2	84.76	-101.92	-7.91	57.73				3
T048	TI095	2008-12-05T14:25:45	960.510 53	281759210	351.44	46.96	47.03	77.68	-101.48	-5.38	85.57				3
T049	TI097	2008-12-21T12:59:52	970.886 78	283136457	351.99	42.61	45.63	71.26	-104.01	-1.53	89.57	3.9	154.79	-51.43	6
T050	TI102	2009-02-07T08:50:52	967.024 19	287 268 717.8	353.64	42.42	49.62	70.66	-101.92	-0.9	118.46	0.88	0	152.1	5
T051	TI106	2009-03-27T04:43:36	962.880 46	291 401 082.3	355.29	44.2	53.04	75.21	-98.58	-5.04	127.55				3
T053	TI109	2009-04-20T00:20:45	3 598.575 5	293 458 911.1	356.14	37.63	56.47	68.02	62.41	-3.46	110.16				3
T054	TI110	2009-05-05T22:54:15	3 242.262 8	294 836 120.9	356.68	24.4	55.23	62.78	47.87	0.88	106.01	4.72	-40.04	-73.18	7

Appx. Table 5
(Continued)

Flyby	Rev	CA UTC	CA Altitude (km)	CA Ephemeris Time	Planetocentric Longitude of the Sun (L_S)	Average Incidence (deg)	Average Emission (deg)	Average Phase (deg)	Central Longitude (deg)	Average Latitude (deg)	Average Pixel Scale (km ²)	Tilt from North Pole (deg)	Prime Meridian Offset (deg, E+)	Subsolar Longitude Offset (deg, E+)	# of Longitude Bins
T055	TI111	2009-05-21T21:26:41	965.623 78	296 213 267.1	357.24	23.79	49.97	52.13	29.55	-1.55	194.95	1.44	-60.71	-94.47	7
T056	TI112	2009-06-06T20:00:00	967.717 2	297 590 466.1	357.79	33.54	48.82	44.21	49.64	-2.47	163.46	3.56	-57.21	-91.59	10
T057	TI113	2009-06-22T18:32:35	955.214 66	298967621	358.32	29.42	44.67	36.87	35.92	-1.9	91.92	3.41	-53.53	-88.53	10
T058	TI114	2009-07-08T17:04:03	966.055 3	300 344 709.3	358.86	27.86	38.62	29.9	51.37	-1.94	49.59	4.16	-60.44	-96.09	11
T059	TI115	2009-07-24T15:34:03	956.582 69	301 721 709.1	359.41	18.39	27.89	22.52	30.89	-4.11	36.5	3.98	-65.48	-101.8	6
T061	TI117	2009-08-25T12:51:37	960.837 48	304 476 763.6	0.5	26.14	32.34	12.95	30.41	-3.18	22.72	2.76	-62.07	-99.44	13
T062	TI119	2009-10-12T08:36:24	1 299.964 9	308 608 650.2	2.14	31.55	30.4	10.5	10.19	-3.17	129.31	3.12	-67.91	-107.04	11
T063	TI122	2009-12-12T01:03:14	4 847.710 8	313 851 859.8	4.19	42.19	23.3	46.81	145.57	-1.91	55.65	1.98	40.56	-70.32	9
T064	TI123	2009-12-28T00:16:58	951.817 66	315 231 484.6	4.73	40.78	22.31	44.29	147.41	-2.15	30.55	3.33	34.49	-76.37	8
T065	TI124	2010-01-12T23:10:36	1 074.516	316 609 901.9	5.27	27.33	38.94	44.17	113.07	-2.02	56.58	4.93	40.89	-70.26	9
T066	TI125	2010-01-28T22:28:50	7 486.939 1	317 989 795.7	5.81	38.7	25.2	43.37	140.44	-0.31	75.38	0.89	0	-111.05	9
T067	TI129	2010-04-05T15:50:54	7 437.318 4	323 754 719.8	8.06	21.12	21.04	13.61	36.75	-3.68	51.67	2.1	-65.1	-111.75	12
T068	TI131	2010-05-20T03:24:20	1 398.006 7	327 597 926.3	9.56	31.66	25.9	31.55	133.37	-2.03	118.34	2.52	46.14	-77.6	10
T069	TI132	2010-06-05T02:26:27	2 042.953	328976853	10.09	31.33	35.09	31.05	117.8	-1.26	71.79	3.84	50.77	-73.12	11
T070	TI133	2010-06-21T01:27:43	878.567 51	330 355 728.9	10.62	33.88	25.04	32.24	146.06	-2	36.56	3.05	48.82	-75.25	11
T071	TI134	2010-07-07T00:22:45	1 004.078 5	331 734 231.1	11.16	36.43	23.32	35.03	143.59	-2.41	76.2	2.08	51.21	-73.12	9
nT136	TI136	2010-08-11T13:35:03	417 252.75	334 805 769.2	12.35	48.94	23.86	56.38	78.24	-1.47	178.1	2.1	0.01	-42.77	6
T072	TI138	2010-09-24T18:38:41	8 177.99	338 625 587.1	13.81	27.09	30.66	24.09	114.76	-3.06	17.12	0.54	0.01	-125.96	9
T074	TI145	2011-02-18T16:04:11	3 651.096 8	351 317 117.2	18.69	33.33	29.51	31.36	16.38	-4.23	150.65	1.71	-70.15	-124.13	11
T075	TI147	2011-04-19T05:00:39	10 052.942	356461305	20.64	31.88	32.02	18.21	127.75	-2.7	77.18	1.54	58.84	-92.75	11
T076	TI148	2011-05-08T22:53:44	1 872.807 1	358 167 290.5	21.28	31.33	22.26	42.38	36.87	-4.94	24.59	3.48	-60.78	-127.14	9
T077	TI149	2011-06-20T18:32:00	1 358.992 4	361 866 786.6	22.68	33.57	31.88	21.17	126.38	-3.95	51.2	2.13	76.03	-104.96	10

Appx. Table 5
(Continued)

Flyby	Rev	CA UTC	CA Altitude (km)	CA Ephemeris Time	Planetocentric Longitude of the Sun (L_S)	Average Incidence (deg)	Average Emission (deg)	Average Phase (deg)	Central Longitude (deg)	Average Latitude (deg)	Average Pixel Scale (km ²)	Tilt from North Pole (deg)	Prime Meridian Offset (deg, E+)	Subsolar Longitude Offset (deg, E+)	# of Longitude Bins
T078	TI153	2011-09-12T02:50:06	5 821.661 5	369 067 871.9	25.4	52.85	30.6	75.85	46.71	-5.86	57.86	4.22	-34.8	-136.56	6
T079	TI158	2011-12-13T20:11:23	3 583.241 3	377 079 149.2	28.41	33.33	22.99	23.23	144.81	-4.65	16.84	3.15	69.1	-102.1	12
T081	TI160	2012-01-30T13:39:48	31 130.577	381 202 854.1	29.96	34.31	38.73	28.17	-140.56	-3.89	73.62	3.36	74.4	-100.7	12
T082	TI161	2012-02-19T08:43:17	3 803.185	382 913 062.9	30.59	53.04	21.81	63.85	35.22	-4	38.83	3.63	-35.13	-123.89	6
T083	TI166	2012-05-22T01:10:11	953.990 5	390 921 076.9	33.58	32.06	27.24	21.93	134.49	-4.56	71.74	1.92	50.92	-108.15	11
T084	TI167	2012-06-07T00:07:21	959.347 58	392 299 706.8	34.09	37.44	37.38	28.4	119.55	-4.26	103.69	4.02	60.22	-99.09	11
T085	TI169	2012-07-24T20:03:07	1 012.449 8	396 432 253.9	35.61	26.95	20.75	33.04	155.36	-3.89	15.92	1.45	71.49	-89.43	11
T086	TI172	2012-09-26T14:35:38	956.550 55	401942205	37.66	34.94	32.96	47.11	136.86	-3.54	128.58	0.64	49.84	-113.24	8
T087	TI174	2012-11-13T10:22:08	973.650 52	406074195	39.17	31.65	38.91	52.92	146.05	-4.43	75.31	2.43	53.44	-111.4	10
T088	TI175	2012-11-29T08:56:59	1 014.693 4	407 451 486.1	39.66	29.98	28.63	58.32	157.04	-3.17	19.94	1.95	55.57	-109.87	6
T089	TI181	2013-02-17T01:56:35	1 978.042 3	414338262	42.19	40.74	38.25	68.48	113.47	-5.54	181.36				2
T090	TI185	2013-04-05T21:43:30	1 400.076 1	418 470 277.6	43.7	41.84	40.49	73.85	136.55	-7.03	49.82	0.06	0	-170.11	5
T091	TI190	2013-05-23T17:32:55	970.052 55	422 602 441.7	45.21	35.4	46.7	80.58	140.05	-6.98	94.14				1
T101	TI204	2014-05-17T16:12:15	2 991.882 4	453615202	56.4	40.69	38.55	67.89	-15.37	-6.79	130.88				3
T102	TI205	2014-06-18T13:28:25	3 658.690 5	456370172	57.39	36.77	44.8	75.21	-15.73	-7.18	120.87				2
T106	TI209	2014-10-24T02:40:30	1 013.168 4	467390497	61.32	33.76	35.88	66.44	-4.72	-5.55	50.22				3
T107	TI210	2014-12-10T22:26:35	980.572 19	471 522 462.4	62.79	40.16	31.86	59.21	-7.63	-1.5	90.91	7.58	80.23	73.43	5
T108	TI211	2015-01-11T19:48:35	970.385 16	474277782	63.77	39.07	27.95	52.07	-10.92	-4.77	31.13	2.13	-100.52	-108.37	5
T109	TI212	2015-02-12T17:08:04	1 200.149 1	477 032 951.1	64.75	24.41	22.94	42.12	-1.28	6.67	13.6				4
T112	TI218	2015-07-07T08:09:50	10 952.196	489 528 658.1	69.17	37.48	19.64	24.85	-26.09	-4.98	42.5				3
T114	TI225	2015-11-13T05:46:31	11 927.57	500 665 658.9	73.1	35.63	19.64	28.11	-25.85	-7.69	39.82				3
T116	TI231	2016-02-01T01:00:05	1 398.535 8	507 560 472.7	75.52	32.56	11.54	32.21	-25.06	-5.26	36.88				2

Appx. Table 5

(Continued)

Flyby	Rev	CA UTC	CA Altitude (km)	CA Ephemeris Time	Planetocentric Longitude of the Sun (L_S)	Average Incidence (deg)	Average Emission (deg)	Average Phase (deg)	Central Longitude (deg)	Average Latitude (deg)	Average Pixel Scale (km ²)	Tilt from North Pole (deg)	Prime Meridian Offset (deg, E+)	Subsolar Longitude Offset (deg, E+)	# of Longitude Bins
<i>Secondary 1</i>															
T062	TI119	2009-10-12T08:36:24	1 299.964 9	308 608 650.2	2.14	55.31	56.25	10.69	9.58	57.77	177.46	3.85	19.01	-20.12	10
T067	TI129	2010-04-05T15:50:54	7 437.318 4	323 754 719.8	8.06	49.14	50.53	14.42	21.25	47.94	79.58				3
T071	TI134	2010-07-07T00:22:45	1 004.078 5	331 734 231.1	11.16	49.9	39.91	34.91	159	32.32	84.03				3
T076	TI148	2011-05-08T22:53:44	1 872.807 1	358 167 290.5	21.28	46.32	51.75	46.18	34.07	47.25	64.11				3
T079	TI158	2011-12-13T20:11:23	3 583.241 3	377 079 149.2	28.41	43.06	52.61	18.97	142.38	52.31	55.65	1.56	60.19	-111.01	7
T082	TI161	2012-02-19T08:43:17	3 803.185	382 913 062.9	30.59	54.82	47.6	62.79	31.77	43.86	62.07				4
T098	TI201	2014-02-02T19:12:38	1 235.470 6	444640425	53.17	35.97	18.94	52.16	-148.08	51.55	94.63				4
T100	TI203	2014-04-07T13:41:14	963.449 34	450150141	55.16	33.88	14.63	34.86	-153.57	49.28	54.18	2.42	118.8	-64.74	6
T114	TI225	2015-11-13T05:46:31	11 927.57	500 665 658.9	73.1	29.19	51.91	27.2	-3.79	39.47	87.69				3
nT264	TI264	2017-03-05T11:44:03	489 890.93	541 986 902.8	87.57	29.73	18.25	42.71	-28.68	51.78	197.65	2.5	-114.84	-95.99	6
TI126	TI270	2017-04-22T05:52:13	980.236 27	546 113 356.1	89.01	61.52	52.98	111.94	52.75	47.52	99.6				4
<i>Secondary 2</i>															
T00A	TI00A	2004-10-26T15:30:05	1 174.330 6	152076669	297.26	43.1	23.85	19.58	-159.81	18.68	89.13				1
T008	TI017	2005-10-28T04:15:25	1 352.876 1	183 744 988.8	310.81	42.52	21.73	23.16	-163.23	9.42	62.06				3
T036	TI050	2007-10-02T04:42:43	973.489 1	244 572 228.1	336.33	53.8	26.32	32.28	136.42	18.44	89.87				4
T037	TI052	2007-11-19T00:47:25	999.652 91	248705310	338.03	48.99	16.04	39.58	145.28	17.64	36.84				2
T071	TI134	2010-07-07T00:22:45	1 004.078 5	331 734 231.1	11.16	49.9	39.91	34.91	159	32.32	84.03				3
T083	TI166	2012-05-22T01:10:11	953.990 5	390 921 076.9	33.58	23.06	27.05	22.14	130.19	11.54	70.46				1

Appx. Table 5

(Continued)

Flyby	Rev	CA UTC	CA Altitude (km)	CA Ephemeris Time	Planetocentric Longitude of the Sun (L_S)	Average Incidence (deg)	Average Emission (deg)	Average Phase (deg)	Central Longitude (deg)	Average Latitude (deg)	Average Pixel Scale (km ²)	Tilt from North Pole (deg)	Prime Meridian Offset (deg, E+)	Subsolar Longitude Offset (deg, E+)	# of Longitude Bins
T098	TI201	2014-02-02T19:12:38	1 235.470 6	444640425	53.17	40.17	47.3	52.26	-127.24	15.44	120.7	0.55	-0.04	178.74	6
T099	TI202	2014-03-06T16:26:47	1 499.789 9	447395274	54.16	28.64	38.65	43.33	-133.43	19.24	169.07	0.17	-0.01	177.61	7
T100	TI203	2014-04-07T13:41:14	963.449 34	450150141	55.16	27.94	37.78	35.19	-135.75	15.4	61.86	0.04	0	176.46	10
T107	TI210	2014-12-10T22:26:35	980.572 19	471 522 462.4	62.79	20.67	51.04	59.5	-5.6	18.36	109.36				2
T108	TI211	2015-01-11T19:48:35	970.385 16	474277782	63.77	27.07	45.83	52.46	-10.82	20.07	33.53	1.65	-104.06	-111.91	9
T109	TI212	2015-02-12T17:08:04	1 200.149 1	477 032 951.1	64.75	45.53	29.88	41.8	-32.66	8.94	17.44				4
T110	TI213	2015-03-16T12:59:36	2 274.981 7	479 788 255.4	65.72	33.43	19.31	36.4	-18.59	17.67	13.92	4.38	-119.6	-129.61	5
T111	TI215	2015-05-07T20:38:58	2 722.237 4	484 311 090.4	67.33	49.1	23.16	65.69	-134.97	17.69	22.26	2.79	135.65	-134.3	8
T112	TI218	2015-07-07T08:09:50	10 952.196	489 528 658.1	69.17	25.45	24.21	25.75	-15.88	19.14	58.49	2.19	-104.01	-92.53	6
T114	TI225	2015-11-13T05:46:31	11 927.57	500 665 658.9	73.1	28.62	17.41	29.66	-38.52	-1.47	34.56				3
T116	TI231	2016-02-01T01:00:05	1 398.535 8	507 560 472.7	75.52	19.62	27.91	32.81	-23.67	14.43	37.39	6.03	-109.79	-73.44	5
T119	TI235	2016-05-06T16:54:37	969.201 5	515 825 744.7	78.42	27.94	35.09	53.8	-0.16	8.45	119				1
T124	TI248	2016-11-13T23:55:56	1 585.323 9	532 353 423.8	84.21	41.82	40.87	69.7	-55.84	2.88	44.31				4
T125	TI250	2016-11-29T19:16:29	3 159.020 5	533729740	84.69	47.79	37.41	68.32	-66.49	10.38	32.4	1.33	-150.44	-126.03	5
TI126	TI270	2017-04-22T05:52:13	980.236 27	546 113 356.1	89.01	41.7	35.65	72.13	-35.69	-0.04	96.66				4
nT275	TI275	2017-05-24T03:17:28	117 952.41	548 857 163.5	89.97	48.78	36.63	84.56	15.09	8.46	105.94	0.67	-108.8	-97.37	8
Flyby	Rev	CA UTC	CA Altitude (km)	CA Ephemeris Time	Planetocentric Longitude of the Sun (L_S)	Average Incidence (Deg)	Average Emission (Deg)	Average Phase (Deg)	Central Longitude (Deg)	Average Latitude (Deg)	Average Pixel Scale (km ²)	Tilt from North Pole (Deg)	Prime Meridian Offset (Deg, E+)	Subsolar Longitude Offset (Deg, E+)	# of Longitude Bins
<i>Secondary 3</i>															
T003	TI003	2005-02-15T06:57:53	1 578.974 6	161 722 737.3	301.4	10.35	20.03	13.59	-148.7	-29.78	72.81				3
T011	TI021	2006-02-27T08:25:18	1 812.311 4	194 300 783.6	315.29	15.55	32.18	18.38	7.64	-25.94	125.32				3

Appx. Table 5
(Continued)

Flyby	Rev	CA UTC	CA Altitude (km)	CA Ephemeris Time	Planetocentric Longitude of the Sun (L_S)	Average Incidence (deg)	Average Emission (deg)	Average Phase (deg)	Central Longitude (deg)	Average Latitude (deg)	Average Pixel Scale (km ²)	Tilt from North Pole (deg)	Prime Meridian Offset (deg, E+)	Subsolar Longitude Offset (deg, E+)	# of Longitude Bins
T012	TI022	2006-03-19T00:05:55	1 949.351	195 998 820.6	316.02	31.28	41.31	64.45	-122.88	-26.71	48.22				3
T016	TI026	2006-07-22T00:25:26	950.385 67	206799991	320.6	45.94	28.08	59.47	4.49	-31.95	82.84				2
T017	TI028	2006-09-07T20:16:51	999.713 19	210932276	322.33	41.31	25.19	62.02	6.07	-23.94	21.08				3
T018	TI029	2006-09-23T18:58:48	960.198 92	212 309 993.5	322.92	47.84	18.47	64.22	10.72	-23.87	63.13				3
T051	TI106	2009-03-27T04:43:36	962.880 46	291 401 082.3	355.29	42.79	36.92	75.28	-107.51	-24.36	80.09				2
T057	TI113	2009-06-22T18:32:35	955.214 66	298967621	358.32	24.51	18.63	36.77	20.08	-23.85	77.08				1
T058	TI114	2009-07-08T17:04:03	966.055 3	300 344 709.3	358.86	35.98	24.14	30.34	58.67	-24.23	30.11				2
T059	TI115	2009-07-24T15:34:03	956.582 69	301 721 709.1	359.41	28.23	15.84	22.8	49.48	-23.33	22.78				1
T061	TI117	2009-08-25T12:51:37	960.837 48	304 476 763.6	0.5	30.99	28.2	12.2	45.19	-26.49	32.74				4
T063	TI122	2009-12-12T01:03:14	4 847.710 8	313 851 859.8	4.19	30.28	53.4	46.94	106.41	-27.7	87.95				2
T065	TI124	2010-01-12T23:10:36	1 074.516	316 609 901.9	5.27	29.97	62.21	45.54	90.52	-21.79	47.31				1
T066	TI125	2010-01-28T22:28:50	7 486.939 1	317 989 795.7	5.81	39.02	24.26	43.33	133.47	-23.01	74.77				2
T069	TI132	2010-06-05T02:26:27	2 042.953	328976853	10.09	34.6	25.14	30.69	139.53	-21.67	65.6				1
T077	TI149	2011-06-20T18:32:00	1 358.992 4	361 866 786.6	22.68	41.51	27.69	19.81	154.84	-24.27	40.69				2
T079	TI158	2011-12-13T20:11:23	3 583.241 3	377 079 149.2	28.41	58.13	41.55	17.39	114.06	-20.86	53.9				3
T081	TI160	2012-01-30T13:39:48	31 130.577	381 202 854.1	29.96	33.83	13.47	26.56	168.42	-19.1	71.5				2
T083	TI166	2012-05-22T01:10:11	953.990 5	390 921 076.9	33.58	42.22	24.31	21.56	128.95	-19.66	71.22				4
T084	TI167	2012-06-07T00:07:21	959.347 58	392 299 706.8	34.09	38.28	12.95	28.22	157.57	-21.09	96.53				3
T085	TI169	2012-07-24T20:03:07	1 012.449 8	396 432 253.9	35.61	36.79	10.44	32.69	158.09	-20.02	18.46				4
T087	TI174	2012-11-13T10:22:08	973.650 52	406074195	39.17	39.67	17.95	52.68	148.72	-20.43	66.26	0.01	0	-164.84	5
<i>Secondary 4</i>															
T009	TI019	2005-12-26T18:59:26	10 411.572	188895630	313.01	38.4	50.36	27.69	-6.32	-47.47	91.9	1.5	-95.39	-50.92	6

Appx. Table 5
(Continued)

Flyby	Rev	CA UTC	CA Altitude (km)	CA Ephemeris Time	Planetocentric Longitude of the Sun (L_S)	Average Incidence (deg)	Average Emission (deg)	Average Phase (deg)	Central Longitude (deg)	Average Latitude (deg)	Average Pixel Scale (km ²)	Tilt from North Pole (deg)	Prime Meridian Offset (deg, E+)	Subsolar Longitude Offset (deg, E+)	# of Longitude Bins
T067	TI129	2010-04-05T15:50:54	7 437.318 4	323 754 719.8	8.06	53.98	50.28	15.17	18.87	-49.93	93.38	2.03	118.44	71.79	5
T119	TI235	2016-05-06T16:54:37	969.201 5	515 825 744.7	78.42	68.6	30.91	53.39	-31.99	-42.65	102.99	0.08	0.02	32.94	9
T120	TI236	2016-06-07T14:06:17	974.555 42	518 580 444.9	79.39	78.03	26.04	61.43	-30.34	-45.19	91.13	0.05	0.01	31.69	8
T121	TI238	2016-07-25T09:58:23	975.407 36	522 712 770.8	80.84	74.49	26.02	67	-55.69	-42.04	68.73	4.08	40.08	69.96	5
T123	TI243	2016-09-27T04:16:59	1 775.659 2	528221887	82.77	61.07	19.08	69.09	-41.39	-44.94	74.66	0.34	-127.27	-99.96	6
T124	TI248	2016-11-13T23:55:56	1 585.323 9	532 353 423.8	84.21	67.14	19.3	68.96	-39.1	-45.93	48.12	2.55	60.25	85.55	7

Note. A digital version of this table can be provided upon request to the first author.

Appx. Table 6
Coefficients for the functions displayed in Figure 24

Figure 24(A)	Coefficients								
	R^2	$\Delta I/F_0$	$P_{95\%}$	$d\Delta I/F$	$P_{95\%}$	Period (P)	$P_{95\%}$	Phase (ψ)	$P_{95\%}$
EQA Max (EQ 1)	0.567 134 084	0.001 045 799	(0.0009755, 0.001 116)	0.000 505 815	(0.0004142, 0.000 597 4)	108.714 098 7	(96.42, 121)	46.645 061 2	(34.78, 58.51)
EQA Min (EQ 1)	0.555 180 381	-0.000800664	(-0.0008791, -0.0007223)	-0.000584556	(-0.0006903, -0.0004788)	97.275 427 31	(88.58, 106)	62.814 466 72	(51.65, 73.98)
		$d(I/F)/dL_S$	$P_{95\%}$	$\Delta I/F(L_S(0))$	$P_{95\%}$				
NPA Max (EQ 2)	0.831 186 229	-2.10E-05	(-2.777e-05, -1.419e-05)	0.002 185 821	(0.001763, 0.002 608)				
NPA Min (EQ 2)	0.383 779 961	-2.79E-05	(-3.853e-05, -1.729e-05)	0.001 040 415	(0.0003801, 0.001 701)				
Figure 24(B)	Coefficients								
	R^2	$d\lambda/dL_S$	$P_{95\%}$	$\lambda(L_S(0))$	$P_{95\%}$				
EQA Max (EQ 3)	0.534 429 624	9.02E-05	(-0.0002733, 0.000 453 8)	0.880 850 658	(0.8689, 0.892 8)				
EQA Min (EQ 3)	0.952 738 203	-2.19E-05	(-0.000729, 0.000 685 3)	0.519 985 156	(0.4967, 0.543 3)				
NPA Max (EQ 3)	0.618 118 166	0.004 308 898	(0.000602, 0.008 016)	0.625 063 359	(0.3945, 0.855 6)				
NPA Min (EQ 3)	0.898 577 491	5.36E-06	(-0.005123, 0.005 134)	0.497 419 496	(0.1785, 0.816 4)				

Note. The columns labeled $P_{95\%}$ are the 95th percentile confidence bounds of the coefficients in the respective columns to the left.

EQ1) $\Delta I/F = \Delta I/F_0 + d\Delta I/F \sin(L_S/P + \psi)$

EQ2) $\Delta I/F = \Delta I/F(L_S(0)) + d(I/F)/dL_S \times L_S$

EQ3) $\lambda = \lambda(L_S(0)) + d\lambda/(dL_S) \times L_S$

References

- Aartsen, M. G., R. Abbasi, Y. Abdou, M. Ackermann, J. Adams, J. A. Aguilar, M. Ahlers, *et al.* "Measurement of South Pole Ice Transparency with the Icecube Led Calibration System." *Nuclear Instruments and Methods in Physics Research A* 711 (May 01, 2013 2013): 73. <https://doi.org/10.1016/j.nima.2013.01.054>. <https://ui.adsabs.harvard.edu/abs/2013NIMPA.711...73A>.
- Achterberg, Richard K., Barney J. Conrath, Peter J. Gierasch, F. Michael Flasar, and Conor A. Nixon. "Observation of a Tilt of Titan's Middle-Atmospheric Superrotation." *Icarus* 197, no. 2 (2008): 549-55. <https://doi.org/10.1016/j.icarus.2008.05.014>.
- Achterberg, Richard K., Peter J. Gierasch, Barney J. Conrath, F. Michael Flasar, and Conor A. Nixon. "Temporal Variations of Titan's Middle-Atmospheric Temperatures from 2004 to 2009 Observed by Cassini/CIRS." *Icarus* 211, no. 1 (2011): 686-98. <https://doi.org/10.1016/j.icarus.2010.08.009>.
- Acton, Charles, Nathaniel Bachman, Boris Semenov, and Edward Wright. "A Look Towards the Future in the Handling of Space Science Mission Geometry." *Planetary and Space Science* 150 (January 01, 2018 2018): 9-12. <https://doi.org/10.1016/j.pss.2017.02.013>. <https://ui.adsabs.harvard.edu/abs/2018P&SS..150....9A>.
- Ádámkóvics, Máté, Jonathan L. Mitchell, Alexander G. Hayes, Patricio M. Rojo, Paul Corlies, Jason W. Barnes, Valentin D. Ivanov, *et al.* "Meridional Variation in Tropospheric Methane on Titan Observed with Ao Spectroscopy at Keck and Vlt." *Icarus* 270 (2016): 376-88. <https://doi.org/10.1016/j.icarus.2015.05.023>.
- Bagenal, Fran. "Giant Planet Magnetospheres." *Annual Review of Earth and Planetary Sciences* 20, no. 1 (1992): 289-328.
- Barnes, Jason W., Jacob Bow, Jacob Schwartz, Robert H. Brown, Jason M. Soderblom, Alexander G. Hayes, Graham Vixie, *et al.* "Organic Sedimentary Deposits in Titan's Dry Lakebeds: Probable Evaporite." *Icarus* 216 (November 01, 2011 2011): 136-40. <https://doi.org/10.1016/j.icarus.2011.08.022>. <https://ui.adsabs.harvard.edu/abs/2011Icar..216..136B>.
- Barnes, Jason W., Robert H. Brown, Jani Radebaugh, Bonnie J. Buratti, Christophe Sotin, Stéphane Le Mouélic, Sébastien Rodriguez, *et al.* "Cassini Observations of Flow-Like Features in Western Tui Regio, Titan." *Geophysical Research Letters* 33 (August 01, 2006 2006): L16204. <https://doi.org/10.1029/2006gl026843>. <https://ui.adsabs.harvard.edu/abs/2006GeoRL..3316204B>.
- Barnes, Jason W., Robert H. Brown, Laurence Soderblom, Bonnie J. Buratti, Christophe Sotin, Sébastien Rodriguez, Stéphane Le Mouélic, *et al.* "Global-Scale Surface Spectral Variations on Titan Seen from Cassini/Vims." *Icarus* 186 (January 01, 2007 2007): 242-58. <https://doi.org/10.1016/j.icarus.2006.08.021>. <https://ui.adsabs.harvard.edu/abs/2007Icar..186..242B>.
- Barnes, Jason W., Robert H. Brown, Laurence Soderblom, Christophe Sotin, Stéphane Le Mouélic, Sébastien Rodriguez, Ralf Jaumann, *et al.* "Spectroscopy, Morphometry, and Photoclinometry of Titan's Dunefields from Cassini/Vims." *Icarus* 195 (May 01, 2008

- 2008): 400-14. <https://doi.org/10.1016/j.icarus.2007.12.006>.
<https://ui.adsabs.harvard.edu/abs/2008Icar..195..400B>.
- Barnes, Jason W., Ralph D. Lorenz, Jani Radebaugh, Alexander G. Hayes, Karl Arnold, and Clayton Chandler. "Production and Global Transport of Titan's Sand Particles." *Planetary Science* 4 (December 01, 2015 2015): 1. <https://doi.org/10.1186/s13535-015-0004-y>.
<https://ui.adsabs.harvard.edu/abs/2015PISci...4....1B>.
- Barnes, Jason W., Jani Radebaugh, Robert H. Brown, Steve Wall, Laurence Soderblom, Jonathan Lunine, Devon Burr, *et al.* "Near-Infrared Spectral Mapping of Titan's Mountains and Channels." *Journal of Geophysical Research (Planets)* 112 (November 01, 2007 2007): E11006. <https://doi.org/10.1029/2007je002932>.
<https://ui.adsabs.harvard.edu/abs/2007JGRE..11211006B>.
- Battalio, J. Michael, and Juan M. Lora. "Annular Modes of Variability in the Atmospheres of Mars and Titan." *Nature Astronomy* 5 (August 01, 2021 2021): 1139-47.
<https://doi.org/10.1038/s41550-021-01447-4>.
<https://ui.adsabs.harvard.edu/abs/2021NatAs...5.1139B>.
- Battalio, Joseph Michael, and Juan Manuel Lora. "Global Impacts from High-Latitude Storms on Titan." *Geophysical Research Letters* 48 (September 01, 2021 2021): e94244.
<https://doi.org/10.1029/2021gl094244>.
<https://ui.adsabs.harvard.edu/abs/2021GeoRL..4894244B>.
- Battalio, J. Michael, Juan M. Lora, Scot Rafkin, and Alejandro Soto. "The Interaction of Deep Convection with the General Circulation in Titan's Atmosphere. Part 2: Impacts on the Climate." *Icarus* 373 (February 01, 2022 2022): 114623.
<https://doi.org/10.1016/j.icarus.2021.114623>.
<https://ui.adsabs.harvard.edu/abs/2022Icar..37314623B>.
- BenZvi, S. Y., B. M. Connolly, J. A. J. Matthews, M. Prouza, E. F. Visbal, and S. Westerhoff. "Measurement of the Aerosol Phase Function at the Pierre Auger Observatory." *Astroparticle Physics* 28 (November 01, 2007 2007): 312.
<https://doi.org/10.1016/j.astropartphys.2007.06.005>.
<https://ui.adsabs.harvard.edu/abs/2007APh....28..312B>.
- Bertrand, Tanguy, and François Forget. "3d Modeling of Organic Haze in Pluto's Atmosphere." *Icarus* 287 (2017): 72-86. <https://doi.org/10.1016/j.icarus.2017.01.016>.
- Birch, Cathryn E., John H. Marsham, Douglas J. Parker, and Christopher M. Taylor. "The Scale Dependence and Structure of Convergence Fields Preceding the Initiation of Deep Convection." *Geophysical Research Letters* 41 (July 01, 2014 2014): 4769-76.
<https://doi.org/10.1002/2014gl060493>.
<https://ui.adsabs.harvard.edu/abs/2014GeoRL..41.4769B>.
- Bourassa, A. E., D. A. Degenstein, and E. J. Llewellyn. "Retrieval of Stratospheric Aerosol Size Information from Osiris Limb Scattered Sunlight Spectra." *Atmospheric Chemistry & Physics* 8 (November 01, 2008 2008): 6375.
<https://ui.adsabs.harvard.edu/abs/2008ACP.....8.6375B>.
- Broadfoot, A. L., B. R. Sandel, D. E. Shemansky, J. B. Holberg, G. R. Smith, D. F. Strobel, J. C.

- McConnell, *et al.* "Extreme Ultraviolet Observations from Voyager 1 Encounter with Saturn." *Science* 212 (April 01, 1981 1981): 206-11.
<https://doi.org/10.1126/science.212.4491.206>.
<https://ui.adsabs.harvard.edu/abs/1981Sci...212..206B>.
- Brossier, J. F., S. Rodriguez, T. Cornet, A. Lucas, J. Radebaugh, L. Maltagliati, S. Le Mouélic, *et al.* "Geological Evolution of Titan's Equatorial Regions: Possible Nature and Origin of the Dune Material." *Journal of Geophysical Research (Planets)* 123 (May 01, 2018 2018): 1089-112. <https://doi.org/10.1029/2017je005399>.
<https://ui.adsabs.harvard.edu/abs/2018JGRE..123.1089B>.
- Brown, Michael E., Antonin H. Bouchez, and Caitlin A. Griffith. "Direct Detection of Variable Tropospheric Clouds near Titan's South Pole." *Nature* 420 (December 01, 2002 2002): 795. <https://doi.org/10.1038/nature01302>.
<https://ui.adsabs.harvard.edu/abs/2002Natur.420..795B>.
- Brown, R. H., K. H. Baines, G. Bellucci, J. -P. Bibring, B. J. Buratti, F. Capaccioni, P. Cerroni, *et al.* "The Cassini Visual and Infrared Mapping Spectrometer (Vims) Investigation." *Space Science Reviews* 115 (December 01, 2004 2004): 111.
<https://doi.org/10.1007/s11214-004-1453-x>.
<https://ui.adsabs.harvard.edu/abs/2004SSRv..115..111B>.
- Buie, Marc W., William M. Grundy, Eliot F. Young, Leslie A. Young, and S. Alan Stern. "Pluto and Charon with the Hubble Space Telescope. Ii. Resolving Changes on Pluto's Surface and a Map for Charon." *The Astronomical Journal* 139 (March 01, 2010 2010): 1128.
<https://doi.org/10.1088/0004-6256/139/3/1128>.
<https://ui.adsabs.harvard.edu/abs/2010AJ....139.1128B>.
- Buratti, B. J., J. D. Hofgartner, M. D. Hicks, H. A. Weaver, S. A. Stern, T. Momary, J. A. Mosher, *et al.* "Global Albedos of Pluto and Charon from Lorri New Horizons Observations." *Icarus* 287 (May 01, 2017 2017): 207.
<https://doi.org/10.1016/j.icarus.2016.11.012>.
<https://ui.adsabs.harvard.edu/abs/2017Icar..287..207B>.
- Cabane, M., P. Rannou, E. Chassefiere, and G. Israel. "Fractal Aggregates in Titan's Atmosphere." *Planetary and Space Science* 41 (April 01, 1993 1993): 257-67.
[https://doi.org/10.1016/0032-0633\(93\)90021-s](https://doi.org/10.1016/0032-0633(93)90021-s).
<https://ui.adsabs.harvard.edu/abs/1993P&SS...41..257C>.
- Caldwell, John, Cindy C. Cunningham, David Anthony, H. P. White, E. J. Groth, H. Hasan, K. Noll, *et al.* "Titan: Evidence for Seasonal Change—a Comparison of Hubble Space Telescope and Voyager Images." *Icarus* 97 (May 01, 1992 1992): 1.
[https://doi.org/10.1016/0019-1035\(92\)90053-a](https://doi.org/10.1016/0019-1035(92)90053-a).
<https://ui.adsabs.harvard.edu/abs/1992Icar...97....1C>.
- Catling, David C., and James F. Kasting. *Atmospheric Evolution on Inhabited and Lifeless Worlds*. April 01, 2017, 2017. <https://ui.adsabs.harvard.edu/abs/2017aeil.book.....C>.
- Charlot, P., C. S. Jacobs, D. Gordon, S. Lambert, A. de Witt, J. Böhm, A. L. Fey, *et al.* "The Third Realization of the International Celestial Reference Frame by Very Long Baseline

- Interferometry." *Astronomy & Astrophysics* 644 (2020): 28.
<https://doi.org/10.1051/0004-6361/202038368>.
- Charnay, Benjamin, Erika Barth, Scot Rafkin, Clément Narteau, Sébastien Lebonnois, Sébastien Rodriguez, Sylvain Courrech Du Pont, and Antoine Lucas. "Methane Storms as a Driver of Titan's Dune Orientation." *Nature Geoscience* 8 (May 01, 2015 2015): 362-66.
<https://doi.org/10.1038/ngeo2406>.
<https://ui.adsabs.harvard.edu/abs/2015NatGe...8..362C>.
- Cheng, A. F., M. E. Summers, G. R. Gladstone, D. F. Strobel, L. A. Young, P. Lavvas, J. A. Kammer, *et al.* "Haze in Pluto's Atmosphere." *Icarus* 290 (July 01, 2017 2017): 112.
<https://doi.org/10.1016/j.icarus.2017.02.024>.
<https://ui.adsabs.harvard.edu/abs/2017Icar..290..112C>.
- Clark, Roger N, Robert H Brown, Dyer M Lytle, and Matt Hedman. "The Vims Wavelength and Radiometric Calibration 19, Final Report." *NASA Planetary Data System* (2018).
- Clark, Roger N., John M. Curchin, Jason W. Barnes, Ralf Jaumann, Larry Soderblom, Dale P. Cruikshank, Robert H. Brown, *et al.* "Detection and Mapping of Hydrocarbon Deposits on Titan." *Journal of Geophysical Research (Planets)* 115 (October 01, 2010 2010): E10005. <https://doi.org/10.1029/2009je003369>.
<https://ui.adsabs.harvard.edu/abs/2010JGRE..11510005C>.
- Cleveland, William S. "Robust Locally Weighted Regression and Smoothing Scatterplots." *Journal of American Statistical Association* 74, no. 368 (1979): 829-36.
<https://doi.org/10.1080/01621459.1979.10481038>.
- Cordier, D., T. Cornet, J. W. Barnes, S. M. MacKenzie, T. Le Bahers, D. Nna-Mvondo, P. Rannou, and A. G. Ferreira. "Structure of Titan's Evaporites." *Icarus* 270 (May 01, 2016 2016): 41-56. <https://doi.org/10.1016/j.icarus.2015.12.034>.
<https://ui.adsabs.harvard.edu/abs/2016Icar..270...41C>.
- Corlies, P., A. G. Hayes, S. P. D. Birch, R. Lorenz, B. W. Stiles, R. Kirk, V. Poggiali, H. Zebker, and L. Iess. "Titan's Topography and Shape at the End of the Cassini Mission." *Geophysical Research Letters* 44 (December 01, 2017 2017): 11,754-11,61.
<https://doi.org/10.1002/2017gl075518>.
<https://ui.adsabs.harvard.edu/abs/2017GeoRL..4411754C>.
- Corlies, Paul, George D. McDonald, Alexander G. Hayes, James J. Wray, Máté Ádámkóvics, Michael J. Malaska, Morgan L. Cable, *et al.* "Modeling Transmission Windows in Titan's Lower Troposphere: Implications for Infrared Spectrometers Aboard Future Aerial and Surface Missions." *Icarus* 357 (March 01, 2021 2021): 114228.
<https://doi.org/10.1016/j.icarus.2020.114228>.
<https://ui.adsabs.harvard.edu/abs/2021Icar..35714228C>.
- Cornette, William M., and Joseph G. Shanks. "Physically Reasonable Analytic Expression for the Single-Scattering Phase Function." *Applied Optics* 31 (June 01, 1992 1992): 3152.
<https://doi.org/10.1364/ao.31.003152>.
<https://ui.adsabs.harvard.edu/abs/1992ApOpt..31.3152C>.
- Cunnold, D. M., C. R. Gray, and D. C. Merritt. "Stratospheric Aerosol Layer Detection." *Journal*

- of Geophysical Research* 78 (February 01, 1973 1973): 920.
<https://doi.org/10.1029/JC078i006p00920>.
<https://ui.adsabs.harvard.edu/abs/1973JGR....78..920C>.
- Czaplinski, Ellen, Xinting Yu, Katherine Dzurilla, and Vincent Chevrier. "Experimental Investigation of the Acetylene-Benzene Cocrystal on Titan." *The Planetary Science Journal* 1 (December 01, 2020 2020): 76. <https://doi.org/10.3847/PSJ/abfb57>.
<https://ui.adsabs.harvard.edu/abs/2020PSJ.....1...76C>.
- de Kok, R., P. G. J. Irwin, N. A. Teanby, S. Vinatier, F. Tosi, A. Negrão, S. Osprey, *et al.* "A Tropical Haze Band in Titan's Stratosphere." *Icarus* 207, no. 1 (2010): 485-90.
<https://doi.org/10.1016/j.icarus.2009.10.021>.
- Degenstein, D. A., A. E. Bourassa, C. Z. Roth, and E. J. Llewellyn. "Limb Scatter Ozone Retrieval from 10 to 60 Km Using a Multiplicative Algebraic Reconstruction Technique." *Atmospheric Chemistry & Physics* 9 (September 01, 2009 2009): 6521.
<https://ui.adsabs.harvard.edu/abs/2009ACP.....9.6521D>.
- Draine, B. T. "Interstellar Dust Grains." *Annual Review of Astronomy and Astrophysics* 41 (January 01, 2003 2003): 241. <https://doi.org/10.1146/annurev.astro.41.011802.094840>.
<https://ui.adsabs.harvard.edu/abs/2003ARA&A..41..241D>.
- Elachi, C., M. D. Allison, L. Borgarelli, P. Encrenaz, E. Im, M. A. Janssen, W. T. K. Johnson, *et al.* "Radar: The Cassini Titan Radar Mapper." *Space Science Reviews* 115 (December 01, 2004 2004): 71-110. <https://doi.org/10.1007/s11214-004-1438-9>.
<https://ui.adsabs.harvard.edu/abs/2004SSRv..115...71E>.
- Elliot, J. L., A. Ates, B. A. Babcock, A. S. Bosh, M. W. Buie, K. B. Clancy, E. W. Dunham, *et al.* "The Recent Expansion of Pluto's Atmosphere." *Nature* 424 (July 01, 2003 2003): 165. <https://doi.org/10.1038/nature01762>.
<https://ui.adsabs.harvard.edu/abs/2003Natur.424..165E>.
- Filacchione, G., F. Capaccioni, T. B. McCord, A. Coradini, P. Cerroni, G. Bellucci, F. Tosi, *et al.* "Saturn's Icy Satellites Investigated by Cassini-Vims." *Icarus* 186, no. 1 (2007): 259-90. <https://doi.org/10.1016/j.icarus.2006.08.001>.
- . "Saturn's Icy Satellites Investigated by Cassini-Vims. I. Full-Disk Properties: 350 5100 Nm Reflectance Spectra and Phase Curves." *Icarus* 186 (January 01, 2007 2007): 259-90. <https://doi.org/10.1016/j.icarus.2006.08.001>.
<https://ui.adsabs.harvard.edu/abs/2007Icar..186..259F>.
- Flasar, F. M., and R. K. Achterberg. "The Structure and Dynamics of Titan's Middle Atmosphere." *Philos Trans A Math Phys Eng Sci* 367, no. 1889 (Feb 28 2009): 649-64. <https://doi.org/10.1098/rsta.2008.0242>. <https://www.ncbi.nlm.nih.gov/pubmed/19073460>.
- Fletcher, L. N., Y. Kaspi, T. Guillot, and A. P. Showman. "How Well Do We Understand the Belt/Zone Circulation of Giant Planet Atmospheres?". *Space Sci Rev* 216, no. 2 (2020): 30. <https://doi.org/10.1007/s11214-019-0631-9>.
<https://www.ncbi.nlm.nih.gov/pubmed/32214508>.
- Flittner, D. E., P. K. Bhartia, and B. M. Herman. "O₃ Profiles Retrieved from

- Limb Scatter Measurements: Theory." *Geophysical Research Letters* 27 (September 01, 2000 2000): 2601. <https://doi.org/10.1029/1999gl011343>.
<https://ui.adsabs.harvard.edu/abs/2000GeoRL..27.2601F>.
- Galilei, Galileo. *Sidereus Nuncius Magna, Longeque Admirabilia Spectacula Pandens Lunae Facie, Fixis Innumeris, Lacteo Circulo, Stellis Nebulosis, ... Galileo Galileo : Nuper a Se Reperti Beneficio Sunt Observata in Apprime Vero in Quatuor Planetis Circa Iovis Stellam Disparibus Intervallis, Atque Periodis, Celeritate Mirabili Circumvolutis ... Atque Medicea Sidera Nuncupandos Decrevit*. January 01, 1610, 1610.
doi:10.3931/e-rara-695. <https://ui.adsabs.harvard.edu/abs/1610snml.book.....G>.
- Gao, Peter, Siteng Fan, Michael L. Wong, Mao-Chang Liang, Run-Lie Shia, Joshua A. Kammer, Yuk L. Yung, *et al.* "Constraints on the Microphysics of Pluto's Photochemical Haze from New Horizons Observations." *Icarus* 287 (May 01, 2017 2017): 116.
<https://doi.org/10.1016/j.icarus.2016.09.030>.
<https://ui.adsabs.harvard.edu/abs/2017Icar..287..116G>.
- Gierasch, P. J. "Meridional Circulation and the Maintenance of the Venus Atmospheric Rotation." *Journal of Atmospheric Sciences* 32 (June 01, 1975 1975): 1038.
[https://doi.org/10.1175/1520-0469\(1975\)032<1038:Mcatmo>2.0.Co;2](https://doi.org/10.1175/1520-0469(1975)032<1038:Mcatmo>2.0.Co;2).
<https://ui.adsabs.harvard.edu/abs/1975JAtS...32.1038G>.
- Gladstone, G. Randall, S. Alan Stern, Kimberly Ennico, Catherine B. Olkin, Harold A. Weaver, Leslie A. Young, Michael E. Summers, *et al.* "The Atmosphere of Pluto as Observed by New Horizons." *Science* 351 (March 01, 2016 2016): aad8866.
<https://doi.org/10.1126/science.aad8866>.
<https://ui.adsabs.harvard.edu/abs/2016Sci...351.8866G>.
- Gladstone, G. Randall, and Leslie A. Young. "New Horizons Observations of the Atmosphere of Pluto." *Annual Review of Earth and Planetary Sciences* 47 (May 01, 2019 2019): 119.
<https://doi.org/10.1146/annurev-earth-053018-060128>.
<https://ui.adsabs.harvard.edu/abs/2019AREPS..47..119G>.
- Goody, Richard, Robert West, Luke Chen, and David Crisp. "The Correlated-K Method for Radiation Calculations in Nonhomogeneous Atmospheres." *Journal of Quantitative Spectroscopy and Radiative Transfer* 42 (December 01, 1989 1989): 539.
[https://doi.org/10.1016/0022-4073\(89\)90044-7](https://doi.org/10.1016/0022-4073(89)90044-7).
<https://ui.adsabs.harvard.edu/abs/1989JQSRT..42..539G>.
- Grainger, Roy Gordon. Some Useful Formulae for Aerosol Size Distributions and Optical Properties. <http://eodg.atm.ox.ac.uk/user/grainger/research/aerosols.pdf>.
- Griffith, Caitlin A., Christopher P. McKay, and Francesca Ferri. "Titan's Tropical Storms in an Evolving Atmosphere." *The Astrophysical Journal* 687 (November 01, 2008 2008): L41.
<https://doi.org/10.1086/593117>. <https://ui.adsabs.harvard.edu/abs/2008ApJ...687L..41G>.
- Griffith, Caitlin A., Tobias Owen, Thomas R. Geballe, John Rayner, and Pascal Rannou. "Evidence for the Exposure of Water Ice on Titan's Surface." *Science* 300 (April 01, 2003 2003): 628-30. <https://doi.org/10.1126/science.1081897>.
<https://ui.adsabs.harvard.edu/abs/2003Sci...300..628G>.

- Griffith, Caitlin A., Paulo F. Penteadó, Jake D. Turner, Catherine D. Neish, Giuseppe Mitri, Nicholas J. Montiel, Ashley Schoenfeld, and Rosaly M. C. Lopes. "A Corridor of Exposed Ice-Rich Bedrock across Titan's Tropical Region." *Nature Astronomy* 3 (April 01, 2019 2019): 642-48. <https://doi.org/10.1038/s41550-019-0756-5>.
<https://ui.adsabs.harvard.edu/abs/2019NatAs...3..642G>.
- Hanel, R., B. Conrath, F. M. Flasar, V. Kunde, W. Maguire, J. C. Pearl, J. Pirraglia, *et al.* "Infrared Observations of the Saturnian System from Voyager 1." *Science* 212 (April 01, 1981 1981): 192-200. <https://doi.org/10.1126/science.212.4491.192>.
<https://ui.adsabs.harvard.edu/abs/1981Sci...212..192H>.
- Hapke, B. "Bidirectional Reflectance Spectroscopy. 1. Theory." *Journal of Geophysical Research* 86 (June 01, 1981 1981): 4571.
<https://ui.adsabs.harvard.edu/abs/1981JGR....86.4571H>.
- Hayes, Alexander G., Jason M. Soderblom, and Máté Ádámkóvics. "Titan's Surface and Atmosphere." *Icarus* 270 (May 01, 2016 2016): 1-1.
<https://doi.org/10.1016/j.icarus.2016.02.029>.
<https://ui.adsabs.harvard.edu/abs/2016Icar..270....1H>.
- Henyey, L. G., and J. L. Greenstein. "Diffuse Radiation in the Galaxy." *The Astrophysical Journal* 93 (January 01, 1941 1941): 70. <https://doi.org/10.1086/144246>.
<https://ui.adsabs.harvard.edu/abs/1941ApJ....93...70H>.
- Hinson, D. P., I. R. Linscott, L. A. Young, G. L. Tyler, S. A. Stern, R. A. Beyer, M. K. Bird, *et al.* "Radio Occultation Measurements of Pluto's Neutral Atmosphere with New Horizons." *Icarus* 290 (July 01, 2017 2017): 96.
<https://doi.org/10.1016/j.icarus.2017.02.031>.
<https://ui.adsabs.harvard.edu/abs/2017Icar..290...96H>.
- Hirtzig, M., B. Bézard, E. Lellouch, A. Coustenis, C. de Bergh, P. Drossart, A. Campargue, *et al.* "Titan's Surface and Atmosphere from Cassini/Vims Data with Updated Methane Opacity." *Icarus* 226 (September 01, 2013 2013): 470-86.
<https://doi.org/10.1016/j.icarus.2013.05.033>.
<https://ui.adsabs.harvard.edu/abs/2013Icar..226..470H>.
- Horinouchi, T., S. Y. Murakami, T. Satoh, J. Peralta, K. Ogohara, T. Kouyama, T. Imamura, *et al.* "Equatorial Jet in the Lower to Middle Cloud Layer of Venus Revealed by Akatsuki." *Nat Geosci* 10 (2017): 646-51. <https://doi.org/10.1038/ngeo3016>.
<https://www.ncbi.nlm.nih.gov/pubmed/29887914>.
- Hörst, S. M. "Titan's Atmosphere and Climate." *Journal of Geophysical Research: Planets* 122, no. 3 (2017): 432-82. <https://doi.org/10.1002/2016je005240>.
- Hourdin, Frédéric, Oliver Talagrand, Robert Sadourny, Régis Courtin, Daniel Gautier, and Christopher P. McKay. "Numerical Simulation of the General Circulation of the Atmosphere of Titan." *Icarus* 117 (October 01, 1995 1995): 358.
<https://doi.org/10.1006/icar.1995.1162>.
<https://ui.adsabs.harvard.edu/abs/1995Icar..117..358H>.
- Howett, C. J. A., A. H. Parker, C. B. Olkin, D. C. Reuter, K. Ennico, W. M. Grundy, A. L.

- Graps, *et al.* "Inflight Radiometric Calibration of New Horizons' Multispectral Visible Imaging Camera (Mvic)." *Icarus* 287 (May 01, 2017 2017): 140.
<https://doi.org/10.1016/j.icarus.2016.12.007>.
<https://ui.adsabs.harvard.edu/abs/2017Icar..287..140H>.
- Huygens, Christiaan. *Cristiani Hugeni... Systema Saturnium Sive De Causis Mirandorum Saturni Phaenomenon Et Comite Ejus Planeta Novo*. January 01, 1659, 1659.
[doi:10.3931/e-rara-3178](https://ui.adsabs.harvard.edu/abs/1659chss.book.....H). <https://ui.adsabs.harvard.edu/abs/1659chss.book.....H>.
- Jennings, Donald E., R. K. Achterberg, V. Cottini, C. M. Anderson, F. M. Flasar, C. A. Nixon, G. L. Bjoraker, *et al.* "Evolution of the Far-Infrared Cloud at Titan's South Pole." *The Astrophysical Journal* 804, no. 2 (2015): 5. <https://doi.org/10.1088/2041-8205/804/2/134>.
- Kelland, John, Elizabeth Turtle, Sebastien Rodriguez, Alexander Hayes, and Paul Corlies. "Analyzing the Dynamic and Morphological Characteristics of Clouds on Titan Using the Cassini Vims." July 01, 2018 2018.
- . "Analyzing the Dynamic and Morphological Characteristics of Clouds on Titan Using the Cassini Vims." *42nd COSPAR Scientific Assembly* 42 (2018): B5. 2-43-18.
- Knowles, Ben. "Cassini Imaging Science Subsystem (Iss) Data User's Guide." *PDS* <https://pds-rings.seti.org/cassini/iss> (2016).
- Krasnopolsky, Vladimir A., and Dale P. Cruikshank. "Photochemistry of Pluto's Atmosphere and Ionosphere near Perihelion." *Journal of Geophysical Research* 104 (September 01, 1999 1999): 21979. <https://doi.org/10.1029/1999je001038>.
<https://ui.adsabs.harvard.edu/abs/1999JGR...10421979K>.
- Kutsop, N. W., A. G. Hayes, P. M. Corlies, S. Le Mouélic, J. I. Lunine, C. A. Nixon, P. Rannou, *et al.* "Titan Stratospheric Haze Bands Observed in Cassini Vims as Tracers of Meridional Circulation." *The Planetary Science Journal* 3 (May 01, 2022 2022): 114.
<https://doi.org/10.3847/PSJ/ac582d>.
<https://ui.adsabs.harvard.edu/abs/2022PSJ.....3..114K>.
- Langhans, M. H., R. Jaumann, K. Stephan, R. H. Brown, B. J. Buratti, R. N. Clark, K. H. Baines, *et al.* "Titan's Fluvial Valleys: Morphology, Distribution, and Spectral Properties." *Planetary and Space Science* 60 (January 01, 2012 2012): 34-51.
<https://doi.org/10.1016/j.pss.2011.01.020>.
<https://ui.adsabs.harvard.edu/abs/2012P&SS...60...34L>.
- Lara, L. M., W. -H. Ip, and R. Rodrigo. "Photochemical Models of Pluto's Atmosphere." *Icarus* 130 (November 01, 1997 1997): 16. <https://doi.org/10.1006/icar.1997.5798>.
<https://ui.adsabs.harvard.edu/abs/1997Icar..130...16L>.
- Larson, Erik JL, Owen B Toon, and Andrew J Friedson. "Simulating Titan's Aerosols in a Three Dimensional General Circulation Model." *Icarus* 243 (2014): 400-19.
<https://doi.org/10.1016/j.icarus.2014.09.003>.
- Larson, Erik J. L., Owen B. Toon, Robert A. West, and A. James Friedson. "Microphysical Modeling of Titan's Detached Haze Layer in a 3d Gcm." *Icarus* 254 (2015): 122-34.
<https://doi.org/10.1016/j.icarus.2015.03.010>.

- Lavvas, P., R. V. Yelle, and C. A. Griffith. "Titan's Vertical Aerosol Structure at the Huygens Landing Site: Constraints on Particle Size, Density, Charge, and Refractive Index." *Icarus* 210, no. 2 (2010): 832-42. <https://doi.org/10.1016/j.icarus.2010.07.025>.
- Lavvas, Panayotis, Roger V Yelle, Tommi Koskinen, Axel Bazin, Véronique Vuitton, Erik Vigren, Marina Galand, *et al.* "Aerosol Growth in Titan's Ionosphere." *Proceedings of the National Academy of Sciences* 110, no. 8 (2013): 2729-34. <https://doi.org/10.1073/pnas.1217059110>.
- Lavvas, P. P., A. Coustenis, and I. M. Vardavas. "Coupling Photochemistry with Haze Formation in Titan's Atmosphere, Part I: Model Description." *Planetary and Space Science* 56, no. 1 (2008): 27-66. <https://doi.org/10.1016/j.pss.2007.05.026>.
- . "Coupling Photochemistry with Haze Formation in Titan's Atmosphere, Part II: Results and Validation with Cassini/Huygens Data." *Planetary and Space Science* 56, no. 1 (2008): 67-99. <https://doi.org/10.1016/j.pss.2007.05.027>.
- Le Mouélic, S., T. Cornet, S. Rodriguez, C. Sotin, B. Seignovert, J. W. Barnes, R. H. Brown, *et al.* "The Cassini Vims Archive of Titan: From Browse Products to Global Infrared Color Maps." *Icarus* 319 (February 01, 2019 2019): 121-32. <https://doi.org/10.1016/j.icarus.2018.09.017>. <https://ui.adsabs.harvard.edu/abs/2019Icar..319..121L>.
- Le Mouélic, Stéphane, Pascal Rannou, Sébastien Rodriguez, Christophe Sotin, Caitlin A. Griffith, Lucille Le Corre, Jason W. Barnes, *et al.* "Dissipation of Titan's North Polar Cloud at Northern Spring Equinox." *Planetary and Space Science* 60, no. 1 (2012): 86-92. <https://doi.org/10.1016/j.pss.2011.04.006>.
- Le Mouélic, S., S. Rodriguez, R. Robidel, B. Rousseau, B. Seignovert, C. Sotin, J. W. Barnes, *et al.* "Mapping Polar Atmospheric Features on Titan with Vims: From the Dissipation of the Northern Cloud to the Onset of a Southern Polar Vortex." *Icarus* 311 (2018): 371-83. <https://doi.org/10.1016/j.icarus.2018.04.028>.
- Lebonnois, Sébastien, E. L. O. Bakes, and Christopher P. McKay. "Transition from Gaseous Compounds to Aerosols in Titan's Atmosphere." *Icarus* 159 (October 01, 2002 2002): 505-17. <https://doi.org/10.1006/icar.2002.6943>. <https://ui.adsabs.harvard.edu/abs/2002Icar..159..505L>.
- Lebonnois, Sébastien, Jérémie Burgalat, Pascal Rannou, and Benjamin Charnay. "Titan Global Climate Model: A New 3-Dimensional Version of the Ipl Titan Gcm." *Icarus* 218, no. 1 (2012): 707-22. <https://doi.org/10.1016/j.icarus.2011.11.032>.
- Lebonnois, S., F. M. Flasar, T. Tokano, C. E. Newman, Ingo Muller-Wodarg, Caitlin A. Griffith, Emmanuel Lellouch, and Thomas E. Cravens. "The General Circulation of Titan's Lower and Middle Atmosphere." Chap. 4 In *Titan*, 122-57, 2013.
- Lellouch, E, M Gurwell, B Butler, T Fouchet, P Lavvas, DF Strobel, B Sicardy, *et al.* "Detection of Co and Hcn in Pluto's Atmosphere with Alma." *Icarus* 286 (2017): 289-307. <https://doi.org/10.1016/j.icarus.2016.10.013>.

This entry was generated through inserting a Personal Communication citation for Lemmon,

Mark. Personal Communication references should appear only in the notes. Remove field codes in the final document and then remove this entry.

- Liou, Kuo-Nan. *An Introduction to Atmospheric Radiation*. Elsevier, 2002.
<https://www.elsevier.com/books/an-introduction-to-atmospheric-radiation/liou/978-0-12-451451-5>.
- Liu, Pingyu. "A New Phase Function Approximating to Mie Scattering for Radiative Transport Equations." *Physics in Medicine and Biology* 39 (June 01, 1994 1994): 1025.
<https://doi.org/10.1088/0031-9155/39/6/008>.
<https://ui.adsabs.harvard.edu/abs/1994PMB....39.1025L>.
- Lopes, R. M. C., R. L. Kirk, K. L. Mitchell, A. Legall, J. W. Barnes, A. Hayes, J. Kargel, *et al.* "Cryovolcanism on Titan: New Results from Cassini Radar and Vims." *Journal of Geophysical Research (Planets)* 118 (March 01, 2013 2013): 416-35.
<https://doi.org/10.1002/jgre.20062>.
<https://ui.adsabs.harvard.edu/abs/2013JGRE..118..416L>.
- Lopes, R. M. C., M. J. Malaska, A. M. Schoenfeld, A. Solomonidou, S. P. D. Birch, M. Florence, A. G. Hayes, *et al.* "A Global Geomorphologic Map of Saturn's Moon Titan." *Nature Astronomy* 4 (January 01, 2020 2020): 228-33.
<https://doi.org/10.1038/s41550-019-0917-6>.
<https://ui.adsabs.harvard.edu/abs/2020NatAs...4..228L>.
- Lopes, Rosaly M. C., M. J. Malaska, A. Solomonidou, A. Le Gall, M. A. Janssen, C. D. Neish, E. P. Turtle, *et al.* "Nature, Distribution, and Origin of Titan's Undifferentiated Plains." *Icarus* 270 (May 01, 2016 2016): 162-82. <https://doi.org/10.1016/j.icarus.2015.11.034>.
<https://ui.adsabs.harvard.edu/abs/2016Icar..270..162L>.
- Lora, Juan M., Jonathan I. Lunine, and Joellen L. Russell. "Gcm Simulations of Titan's Middle and Lower Atmosphere and Comparison to Observations." *Icarus* 250 (2015): 516-28.
<https://doi.org/10.1016/j.icarus.2014.12.030>.
- Lora, Juan M., Tetsuya Tokano, Jan Vatant d'Ollone, Sébastien Lebonnois, and Ralph D. Lorenz. "A Model Intercomparison of Titan's Climate and Low-Latitude Environment." *Icarus* 333 (November 01, 2019 2019): 113-26. <https://doi.org/10.1016/j.icarus.2019.05.031>.
<https://ui.adsabs.harvard.edu/abs/2019Icar..333..113L>.
- Lorenz, Ralph D., Karl L. Mitchell, Randolph L. Kirk, Alexander G. Hayes, Oded Aharonson, Howard A. Zebker, Phillipe Paillou, *et al.* "Titan's Inventory of Organic Surface Materials." *Geophysical Research Letters* 35 (January 01, 2008 2008): L02206.
<https://doi.org/10.1029/2007gl032118>.
<https://ui.adsabs.harvard.edu/abs/2008GeoRL..35.2206L>.
- Lorenz, Ralph D, Peter H Smith, Mark T Lemmon, Erich Karkoschka, GW Lockwood, and John Caldwell. "Titan's North-South Asymmetry from Hst and Voyager Imaging: Comparison with Models and Ground-Based Photometry." *Icarus* 127, no. 1 (1997): 173-89.
- Lorenz, Ralph D., Peter H. Smith, Mark T. Lemmon, Erich Karkoschka, G. W. Lockwood, and John Caldwell. "Titan's North-South Asymmetry from Hst and Voyager Imaging: Comparison with Models and Ground-Based Photometry." *Icarus* 127 (May 01, 1997

- 1997): 173. <https://doi.org/10.1006/icar.1997.5687>.
<https://ui.adsabs.harvard.edu/abs/1997Icar..127..173L>.
- Lorenz, Ralph D., Bryan W. Stiles, Oded Aharonson, Antoine Lucas, Alexander G. Hayes, Randolph L. Kirk, Howard A. Zebker, *et al.* "A Global Topographic Map of Titan." *Icarus* 225 (July 01, 2013 2013): 367-77. <https://doi.org/10.1016/j.icarus.2013.04.002>.
<https://ui.adsabs.harvard.edu/abs/2013Icar..225..367L>.
- Lorenz, R. D., E. F. Young, and M. T. Lemmon. "Titan's Smile and Collar: Hst Observations of Seasonal Change 1994-2000." *Geophysical Research Letters* 28, no. 23 (2001): 4453-56. <https://doi.org/10.1029/2001gl013728>.
- Lunine, J. I., D. J. Stevenson, and Y. L. Yung. "Ethane Ocean on Titan." *Science* 222 (December 01, 1983 1983): 1229-30. <https://doi.org/10.1126/science.222.4629.1229>.
<https://ui.adsabs.harvard.edu/abs/1983Sci...222.1229L>.
- Luz, D, and F Hourdin. "Latitudinal Transport by Barotropic Waves in Titan's Stratosphere.: I. General Properties from a Horizontal Shallow-Water Model." *Icarus* 166, no. 2 (2003): 328-42.
- MacKenzie, S. M., and Jason W. Barnes. "Compositional Similarities and Distinctions between Titan's Evaporitic Terrains." *The Astrophysical Journal* 821 (April 01, 2016 2016): 17. <https://doi.org/10.3847/0004-637x/821/1/17>.
<https://ui.adsabs.harvard.edu/abs/2016ApJ...821...17M>.
- Malaska, Michael J., Rosaly M. Lopes, Alex G. Hayes, Jani Radebaugh, Ralph D. Lorenz, and Elizabeth P. Turtle. "Material Transport Map of Titan: The Fate of Dunes." *Icarus* 270 (May 01, 2016 2016): 183-96. <https://doi.org/10.1016/j.icarus.2015.09.029>.
<https://ui.adsabs.harvard.edu/abs/2016Icar..270..183M>.
- Malaska, Michael J., Rosaly M. C. Lopes, David A. Williams, Catherine D. Neish, Anezina Solomonidou, Jason M. Soderblom, Ashley M. Schoenfeld, *et al.* "Geomorphological Map of the Afekan Crater Region, Titan: Terrain Relationships in the Equatorial and Mid-Latitude Regions." *Icarus* 270 (May 01, 2016 2016): 130-61. <https://doi.org/10.1016/j.icarus.2016.02.021>.
<https://ui.adsabs.harvard.edu/abs/2016Icar..270..130M>.
- Mätzler, Christian. "Matlab Functions for Mie Scattering and Absorption, Version 2." *IAP Res. Rep* 8, no. 1 (2002): 9. <https://boris.unibe.ch/146550/1/199.pdf>.
- Mayo, Louis A, and Robert E Samuelson. "Condensate Clouds in Titan's North Polar Stratosphere." *Icarus* 176, no. 2 (2005): 316-30.
- McCord, Thomas B., Paul Hayne, Jean-Philippe Combe, Gary B. Hansen, Jason W. Barnes, Sébastien Rodriguez, Stéphane Le Mouélic, *et al.* "Titan's Surface: Search for Spectral Diversity and Composition Using the Cassini Vims Investigation." *Icarus* 194 (March 01, 2008 2008): 212-42. <https://doi.org/10.1016/j.icarus.2007.08.039>.
<https://ui.adsabs.harvard.edu/abs/2008Icar..194..212M>.
- McCord, Thomas B., Paul Hayne, Jean-Philippe Combe, Gary B. Hansen, Jason W. Barnes, Sébastien Rodriguez, Stéphane Le Mouélic, *et al.* "Titan's Surface: Search for Spectral

- Diversity and Composition Using the Cassini Vims Investigation." *Icarus* 194, no. 1 (2008): 212-42. <https://doi.org/10.1016/j.icarus.2007.08.039>.
- McKay, Christopher P. "Elemental Composition, Solubility, and Optical Properties of Titan's Organic Haze." *Planetary and Space Science* 44 (August 01, 1996 1996): 741-47. [https://doi.org/10.1016/0032-0633\(96\)00009-8](https://doi.org/10.1016/0032-0633(96)00009-8). <https://ui.adsabs.harvard.edu/abs/1996P&SS...44..741M>.
- McLinden, C. A., A. E. Bourassa, S. Brohede, M. Cooper, D. A. Degenstein, W. J. F. Evans, R. L. Gattinger, *et al.* "Osiris: A Decade of Scattered Light." *Bulletin of the American Meteorological Society* 93 (December 01, 2012 2012): 1845. <https://doi.org/10.1175/bams-d-11-00135.1>. <https://ui.adsabs.harvard.edu/abs/2012BAMS...93.1845M>.
- McPeters, Richard D., Scott J. Janz, Ernest Hilsenrath, Tammy L. Brown, David E. Flittner, and Donald F. Heath. "The Retrieval of O₃ Profiles from Limb Scatter Measurements: Results from the Shuttle Ozone Limb Sounding Experiment." *Geophysical Research Letters* 27 (September 01, 2000 2000): 2597. <https://doi.org/10.1029/1999gl011342>. <https://ui.adsabs.harvard.edu/abs/2000GeoRL..27.2597M>.
- Mitchell, Jonathan L., Raymond T. Pierrehumbert, Dargan M. W. Frierson, and Rodrigo Caballero. "The Dynamics Behind Titan's Methane Clouds." *Proceedings of the National Academy of Sciences* 103, no. 49 (2006): 18421-26. <https://doi.org/10.1073/pnas.0605074103>. <https://www.pnas.org/content/pnas/103/49/18421.full.pdf>.
- Moore, Jeffrey M., and Alan D. Howard. "Are the Basins of Titan's Hotei Regio and Tui Regio Sites of Former Low Latitude Seas?". *Geophysical Research Letters* 37 (November 01, 2010 2010): L22205. <https://doi.org/10.1029/2010gl045234>. <https://ui.adsabs.harvard.edu/abs/2010GeoRL..3722205M>.
- Murtagh, Donal, Urban Frisk, Frank Merino, Martin Ridal, Andreas Jonsson, Jacek Stegman, Georg Witt, *et al.* "Review: An Overview of the Odin Atmospheric Mission." *Canadian Journal of Physics* 80 (April 01, 2002 2002): 309. <https://doi.org/10.1139/p01-157>. <https://ui.adsabs.harvard.edu/abs/2002CaJPh..80..309M>.
- Negrão, A., A. Coustenis, E. Lellouch, J. -P. Maillard, P. Rannou, B. Schmitt, C. P. McKay, and V. Boudon. "Titan's Surface Albedo Variations over a Titan Season from near-Infrared Cfht/Fts Spectra." *Planetary and Space Science* 54 (October 01, 2006 2006): 1225-46. <https://doi.org/10.1016/j.pss.2006.05.031>. <https://ui.adsabs.harvard.edu/abs/2006P&SS...54.1225N>.
- Neish, C. D., J. W. Barnes, C. Sotin, S. MacKenzie, J. M. Soderblom, S. Le Mouélic, R. L. Kirk, *et al.* "Spectral Properties of Titan's Impact Craters Imply Chemical Weathering of Its Surface." *Geophysical Research Letters* 42 (May 01, 2015 2015): 3746-54. <https://doi.org/10.1002/2015gl063824>. <https://ui.adsabs.harvard.edu/abs/2015GeoRL..42.3746N>.
- Nelson, Robert M., Lucas W. Kamp, Rosaly M. C. Lopes, Dennis L. Matson, Randolph L. Kirk,

- Bruce W. Hapke, Stephen D. Wall, *et al.* "Photometric Changes on Saturn's Titan: Evidence for Active Cryovolcanism." *Geophysical Research Letters* 36 (February 01, 2009 2009): L04202. <https://doi.org/10.1029/2008gl036206>.
<https://ui.adsabs.harvard.edu/abs/2009GeoRL..36.4202N>.
- Newman, Claire E., Christopher Lee, Yuan Lian, Mark I. Richardson, and Anthony D. Toigo. "Stratospheric Superrotation in the Titanwrf Model." *Icarus* 213, no. 2 (2011): 636-54. <https://doi.org/10.1016/j.icarus.2011.03.025>.
- Newman, Claire E., Mark I. Richardson, Yuan Lian, and Christopher Lee. "Simulating Titan's Methane Cycle with the Titanwrf General Circulation Model." *Icarus* 267 (March 01, 2016 2016): 106-34. <https://doi.org/10.1016/j.icarus.2015.11.028>.
<https://ui.adsabs.harvard.edu/abs/2016Icar..267..106N>.
- Nixon, Conor A., Richard K. Achterberg, Máté Ádámkovics, Bruno Bézard, Gordon L. Bjoraker, Thomas Cornet, Alexander G. Hayes, *et al.* "Titan Science with the James Webb Space Telescope." *Publications of the Astronomical Society of the Pacific* 128, no. 959 (2016): 23. <https://doi.org/10.1088/1538-3873/128/959/018007>.
- Nixon, C. A., R. D. Lorenz, R. K. Achterberg, A. Buch, P. Coll, R. N. Clark, R. Courtin, *et al.* "Titan's Cold Case Files - Outstanding Questions after Cassini-Huygens." *Planetary and Space Science* 155 (2018): 50-72. <https://doi.org/10.1016/j.pss.2018.02.009>.
- Normand, E. N., J. T. Wiensz, A. E. Bourassa, and D. A. Degenstein. "Cloud Discrimination in Probability Density Functions of Limb-Scattered Sunlight Measurements." *Atmospheric Measurement Techniques* 6 (December 01, 2013 2013): 3359. <https://doi.org/10.5194/amt-6-3359-2013>.
<https://ui.adsabs.harvard.edu/abs/2013AMT.....6.3359N>.
- O'Donoghue, J., L. Moore, T. Bhakyaipaul, H. Melin, T. Stallard, J. E. P. Connerney, and C. Tao. "Global Upper-Atmospheric Heating on Jupiter by the Polar Aurorae." *Nature* 596, no. 7870 (Aug 2021): 54-57. <https://doi.org/10.1038/s41586-021-03706-w>.
<https://www.ncbi.nlm.nih.gov/pubmed/34349293>.
- Penteado, Paulo F., Caitlin A. Griffith, Martin G. Tomasko, Steffi Engel, Charles See, Lyn Doose, Kevin H. Baines, *et al.* "Latitudinal Variations in Titan's Methane and Haze from Cassini Vims Observations." *Icarus* 206, no. 1 (2010): 352-65. <https://doi.org/10.1016/j.icarus.2009.11.003>.
- Peterson, J., B. Carcich, T. Finley, M. H. Versteeg, J. W. Parker, A. J. Steffl, G. McCabe, *et al.* *New Horizons Soc to Instrument Pipeline Icd*. Southwest Research Indtitute (Southwest Research Indtitute: 2017 September 2017).
https://pds-ppi.igpp.ucla.edu/data/NH-P-PEPSSI-2-PLUTO-V3.0/DOCUMENT/soc_inst_icd.pdf.
- Poggiali, V., A. G. Hayes, M. Mastrogiuseppe, A. Le Gall, D. Lalich, I. Gómez-Leal, and J. I. Lunine. "The Bathymetry of Moray Sinus at Titan's Kraken Mare." *Journal of Geophysical Research (Planets)* 125 (December 01, 2020 2020): e06558. <https://doi.org/10.1029/2020je006558>.
<https://ui.adsabs.harvard.edu/abs/2020JGRE..12506558P>.

- Pollack, J. B., and C. P. McKay. "The Impact of Polar Stratospheric Clouds on the Heating Rates of the Winter Polar Stratosphere." *Journal of Atmospheric Sciences* 42 (February 01, 1985 1985): 245-62.
[https://doi.org/10.1175/1520-0469\(1985\)042<0245:Tiopsc>2.0.Co;2](https://doi.org/10.1175/1520-0469(1985)042<0245:Tiopsc>2.0.Co;2).
<https://ui.adsabs.harvard.edu/abs/1985JAtS...42..245P>.
- Porco, Carolyn C., Robert A. West, Steven Squyres, Alfred McEwen, Peter Thomas, Carl D. Murray, Anthony Del Genio, *et al.* "Cassini Imaging Science: Instrument Characteristics and Anticipated Scientific Investigations at Saturn." *Space Science Reviews* 115 (December 01, 2004 2004): 363-497. <https://doi.org/10.1007/s11214-004-1456-7>.
<https://ui.adsabs.harvard.edu/abs/2004SSRv..115..363P>.
- Rages, K., and J. B. Pollack. "Vertical Distribution of Scattering Hazes in Titan's Upper Atmosphere." *Icarus* 55 (July 01, 1983 1983): 50-62.
[https://doi.org/10.1016/0019-1035\(83\)90049-0](https://doi.org/10.1016/0019-1035(83)90049-0).
<https://ui.adsabs.harvard.edu/abs/1983Icar...55...50R>.
- Rages, K., J. B. Pollack, and P. H. Smith. "Size Estimates of Titan's Aerosols Based on Voyager High-Phase-Angles Images." *Journal of Geophysical Research* 88 (November 01, 1983 1983): 8721. <https://doi.org/10.1029/JA088iA11p08721>.
<https://ui.adsabs.harvard.edu/abs/1983JGR....88.8721R>.
- Ramirez, S. I., P. Coll, A. da Silva, R. Navarro-González, J. Lafait, and F. Raulin. "Complex Refractive Index of Titan's Aerosol Analogues in the 200-900 Nm Domain." *Icarus* 156 (April 01, 2002 2002): 515. <https://doi.org/10.1006/icar.2001.6783>.
<https://ui.adsabs.harvard.edu/abs/2002Icar..156..515R>.
- Rannou, P. "Characterization of Aerosols in the Detached Haze Layer of Titan." *Icarus* 147, no. 1 (2000): 267-81. <https://doi.org/10.1006/icar.2000.6416>.
- Rannou, P., F. Hourdin, C. P. McKay, and D. Luz. "A Coupled Dynamics-Microphysics Model of Titan's Atmosphere." *Icarus* 170, no. 2 (2004): 443-62.
<https://doi.org/10.1016/j.icarus.2004.03.007>.
- Rannou, P., S. Le Mouélic, C. Sotin, and R. H. Brown. "Cloud and Haze in the Winter Polar Region of Titan Observed with Visual and Infrared Mapping Spectrometer on Board Cassini." *The Astrophysical Journal* 748 (March 01, 2012 2012): 4.
<https://doi.org/10.1088/0004-637x/748/1/4>.
<https://ui.adsabs.harvard.edu/abs/2012ApJ...748....4R>.
- Rannou, P., C. P. McKay, and R. D. Lorenz. "A Model of Titan's Haze of Fractal Aerosols Constrained by Multiple Observations." *Planetary and Space Science* 51 (December 01, 2003 2003): 963-76. <https://doi.org/10.1016/j.pss.2003.05.008>.
<https://ui.adsabs.harvard.edu/abs/2003P&SS...51..963R>.
- Rannou, P., D. Toledo, P. Lavvas, E. D'Aversa, M. L. Moriconi, A. Adriani, S. Le Mouélic, C. Sotin, and R. Brown. "Titan's Surface Spectra at the Huygens Landing Site and Shangri-La." *Icarus* 270 (2016): 291-306. <https://doi.org/10.1016/j.icarus.2015.09.016>.
- Rault, Didier F. "Ozone Profile Retrieval from Stratospheric Aerosol and Gas Experiment (Sage Ii) Limb Scatter Measurements." *Journal of Geophysical Research (Atmospheres)* 110

- (May 01, 2005 2005): D09309. <https://doi.org/10.1029/2004jd004970>.
<https://ui.adsabs.harvard.edu/abs/2005JGRD..110.9309R>.
- Reuter, Dennis C., S. Alan Stern, John Scherrer, Donald E. Jennings, James W. Baer, John Hanley, Lisa Hardaway, *et al.* "Ralph: A Visible/Infrared Imager for the New Horizons Pluto/Kuiper Belt Mission." *Space Science Reviews* 140 (October 01, 2008 2008): 129. <https://doi.org/10.1007/s11214-008-9375-7>.
<https://ui.adsabs.harvard.edu/abs/2008SSRv..140..129R>.
- Rodriguez, S., S. Le Mouélic, P. Rannou, C. Sotin, R. H. Brown, J. W. Barnes, C. A. Griffith, *et al.* "Titan's Cloud Seasonal Activity from Winter to Spring with Cassini/Vims." *Icarus* 216, no. 1 (2011): 89-110. <https://doi.org/10.1016/j.icarus.2011.07.031>.
- Rodriguez, S., S. Le Mouelic, P. Rannou, G. Tobie, K. H. Baines, J. W. Barnes, C. A. Griffith, *et al.* "Global Circulation as the Main Source of Cloud Activity on Titan." *Nature* 459, no. 7247 (Jun 4 2009): 678-82. <https://doi.org/10.1038/nature08014>.
<https://www.ncbi.nlm.nih.gov/pubmed/19494910>.
- Roe, Henry G. "Titan's Methane Weather." *Annual Review of Earth and Planetary Sciences* 40, no. 1 (2012): 355-82. <https://doi.org/10.1146/annurev-earth-040809-152548>.
- Roe, Henry G., Imke de Pater, Bruce A. Macintosh, Seran G. Gibbard, Claire E. Max, and Chris P. McKay. "Titan's Atmosphere in Late Southern Spring Observed with Adaptive Optics on the W. M. Keck II 10-Meter Telescope." *Icarus* 157, no. 1 (2002): 254-58. <https://doi.org/10.1006/icar.2002.6831>.
- Roman, Michael T., Robert A. West, Donald J. Banfield, Peter J. Gierasch, Richard K. Achterberg, Conor A. Nixon, and Peter C. Thomas. "Determining a Tilt in Titan's North-South Albedo Asymmetry from Cassini Images." *Icarus* 203, no. 1 (2009): 242-49. <https://doi.org/10.1016/j.icarus.2009.04.021>.
- Rossow, W. B., and G. P. Williams. "Large-Scale Motion in the Venus Stratosphere." *Journal of Atmospheric Sciences* 36 (March 01, 1979 1979): 377. [https://doi.org/10.1175/1520-0469\(1979\)036<0377:Lsmitv>2.0.Co;2](https://doi.org/10.1175/1520-0469(1979)036<0377:Lsmitv>2.0.Co;2).
<https://ui.adsabs.harvard.edu/abs/1979JAAtS...36..377R>.
- Saur, Joachim, Stefan Duling, Lorenz Roth, Xianzhe Jia, Darrell F. Strobel, Paul D. Feldman, Ulrich R. Christensen, *et al.* "The Search for a Subsurface Ocean in Ganymede with Hubble Space Telescope Observations of Its Auroral Ovals." *Journal of Geophysical Research: Space Physics* 120, no. 3 (2015): 1715-37. <https://doi.org/10.1002/2014ja020778>.
- Savitzky, A., and M. J. E. Golay. "Smoothing and Differentiation of Data by Simplified Least Squares Procedures." *Analytical Chemistry* 36 (January 01, 1964 1964): 1627. <https://ui.adsabs.harvard.edu/abs/1964AnaCh..36.1627S>.
- Schoenfeld, Ashley M., Rosaly M. C. Lopes, Michael J. Malaska, Anezina Solomonidou, David A. Williams, Samuel P. D. Birch, Alexander G. Hayes, *et al.* "Geomorphological Map of the South Belet Region of Titan." *Icarus* 366 (September 01, 2021 2021): 114516. <https://doi.org/10.1016/j.icarus.2021.114516>.
<https://ui.adsabs.harvard.edu/abs/2021Icar..36614516S>.

- Seignovert, Benoît , Stéphane Le Mouélic, Robert H. Brown, Erich Karkoschka, Virginia Pasek, Christophe Sotin, and Elizabeth P. Turtle. "Titan's Global Map Combining Vims and Iss Mosaics." *CaltechDATA* 0, no. 0 (2019): 4. <https://doi.org/10.22002/D1.1173>. <https://data.caltech.edu/records/1173>.
- Seignovert, Benoît, Pascal Rannou, Robert A. West, and Sandrine Vinatier. "Haze Seasonal Variations of Titan's Upper Atmosphere During the Cassini Mission." *The Astrophysical Journal* 907, no. 1 (2021): 17. <https://doi.org/10.3847/1538-4357/abcd3b>.
- Sharma, Subodh Kumar. *Elastic Scattering of Electromagnetic Radiation: Analytic Solutions in Diverse Backgrounds*. CRC Press, 2018. https://www.google.com/books/edition/Elastic_Scattering_of_Electromagnetic_Ra/UXJQDwAAQBAJ?hl=en&gbpv=0.
- Sicardy, B., J. Talbot, E. Meza, J. I. B. Camargo, J. Desmars, D. Gault, D. Herald, *et al.* "Pluto's Atmosphere from the 2015 June 29 Ground-Based Stellar Occultation at the Time of the New Horizons Flyby." *The Astrophysical Journal* 819 (March 01, 2016 2016): L38. <https://doi.org/10.3847/2041-8205/819/2/138>. <https://ui.adsabs.harvard.edu/abs/2016ApJ...819L..38S>.
- Sicardy, B., T. Widemann, E. Lellouch, C. Veillet, J. -C. Cuillandre, F. Colas, F. Roques, *et al.* "Large Changes in Pluto's Atmosphere as Revealed by Recent Stellar Occultations." *Nature* 424 (July 01, 2003 2003): 168. <https://doi.org/10.1038/nature01766>. <https://ui.adsabs.harvard.edu/abs/2003Natur.424..168S>.
- Singh, S., T. B. McCord, J. -Ph. Combe, S. Rodriguez, T. Cornet, S. Le Mouélic, R. N. Clark, L. Maltagliati, and V. F. Chevrier. "Acetylene on Titan's Surface." *The Astrophysical Journal* 828 (September 01, 2016 2016): 55. <https://doi.org/10.3847/0004-637x/828/1/55>. <https://ui.adsabs.harvard.edu/abs/2016ApJ...828...55S>.
- Smith, B. A., L. Soderblom, R. M. Batson, P. M. Bridges, J. L. Inge, H. Masursky, E. Shoemaker, *et al.* "A New Look at the Saturn System: The Voyager 2 Images." *Science* 215 (January 01, 1982 1982): 504. <https://doi.org/10.1126/science.215.4532.504>. <https://ui.adsabs.harvard.edu/abs/1982Sci...215..504S>.
- Smith, B. A., L. Soderblom, R. F. Beebe, J. M. Boyce, G. Briggs, A. Bunker, S. A. Collins, *et al.* "Encounter with Saturn: Voyager 1 Imaging Science Results." *Science* 212 (April 01, 1981 1981): 163. <https://doi.org/10.1126/science.212.4491.163>. <https://ui.adsabs.harvard.edu/abs/1981Sci...212..163S>.
- Sneep, Maarten, and Wim Ubachs. "Direct Measurement of the Rayleigh Scattering Cross Section in Various Gases." *Journal of Quantitative Spectroscopy and Radiative Transfer* 92 (May 01, 2005 2005): 293. <https://doi.org/10.1016/j.jqsrt.2004.07.025>. <https://ui.adsabs.harvard.edu/abs/2005JQSRT..92..293S>.
- Soderblom, Laurence A., Randolph L. Kirk, Jonathan I. Lunine, Jeffrey A. Anderson, Kevin H. Baines, Jason W. Barnes, Janet M. Barrett, *et al.* "Correlations between Cassini Vims Spectra and Radar Sar Images: Implications for Titan's Surface Composition and the Character of the Huygens Probe Landing Site." *Planetary and Space Science* 55 (November 01, 2007 2007): 2025-36. <https://doi.org/10.1016/j.pss.2007.04.014>.

- <https://ui.adsabs.harvard.edu/abs/2007P&SS...55.2025S>.
- Solomonidou, A., A. Coustenis, R. M. C. Lopes, M. J. Malaska, S. Rodriguez, P. Drossart, C. Elachi, *et al.* "The Spectral Nature of Titan's Major Geomorphological Units: Constraints on Surface Composition." *Journal of Geophysical Research (Planets)* 123 (February 01, 2018 2018): 489-507. <https://doi.org/10.1002/2017je005477>.
<https://ui.adsabs.harvard.edu/abs/2018JGRE..123..489S>.
- Solomonidou, A., A. Le Gall, M. J. Malaska, S. P. D. Birch, R. M. C. Lopes, A. Coustenis, S. Rodriguez, *et al.* "Spectral and Emissivity Analysis of the Raised Ramparts around Titan's Northern Lakes." *Icarus* 344 (July 01, 2020 2020): 113338.
<https://doi.org/10.1016/j.icarus.2019.05.040>.
<https://ui.adsabs.harvard.edu/abs/2020Icar..34413338S>.
- Sromovsky, L. A., V. E. Suomi, J. B. Pollack, R. J. Krauss, S. S. Limaye, T. Owen, H. E. Revercomb, and C. Sagan. "Implications of Titan's North-South Brightness Asymmetry." *Nature* 292 (August 01, 1981 1981): 698. <https://doi.org/10.1038/292698a0>.
<https://ui.adsabs.harvard.edu/abs/1981Natur.292..698S>.
- Stern, A. "New Horizons Calibrated Leisa Pluto Encounter V3.0, Nh-P-Leisa-3-Pluto-V3.0." NASA Planetary Data System, 2018.
<https://pds.nasa.gov/ds-view/pds/viewProfile.jsp?dsid=NH-P-LEISA-3-PLUTO-V3.0>.
- Stern, S. A., F. Bagenal, K. Ennico, G. R. Gladstone, W. M. Grundy, W. B. McKinnon, J. M. Moore, *et al.* "The Pluto System: Initial Results from Its Exploration by New Horizons." *Science* 350 (October 01, 2015 2015): aad1815. <https://doi.org/10.1126/science.aad1815>.
<https://ui.adsabs.harvard.edu/abs/2015Sci...350.1815S>.
- Stern, S. A., M. W. Buie, and L. M. Trafton. "Hst High-Resolution Images and Maps of Pluto." *The Astronomical Journal* 113 (February 01, 1997 1997): 827.
<https://doi.org/10.1086/118304>. <https://ui.adsabs.harvard.edu/abs/1997AJ....113..827S>.
- Stern, S. A., J. A. Kammer, G. R. Gladstone, A. J. Steffl, A. F. Cheng, L. A. Young, H. A. Weaver, *et al.* "New Horizons Constraints on Charon's Present Day Atmosphere." *Icarus* 287 (May 01, 2017 2017): 124. <https://doi.org/10.1016/j.icarus.2016.09.019>.
<https://ui.adsabs.harvard.edu/abs/2017Icar..287..124S>.
- Stern, S. A., D. C. Slater, J. Scherrer, J. Stone, M. Versteeg, M. F. A'Hearn, J. L. Bertaux, *et al.* "Alice: The Rosetta Ultraviolet Imaging Spectrograph." *Space Science Reviews* 128 (February 01, 2007 2007): 507. <https://doi.org/10.1007/s11214-006-9035-8>.
<https://ui.adsabs.harvard.edu/abs/2007SSRv..128..507S>.
- Stiles, Bryan W., Randolph L. Kirk, Ralph D. Lorenz, Scott Hensley, Ella Lee, Steven J. Ostro, Michael D. Allison, *et al.* "Determining Titan's Spin State Fromcassiniradar Images." *The Astronomical Journal* 135, no. 5 (2008): 1669-80.
<https://doi.org/10.1088/0004-6256/135/5/1669>.
- Strobel, D. F. "Chemistry and Evolution of Titan's Atmosphere." *Planetary and Space Science* 30 (August 01, 1982 1982): 839-48. [https://doi.org/10.1016/0032-0633\(82\)90116-7](https://doi.org/10.1016/0032-0633(82)90116-7).
<https://ui.adsabs.harvard.edu/abs/1982P&SS...30..839S>.

- Strobel, D. F., D. T. Hall, X. Zhu, and M. E. Summers. "Upper Limit on Titan's Atmospheric Argon Abundance." *Icarus* 103 (June 01, 1993 1993): 333-36.
<https://doi.org/10.1006/icar.1993.1075>.
<https://ui.adsabs.harvard.edu/abs/1993Icar..103..333S>.
- Summers, MICHAEL E, DARRELL F Strobel, and G RANDALL Gladstone. "Chemical Models of Pluto's Atmosphere." In *Pluto and Charon*, edited by S. Alan Stern David J. Tholen, 728: University of Arizona Press, 1997.
- Teanby, N. A., R. de Kok, and P. G. J. Irwin. "Small-Scale Composition and Haze Layering in Titan's Polar Vortex." *Icarus* 204, no. 2 (2009): 645-57.
<https://doi.org/10.1016/j.icarus.2009.07.027>.
- Teanby, N. A., P. G. Irwin, C. A. Nixon, R. de Kok, S. Vinatier, A. Coustenis, E. Sefton-Nash, S. B. Calcutt, and F. M. Flasar. "Active Upper-Atmosphere Chemistry and Dynamics from Polar Circulation Reversal on Titan." *Nature* 491, no. 7426 (Nov 29 2012): 732-5.
<https://doi.org/10.1038/nature11611>. <https://www.ncbi.nlm.nih.gov/pubmed/23192150>.
- Teanby, N. A., P. G. J. Irwin, and R. de Kok. "Compositional Evidence for Titan's Stratospheric Tilt." *Planetary and Space Science* 58, no. 5 (2010): 792-800.
<https://doi.org/10.1016/j.pss.2009.12.005>.
- Tokano, Tetsuya. "Precipitation Climatology on Titan." *Science* 331, no. 6023 (2011): 1393-94.
- . "Westward Rotation of the Atmospheric Angular Momentum Vector of Titan by Thermal Tides." *Planetary and Space Science* 58, no. 5 (2010): 814-29.
<https://doi.org/10.1016/j.pss.2010.01.001>.
- Tokano, Tetsuya, and Fritz M. Neubauer. "Wind-Induced Seasonal Angular Momentum Exchange at Titan's Surface and Its Influence on Titan's Length-of-Day." *Geophysical Research Letters* 32 (December 01, 2005 2005): L24203.
<https://doi.org/10.1029/2005gl024456>.
<https://ui.adsabs.harvard.edu/abs/2005GeoRL..3224203T>.
- Tomasko, M. G., L. Doose, S. Engel, L. E. Dafoe, R. West, M. Lemmon, E. Karkoschka, and C. See. "A Model of Titan's Aerosols Based on Measurements Made inside the Atmosphere." *Planetary and Space Science* 56 (April 01, 2008 2008): 669.
<https://doi.org/10.1016/j.pss.2007.11.019>.
<https://ui.adsabs.harvard.edu/abs/2008P&SS...56..669T>.
- Tomasko, M. G., and P. H. Smith. "Photometry and Polarimetry of Titan: Pioneer 11 Observations and Their Implications for Aerosol Properties." *Icarus* 51 (July 01, 1982 1982): 65. [https://doi.org/10.1016/0019-1035\(82\)90030-6](https://doi.org/10.1016/0019-1035(82)90030-6).
<https://ui.adsabs.harvard.edu/abs/1982Icar...51...65T>.
- Turtle, E. P., J. E. Perry, J. M. Barbara, A. D. Del Genio, S. Rodriguez, S. Le Mouélic, C. Sotin, *et al.* "Titan's Meteorology over the Cassini Mission: Evidence for Extensive Subsurface Methane Reservoirs." *Geophysical Research Letters* 45, no. 11 (2018): 5320-28.
<https://doi.org/10.1029/2018gl078170>.
- Vervack, Ronald J., Bill R. Sandel, and Darrell F. Strobel. "New Perspectives on Titan's Upper

- Atmosphere from a Reanalysis of the Voyager 1 Uvs Solar Occultations." *Icarus* 170 (July 01, 2004 2004): 91-112. <https://doi.org/10.1016/j.icarus.2004.03.005>.
<https://ui.adsabs.harvard.edu/abs/2004Icar..170...91V>.
- Veverka, J. "Titan: Polarimetric Evidence for an Optically Thick Atmosphere?." *Icarus* 18 (April 01, 1973 1973): 657-60. [https://doi.org/10.1016/0019-1035\(73\)90069-9](https://doi.org/10.1016/0019-1035(73)90069-9).
<https://ui.adsabs.harvard.edu/abs/1973Icar...18..657V>.
- Wall, S. D., R. M. Lopes, E. R. Stofan, C. A. Wood, J. L. Radebaugh, S. M. Hörst, B. W. Stiles, *et al.* "Cassini Radar Images at Hotei Arcus and Western Xanadu, Titan: Evidence for Geologically Recent Cryovolcanic Activity." *Geophysical Research Letters* 36 (February 01, 2009 2009): L04203. <https://doi.org/10.1029/2008gl036415>.
<https://ui.adsabs.harvard.edu/abs/2009GeoRL..36.4203W>.
- Werynski, A., C. D. Neish, A. Le Gall, M. A. Janssen, and Cassini Radar Team. "Compositional Variations of Titan's Impact Craters Indicates Active Surface Erosion." *Icarus* 321 (March 01, 2019 2019): 508-21. <https://doi.org/10.1016/j.icarus.2018.12.007>.
<https://ui.adsabs.harvard.edu/abs/2019Icar..321..508W>.
- West, R. A., A. D. Del Genio, J. M. Barbara, D. Toledo, P. Lavvas, P. Rannou, E. P. Turtle, and J. Perry. "Cassini Imaging Science Subsystem Observations of Titan's South Polar Cloud." *Icarus* 270 (2016): 399-408. <https://doi.org/10.1016/j.icarus.2014.11.038>.
- West, Robert A., Benoît Seignovert, Pascal Rannou, Philip Dumont, Elizabeth P. Turtle, Jason Perry, Mou Roy, and Aida Ovanessian. "The Seasonal Cycle of Titan's Detached Haze." *Nature Astronomy* 2, no. 6 (2018): 495-500. <https://doi.org/10.1038/s41550-018-0434-z>.
- Wiacek, A., R. V. Martin, A. E. Bourassa, N. D. Lloyd, and D. A. Degenstein. "Absorbing Aerosol Radiative Effects in the Limb-Scatter Viewing Geometry." *Atmospheric Measurement Techniques* 6 (October 01, 2013 2013): 2761.
<https://doi.org/10.5194/amt-6-2761-2013>.
<https://ui.adsabs.harvard.edu/abs/2013AMT.....6.2761W>.
- Williams, David A., Jani Radebaugh, Rosaly M. C. Lopes, and Ellen Stofan. "Geomorphologic Mapping of the Menrva Region of Titan Using Cassini Radar Data." *Icarus* 212 (April 01, 2011 2011): 744-50. <https://doi.org/10.1016/j.icarus.2011.01.014>.
<https://ui.adsabs.harvard.edu/abs/2011Icar..212..744W>.
- Wilmouth, David M., and David S. Sayres. "Rayleigh Scattering Cross Sections of Argon, Carbon Dioxide, Sulfur Hexafluoride, and Methane in the Uv-a Region Using Broadband Cavity Enhanced Spectroscopy." *Journal of Quantitative Spectroscopy and Radiative Transfer* 234 (September 01, 2019 2019): 32. <https://doi.org/10.1016/j.jqsrt.2019.05.031>.
<https://ui.adsabs.harvard.edu/abs/2019JQSRT.234...32W>.
- Wong, Michael L., Siteng Fan, Peter Gao, Mao-Chang Liang, Run-Lie Shia, Yuk L. Yung, Joshua A. Kammer, *et al.* "The Photochemistry of Pluto's Atmosphere as Illuminated by New Horizons." *Icarus* 287 (May 01, 2017 2017): 110.
<https://doi.org/10.1016/j.icarus.2016.09.028>.
<https://ui.adsabs.harvard.edu/abs/2017Icar..287..110W>.
- Wong, Michael L, Yuk L Yung, and G Randall Gladstone. "Pluto's Implications for a Snowball

- Titan." *Icarus* 246 (2015): 192-96. <https://doi.org/10.1016/j.icarus.2014.05.019>.
- Wye, Lauren C., Howard A. Zebker, Steven J. Ostro, Richard D. West, Yonggyu Gim, Ralph D. Lorenz, and Cassini RADAR Team. "Electrical Properties of Titan's Surface from Cassini Radar Scatterometer Measurements." *Icarus* 188 (June 01, 2007 2007): 367-85. <https://doi.org/10.1016/j.icarus.2006.12.008>. <https://ui.adsabs.harvard.edu/abs/2007Icar..188..367W>.
- Young, Leslie A., Joshua A. Kammer, Andrew J. Steffl, G. Randall Gladstone, Michael E. Summers, Darrell F. Strobel, David P. Hinson, *et al.* "Structure and Composition of Pluto's Atmosphere from the New Horizons Solar Ultraviolet Occultation." *Icarus* 300 (January 01, 2018 2018): 174. <https://doi.org/10.1016/j.icarus.2017.09.006>. <https://ui.adsabs.harvard.edu/abs/2018Icar..300..174Y>.
- Yu, Xinting, Sarah M. Hörst, Chao He, Patricia McGuiggan, and Bryan Crawford. "Where Does Titan Sand Come From: Insight from Mechanical Properties of Titan Sand Candidates." *Journal of Geophysical Research (Planets)* 123 (September 01, 2018 2018): 2310-21. <https://doi.org/10.1029/2018je005651>. <https://ui.adsabs.harvard.edu/abs/2018JGRE..123.2310Y>.
- Yung, Y. L., M. Allen, and J. P. Pinto. "Photochemistry of the Atmosphere of Titan - Comparison between Model and Observations." *The Astrophysical Journal Supplement Series* 55 (July 01, 1984 1984): 465. <https://doi.org/10.1086/190963>. <https://ui.adsabs.harvard.edu/abs/1984ApJS...55..465Y>.
- Zhao, Jian-Qi, Guangyu Shi, Huizheng Che, and Guangguang Cheng. "Approximations of the Scattering Phase Functions of Particles." *Advances in Atmospheric Sciences* 23 (October 01, 2006 2006): 802. <https://doi.org/10.1007/s00376-006-0802-y>. <https://ui.adsabs.harvard.edu/abs/2006AdAtS..23..802Z>.